


國立交通大學

材料科學與工程學系

博士論文

奈米結構性材料之製作與合成及其於
直接甲醇燃料電池之應用



**Fabrication and Synthesis of Nanostructured
Materials for Direct Methanol Fuel Cell Applications**

研究生：Jitendra Nath Tiwari

指導教授：潘扶民教授

中華民國 九十八年七月

奈米結構性材料之製作與合成及其於

直接甲醇燃料電池之應用

Fabrication and Synthesis of Nanostructured Materials for

Direct Methanol Fuel Cell Applications

研究生: Jitendra Nath Tiwari

Student: Jitendra Nath Tiwari

指導教授: 潘扶民 博士

Advisor: Dr. Fu-Ming Pan

國立交通大學



Submitted to Department of Materials Science and Engineering

College of Engineering

National Chiao Tung University

in Partial Fulfillment of the Requirements

for the Degree of Doctor of Philosophy

in Materials Science and Engineering

July 2009

Hsinchu, Taiwan, Republic of China

中華民國 九十八年七月

奈米結構性材料之製作與合成及其於直接 甲醇燃料電池之應用

研究生: Jitendra N. Tiwari

指導教授: 潘扶民 博士

國立交通大學

材料科學與工程學系

摘要

現今奈米尺度的科學與科技快速發展下，將化學能轉換成電能與低環境汙染優點的高效率直接甲醇燃料電池(DMFC) 提供了一個新的契機與方向。藉由奈米結構材料的大表面積，提供高分散性的鉑與鉑鈦合金承載，因此提升直接甲醇燃料電池的功率密度。在這論文裡，我們研究奈米結構陽極觸媒的合成技術以及奈米結構觸媒的電催化特性。

製備觸媒載體採用兩個不同的方法，分別為奈米結構材料陽極氧化鋁(AAO)模板以及奈米孔洞的石墨化碳(g-C)。關於氧化鋁(AAO)模板方式，首先在矽晶片上成長矽奈米尖錐(SNCs)和非晶型碳(α -C)覆蓋的矽奈米尖錐陣列，用來做為觸媒的載體，接著電鍍奈米鉑觸媒。有序排列的非晶型碳包覆矽奈米錐 (ACNC) 陣列產生，所造成的氧化鋁孔隙通道陣列安排模式，藉由電漿蝕刻在微波電漿化學氣相沉積(MPCVD)系統，轉移到有氧化鈦 TiO_x 光罩的矽載體。在 MPCVD 過程，一層約 5 奈米厚的 α -C 在矽奈米尖錐上沉澱。為了獲得高電流密度和重量活性，利用雙極性脈衝電鍍粒徑分佈均勻低於 5 奈米的奈米鉑沉積在有秩序的矽奈米尖錐和 α -C 包覆矽奈米尖錐上。藉著包覆一層奈米結晶石墨化碳，可以增加在矽奈米錐上的鉑奈米球分散度。根據電化學測量，奈米結構

對甲醇氧化反應的催化活性優於全部覆蓋像平板狀的陽極。

此外，我們開發了一種新方法，形成奈米孔洞的石墨烯，這是用來作為承載鉑和鉑鈦合金催化劑，所使用的金剛烷火焰。電化學測試結果表明，鉑鈦承載在奈米孔洞的石墨烯對於甲醇電化學氧化有很好的催化活性和穩定性。良好的催化活性歸因於較高表面積的石墨烯。

為了瞭解對於甲醇氧化反應在鉑觸媒的形態上的電催化活性的相關性，藉由在 25°C 下，直接雙極脈衝電化學沉積合成二維和三維鉑奈米結構材料。我們同時成功的在室溫下，合成了不同形狀的奈米鉑，如四面體和立方體在矽基板上。電化學研究中，二維和三維和形狀控制鉑的奈米結構顯示出對於直接甲醇燃料電池效率有潛在的應用。



Fabrication and Synthesis of Nanostructured Materials for Direct Methanol Fuel Cell Applications

Student: Jitendra N. Tiwari

Advisor: Dr. Fu-Ming Pan

Department of Materials Science and Engineering

National Chiao Tung University

Abstract

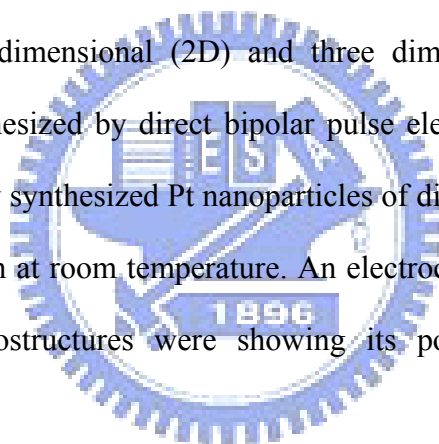
Nanostructured materials can provide a large surface area for the loading of highly dispersed catalyst nanoparticles, such as Pt and Pt-Ru, thereby improving the power density of direct methanol fuel cells (DMFCs). The thesis prepares various nanostructured anode electrocatalysts, and investigates electrocatalytic characteristics of the nanostructured catalysts.

Two different approaches are adopted to prepare electrocatalyst supports, which are anodic aluminum oxide (AAO) templated nanostructured materials and nanoporous graphitic carbon (g-C). For the AAO templation approach, Si nanocones (SNCs) and amorphous carbon (α -C) coated Si nanocones arrays are first fabricated on the Si wafer for the use as the catalyst support, followed by electrodeposition of Pt nanoparticles. Well-ordered α -C coated Si nanocone (ACNC) arrays were produced as a result of the arrangement pattern transfer of AAO pore channel arrays to Si substrates with TiO_x nanomasks by the plasma etch in the microwave plasma chemical vapor deposition (MPCVD) system. A layer of α -C about 5 nm thick was in-situ deposited on the SNCs during the MPCVD process. In order to obtain the high current density and mass activity, well dispersed Pt nanoparticles with a uniform size distribution below 5 nm were deposited on ordered SNC and ACNC by bipolar pulse

electrodeposition. The dispersion of Pt nanoparticles on SNC was improved by coating a nanocrystalline g-C. The electrocatalytic activity of the nanostructured anodes toward methanol oxidation reaction (MOR) are superior to anodes with a blanket surface according to electrochemical measurements.

In addition, we developed a new method to form nanoporous g-C, which was utilized as the support for Pt and Pt-Ru alloy catalysts, by the used of an adamantane flame. Electrochemical tests and results show the Pt-Ru supported on nanoporous g-C had excellent catalytic activity and stability toward methanol electrooxidation. The excellent catalytic activity may be attributed to the higher surface area of g-C.

To investigate the dependence of electrocatalytic activity toward MOR on the morphology of Pt catalyst, the two dimensional (2D) and three dimensional (3D) Pt nanostructured materials were also synthesized by direct bipolar pulse electrochemical deposition at 25°C. We have also successfully synthesized Pt nanoparticles of different shapes such as tetrahedron and cube by fasten silicon at room temperature. An electrochemical study of 2D, 3D and the shape-controlled Pt nanostructures were showing its potential application for efficient DMFCs.



Acknowledgements

Ph.D. study at National Chiao Tung University (NCTU) will be a precious experience in my life. I would like to thank all the people who have supported and helped me during this period.

First of all, I would like to express my sincere thanks to my supervisor, Prof. Fu-Ming Pan, for introducing me to the area of fuel cells and his inspiring and encouraging way to guide me to a deep understanding of knowledge work. Prof. Pan is an excellent teacher and an example of how to do research. His intelligent guidance, invaluable comments and detailed training during the whole work with this dissertation are deeply appreciated. His strict and preciseness in pursuing knowledge and hardworking impressed and encouraged me to fulfill my dissertation in the past years. He has been a great mentor with his enthusiasm, understanding and willingness to help students professionally and personally. I also appreciate Dr. K.-K. Lin and Dr. T.-M. Chen for serving as my experimental supports and for their precious suggestions to my study. I would like to express my thanks to all my group members for their friendship: C.-C. Chang, C.-S. Chen, Y.-F. Hsieh, Y.-M. Chang, C.-H. Lai, K.-D. Ko, Dr. C.-C. Lin, Dr. P.-Y. Kuo, C.-J. Huang and Dr. C.-H. Tsai.

Most of all, I would like to dedicate this work to my parents, my sister and brother for their endless love and supports throughout my life. Their encouragement has been a source of inspiration that led to the completion of this thesis.

The financial support of my Ph.D. research work by a grant from the Ministry of Economic Affairs (MOEA), Taiwan, R.O.C., and NCTU, Taiwan, R.O.C. is grateful acknowledged.

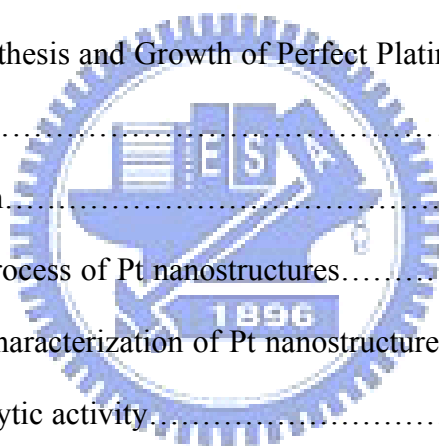
Contents

Abstract (in Chinese).....	I
Abstract (in English)	III
Acknowledgements.....	V
Contents.....	VI
Abbreviations.....	X
Table Captions.....	XIII
Figure Captions.....	XIV
Chapter 1 Introduction.....	1
1.1 Background.....	1
1.2 Motivation.....	3
Chapter 2 Literature Review.....	5
2.1 Fuel cells.....	5
2.1.1 Introduction.....	5
2.1.2 Principles of fuel cells.....	5
2.1.3 Types of fuel cells.....	7
2.2 Direct methanol fuel cells (DMFCs).....	12
2.2.1 Introduction.....	12
2.2.2 Principle of DMFC operation.....	13
2.2.3 DMFC anode.....	15
2.2.4 DMFC cathode.....	17
2.3 Mechanism of methanol oxidation.....	18
2.4 Features.....	19
2.5 Challenges.....	19

2.6 Anode catalysts for DMFC.....	20
2.6.1 Pt nanostructures.....	21
2.6.2 New cost-effective synthesis routes.....	22
2.6.3 Binary and multiple catalysts.....	23
2.6.4 New catalyst supports.....	29
2.7 Pulse electrodeposition.....	30
2.7.1 Pulse waveform.....	30
2.7.2 Potentiostatic bipolar pulse electrodeposition.....	31
2.7.3 Advantages of pulse plating.....	33
2.7.4 Theory of pulse plating.....	34
2.8 Structure of the thesis.....	35
Chapter 3 Experimental methods.....	37
3.1 Experimental flowcharts.....	37
3.2 Deposition of TiN and Al films.....	39
3.3 Anodic aluminum oxide.....	40
3.4 Reactive-ion-etch system.....	41
3.5 MPCVD system.....	43
3.6 Electrodeposition of Pt nanostructures.....	44
3.7 Material analysis methods.....	45
3.7.1 Raman spectroscopy.....	45
3.7.2 SEM.....	45
3.7.3 TEM.....	46
3.7.4 AES and XPS.....	48
3.8 Electrochemical measurements.....	49
Chapter 4 Pt Nanoparticles Supported on Ordered Si Nanocones as Catalyst for Methanol Oxidation.....	50

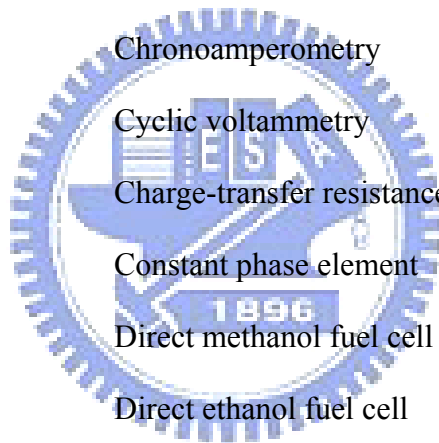
4.1 Introduction.....	50
4.2 Fabrication procedure of the SNC array.....	51
4.3 Electrodeposition of Pt nanoparticles on SNC array.....	53
4.4 Structural characterization of SNC array.....	53
4.5 Structural characterization of Pt/SNC array.....	56
4.6 Electrochemical characterization.....	59
4.7 Summary.....	65
Chapter 5 Fabrication and Electrocatalytic Properties of Pt Nanoparticles Electrodeposited on Amorphous Carbon Coated Silicon Nanocones.....	66
5.1 Introduction.....	66
5.2 Fabrication procedure of the ACNC array.....	67
5.3 Electrodeposition of Pt nanoparticles.....	70
5.4 Material properties of the Pt-ACNC electrode.....	71
5.5 Electrocatalytic activity.....	76
5.6 Summary.....	83
Chapter 6 Novel New Approach to the Synthesis of Nanoporous Graphitic Carbon as a Unique Electrocatalysts Support for Methanol Oxidation.....	85
6.1 Introduction.....	85
6.2 Synthesis of 3D nanoporous g-C, Pt/3D nanoporous g-C and Pt ₅₀ -Ru ₅₀ /3D nanoporous g-C.....	86
6.3 Physico-chemical characterization.....	87
6.4 Electrocatalytic activity.....	92
6.5 Summary.....	98
Chapter 7 Synthesis of 2D Continuous Pt Island Networks for Methanol Electrooxidation.....	99
7.1 Introduction.....	99
7.2 Fabrication steps for the continuous Pt island network electrode.....	100

7.3 Structural characterization	101
7.4 Electrochemical measurements.....	103
7.5 Summary.....	108
Chapter 8 Synthesis of 3D Platinum Nanoflowers and Their Electrochemical Characteristics.....	110
8.1 Introduction.....	110
8.2 Synthesis of the 3D Pt nanoflowers.....	110
8.3 Characterization of the 3D Pt nanoflowers.....	111
8.4 Electrochemical characteristics.....	114
8.5 Summary.....	121
Chapter 9 Controlled Synthesis and Growth of Perfect Platinum Nanocubes by Fasten Silicon at NTP.....	122
9.1 Introduction.....	122
9.2 Synthesis process of Pt nanostructures.....	123
9.3 Structural characterization of Pt nanostructures.....	124
9.4 Electrocatalytic activity.....	136
9.5 Summary.....	139
Chapter 10 Conclusions and Future Works.....	140
10.1 Conclusions.....	140
10.2 Future Works.....	144
References.....	146
Appendix.....	174
List of Publications.....	174

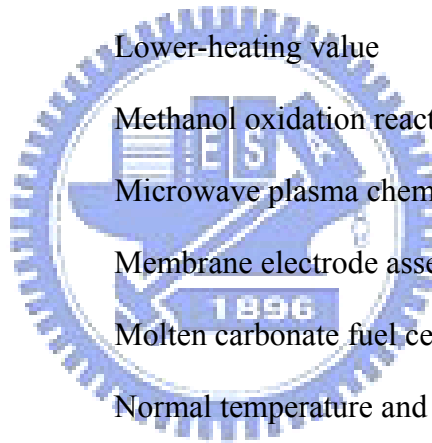


Abbreviations

AAO	Anodic aluminum oxides
ACNC	Amorphous carbon coated Si nanocone
α -C	Amorphous carbon
AFC	Alkaline fuel cell
E_c	Average current density
AES	Auger electron spectroscopy
BPPE	Bipolar potentiostatic pulse electrodeposition
CNT	Carbon nanotube
CA	Chronoamperometry
CV	Cyclic voltammetry
R_{ct}	Charge-transfer resistance
CPE	Constant phase element
DMFC	Direct methanol fuel cell
DEFC	Direct ethanol fuel cell
DMF	Dimethyl formamide
DC	Direct current
EOR	Ethanol oxygen reaction
EDX	Energy-dispersive X-ray analysis
EELS	Electron energy loss spectroscopy
EIS	Electrochemical impedance spectroscopy
ESA	Electroactive surface area
F	Faraday's constant
ΔG	Free energy change
FCC	Face center cubic



FS	Fasten silicon
FFT	Fast Fourier transform
g-C	Graphitic carbon
Q_H	Hydrogen adsorption charge
HDP	High-density plasma
HRTEM	High-resolution TEM
HHV	Higher-heating value
V_H	High potential
ICP-RIE	Inductively coupled plasma reactive ion etch
V_L	Lower potential
LHV	Lower-heating value
MOR	Methanol oxidation reaction
MPCVD	Microwave plasma chemical vapor deposition
MEA	Membrane electrode assembly
MCFC	Molten carbonate fuel cell
NTP	Normal temperature and pressure
n	Number of moles
η	Overpotential
η_o	Overpotential at the exchange potential
ORR	Oxygen reduction reaction
PPE	Potentiostatic pulse electrodeposition
T_{on}	Potential on time
T_{off}	Potential off time
PAFC	Phosphoric acid fuel cell
PEMFC	Polymer electrolyte membrane fuel cells
PBPP	Potentiostatic bipolar pulse plating



PRC	Pulse reverse current
RIE	Reactive-ion-etch
E_r	Reversible potential
E_r°	Reversible cell voltage
SCE	Saturated calomel electrode
SAED	Selected area electron diffraction
SAD	Selected area electron diffraction
R_s	Solution resistance
SOFC	Solid oxide fuel cell
SNC	Si nanocone
SEM	Scanning electron microscope
2D	Two dimensional
3D	Three dimensional
TiO_x	Titanium oxide
TEM	Transmission electron microscopy
XPS	X-ray photoelectron spectroscopy



Table Captions

Table 2-1 Compilation of calculated segregation energies on the closest packed surface of all binary combinations of the transition metals.....	25
Table 2-2 Shifts in <i>d</i> -band centres of surface impurities (A) and overlayers (B) relative to the clean metal values (bold).....	25
Table 2-3 Possible occurrence of segregation and possible shift in <i>d</i> -band centre for the elements of the trimetallic Pt-Ru-M alloy with metals (M) as Mo, W, Co, Fe, Ni, Cu, Sn and Au.....	28



Figure Captions

Figure 2-1 Simplistic representation of a various types of fuel cells.....	8
Figure 2-2 Schematic diagram of the DMFCs.....	14
Figure 2-3 TEM images of Pt hollow nanospheres.....	22
Figure 2-4 The simple template-free electrochemical lithiation synthesis of nanoporous structures.....	23
Figure 2-5 shows the electronegativities (eV) of the transition metals.....	24
Figure 2-6 shows the Bulk Wigner-Seitz radius [a.u.] of the transition metals.....	24
Figure 2-7 shows the schematic diagram of apparatus for potentiostatic measurements; E, controlled potential; e ₁ , test electrode; e ₂ , reference electrode; e ₃ , counter electrode.....	32
Figure 2-8 shows the variation of current with time during potentiostatic electrolysis.....	32
Figure 2-9 shows the schematic diagram of potential pulse waveform and pulse-current waveform.....	33
Figure 3-1 Experimental flowchart of fabrications and analyses of Pt/SNC and Pt/ACNC arrays.....	38
Figure 3-2 Experimental flowchart of fabrications and analyses of Pt-Ru/g-C/Si, 2D Pt networks/Si and 3D Pt nanoflowers/Si.....	39
Figure 3-3 Experimental flowchart of synthesis and analyses of shape-controlled Pt nanoparticles.....	40
Figure 3-4 Schematic diagram of experiment setup for aluminum anodization.....	41
Figure 3-5 Schematic diagram of ICP chamber.....	42

Figure 3-6 Schematic diagram of the bias assisted microwave plasma chemical vapor deposition system.....	43
Figure 3-7 Schematic diagram of the electrochemical deposition setup.....	44
Figure 3-8 Schematic drawing of the basic principle of the SEM.....	46
Figure 3-9 Schematic diagram of the TEM image modes (a) Bright field image (b) Dark field image.....	47
Figure 3-10 Schematic diagram of the electrochemical measurements setup.....	49
Figure 4-1 shows the fabrication scheme of SNC arrays: (a) deposition of TiN and Al thin film on the Si wafer by sputter deposition and thermal evaporation, respectively, (b) anodic oxidation of the Al film and formation of TiO _x nanodots, (c) removal of the AAO by wet etch, (d) reactive ion etch (RIE) of the remaining TiN and the Si substrate, and (e) formation of the SNC arrays.....	52
Figure 4-2 shows the side-view SEM images of the fabrication of SNC arrays: (a) TiO _x nanomasks after the removal of the AAO layer by wet etch, (b) the TiO _x /TiN/SNC arrays after the RIE etch by SF ₆ , Cl ₂ and O ₂ for 40 sec. and (c) removal of the oxide layer by wet chemical etch and the formation of highly ordered SNC arrays.....	54
Figure 4-3 shows (a) TEM image of the SNC array and (b) high-resolution TEM image of the SNC array in which the inset reveals the selected area diffraction pattern.....	55
Figure 4-4 shows SEM images of the SNC array with electrodeposited Pt nanoparticles; (a) a side view, and (b) cross-sectional view.....	57
Figure 4-5 shows the XPS spectrum of the Pt/SNC arrays.....	58
Figure 4-6 shows HRTEM image of the Pt/SNC array in which the inset reveals the selected area diffraction pattern of the nanocone.....	58
Figure 4-7 EELS mapping images of (a) Silicon, and (b) Pt for the Pt nanoparticles loaded SNCs.....	59

Figure 4-8 CO stripping cyclic voltammograms of (a) Pt nanoparticles electrodeposited on the ordered SNCs and (b) the Pt film electrodeposited on the flat silicon substrate in a CO saturated 1M H ₂ SO ₄ solution. The scan rate is 20 mVs ⁻¹	60
Figure 4-9 Cyclic voltammograms for Pt/SNC electrode in 1M H ₂ SO ₄ aqueous solution at room temperature and with a scan rate of 25 mVs ⁻¹ : (a) the 2 nd cycle and (b) the 1000 th cycle.....	61
Figure 4-10 shows the plot of electroactive surface area (ESA) as a function of the number of the cyclic voltammetric scan for (a) the Pt film electrodeposited on the flat Si substrate and, (b) the ordered Pt/SNC electrode.....	61
Figure 4-11 shows the cyclic voltammograms of (a) the Pt catalyst nanoparticles on the ordered SNC array and (b) the Pt film electrodeposited on the flat silicon substrate in an argon saturated 1 M CH ₃ OH/1 M H ₂ SO ₄ aqueous solution. The scan rate is 25mVs ⁻¹	62
Figure 4-12 shows the chronoamperometric response of (a) Pt nanoparticles electrodeposited on the ordered SNCs, and (b) the Pt film electrodeposited on the flat Si substrate in a saturated 1 M CH ₃ OH/1 M H ₂ SO ₄ aqueous solution at 0.3V (SCE) for 2 h. The scale of curve b is multiplies by 100.....	63
Figure 5-1 shows the fabrication processes of the ordered α -C coated SNC array: (a) deposition of TiN and Al thin films on the Si wafer by sputter deposition and thermal evaporation, respectively, (b) formation of the porous AAO template (c) formation of TiO _x nanodots in the AAO pore channels, (d) removal of AAO by wet etch, (e) RIE of the remaining TiN and silicon substrate, forming Si nanocones, and (f) deposition of the α -C layer on SNCs by MPCVD.....	68
Figure 5-2 shows the side-view SEM image of TiO _x nanopillars after the removal of the AAO layer by wet etch. The inset shows the plane-view SEM image of TiO _x nanopillar arrays.....	69
Figure 5-3 shows the side-view SEM images of the α -C coated SNC array (A) before and (B) after the electrodeposition of Pt nanoparticles.....	72
Figure 5-4 shows TEM images (A) Bright-field TEM image of the α -C coated SNC with electrodeposited Pt nanoparticles, (B) high resolution TEM image of the α -C coated SNC with Pt nanoparticles; (C) the SAD pattern, and (D) bright-field image of the	

α -C coated SNC without the Pt nanoparticle.....	73
Figure 5-5 shows the wide scan XPS of the Pt nanoparticles deposited on the ACNC array, (B) the C(1s) XPS spectrum with curve fitted peaks, and (C) the Pt(4f) XPS spectrum.....	74
Figure 5-6 shows the Raman spectrum of the α -C coated SNCs without Pt nanoparticles...	75
Figure 5-7 shows the room temperature cyclic voltammograms of (a) Pt/ACNC and (b) Pt film/Si electrodes measured at 25 mV s ⁻¹ in 1 M H ₂ SO ₄	76
Figure 5-8 shows the CO stripping cyclic voltammograms of the Pt/ACNCs electrode in a CO saturated 1 M H ₂ SO ₄ solution. The scan rate was 25 mV s ⁻¹	77
Figure 5-9 (A) Current density and mass activity of the Pt/ACNC electrode (solid rectangle) and the Pt film/Si electrode (open rectangle). (B) Loss of the Pt electrochemical surface area of (a) the Pt/ACNC electrode and (b) the Pt film/Si electrode as a function of the number of CV cycles in argon saturated 1 M H ₂ SO ₄ aqueous solution at room temperature (scan rate: 25 mV s ⁻¹).....	79
Figure 5-10 (A) Cyclic voltammograms of ORR in O ₂ saturated 1 M H ₂ SO ₄ aqueous solution at 25°C for (a) the Pt/ACNC electrode and (b) the Pt film/Si electrode; and (B) ORR current density loss as a function of the number of CV cycles in oxygen saturated 1 M H ₂ SO ₄ at room temperature for (a) the Pt/ACNC electrode and (b) the Pt film/Si electrode (scan rate: 25 mV s ⁻¹).....	82
Figure 6-1 shows the synthesis scheme of 3D nanoporous g-C: (a) the Si wafer was cut into 2 x 2 cm ² dimension (b) SiO ₂ layer was removed by treating with 10 % HF for 5 min and dried by N ₂ gas (c) the cleaned sample was immediately placed in front of flame adamantane for 7 minute, and (d) finally, sample was heated at 300°C for one hour to obtain a good depositing of 3D nanoporous g-C over the silicon substrate.....	87
Figure 6-2 shows the SEM image of the resulting 3D nanoporous g-C.....	87
Figure 6-3 Raman spectrum of 3D nanoporous g-C deposited on Si substrate.....	88
Figure 6-4 shows the plane-view SEM images (A) Pt/3D nanoporous g-C, and (B) typical Pt ₅₀ -Ru ₅₀ /3D nanoporous g-C.....	89

Figure 6-5 shows the TEM images (A) Pt/3D nanoporous g-C, and (B) typical Pt ₅₀ -Ru ₅₀ /3D nanoporous g-C.....	90
Figure 6-6 shows the EDX spectrum of the Pt catalyst on the g-C.....	91
Figure 6-7 shows the EDX spectrum of the Pt ₅₀ -Ru ₅₀ alloy catalyst on the g-C, showing the presence of Pt and Ru nanoparticles on the 3D nanoporous g-C.....	91
Figure 6-8 shows the XPS survey spectrum of the 3D nanoporous g-C supported Pt and Pt-Ru alloy catalysts.....	92
Figure 6-9 shows the cyclic voltammograms of the Pt ₅₀ -Ru ₅₀ /3D nanoporous g-C and Pt/3D nanoporous g-C electrodes in aqueous solution in N ₂ saturated aqueous solution of 1 M H ₂ SO ₄ . The scan rate was 25 mV s ⁻¹	93
Figure 6-10 shows the CO-stripping CVs in a CO saturated 1 M H ₂ SO ₄ solution (A) the 3D nanoporous g-C electrode; and (B) the Pt ₅₀ -Ru ₅₀ /3D nanoporous g-C electrode. The scan rate was 25 mV s ⁻¹	95
Figure 6-11 (A) CVs of the Pt ₅₀ -Ru ₅₀ /3D nanoporous g-C and Pt/3D nanoporous g-C electrodes in aqueous solution of 1 M H ₂ SO ₄ - 1 M CH ₃ OH at a scan rate of 25 mV s ⁻¹ , and (B) Chronoamperometric curves for the Pt ₅₀ -Ru ₅₀ /3D nanoporous g-C and Pt/3D nanoporous g-C electrodes in aqueous solution of 1 M H ₂ SO ₄ - 1 M CH ₃ OH at a constant potential of 0.4 V vs. SCE.....	97
Figure 7-1 shows a schematic illustration of the continuous Pt island network on the flat silicon substrate. The right hand side exhibits the bifunctional mechanism of CO electrooxidation. The adsorbed oxygen containing species on the surface of SiO ₂ can facilitate the oxidation of CO-like poisoning species adsorbed on the active Pt sites.....	100
Figure 7-2 shows the SEM images: (A) blanket Pt on flat Si substrate; and (B) Ru on blanket Pt/Si.....	101
Figure 7-3 shows the SEM image of the continuous Pt island network on the flat silicon substrate.....	102
Figure 7-4 shows the x-ray photoelectron spectrum (XPS) of (a) blanket Pt/Si; (b) Ru	

decorated blanket Pt; and (c) continuous Pt island network.....	102
Figure 7-5 shows the CO stripping cyclic voltammetry curves recorded at room temperature in a CO saturated 1 M H ₂ SO ₄ solution at a scan rate of 20 mV s ⁻¹	103
Figure 7-6 shows the cyclic voltammograms in 1 M CH ₃ OH+1 M H ₂ SO ₄ at a scan rate of 25 mV s ⁻¹	105
Figure 7-7 shows the chronoamperometry curves in 1 M CH ₃ OH+1 M H ₂ SO ₄ at the potential of 0.4 V.....	106
Figure 7-8 shows the Tafel plots for the electrochemical oxidation of 1 M CH ₃ OH/1 M H ₂ SO ₄ aqueous solution at a scan rate of 1 mV s ⁻¹	107
Figure 7-9 shows the electrochemical impedance spectra in 1 M CH ₃ OH + 1 M H ₂ SO ₄ at the potential 0.3 V. The inset in figure shows the equivalent circuit model.....	108
Figure 8-1 shows the scanning electron micrographs of the 3D Pt nanoflower on the Si substrate.....	111
Figure 8-2 shows the XPS survey spectrum of the 3D Pt nanoflower on the silicon substrate.....	112
Figure 8-3 shows the energy window of Pt (4f) electrons.....	112
Figure 8-4 shows the TEM of nanopetals mechanical scratched off the 3D Pt nanoflower/Si sample. The inset shows the SAED pattern, and (B) a high resolution TEM image of a nanopetal.....	113
Figure 8-5 shows the CVs of the 3D Pt nanoflower/Si and the Pt thin film /Si electrodes in the 1 M H ₂ SO ₄ solution. The scan rate was 20 mV s ⁻¹	115
Figure 8-6 shows the CVs of the 3D Pt nanoflower/Si and the Pt thin film /Si electrodes in the 1 M CH ₃ OH/1 M H ₂ SO ₄ solution. The scan rate was 25 mV s ⁻¹	117
Figure 8-7 shows the CO stripping CVs of the 3D Pt nanoflower/Si and the Pt thin film /Si electrodes in the CO saturated 1 M H ₂ SO ₄ solution. The scan rate was 25 mV s ⁻¹	118

- Figure 8-8 shows the chronoamperograms of the 3D Pt nanoflower/Si and the Pt thin film /Si electrodes in the 1 M CH₃OH/1 M H₂SO₄ solution at the polarization potential of 0.4 V.....119
- Figure 8-9 shows the Nyquist plot of electrochemical impedance spectra (EIS) of the 3D Pt nanoflowers and the Pt thin film catalysts in the 1 M CH₃OH + 1 M H₂SO₄ solution at the potential of 0.3 V. Insert is the equivalent circuit model used to fit the impedance spectra..... 120
- Figure 9-1 shows the synthesis procedure of Pt nanostructures: (A) the Si-wafer is cut into 1.5 x 2 cm² samples, (B) dipped into HF aqueous solution for 5 minutes in order to remove any native oxide layer on the Si samples, (C) then the polished side of cut two identical piece of the Si-wafer was fasten together and dipped into stirred 1 M H₂PtCl₆+ 1 M H₂SO₄ aqueous solutions, {after stirring for (a) 3 hr and (b) 5 hr to form the truncated (cubes + tetrahedron) and truncated cubes respectively}, (D) furthermore, the perfect Pt nanocubes produced by mixing 1 M HCl into 1 M H₂PtCl₆+ 1 M H₂SO₄ aqueous solutions (vigorous stirring for 5 hr)123
- Figure 9-2 shows the SEM images of truncated Pt (cubes + tetrahedron) deposited on the FS sample at NTP for (A) 10, (B) 13, and (C) 15 min; (solution stirring for 3 hr). (D) Low-magnification TEM image of individual truncated Pt tetrahedron synthesized with the FS sample. (E) High-resolution TEM lattice image of the square region in single truncated Pt tetrahedron. The *d*-spacing between the fringes was ~0.23 nm, which was identified {111} plane of Pt; the inset shows the FFT of the lattice image gives the optical diffractogram, which clearly shows the presence of {111} plane 1 2 6
- Figure 9-3 shows the SEM images of truncated Pt nanocubes deposited on the FS sample at NTP for (A) 13, (B) 15, and (C) 20 min; (solution stirring for 5 hr) 127
- Figure 9-4 (A) Low-magnification TEM image of individual truncated Pt nanocubes and (B) High-resolution TEM lattice image of the square region in single truncated Pt nanocubes. The *d*-spacing between the fringes was ~0.20 nm, which was identified {200} plane of Pt..... 127
- Figure 9-5 Shows the SEM images of Pt nanostructures formed by immersing FS samples into aqueous solutions of H₂SO₄- H₂PtCl₆ for 20 min at NTP (stirring time = 5 h). The images clearly show the presence of Pt nanocrystals with cube and rod shapes. The mechanism of rod growth is Ostwald ripening, define as the dissolution of the fine

particles and their redeposition on large particles [198]. According to the well-known Gibbs–Thomson law, there is energy difference between large particles and small particles result in vanishing of smaller particles and formation of longer nanorods with the reaction in progress [199]128

Figure 9-6 FFT image obtained from fig. 3E. The FFT pattern exhibits only a diffraction spots, revealing a good single-crystal property..... 128

Figure 9-7 SAED image obtained from fig. 9-5 (A). SAED pattern also confirms the single crystal structure of the truncated Pt nanocubes.....129

Figure 9-8 shows the SEM images of perfect Pt nanocubes deposited on the FS sample at NTP for (A) 10, (B) 13, and (C) 15 min; (solution stirring for 5 hr) 130

Figure 9-9 shows the typical XPS survey spectrum of perfect Pt nanocubes deposited on the surface of FS sample. XPS clearly show the presence of Pt nanocube catalyst..... 130

Figure 9-10 XPS deconvoluted Pt(4f) doublet of perfect Pt nanocubes deposited on the surface of FS sample. The peaks can be attributed to Pt(4f_{7/2}) and Pt(4f_{5/2}) of metallic Pt, respectively..... 131

Figure 9-11 Cl(2p) XPS narrow scan spectra of the perfect Pt nanocubes deposited on the surface of FS sample. This figure clearly shows the complete absence of chloride ion at the perfect Pt nanocubes..... 132

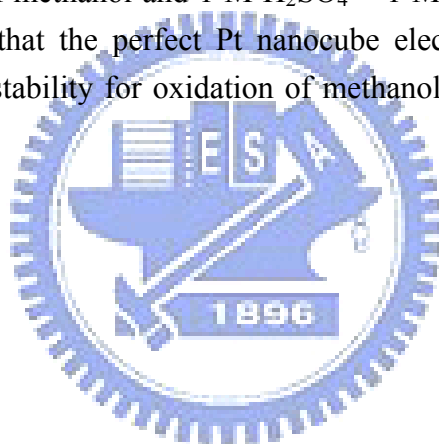
Figure 9-12 (A) High-resolution TEM image of individual perfect Pt nanocube. The *d*-spacing between the fringes was ~0.20 nm, which was identified {200} plane of Pt; the inset shows the FFT of the lattice image gives the optical diffractogram, which clearly shows the presence of {200} plane and (B) Corresponding SAED pattern, showing the single crystal structure of the perfect Pt nanocubes..... 133

Figure 9-13 Plane views SEM images of the silicon after electroless deposition of Pt for 6 h. Compositions of solutions were (A) 2 M H₂PtCl₆ + 1 M H₂SO₄ + 1 HCl and (B) 2 M H₂PtCl₆ + 1 M H₂SO₄. Both the aqueous solution was stirred continuously for 5 h..... 134

Figure 9-14 (A) FE-SEM image of the electrodeposited polycrystalline Pt nanosphere on silicon substrate. (B) HRTEM image recorded from a region at the edge of a

sphere, showing that the surfaces are covered by Pt nanoparticles of a few nanometers in size, and the Pt nanocrystallites dominated by {111}-type exposed surface. (C) SAED pattern showing that the formed nanoparticles are polycrystalline. The as-labelled diffraction rings 1–4 correspond to {111}, {200}, {220}, and {311} reflections, respectively, all of which reveal the fcc crystal structure.....137

Figure 9-15 Comparison of catalytic activity and stability of the Pt nanoshapes. (A) and (B) Cyclic voltammograms for (a) perfect Pt nanocubes, (b) truncated Pt nanocubes, (c) truncated Pt (cubes + tetrahedron), and (d) spherical Pt nanoparticles were obtained at a scan rate 25 mVs^{-1} in $1 \text{ M H}_2\text{SO}_4 + 1 \text{ M methanol}$ and $1 \text{ M H}_2\text{SO}_4 + 1 \text{ M ethanol}$ respectively. (C) and (D) Chronoamperometric curves for (a) perfect Pt nanocubes, (b) truncated Pt nanocubes, (c) truncated Pt (cubes + tetrahedron), and (d) spherical Pt nanoparticles were recorded at 0.40 V in oxygen free $1 \text{ M H}_2\text{SO}_4 + 1 \text{ M methanol}$ and $1 \text{ M H}_2\text{SO}_4 + 1 \text{ M ethanol}$, respectively. The results demonstrate that the perfect Pt nanocube electrode showed excellent catalytic activity and stability for oxidation of methanol and ethanol.....138



Chapter 1

Introduction

1.1 Background

One of the great challenges in the 21st century is unquestionably electrochemical energy conversion. In response to the needs of modern society and emerging ecological concerns, it is highly desirable to find new, low-cost and environmentally friendly electrochemical energy conversion for powering an increasingly diverse range of applications, ranging from portable power for consumer electronics to potential transport applications [1-2]. This allowed for rapid research in electrochemical energy conversion devices such as polymer electrolyte membrane fuel cells (PEMFCs), direct methanol fuel cells (DMFCs), and direct ethanol fuel cells (DEFCs). As the performance of these devices depends intimately on the properties of their materials, considerable attention has been given to the research and development of key materials [2-7]. Micrometer sized bulk materials are reaching their inherent limits in performance and cannot fully satisfy the increasing desires of consumer devices. Therefore, rapid development of new materials with high performance is essential. Nanostructured materials are becoming increasingly important in the development of electrochemical energy conversion devices and hence have attracted great interest in recent years. A variety of nanometer size effects have been found in the materials used in electrochemical energy conversion, which can be divided into two types: (i) ‘trivial size effects’, which rely solely on the increased surface-to volume ratio and (ii) ‘true size effects’, which also involve changes of local materials properties [7]. Many approaches are used to accomplish nanostructures for DMFC applications. One approach to the synthesis of nanostructured materials has centered on the replication of nanostructured silica templates followed by template removal. Various lengths and shapes of monometallic nanowires templated by various silica structures have been reported [8–10]. Bimetallic structures templated by nanostructured silica have also been

reported which include Pt–Rh and Pt–Pd nanowires [11]. The synthesis of nanostructured Pt–Ru electrocatalysts includes the synthesis of a bimetallic Pt–Ru nanowire network templated by mesoporous silica, specifically SBA-15 [12]. The SBA-15 silica template is synthesized separately and is then immersed in a solution of Pt and Ru precursors. This infiltration procedure has to be repeated numerous times, usually about ten, before full pore infiltration can be accomplished [12]. Following this approach, a significant increase in the electrocatalytic current was found when compared to a commercial Pt–Ru black. Impregnation synthesis of a bimetallic network in mesoporous silica presents an interesting material design approach, although it is limited in application due to its complexity, parameter variability and time-consuming synthesis. Alternative approach that utilizes the advantages of anodic aluminum oxide (AAO) templates for the synthesis of Pt and Pt alloy catalysts nanostructured materials [13, 14]. A mesoporous platinum film was prepared by electrodeposition of Pt into a liquid crystal surfactant template [15-18]. With this method it is easy to control the size of the porous structures, but it is difficult and time-consuming to implement and to scale up the liquid crystal template techniques. Other promising areas of nanostructure development are in microemulsions [19], lyotropic liquid crystalline phases [20], microwave irradiation [21], sonochemistry [22, 23], electrochemical deposition [24], and sol-gel processing [25]. Recent work has been done by Liang et al. [3] to make hollow nanospheres of Pt by a redox replacement reaction from Co nanosphere precursors. Additionally, Jiang and Kucernak [26] reported high surface area mesoporous microspheres of Pt/Ru by electrocoreduction of the two precursor salts within a surfactant template. These works are only a fraction of the entire effort in this field, and it is expected that such routes will bridge the gap to the discovery of new materials.

1.2 Motivation

Recently, substantial attention has been paid to the development of fuel cells with solid polymeric electrolytes that operate on liquid fuel, in particular, methanol, in which methanol directly oxidizes on the anode, i.e. the so-called direct methanol fuel cells (DMFCs). Although the technology of such fuel cells was developed to an extent, some fundamental problems remain unclear and only their solution can result in wide-scale commercialization of DMFC, especially as the efficient current sources for portable devices. The most important problem is the development of efficient catalysts, which would provide the long-term (for several thousand hours) operation of fuel cells without sacrificing their characteristics. However, their sluggish electrochemical reactions result in inevitable high Pt-catalyst loading and low catalyst utilization, in addition to the well-known methanol crossover problem. It is essential to improve Pt-catalyst utilization in DMFCs, because the high cost of Pt-based catalyst understandably dominates the material cost of membrane electrode assembly (MEA) for low temperature fuel cells. There are two ways to overcome this problem. First, the synthesis of ordered nanostructure materials with high surface area as supports of Pt or Pt alloy catalysts. Secondly, direct synthesis of nanostructure materials (Pt or Pt alloy catalysts) with high surface area. Moreover, an appropriate synthetic route ultimately determines the success or failure of nanostructured materials synthesis, because the physical properties and applications of nanostructured materials are heavily dependent upon their synthetic method. As a result, there have been tremendous efforts toward the development of new synthetic methodologies for several decades.

In this study, we have proposed very simple methods for fabrication and synthesis of nanostructured materials for supporting nanoparticles Pt or Pt alloy catalysts. Well-ordered arrays of Si nanocones (SNCs) were fabricated using the combination of anodic aluminum oxide (AAO) templating and dry etching techniques. The self-organized nanodot array of

titanium oxide (TiO_x) in use is prepared from TiN/Al film on the silicon substrate by electrochemical anodization. This novel method can not only reveal highly ordered nanostructures but also overcome lithography limitation. TiO_x nanodots were then used as nanomasks to etch TiN layers and the underlying layers in an inductively coupled plasma reactive ion etch (ICP-RIE) system. The ICP-RIE is a plasma-based dry etching technique characterized by a combination of physical sputtering and chemical activity of reactive species. Owing to the well-controlled etching depth and profile for nanostructures, TiO_x nanodots were used as nanomasks to fabricate well ordered SNC arrays. Then Pt nanoparticles were electrochemically deposited on the SNCs for fuel cell electrode. An amorphous carbon coated Si nanocones (ACNCs) were used to obtain well-dispersed Pt nanoparticles with high mass activity, where bipolar pulse electrodeposition was used to deposit Pt nanoparticles.

In order to increase the performance of DMFCs electrode, we synthesized the graphitic carbon (g-C) with a high surface area on the Si substrate and thus were used as a support of Pt and Pt-Ru alloy catalysts.

We have also developed new simple and efficient techniques for direct synthesis of Pt nanostructures. In this regards, we have synthesized the two-dimensional (2D) continuous Pt island networks and three-dimensional (3D) Pt nanoflowers for DMFCs electrodes. In addition, we have synthesized the shape-controlled Pt nanoparticles by fasten silicon and study there electrochemical performance for DMFCs application.

Chapter 2

Literature Review

2.1 Fuel cells

2.1.1 Introduction

The first fuel cell was demonstrated by Sir William Grove in 1839. Namely, a fuel cell is an electrochemical cell that directly converts chemical energy into electric energy. Hence, a fuel cell is a converter which enables the energy conversion via the electrochemical reaction, like the well-known electrochemical batteries. However, fuel cells are unique in that they consume reactants, which must be replenished, while batteries store electrical energy chemically in a closed system. Additionally, while the electrodes within a battery react and change as a battery is charged or discharged, a fuel cell's electrodes are catalytic and relatively stable. But its commercialization has been limited by high cost, material limitations, and low operational efficiencies. The first successful application of a fuel cell was demonstrated by NASA in the Gemini and Apollo space programs as a way to deliver potable water to the astronaut crew [27]. Today research has focused on developing fuel cells for stationary, automotive, portable, and military power applications. Fuel cells are attractive because they provide an innovative alternative to current power sources with higher efficiencies, renewable fuels, and a lower environmental cost.

2.1.2 Principles of fuel cells

A schematic representation of a various types of fuel cells is shown in Fig. 2-1. The main active components of a fuel cell are fuel electrode (anode), oxidant electrode (cathode), and electrolyte sandwiched between them. Figure 2-1 shows the basic operational principle of a fuel cell with the reactant/product gases and the ion conduction flow directions. In a typical

fuel cell, fuels are fed continuously to the anode (negative electrode) and an oxidant (i.e., pure oxygen or air) is fed continuously to the cathode (positive electrode); the electrochemical. Reactions take place at the electrodes. The fuel is oxidized at the anode to give up electrons which travel through the external load to provide the power while ions migrate through the electrolyte from one electrode to the other. On the cathode, the oxidant combines with the ions and incoming electrons by a reduction reaction to complete the process. Usually, the basic physical structure of an electrode consists of an electrolyte layer in contact with a porous anode and cathode on each side. Triple phase boundaries are established among the reactants, electrolyte, and catalyst in the region of the porous electrode. The nature of this interface plays a critical role in the electrochemical performance of a fuel cell, particularly in those fuel cells with liquid electrolytes. In such fuel cells, the reactant gases diffuse through a thin electrolyte film that wets portions of the porous electrode and react electrochemically on their respective electrode surface. In order to maximize the efficiency of fuel cell, a delicate balance must be maintained among the electrode, electrolyte, and gaseous phases in the porous electrode structure. The electrolyte in fuel cell not only transports dissolved reactants to the electrode, but also conducts ionic charge between the electrodes and thereby completes the cell electric circuit. In addition, it also provides a physical barrier to prevent the fuel and oxidant gas streams from directly mixing.

The simplest and most common reaction encountered fuel cell reaction is:



From a thermodynamic point of view, the maximum-electric work obtained from the above reaction corresponds to the free-energy change (available energy in an isothermal process) of the reaction. Gibbs-free energy is more useful than the change in Helmholtz-free energy, since it is more practical to carry out chemical reactions at a constant temperature and pressure rather than constant temperature and volume.

The above reaction is spontaneous and is also thermodynamically favored because the free

energy of the products is less than that of the reactants. The standard free energy change of the fuel cell reaction is represented by the equation:

$$\Delta G = -nFE_r \quad (2.2)$$

where ΔG is the free energy change, n is the number of moles of electrons involved, E_r is the reversible potential, and F is Faraday's constant. If the reactants and the products are in their standard states i.e., at a temperature of 25°C and 1 atm pressure, the equation can be rewritten as:

$$\Delta G^\circ = -nFE_r^\circ \quad (2.3)$$

Accordingly, the reversible cell voltage (E_r°) of a fuel cell can be calculated from:

$$E_r^\circ = -\Delta G^\circ/nF \quad (2.4)$$

For the reaction (2.1), ΔG° is -229 kJ/mol, $n = 2$, $F = 96,500$ C/eq and, hence, the calculated value of E_r° is ~1.29 V.

Water is the product of the fuel cell reaction and can be produced either as liquid water or steam. The higher-heating value (HHV) corresponds to the released heat when water is produced as liquid water and the lower-heating value (LHV) when water is produced as steam. The difference in the HHV and LHV is the heat required to vaporize the product water.

2.1.3 Types of fuel cells

There are a number of different fuel cells being investigated, which are classified based on the electrolyte used. Each type of fuel cell has intended applications based on power output limitations, operating temperature, and size of the power system. There are presently five major fuel cell types at varying stages of development and commercialization: (1) alkaline fuel cell (AFC), (2) phosphoric acid fuel cell (PAFC), (3) solid oxide fuel cells (SOFC), (4) molten carbonate fuel cells (MCFC), and (5) polymer electrolyte membrane fuel cells (PEMFC). Figure 2-1 shows the operational characteristics of each fuel cell family. A brief

description of different electrolyte cells is as follows.

[1] Alkaline fuel cell (AFC)

The AFCs typically utilize KOH as the electrolyte with the concentration of 35-50 wt% and have the highest electrical efficiency of all fuel cells but suffer economically from the necessity for ultra pure gases for its fuel. The electrolyte is retained in a matrix (usually asbestos), and a wide spectrum of electrocatalysts can be used (e.g., Ni, Ag, metal oxides, spinals, and noble metals). The operating temperature for AFCs is below 100°C, but higher temperatures are desirable for improved hydrogen oxidation kinetics. Furthermore, the AFCs are among the first fuel cells to have been studied and taken into development for practical applications, and they are the first type of fuel cells to have reached successful routine applications, mainly in space programs such as space shuttle missions. However, almost all of the AFC development activities have come to an end now.

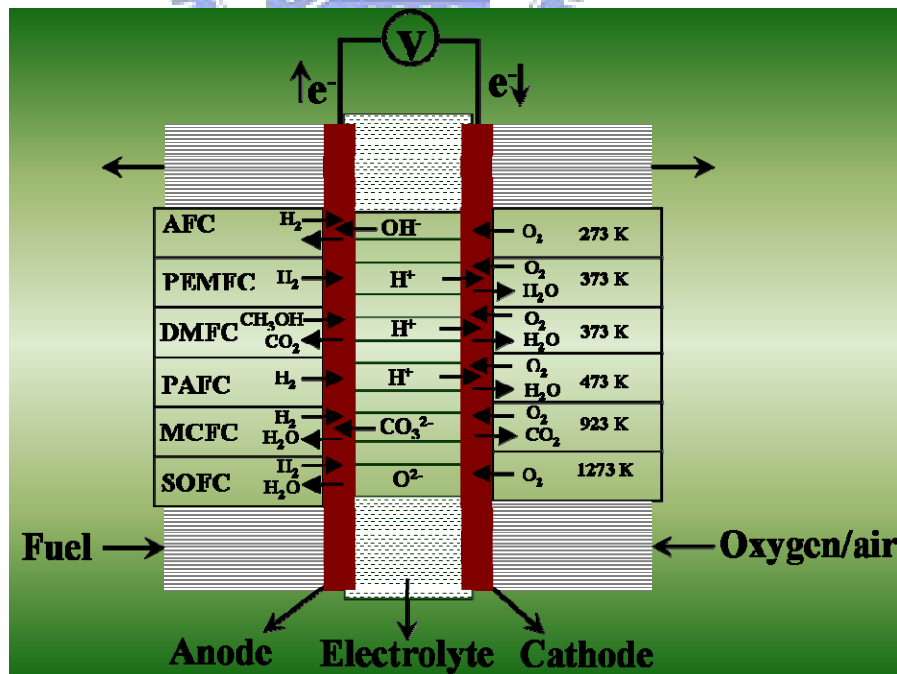


Figure 2-1 Simplistic representation of a various types of fuel cells.

The major challenge is that alkaline electrolytes, like potassium or sodium hydroxide, do not reject carbon dioxide, even the 300-350 ppm of carbon dioxide in atmospheric air is not tolerated, whereas terrestrial applications almost invariably require the use of atmospheric air as oxidant due to technical and economic considerations. The expected power output of an AFC is in the range of tens of MW [27].

[2] Phosphoric acid fuel cell (PAFC)

The PAFCs are commercially the most advanced system due to simple construction and the thermal and chemical stability of the phosphoric acid electrolyte at an operating temperature in the range of 150-200°C. Phosphoric acid concentrated up to 100% is used as the electrolyte in PAFC. The matrix universally used to retain the acid is silicon carbide, and the electrocatalyst in both the anode and cathode is the platinum catalyst. The stability of concentrated phosphoric acid is relatively high compared to other common acids; consequently, PAFC is capable of operating at the high end of the temperature range (100 to 220°C) among the acid-type fuel cells. It is mainly used for stationary power ranging from dispersed power to on-site generation plants. Power outputs of 0.2-20 MW are able to supply shopping malls and hospitals with electricity, heat and hot water and are commonly used as primary or backup power for these sites [27]. There are several disadvantages associated with the PAFC design. These include the need to use the expensive noble metal, platinum, as electrodes. Furthermore the electrodes are susceptible to CO poisoning and the electrolyte in the fuel cells is a corrosive liquid which, is consumed during operation [28].

[3] Solid Oxide Fuel Cell (SOFC)

The electrolyte in this fuel cell is a solid, nonporous metal oxide, usually Y₂O₃- stabilized ZrO₂. The fuel cell operates at 800-1000°C where ionic conduction by oxygen ions takes place. The high-temperature operation results in fast electrochemical kinetics and no need for

noble-metal catalysts. Typically, the anode is Co-ZrO₂ or Ni-ZrO₂ cermet, and the cathode is Sr-doped LaMnO₃. The fuel may be gaseous hydrogen, H₂/CO mixture, or hydrocarbons because internal in-situ reforming of hydrocarbons with water vapor can occur at high temperatures.

The SOFC has been investigated for applications ranging from industrial and home generators, telecommunication systems, and in hybrid electric vehicles. The SOFC provides high-quality waste heat that can be utilized for cogeneration applications or combined cycle operation for additional electric power generation. The operating condition of SOFC is also compatible with the coal gasification process, which makes the systems highly efficient when using coal as the primary fuel. It has been estimated that the chemical to electrical energy conversion efficiency is 50–60%, even though some estimates go as high as 70%–80%. Also, nitrogen oxides are not produced, and the amount of carbon dioxide released per kWh is around 50% less than for power sources based on combustion because of the high efficiency. There are several advantages to using SOFC systems for practical power generation as compared with the other types of fuel cell. SOFCs have a solid electrolyte, which eliminates the corrosion and liquid management problems of the PAFCs [27].

[4] Molten carbonate fuel cell (MCFC)

The MCFCs uses liquid lithium potassium or lithium sodium carbonate stabilized in a matrix as the electrolyte for the system, which is supported on Al₂O₃ fibers for mechanical strength. The fuel cell operates at 600 to 800°C where the alkali carbonates form a highly conductive molten salt, with carbonate ions providing ionic conduction. At the high operating temperatures in MCFCs, Ni (anode) and nickel oxide (cathode) can promote reaction; therefore, noble metals are not required.

MCFCs are aimed at stationary application such as the distributed power plants for industrial and commercial applications. The MCFCs system can attain efficiencies of up to

50 %, or up to 70 % with the combination with other power generators. MCFCs can operate on a wide range of different fuels and are not prone to CO or CO₂ contamination, as is the case for low temperature cells.

[5] Polymer electrolyte membrane fuel cell (PEMFC)

The PEMFCs uses a proton-conducting polymer membrane as the electrolyte at an operating temperature of 80-105°C. The most commonly used reactants for this system are hydrogen and methanol. Due to its low operating temperature, hydrogen and methanol fuel cells are popular for use in automotive and portable electronic applications. The standard membrane is a perfluorinated sulfonic acid membrane developed by DuPont and trademarked as Nafion[®]. The platinum catalyst is widely employed as the catalyst in both the anode and cathode electrode.

Moreover, the PEMFC has fast-start capability and yields the highest output power density among all types of the fuel cells. Because of the solid membrane as the electrolyte, there is no corrosive fluid spillage hazard, and there is lower sensitivity to orientation. It has no volatile electrolyte and has minimal corrosion concerns. It has truly zero pollutant emissions with potable liquid product water when hydrogen is used as fuel. As a result, the PEMFC is particularly suited for vehicular power applications, although it is also being considered for stationary power applications to a lesser degree [29]. The fuel – gas hydrogen can be produced by steam reforming or partial oxidation of hydrocarbons; however, reforming these fuels produces impurities such as carbon monoxide, to which the Pt-based electro-catalyst have very low tolerance. Even a trace amount of CO drastically reduces the performance levels, although CO poisoning effect is reversible and does not cause permanent damages to the PEMFC system [30]. Furthermore, the performance reduction due to CO poisoning takes a long time (on the order of two hours) to reach steady state. This transient effect may have profound implication for transportation applications. Therefore, the PEMFC

requires the use of a fuel virtually free of CO (must be less than a few ppm). Purifying the fuel stream through a water gas shift reaction and preferential oxidation adds both extra equipments and costs to a fuel cell system. Therefore, a fuel cell researcher's dream is to directly electrooxidize an organic fuel, rather than process it to hydrogen. Methanol is one alternative because it is a common, widely used and inexpensive substance that can be easily achieved from natural gas. Methanol offers other advantages over gas hydrogen, including liquid state at room temperature, ease to fuel-feeding, distribute and store. Hence, direct methanol fuel cell (DMFC) can be regarded as a subcategory of PEMFC, in which liquid methanol is directly converted into the electrical energy without the further use of reformer. In this thesis we shall focus our attention on the DMFCs and described in more detail below.

2.2 Direct methanol fuel cell (DMFCs)

2.2.1 Introduction

DMFCs using polymer electrolyte membranes are promising candidates for transportation applications and portable power sources such as replacing batteries. By eliminating reformer, DMFC offer simple system design and potentially higher overall efficiency than the reformat-fed fuel cells. Significant advances in H₂/air polymer electrolyte fuel cells have been reported including the low electrocatalyst consumption and high power density. However, fuel processor-fuel cell stack system on board the vehicle presents problems of packaging, complexity, and an overall system efficiency significantly lower than that of the fuel cell itself. Moreover, methanol is the liquid fuel that has substantial electroactivity and can be directly oxidized to CO₂ and water on catalytically active anodes in DMFC. In addition to high efficiency and environmental compatibility, liquid methanol is inexpensive, widely available and can be handled and distributed to consumers to such an extent that the present supply networks of gasoline can be used for methanol without difficulty. There are several

conditions, which fuel cells must meet in order to become a real alternative to the internal combustion engines. One of the most important requirements is system size, because of the need to generate sufficient power within limited space on car board. This requirement is not met by liquid electrolyte fuel cells as they have considerably lower power density than solid electrolyte fuel cells. Highly efficient molten carbonate and solid oxide electrolytes, operating at temperatures in the range 700 to 1000°C require extended, power consuming periods to reach working temperature. Therefore, they cannot start rapidly and respond quickly to the change in power demand of the particular vehicle. Using a gaseous fuel (commonly hydrogen) is not suitable for small light duty electric cars due to difficulties with fuel distribution and safe handling, and on-vehicle space and weight constraints. Currently methanol and also other organic fuels are steam reformed to hydrogen rich gas before entry into the anode area of a cell. This fuel feed usually contains traces of carbon monoxide, which acts as catalyst poison and needs to be purified. Purification of the fuel feed with water gas shift reaction will reduce the overall system efficiency and increase the weight, volume and start-up time of the device. From the point of view of system simplicity and convenience in operation the direct methanol fuel cell where methanol fuel is supplied directly to the anode is a most attractive technological solution for automotive application. The specific advantages in comparison to other fuel cell types such as high energy efficiency (weight and volume) stationary electrolyte, hence no corrosive liquids, self starting at ambient temperature, long-term experience, up to several 10000 h, stability, etc. make the PEM-DMFC the most promising transportation power source.

2.2.2 Principle of DMFC operation

A schematic drawing of a DMFC is given in Fig. 2-2, which demonstrates the principle of operation of a DMFC. The DMFC works by oxidizing the liquid methanol to CO₂ and water.

This eliminates the need for an external hydrogen supply. A proton conducting solid membrane, used both as electrolyte and separator between anode and cathode, is sandwiched between porous structures (i.e. carbon). The latter serve as current collectors and at the same time as a support for catalyst particles. Before catalyst deposition the current collectors are impregnated with polymer electrolyte to provide the intimate contact of the metal particles both with electron and proton conductors. At the anode a methanol molecule reacts with a water molecule liberating CO_2 , six protons which are free to migrate through the electrolyte towards cathode, and six electrons which can pass through the external load. The CO_2 produced in the reaction is rejected by the acid electrolyte.

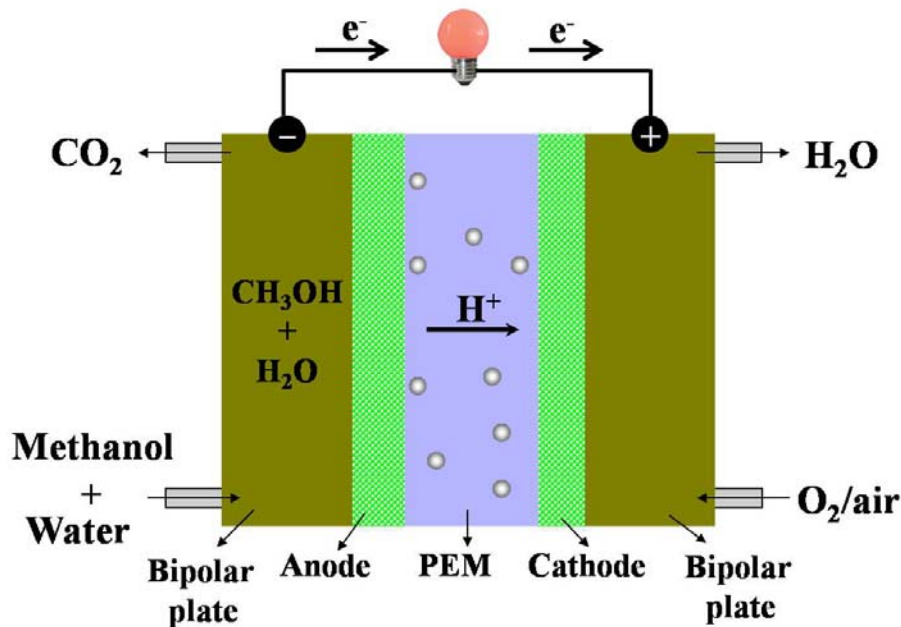
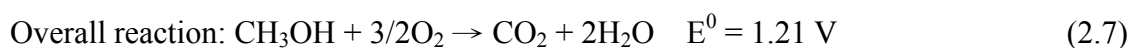


Figure 2-2 Schematic diagram of the DMFCs.

The protons, migrating through electrolyte and electrons, moving via external loaded circuit, have to reach a particle of catalyst on the cathode, where oxygen is electrocatalytically reduced producing water. The water produced is removed by the oxygen flowing through the cathode compartment. An electric potential appears between the electrodes because of the excess of electrons at the anode (where they are generated) compared with the

cathode (where they are consumed). It is this potential difference that drives current through the external load, making fuel cell a real source of power. The maximum voltage attainable from the overall reaction in the methanol-air fuel cell in theory is ~1.21 V with a theoretical efficiency of 96.5%, but in practice it is not achieved due to the poor electrode kinetics and ohmic losses the electrolyte.

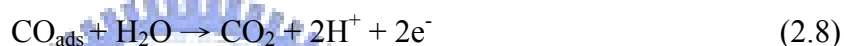
The relevant electrochemical reactions at the electrode are:



2.2.3 DMFC Anode

The electrooxidation of methanol requires the presence of Pt-based catalysts. Pt is involved in the two key steps occurring during oxidation route. One is the dehydrogenation step and the second is the chemisorption of CO. The methanol electrooxidation reaction is a slow process and it involves the transfer of six electrons to the electrode for complete oxidation to carbon dioxide. Various reaction intermediates may be formed during methanol oxidation. Some of CO-like species are irreversibly adsorbed on the surface of the electrocatalyst and severely poison Pt for the occurrence of the overall reaction, which has the effect of significantly reducing the fuel consumption efficiency and the power density of fuel cell. Thus it is very important to develop new electrocatalysts to inhibit the poisoning and significantly increase the rate of electro-oxidation by at least a factor of two to three times. Until now Pt is proved to be the only effective anode catalyst for DMFC. The research in methanol electrooxidation using Pt anode reached important breakthroughs during the last 15 years. The most significant issue in the development of useful low-cost high efficiency methanol fuel cells for generating electric current is the poisoning of the platinum anode by

carbon monoxide that is generated during the oxidation. Carbon monoxide molecules formed from the early steps of methanol oxidation adsorb on and block polycrystalline platinum electrode surfaces and are not oxidized away by the reaction with water to make carbon dioxide unless the anode potential is increased to about 0.6 V (SHE). The net result of doing this is an unacceptable loss of cell voltage and efficiency. It has been found that carbon monoxide can be oxidized at a lower potential by adding oxygen to the system, but the gain in the cell voltage is not large. Furthermore, there is a loss of power because no current is generated when carbon monoxide is oxidized by oxygen on the anode surface whereas, on the other hand, oxidation of carbon monoxide by water yields two electrons and two protons and the CO_{ads} poison that forms is oxidized by water



It was proposed that reaction (2-8) proceeds by direct attack by a H_2O molecule on the adsorbed CO [31]. A molecular orbital study on Pt(111) suggested that for this to occur the H_2O molecule would not need to be adsorbed on the surface [32]. Results of the kinetic isotope study were consistent with the formation of an activated complex of H_2O and CO_{ads} for which deprotonation was not rate limiting [33]. The involvement of OH_{ads} , formed from H_2O decomposition on electrode surfaces in oxidizing organic fuels was proposed four decades ago [34]. Its formation was advanced as the rate-determining step for the electrooxidation process.

Studies involving partial substitution of Pt with other transition metals like W, Pd, Ni, Ti, Rh, Mo have not yielded fruitful results [35]. Accordingly, most work has addressed to the modification of the Pt environment by alloying it with other elements or through the synthesis of multifunctional electrocatalyst. Until now the most successful results have been obtained through the alloying route. Thus the electrocatalyst activity of the new material for anodic oxidation of methanol is ambiguous. The mechanism of oxidation of methanol is discussed in section 2.3.

2.2.4 DMFC Cathode

In the direct methanol fuel cell the oxygen is reduced at the cathode, and so the electrode configuration is the same as that of H₂/O₂ fuel cell because of the same cathodic reaction. So, most of the cathodes developed originally for H₂/O₂ fuel cells are used in DMFC, which is Pt supported on carbon. In direct methanol fuel cell using polymer electrolyte membrane, there is a serious problem of methanol crossover from the anode region to cathode region, which causes a decrease in cathode performance leading to a loss in overall fuel cell efficiency. Not much is known about the chemical and electrochemical processes which methanol is undergoing at the cathode of an operating DMFC. Wang et al. [36] found that methanol is oxidized to carbon dioxide by oxygen in the presence of platinum, which inhibits the oxygen reduction reaction and results in lower cathode potential (depolarization). Keeping in mind that the highest cathode potential is 1V in practice, this kind of loss is certainly a serious problem that needs to be resolved. Some work is being done to develop methanol tolerant catalyst (cathode), however, even if the cathode depolarization is resolved, the methanol crossover is still an issue of considerable significance, which results in a decrease in fuel cell efficiency. From a practical point of view it should be important to stop this methanol crossover through the membrane. Beside the methanol crossover, a general problem related with Pt cathode still exists. The equilibrium potential for oxygen gas reduction to water according to equation 2 is 1.23 V (RHE) at 25°C. In practice the cathode potential on Pt/C electrode does not exceed 1 V. The main reason for this voltage loss is the formation of an oxide film (OH_{ads}) and the presence of strong water dipole, which interacts with positively charged metal surface. It is concluded that the neutral oxygen molecules are unable to displace the water dipoles from the surface when the potential is above 1 V. Consequently, the oxygen molecules are unable to exert their maximum thermodynamic potential in Pt electrode

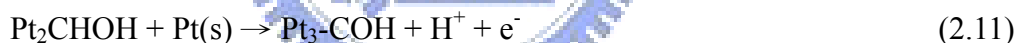
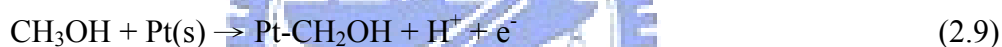
system.

2.3 Mechanism of methanol oxidation

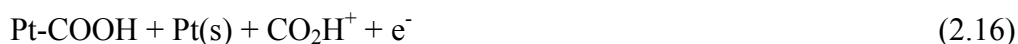
The basic mechanism for methanol oxidation was reviewed in 1988 [37], and can be summarized in terms of two basic functionalities [38]:

- (a) Electrosorption of methanol onto the substrate.
- (b) Addition of oxygen to adsorbed carbon-containing intermediates to generate CO₂.

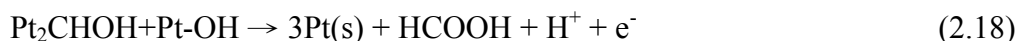
Very few electrode materials are capable of adsorption of methanol; in acid solution only platinum and platinum-based catalysts have been found both to show sensible activity and stability, and almost all mechanistic studies have concentrated on these materials. On platinum itself, adsorption of methanol is now believed to take place through a sequence of steps as:



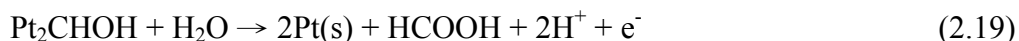
Or



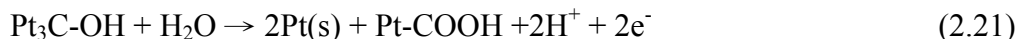
Additional reactions that have also been suggested include:



Or



Or



Reactions (2.9, 2.12) are electrosorption processes, whereas subsequent reactions involve oxygen transfer or oxidation of surface bonded intermediates. Considerable controversy surrounds the relative rates of the above processes and the identity of the dominant species on the surface.

2.4 Features

DMFCs possess a wide spectrum of advantages as compared with PEMFCs that use hydrogen as the fuel. The theoretical energy conversion efficiency of all DMFCs exceeds 90%, which is higher than that of PEMFCs (83%). More importantly, liquid methanol has a much higher volumetric energy density than does gas hydrogen. Hence, DMFCs require much smaller fuel cartridges and they are thus much more compact systems. In addition, methanol is easily handled, the small size, low working temperature, easy fuel-feeding, transported and stored. Unlike hydrogen-feed PEMFCs, liquid fuel-feed DMFCs do not need humidification and separate thermal management ancillary systems. All these features make DMFCs particularly suitable for portable and mobile applications [35].

2.5 Challenges

Currently there are some obstacles which need to be overcome before large scale commercialization of DMFC: (a) the high cost of Nafion membrane in the range of US\$ 800-2000/ m²; (b) the reduction of oxygen on cathode is also low though the problems are not so serious as with aqueous mineral acid electrolytes; (c) the permeability of the current

perfluorosulfonic acid membranes (Nafion) to methanol, which allow considerable crossover of methanol from anode region to cathode region. This leads both to degradation of performance, since mixed potential develops at the cathode, and to deterioration of fuel utilization. Methanol vapor also appears in the cathode exhaust, from which it would have to be removed. (d) and perhaps of greatest concern at the moment is the low activity and high cost of anode electrocatalyst, the anode reaction has poor electrode kinetics, particularly at lower temperatures, making it highly desirable to identify improved catalysts and to work at as high a temperature as possible. With regard to new DMFC anode catalysts, there are two major challenges, namely, the performance, including activity, reliability and durability, and cost reduction.

2.6 Anode catalysts of DMFC

For DMFC anode catalyst performance improvement, the exploration of new catalyst materials including noble and non-noble metals is necessary. In this respect, an alloying strategy is one of the R&D directions. With the help of fast activity screening, a breakthrough could be accelerated to meet the requirements for DMFC commercialization. The other is a support strategy. Rapid development of nanotechnology, especially in the area of the synthesis of carbon nanostructured materials, will create more stable and active supported catalysts. Nanoparticle supported catalysts are believed to be the most promising materials for catalysis in DMFCs. In recent years, significant progresses have been made to improve the performance of DMFCs. And the research activities are mainly focused on the development of the materials including the electrocatalysts and the electrolyte membranes, which are important in DMFC.

Regarding cost reduction, for early DMFC commercialization, DMFC anode catalyst loadings must drop to a level of $<1.0 \text{ mg cm}^{-2}$ from the present $2.0\text{--}8.0 \text{ mg cm}^{-2}$, depending

on applications. Loading reduction through increasing Pt utilization is one of the R&D directions. Alloying and nanoparticle supporting strategies could dramatically reduce the Pt content in the catalysts without performance compromise. Non-noble catalyst development is the other approach for catalyst cost reduction. However, at this current stage, non-noble DMFC anode catalysts are not yet feasible. A more thorough exploration is needed in this area. Real breakthroughs in DMFC anode catalysis are necessary with respect to performance and cost. When such a situation arises, it is important to open up new avenues for making low cost and effective catalysts. Until now many avenues that are already opening up are that of i) novel nanostructures of Pt, ii) new cost-effective synthesis routes, iii) binary or multiple catalysts, and iv) new catalyst supports to replace the generally used activated carbons, besides ideally the Pt-based catalysts should be replaced with abundant, non-precious materials. In the following section, we will present a brief literature review on the development of DMFC anode catalysts.

2.6.1 Pt nanostructures

To lower the cost of Pt catalysts, great efforts have focused on the development of nanostructures of Pt catalysts with a high surface area to achieve high catalytic performance and utilization efficiency. A variety of Pt nanostructures such as nanoparticles [39], nanowires [40, 41], nanocubes [42], 3D nanoflowers [43], multipods [44] dendritic [45] and nanotubes [46] have been proposed.

Recently, it is shown that enhanced electrocatalysts of Pt can be obtained as hollow nanospheres without changing catalyst loading [3]. The individual Pt nanosphere (diameter ca. 24 nm) is composed of a porous shell consisting of 2 nm-Pt nanoparticles (Fig. 2-3). These features endow the Pt hollow nanospheres with a high surface area which contributes to the high catalytic activity towards methanol electrooxidation. The result suggests a simple route

to enhance the catalytic efficiency of Pt catalysts by a simple improvement of the morphology. In the search for novel nanostructures of Pt, high-index facets such as $\{730\}$, $\{210\}$, and $\{520\}$ surfaces of tetrahedral Pt nanocrystals have been pointed out having high catalytic activity for electrooxidation due to the large density of atomic steps and dangling bonds. [47] The large scale synthesis method of them still remains a vital task.

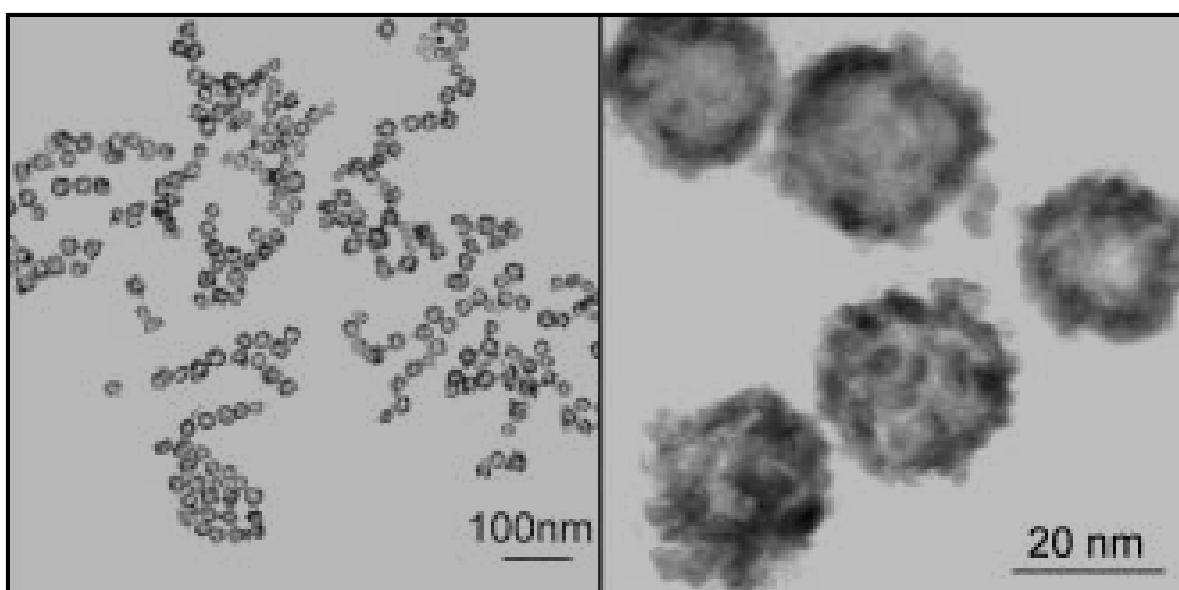


Figure 2-3 TEM images of Pt hollow nanospheres [3].

2.6.2 New cost-effective synthesis routes

Another way to lower the cost of Pt catalyst is to develop cost-effective routes for making more efficient Pt catalysts. Recently nanoporous catalysts have attracted great interest in the field of catalysis. Most syntheses of nanoporous materials reported so far have focused on template-assisted bottom-up processes, including soft templating and hard templating methods, which are relatively complicated. Recently, the conversion Li storage mechanism occurring in transition metal compounds has been developed into a template-free up-down method of wide applicability for the synthesis of well-crystallized materials with favorable nanoporous structures [48]. Based on this strategy, nanoporous Pt can be obtained from

submicrometer PtO_2 by electrochemical lithiation followed by dissolving the Li_2O in acidic aqueous solution or even water (Fig. 2-4). The synthesis is relatively simple (starting from micrometre-sized transition metal oxides), yet very effective. Owing to the high surface area ($142\text{m}^2\text{ g}^{-1}$), the presence of various pore sizes (2–20 nm) and the pronounced stability of the nanoporous Pt, the so-prepared Pt shows outstanding properties when used as an electrocatalyst for methanol oxidation [48].

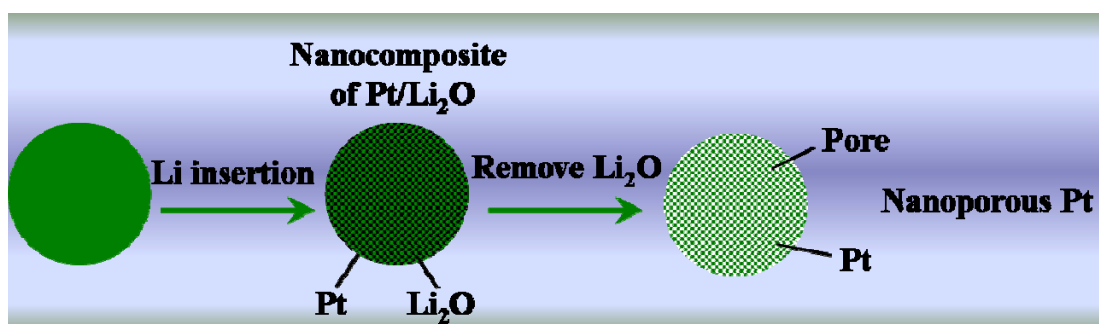


Figure 2-4 The simple template-free electrochemical lithiation synthesis of nanoporous structures [48].

2.6.3 Binary and Multiple Catalysts

Considerable attention has been paid to Pt-based binary catalysts (generally Pt alloys, Pt-M), ternary catalysts (generally Pt- M_1 - M_2), and multiple catalysts (generally Pt- M_1 - M_2 - M_3O) because the systems can not only reduce the cost but also improve the catalytic performance, such as mitigating CO poisoning, lowering overpotential, and suppressing Pt dissolution. According to Wasmus et al. [49], it is virtually undisputed that Pt-Ru is better than Pt and there is a consensus about the fact that, for the methanol oxidation, Pt-Ru is the best material among the Pt-based bimetallic electrocatalysts [49, 50–54]. These two metals, i.e. Pt and Ru, have close electronegativities (Fig. 2-5) [55] and similar bulk Wigner-Seitz radii (Fig. 2-6) [56]. Pt when alloyed with Ru strongly segregates while Ru strongly anti-segregates (Table 2-1), thereby a Ru site should be surrounded with some Pt sites, what is in agreement with the three to five Pt atoms necessary to activate the adsorption of methanol and the single Ru atom

necessary to activate water [57].

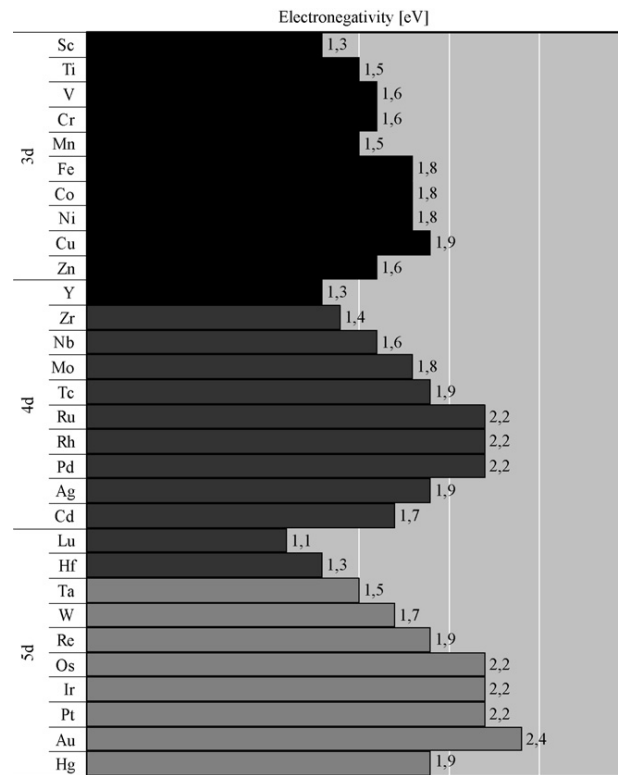


Figure 2-5 shows the electronegativities (eV) of the transition metals [55].

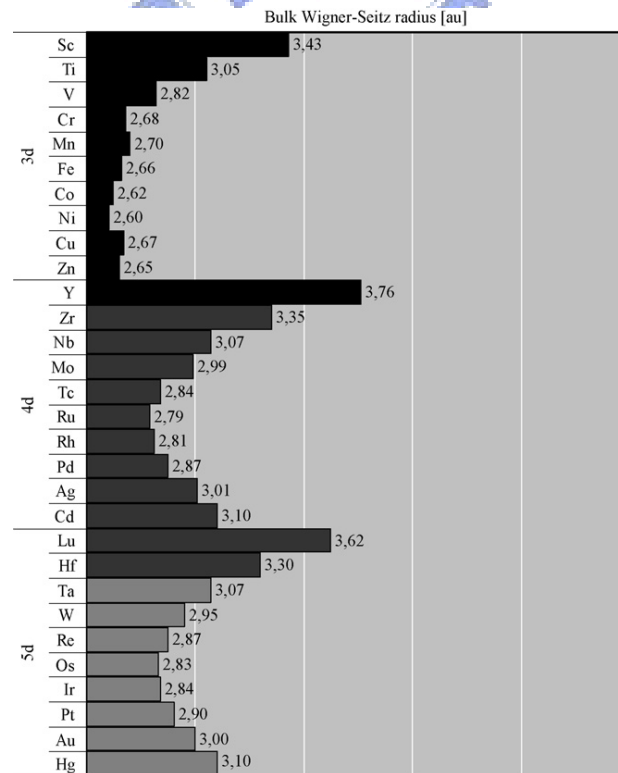


Figure 2-6 shows the Bulk Wigner-Seitz radius [a.u.] of the transition metals [56].

	3d								4d								5d							
	Ti	V	Cr	Mn	Fe	Co	Ni	Cu	Zr	Nb	Mo	Tc	Ru	Rh	Pd	Ag	Hf	Ta	W	Re	Os	Ir	Pt	Au
3d																								
Ti	n	A1	S1	S2	S2	S2	S3	S3	S2	n	A1	S1	S2	S2	S3	S3	S1	A1	A2	A1	n	S2	S3	S3
V	S2	n	A1	A2	A2	A1	S1	S2	S3	S2	A1	A2	A2	A1	S1	S3	S3	S1	A2	A2	A2	A2	A1	S2
Cr	S3	S1	n	S1	S2	S2	S3	S3	S3	S3	S2	S2	S2	S3	S3	S3	S3	S3	S2	S1	S1	S3	S3	S3
Mn	S3	S2	S1	n	S1	S1	S2	S3	S3	S3	S3	S2	S2	S2	S3	S3	S3	S3	S2	S2	S2	S2	S3	S3
Fe	S2	A1	A1	S1	n	S1	S2	S3	S3	S2	S1	A1	S1	S2	S3	S3	S3	S2	A1	A2	A1	S1	S2	S3
Co	S2	A1	A1	A1	n	n	S1	S2	S3	S2	n	A2	A1	S2	S2	S3	S2	S1	A2	A3	A2	S1	S2	S3
Ni	S1	A1	A1	n	A1	A1	n	S1	S3	S1	A1	A2	A1	S1	S2	S3	S3	n	A2	A2	A2	A1	S1	S2
Cu	n	A1	A1	A1	A1	A2	A1	n	S2	n	A1	A2	A1	A1	S1	S2	S2	A1	A2	A2	A2	A1	n	S1
4d																								
Zr	A1	n	S2	S2	S2	S2	S2	S3	n	A1	A1	n	S1	S2	S2	S3	A1	A2	A2	A1	n	S1	S2	S3
Nb	S1	A1	A2	A1	A1	A2	A1	S1	S2	n	A2	A2	A2	A1	S2	S2	A1	A2	A3	A3	A3	A3	A2	n
Mo	S1	A1	n	S2	S2	S3	S3	S3	S3	S1	n	S1	S3	S3	S3	S3	S3	n	A1	A1	S2	S3	S3	S3
Tc	S3	S2	S1	S1	S1	n	S1	S2	S3	S3	S1	n	n	S1	S2	S3	S3	S2	A1	A1	A2	A1	S1	S3
Ru	S2	A1	A1	S2	S2	S2	S3	S3	S3	S2	A1	A1	n	S2	S3	S3	S3	S1	A1	A2	A1	S1	S3	S3
Rh	A1	A2	A2	S1	n	n	S1	S2	S2	A1	A2	A2	A2	n	S2	S3	S1	A2	A2	A3	A2	A1	S1	S3
Pd	A2	A3	A2	A2	A2	A1	A1	n	A2	A3	A3	A3	A3	A2	n	S1	A2	A3	A3	A3	A3	A2	A1	S1
Ag	A2	A2	A1	A1	A2	A2	A2	A1	A2	A2	A3	A2	A2	A2	A1	n	A2	A3	A3	A3	A3	A2	A2	n
5d																								
Hf	n	n	S2	S2	S2	S2	S3	S3	S1	A1	S1	S1	S2	S2	S3	S3	n	A1	A1	n	S1	S2	S3	S3
Ta	S2	n	A1	A1	A1	A1	S1	S2	S3	S1	A1	A2	A2	A1	S1	S2	S2	n	A2	A3	A3	A2	A1	S2
W	n	n	S1	S1	S2	S2	S2	S3	S3	S2	S1	S2	S3	S3	S3	S3	S3	S1	n	S1	S3	S3	S3	S3
Re	S3	S2	S1	S1	S1	S1	S2	S3	S3	S3	S2	S1	S2	S2	S3	S3	S3	S3	S1	n	n	S1	S2	S3
Os	S1	A1	A2	S1	S2	S2	S3	S3	S3	S2	A1	A1	S1	S2	S3	S3	S3	S1	A1	A1	n	S2	S3	S3
Ir	A1	A2	A2	A1	A1	A1	A1	S1	S2	A1	A2	A2	A1	S1	S2	S3	S1	A1	A2	A2	A2	n	S2	S3
Pt	A2	A3	A2	A2	A2	A2	A2	A2	A1	A3	A3	A3	A2	A2	n	S1	A2	A3	A3	A3	A3	A2	n	S2
Au	A2	A2	A2	A2	A2	A2	A2	A2	A1	A2	A2	A2	A2	A2	A1	n	A2	A3	A3	A3	A2	A2	A2	n

Table 2-1 Compilation of calculated segregation energies on the closest packed surface of all binary combinations of the transition metals [55].

	Fe	Co	Ni	Cu	Ru	Rh	Pd	Ag	Ir	Pt	Au
A											
Fe	-0.92	-0.05	-0.20	-0.13	-0.29	-0.54	-1.24	-0.83	-0.36	-1.09	-1.42
Co	0.01	-1.17	-0.28	-0.16	-0.24	-0.58	-1.37	-0.91	-0.36	-1.19	-1.56
Ni	0.09	0.19	-1.29	0.19	-0.14	-0.31	-0.97	-0.53	-0.14	-0.80	-1.13
Cu	0.56	0.60	0.27	-2.67	0.58	0.32	-0.64	-0.70	0.58	-0.33	-1.09
Ru	0.21	0.26	0.01	0.12	-1.41	-0.17	-0.82	-0.27	0.02	-0.62	-0.84
Rh	0.24	0.34	0.16	0.44	0.04	-1.73	-0.54	0.07	0.17	-0.35	-0.49
Pd	0.37	0.54	0.50	0.94	0.24	0.36	-1.83	0.59	0.53	0.19	0.17
Ag	0.72	0.84	0.67	0.47	0.84	0.86	0.14	-4.30	1.14	0.50	-0.15
Ir	0.21	0.27	0.05	0.21	0.09	-0.15	-0.73	-0.13	-2.11	-0.56	-0.74
Pt	0.33	0.48	0.40	0.72	0.14	0.23	-0.17	0.44	0.38	-2.25	-0.05
Au	0.63	0.77	0.63	0.55	0.70	0.75	0.17	0.21	0.98	0.46	-3.56
B											
Fe	-0.92	0.14	-0.04	-0.05	-0.73	-0.72	-1.32	-1.25	-0.95	-1.48	-2.19
Co	-0.01	-1.17	-0.20	-0.06	-0.70	-0.95	-1.65	-1.36	-1.09	-1.89	-2.39
Ni	0.96	0.11	-1.29	0.12	-0.63	-0.74	-1.32	-1.14	-0.86	-1.53	-2.10
Cu	0.25	0.38	0.18	-2.67	-0.22	-0.27	-1.04	-1.21	-0.32	-1.15	-1.96
Ru	0.30	0.37	0.29	0.30	-1.41	-0.12	-0.47	-0.40	-0.13	-0.61	-0.86
Rh	0.31	0.41	0.34	0.22	0.03	-1.73	-0.39	-0.08	0.03	-0.45	-0.57
Pd	0.36	0.54	0.54	0.80	-0.11	0.25	-1.83	0.15	0.31	0.04	-0.14
Ag	0.55	0.74	0.68	0.62	0.50	0.67	0.27	-4.30	0.80	0.37	-0.21
Ir	0.33	0.40	0.33	0.56	-0.01	-0.03	-0.42	-0.09	-2.11	-0.49	-0.59
Pt	0.35	0.53	0.54	0.78	0.12	0.24	0.02	0.19	0.29	-2.25	-0.08
Au	0.53	0.74	0.71	0.70	0.47	0.67	0.35	0.12	0.79	0.43	-3.56

Table 2-2 Shifts in *d*-band centres of surface impurities (A) and overlayers (B) relative to the clean metal values (bold) [55].

Moreover, the Pt electronic structure should be changed by the presence of neighbouring Ru.

According to Table 2-2, the Pt d-band centre shifts down when Pt is alloyed with Ru, what suggests weaker Pt-adsorbate bonds, while the Ru d-band centre slightly shifts up. In other words, when Pt and Ru are alloyed, the adsorption of adsorbates is weaker on the Pt sites and stronger on the Ru sites. These tendencies may explain the enhanced activity of Pt-Ru, which is attributed to both bifunctional mechanism and electronic effect, where the bifunctional mechanism involves the adsorption of OH species on Ru atoms thereby promoting the oxidation of CO to CO₂ [58, 59]. In this way, the Pt poisoning by the CO-like species would be decreased because these species would more weakly adsorb on Pt and Ru would provide the necessary OH species, which would permanently be available on the Ru surface sites, more strongly adsorbing the OH species. Elements as alternative to Ru were investigated. Antolini et al. [52] worked on Pt₃Co₁ and Pt₃Ni₁ (atomic ratio 3:1). The authors chose Co and Ni since their presence lowered the electronic binding energy in Pt and so promoted the C–H cleavage reaction at low potentials and, moreover, they provided OH species necessary for the CO oxidation. The performances of fuel cells with Pt₃Co₁ or Pt₃Ni₁ as anode catalysts were slightly worse than that of the fuel cell with Pt. The performance of Pt₃Co₁ was slightly better than that of Pt₃Ni₁. These two metals, i.e. Co and Ni, have similar electronegativities (Fig. 2-5) and bulk Wigner-Seitz radii (Fig. 2-6).

According to Table 2-1, Pt when alloyed with Co strongly segregates and Pt when alloyed with Ni moderately segregates, as already reported [60]. For both Pt-Co and Pt-Ni, the Pt d-band centre shifts down. The d-band centres of Co and Ni shift up when they are alloyed with Pt. This analysis of the surface modifications suggests the following remarks: compared with Pt-Ru, (i) the adsorption of OH species on the Co or Ni sites should be weaker; (ii) the lower segregation of Pt in either Pt-Co or Pt-Ni is an indication of a higher dilution of Pt and so a decrease in the number of Pt surface sites. Therefore, Pt-Ru should be a better catalyst than both Pt-Co and Pt-Ni, and as the Pt segregation is more severe with Co, Pt-Co should be a better catalyst than Pt-Ni with a larger number of Pt surface sites. However, as underlined by

Antolini et al. [50], conflicting results regarding the Pt-Co and Pt-Ni alloys were reported in the literature. Interestingly, the authors showed that the methanol oxidation activity on Pt-Ni and Pt-Co was improved or unchanged or decreased in relation to pure Pt. It was observed an opposite effect of the Co/Ni presence in going from low-contents (negative effect on the methanol oxidation) to high contents (positive effect) and the decreased activity in the presence of low Co/Ni contents was ascribed to the dilution of Pt, hindering the methanol adsorption, while the positive effect was related to several reasons, namely the electronic effect, an enhancing of the CO oxidation and the presence of oxide species [50]. This study unfortunately shows the limitations of the theoretical understanding of the catalysts behaviors but it fortunately stresses on the essential side of the experiments. Choi et al. [61] observed that the current density produced by methanol oxidation over Pt₂-Rh₁ (atomic ratio 2:1) was larger than that over pure Pt but lower than that over Pt-Ru. The authors concluded that the enhanced activity of Pt₂-Rh₁ was mainly due to an intrinsic improvement in catalytic activity and not to an improvement in CO oxidation. Ru and Rh display similar electronegativities and bulk Wigner-Seitz radii (Figs. 2-1 and 2-2). Pt moderately segregates when alloyed with Rh while it very strongly segregates when alloyed with Ru. The Pt d-band centre shifts down when alloyed with both though the down shift is more important with Ru. These reflections suggest that Pt-Ru should be better with higher surface concentration of Pt sites and lower strength of the adsorption of CO-like species over the Pt sites.

More recently, Choi et al. [62] reported that the Pt-Au alloy and pure Pt showed almost the same activity. Au itself was inactive for methanol oxidation and was not helpful for removing CO_{ads} on the Pt surface. In fact, when alloyed with Au, Pt strongly anti-segregates (Table 2-1). The surface concentration in Pt sites is then reduced. Moreover, Au has one of the lowest d-band centres and the presence of Pt shifts down it, what suggests very poor abilities for the adsorption of OH species. The Pt d-band centre shifts up when alloyed with Au and thereby the adsorption of CO-like species becomes stronger, what favours the Pt sites

poisoning.

Pt-Ru-M alloys								
Pt-Ru-Mo > Pt-Ru-W > Pt-Ru-Co > Pt-Ru-Fe > Pt-Ru-Ni > Pt-Ru-Cu > Pt-Ru > Pt-Ru-Sn > Pt-Ru-Au								
	Mo	W	Co	Fe	Ni	Cu	Sn	Au
M segregation in relation to Pt ^a	A3	A3	A2	A2	A2	A2	S ^b	S2
M segregation in relation to Ru ^a	A1	A1	S2	S2	S3	S3	S ^b	S3
Pt d-band centre [eV] ^a	n.i.	n.i.	Down shift	Down shift	Down shift	Down shift	n.i.	Up shift
Ru d-band centre [eV] ^a	n.i.	n.i.	Down shift	Down shift	Down shift	Up shift	n.i.	Up shift

Table 2-3 Possible occurrence of segregation and possible shift in *d*-band centre for the elements of the trimetallic Pt-Ru-M alloy [5] with metals (M) as Mo, W, Co, Fe, Ni, Cu, Sn and Au [55].

Consequently, Au is not interesting for the preparation of active Pt-based bimetallic alloys devoted to methanol oxidation. Pt-Ru-based trimetallic electrocatalysts were envisaged as well [57]. The addition of a third element, i.e. Au, Co, Cu, Fe, Mo, Ni, Sn and W, gives promising results. The following classification enabled to note that Mo, W, Co, Fe and Ni improved the Pt- Ru activity towards the oxidation of methanol, the best promoter being Mo: Pt-Ru-Mo > Pt-Ru-W > Pt-Ru-Co > Pt-Ru-Fe > Pt-Ru-Ni > Pt-Ru-Cu > Pt-Ru > Pt-Ru-Sn > Pt-Ru-Au. Even if the concepts of Nørskov and co-workers [63–65] do not consider the alloys with three metals, it could be tried out proposing few trends regarding the segregation and the *d*-band centres variations. Table 2-3 proposes the possible occurrence of the segregation and the shifts in *d*-band centres for the different metals, i.e. Pt, Ru, Mo, W, Co, Fe, Ni, Cu and Au. The analysis of the data given by Table 2-1 suggests that the best trimetallic catalysts are the ones for which the third metal M antisegregates while both Pt and Ru segregate. Furthermore, it seems that the *d*-band centres of Pt and Ru should shift down. The trimetallic material for which the *d*-band centres of Pt and Ru shift up is the worst alloy. Unfortunately, these types of data are not available for Mo, W and Sn what would have been useful to completely validate such observations. Consequently, the improvement of the Pt-Ru alloys would require a third metal with which Pt and Ru would segregate and their *d*-band centres would shift down. All of the previous observations could be used as criteria to select, from Tables 2-1 and 2-2,

bimetallic catalysts that could be active for the methanol oxidation. The first criterion could be the d-band centre shift. It should be close to that of Pt and Ru when alloyed together, i.e. about -2.9 and about -1.3 eV, respectively. Thereby, the analysis of Table 2-2 provides Pd-Ni. The second criterion could be the segregation. Hence, Table 2-1 confirms Pd-Ni as Pd has a tendency to strongly segregate (like Pt) while Ni moderately antisegregates (like Ru). Therefore, the Pd-Ni alloy might provide an activity similar to that of Pt-Ru. Nevertheless, for the methanol oxidation, as it is remarked by a large number of investigations, the best current way to improve the anode electrocatalyst would be the addition of a third metal to Pt-Ru [57]. Many investigations about DMFC have more or less regarded all the mono- and bimetallic electrocatalysts displaying catalytic abilities towards methanol oxidation. It seems then that the remaining tracks to follow are the ternary or quaternary compositions and especially the Pt-Ru-based ones. A literature analysis shows that some of the best matrices for such catalyst are the ternary or quaternary compositions: Pt – Ru – Os, Pt – Ru – Ir, and Pt – Ru – Os – Ir [66, 67]. The addition of Ir (cheaper, but less active than Pt) into the conventional Pt – Ru catalyst can suppress Ru dissolution, which is a significant challenge for DMFC anode catalysts utilizing Ru. Dissolution of Ru from the Pt – Ru anode catalyst, followed by the Ru ions crossing over the membrane [68] and depositing on the cathode, can result in degradation of both the anode and cathode catalyst and a decrease in the fuel cell performance. The addition of Ir, however, does not significantly increase the activity of the Pt – Ru catalyst.

As mentioned above, the many favorable effects have been found in Pt-based binary and multiple catalysts, such as the bifunctional effect, the electronic effect, and the hydrogen spillover effect. With progressive understanding of these effects, low-cost Pt catalysts with tunable performance will be developed in the future.

2.6.4 New Catalyst Supports

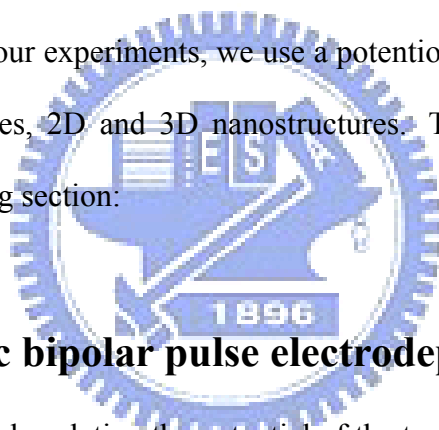
To date, the most promising catalytic materials used for methanol oxidation at room temperature are supported Pt based catalysts. The dispersion and utilization of the catalysts depend on surface area, pore characteristics, and surface functionalities of the supports. Although the widely used catalyst support is activated carbons like Vulcan XC 72R, the search for new efficient supports is still underway. Carbon nanotubes (CNTs) have exceptional mechanical and electronic properties and are attractive support materials for Pt-based catalysts in DMFCs. There mainly are two approaches to achieve high Pt dispersion. One approach is by modifying either CNTs or Pt catalysts. The former has been extensively employed by chemical-oxidation treatments to modify the CNT walls for introducing more defect sites for Pt loading, while the latter has rarely been used. Recently, we have reported a novel process to prepare well-dispersed Pt nanoparticles on CNTs by modifying Pt nanoparticles with organic molecule triphenylphosphine (PPh₃) [55]. In contrast to CNTs, the functionalization of Pt nanoparticles was facile and effective under much more benign conditions, such as no harsh acid and room temperature, more efforts are expected.

Another approach is by in situ growth methods. Zheng et al. [69] reported a one-step in situ method to disperse Pt nanoparticles on CNTs, using H₂PtCl₆ as a Pt source, ethylene glycol as a reducing agent, and dimethyl formamide (DMF) as a solvent. By this method, well-dispersed Pt nanoparticles can be directly loaded onto the CNT walls (Fig. 3d). So far, many in situ methods have been used, but preparing well-dispersed Pt on CNTs still remains a challenge. The thesis is mainly focused on research of electrocatalysts, which are the important materials in DMFC that is a power generator to convert a chemical energy to electrical energy.

2.7 Pulse electrodeposition

2.7.1 Pulse waveform

Generally, the pulse waveform was divided into two groups: (1) unipolar, where all the pulses are in one direction (with no polarity) and (2) bipolar, where anodic and cathodic pulses are mixed. There are many variants on these [70], but the number of variables increases with complexity of the waveform, which makes it more difficult to understand how a particular waveform affects the deposition. Typical waveforms include: (1) cathodic pulse followed by a period without current (or an anodic pulse), (2) direct current (DC) with superimposed modulations, (3) duplex pulse, (4) pulse-on-pulse, (5) cathodic pulses followed by anodic pulses-pulse reverse current (PRC), (6) superimposing periodic reverse on high frequency pulse, (7) modified sine-wave pulses and (8) square-wave pulses (potential/current). Among these, the square wave pulses (potential/current) have the advantage of an extensive duty cycle range [71]. In our experiments, we use a potentiostatic bipolar pulse plating (PBPP) to prepare Pt nanoparticles, 2D and 3D nanostructures. The more detailed explanation of PBPP is given in following section:



2.7.2 Potentiostatic bipolar pulse electrodeposition

In the potentiostatic pulse plating the potential of the test electrode is controlled, while the current, the dependent variable, is measure as a function of time. The potential difference between the test electrode and the reference electrode is controlled by a potentiostat (shown in Fig. 2-7). The input function, a constant potential, and the response potential $i = f(t)$, are shown in Fig. 2-8.

In PBPP [72–74] the potential is alternated swiftly between two different values. This results in a series of pulses of equal amplitude, duration and polarity, separated by zero current. Each pulse consists of an ON-time (t_{on}) during which potential and/current is applied, and an OFF-time (t_{off}) during which zero current is applied as shown in Fig. 2-9. It is possible to control the deposited film composition and thickness in an atomic order by regulating the

pulse amplitude and width [75, 76].

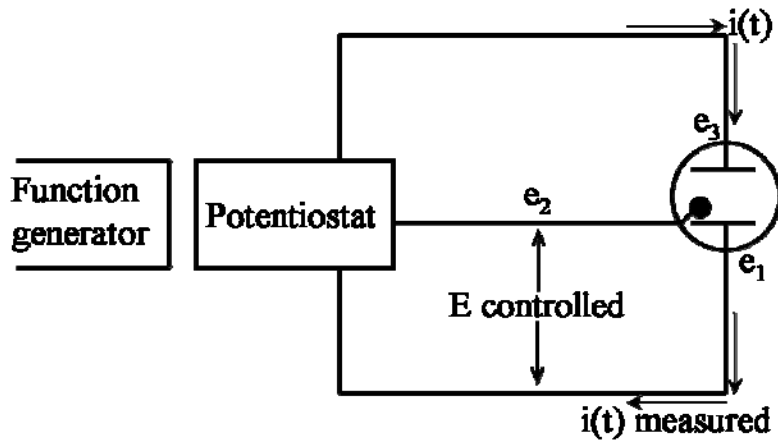


Figure 2-7 shows the schematic diagram of apparatus for potentiostatic measurements; E, controlled potential; e_1 , test electrode; e_2 , reference electrode; e_3 , counter electrode.

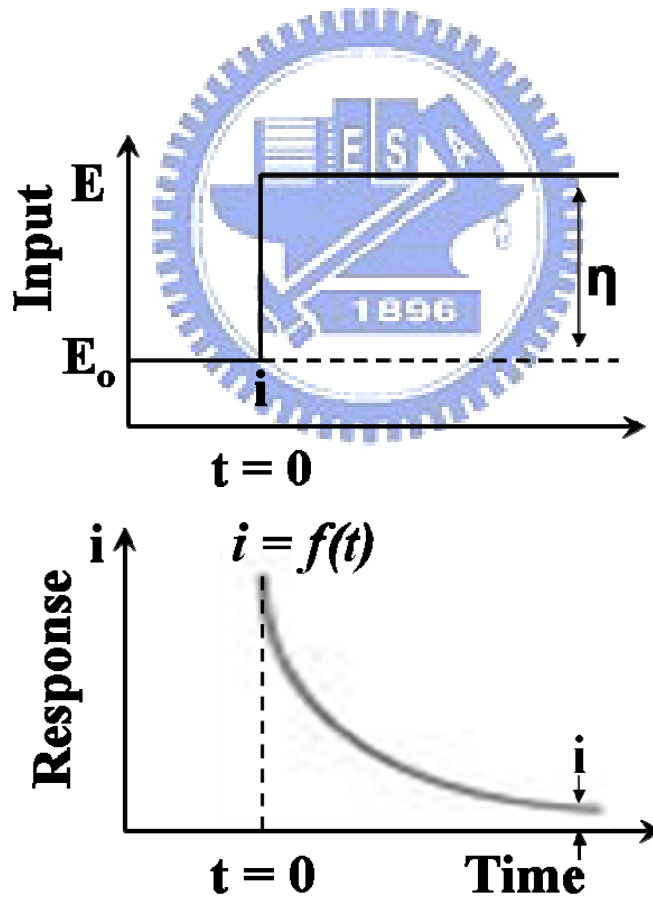


Figure 2-8 shows the variation of current with time during potentiostatic electrolysis.

They favor the initiation of grain nuclei and greatly increase the number of grains per unit area resulting in finer grained deposit with better properties than conventionally plated

coatings. The double-pulse technique is characterized with two pulse potentials and the corresponding pulse durations. The first pulse, being more negative than critical nucleation potential, is used to initiate the nuclei formation and the second pulse, more positive than critical nucleation potential but more negative than the reversible potential, is used to control its growth. It is convenient and easy way to produce custom cluster.

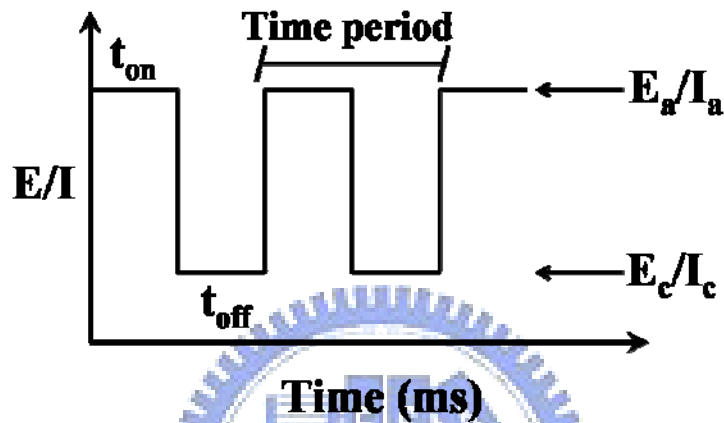


Figure 2-9 shows the schematic diagram of potential pulse waveform and pulse-current waveform.

Nomenclature for Fig. 2-9:

E_a = anodic potential

I_a = anodic current

E_c = cathodic potential

I_c = cathodic current

2.7.3 Advantages of pulse plating

(a) In electroplating, a negatively charged layer is formed around the cathode as the process continues. When using DC, this layer charges to a defined thickness and obstructs the ions from reaching the part. In PBPP, the output is periodically turned off to cause this layer to discharge somewhat. This allows easier passage of the ions through the layer and onto the part.

(b) High current density areas in the bath become more depleted of ions than low current density areas. During t_{off} , ions migrate to the depleted areas in the bath. When pulse t_{on} occurs, more evenly distributed ions are available for deposition onto the part.

2.7.4 Theory of pulse plating

From above discussion, it has become clear that pulse electrodeposition, as compared with DC electrodeposition, has many advantages in terms of controlled particle size, stronger adhesion, uniform electrodeposition, selectivity of hydrogen, reduction of internal stress, etc. Also, DC electrodeposition has only one variable, namely, current density, while pulse electrodeposition, as shown in Fig. 2-9, has four independent variables, namely, t_{on} time, t_{off} time, E_a anodic potential and E_c cathodic potential. In electrodeposition, the time cycle is defined as follows:

$$\text{time cycle (\%)} = \frac{t_{\text{on}}}{t_{\text{on}} + t_{\text{off}}} \times 100 \quad (2.22)$$

In DC electrodeposition, as the deposition current density increases, the deposited metal ions near the cathode are exhausted and dendritic crystals are formed. Eventually, the ion concentration at the cathode surface becomes zero. The current density at which dendrite crystals begin to form is defined as the ‘limiting current density’. At this current density, the ion concentration at the deposited surface is zero. Pulse electrodeposition can raise the limiting current density considerably in comparison with DC electrodeposition because the deposited metal ions of the cathode surface can be supplied from the bulk solution during the t_{off} time of the pulse. The mechanism of pulse electrodeposition, however, has still to be fully understood. Cheh [77] reported that the rate-determining step of pulse electrodeposition is controlled by mass transport.

The rate of nuclei formation, ν , is given by:

$$v = k_1 \exp(-k_2/\eta^2), \quad (2.23)$$

where k_1 , k_2 are constants and η is the overpotential [78]. Therefore, the rate of nuclei formation depends on the anodic overpotential, η_a . The anodic overpotential of DC electrodeposition is given by:

$$\eta_{a,DC} = \eta_0 \ln\left(\frac{E_{DC}}{E_0}\right) \quad (2.24)$$

where η_0 is the overpotential at the exchange potential. The anodic overpotential of pulse electrodeposition is expressed as:

$$\eta_{a,PP} = \eta_0 \ln\left(\frac{E_C}{E_0}\right) + \eta_0 \ln\left(\frac{t_{off}}{t_{on}} + 1\right) \quad (2.25)$$

The average current density, E_C in Eq. (2.25) is equal to E_{DC} because it determines the surface concentration of deposited metal ions, i.e.,

$$E_{DC} = E_C, \quad (2.26)$$

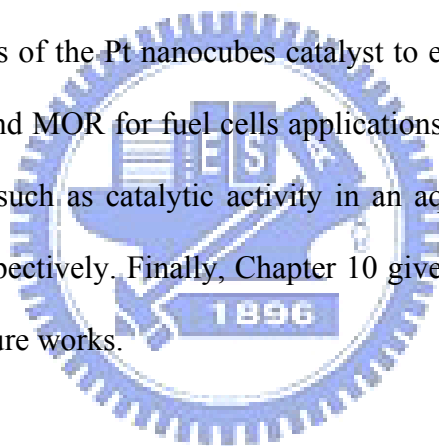
$$\eta_{a,PP} = \eta_{0,PP} + \eta_0 \ln\left(\frac{t_{off}}{t_{on}} + 1\right) \quad (2.27)$$

As the anodic overpotential of pulse electrodeposition is larger than that of DC electrodeposition by $\eta_0 \ln(t_{off}/t_{on} + 1)$, the rate of nuclei formation increases and the size of metal deposits becomes smaller.

2.8 Structure of the thesis

The remainder of this thesis consists of eight chapters and is organized as follows: In chapter 3, gives a detailed description of the experimental methods and procedures used in this study, and the materials and chemical chosen to accomplish the research work. Chapter 4 shows silicon nanocone (SNC) array supported Pt nanoparticles as anode catalyst for direct

methanol fuel cells (DMFCs). A high current density, mass activity and fairly good stability achieved for Pt/SNC anode in DMFCs. Chapter 5 reports an amorphous carbon coated silicon nanocone (ACNCs) array supported Pt nanoparticles for DMFCs applications. The Pt-ACNC electrode exhibited excellent electrocatalytic activity and stability towards both methanol oxidation reaction (MOR) and oxygen reduction reaction. Chapter 6 presents a novel new method to prepare 3D nanoporous graphitic carbon (g-C) supported Pt and Pt-Ru alloy catalysts as anode for DMFCs. The Pt-Ru/3D nanoporous g-C has better electrocatalytic activity towards CO and methanol oxidation in cyclic voltammetry measurements. Chapter 7 and 8 reports a novel 3D Pt nanofloweres structure and 2D contentious island Pt networks as a catalyst to improve the catalytic activity and durability for DMFCs. Chapter 9 presents the new approach to synthesis of the Pt nanocubes catalyst to enhance the CO tolerance, ethanol oxygen reaction (EOR) and MOR for fuel cells applications. In addition, chapter 9 shows the surface dependent study such as catalytic activity in an aqueous solution of ethanol-H₂SO₄ and methanol-H₂SO₄, respectively. Finally, Chapter 10 gives an overviews and conclusion of the present study, and future works.



Chapter 3

Experimental Methods

We have developed a several convenient techniques for the synthesis of nanostructured materials. The processes include the anodic aluminum oxides (AAO) template-assisted, flame-assisted, electrochemical assisted and fasten-silicon-assisted methods. The experimental flowcharts, the experimental procedures and structure property analysis methods for each process is discussed separately in more detail in the following sections.

3.1 Experimental flowcharts

Figure 3-1 shows the experiment flowchart of fabrications and analyses of Pt nanoparticles supported on the highly ordered Si nanocones (SNCs) and on the amorphous carbon coated silicon nanocones (ACNCs), which were fabricated by AAO templation method. During the preparation of highly ordered pore channel arrays, underlying TiN layers were anodically oxidized as well in the late stage of the AAO anodization to form TiO_x nanodots. TiO_x nanodots were then used as nanomasks to etch the TiN layer and the underlying Si substrate in an inductively coupled plasma reactive ion etch (ICP-RIE) system.

Figure 3-2 illustrates experiment flowchart of synthesis and analyses of Pt-Ru alloy catalyst supported on the nanoporous graphitic carbon (g-C)/Si. The nanoporous g-C materials have been synthesized using the flame of adamantane ($\text{C}_{10}\text{H}_{16}$). Additionally, the experimental flowchart in Fig. 3-2 shows the electrochemical synthesis and analyses of the two-dimensional (2D) continuous Pt island networks and the three-dimensional (3D) Pt nanoflowers.

Finally, Fig. 3-3 shows the experiment flowchart for the synthesis and analysis of shape-controlled Pt nanoparticles and their electrochemical properties are measured.

The surface morphology, bonding structure and chemical composition were analyzed by

scanning electron microscope (SEM), transmission electron microscopy (TEM), Raman spectroscopy, Auger electron spectroscopy (AES), and X-ray photoelectron spectroscopy (XPS), etc. The electrochemical measurements of specimens were performed at room temperature using a conventional three-electrode cell, in which specimens was used as a working electrode, Pt wire served as counter electrode and the reference electrode was an aqueous saturated calomel electrode (SCE).

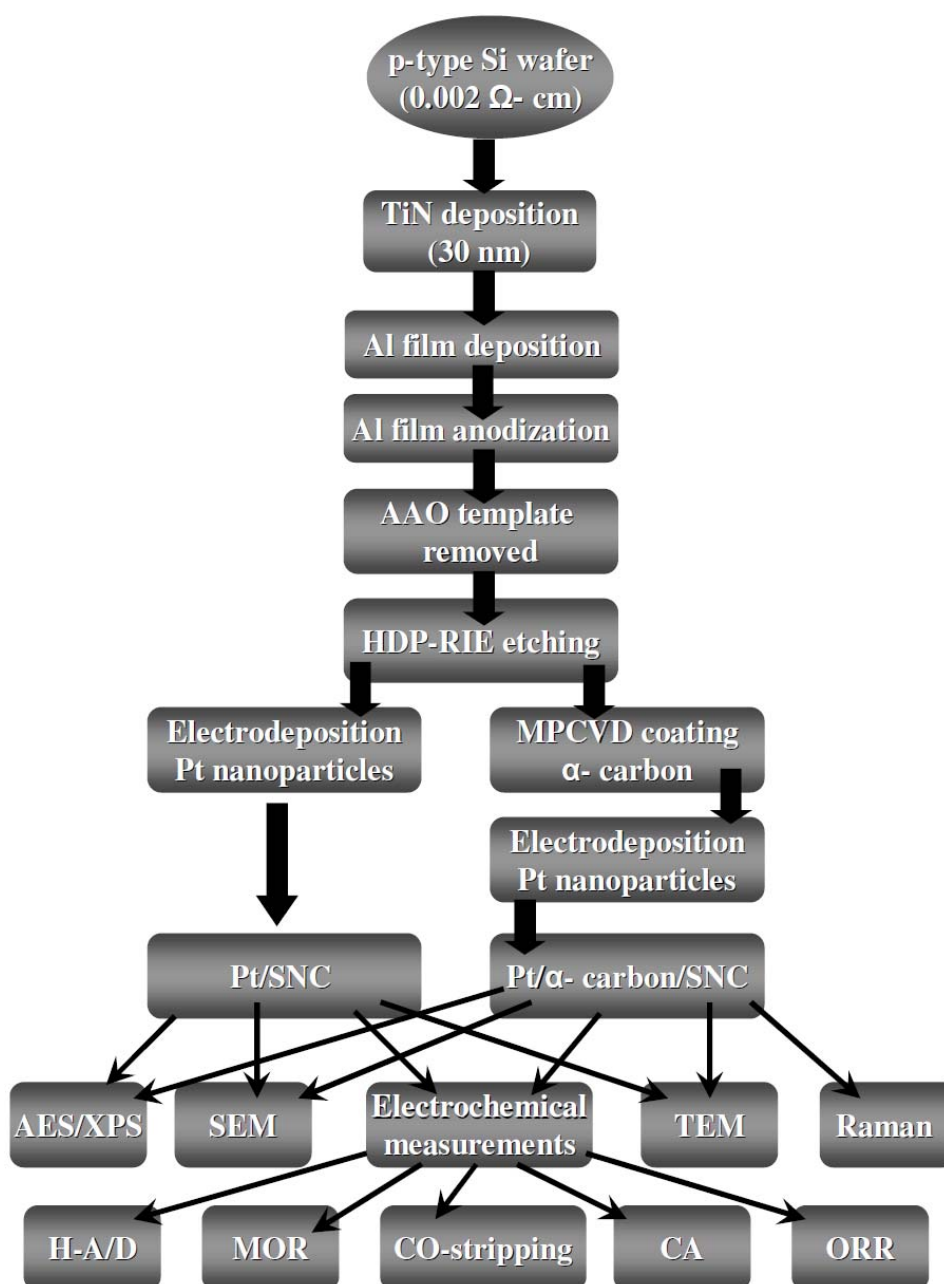


Figure 3-1 Experimental flowchart of fabrications and analyses of Pt/SNC and Pt/ACNC arrays.

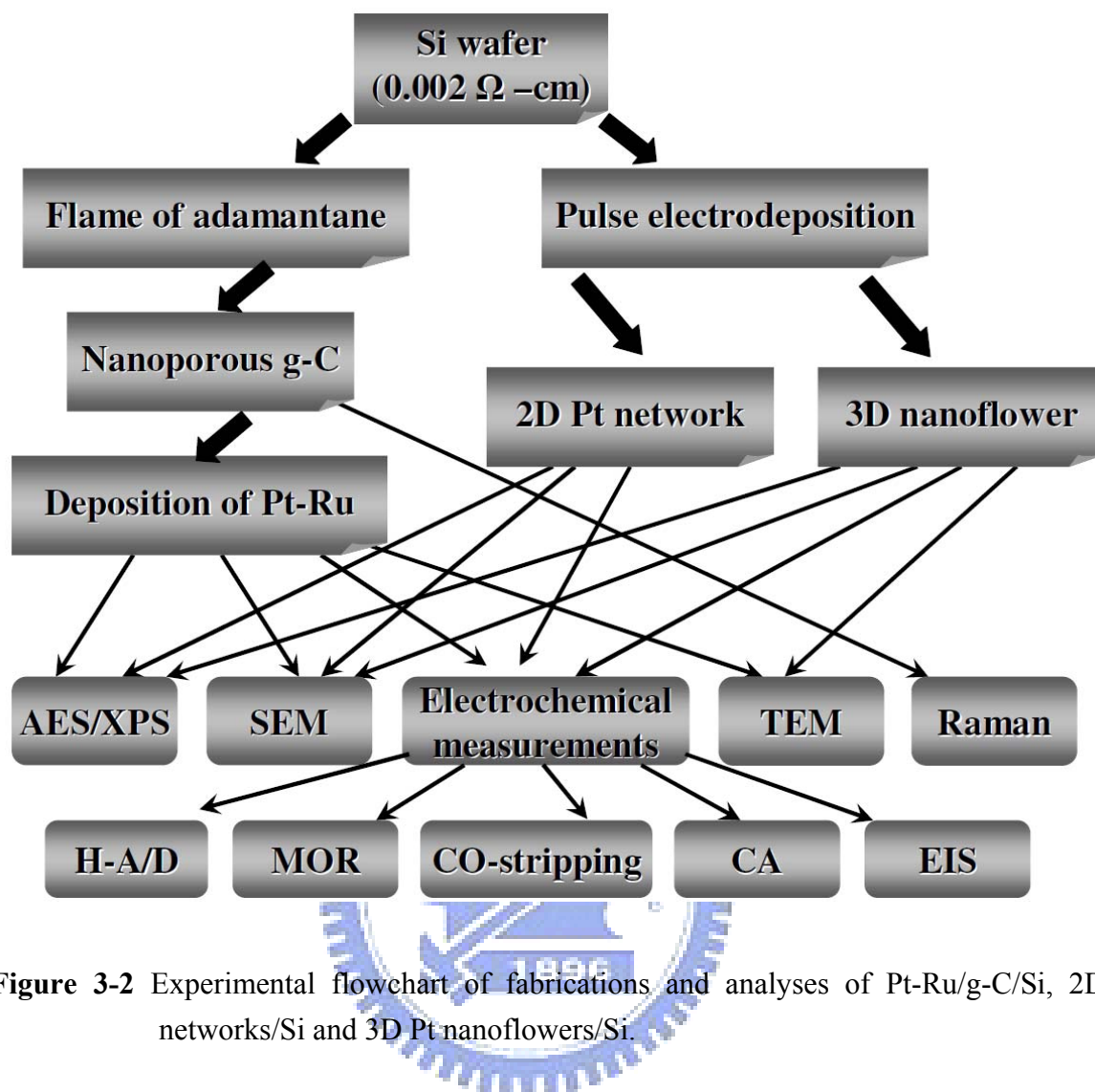


Figure 3-2 Experimental flowchart of fabrications and analyses of Pt-Ru/g-C/Si, 2D Pt networks/Si and 3D Pt nanoflowers/Si.

3.2 Deposition of TiN and Al films

Titanium nitride (TiN) films were deposited on a (100)-oriented p -type 4-inch silicon wafer of low resistivity ($0.002 \Omega\text{-cm}$) in an ultrahigh vacuum reactive dc magnetron sputtering system (MRC PRIMUS 2500TM), with a base pressure of 5×10^{-9} Torr. The titanium target used was 99.9999% pure. TiN films were prepared in a gas mixture of argon and nitrogen. During the deposition, the dc power was set at 8 kW and followed by the deposition of an Al film in $\sim 3 \mu\text{m}$ thickness on the TiN layer by a high vacuum thermal evaporator with the base pressure of 5×10^{-7} Torr. Aluminum ingots with a purity of 99.999% were used as the aluminum source. Tungsten boats were used to melt and evaporate aluminum

ingots.

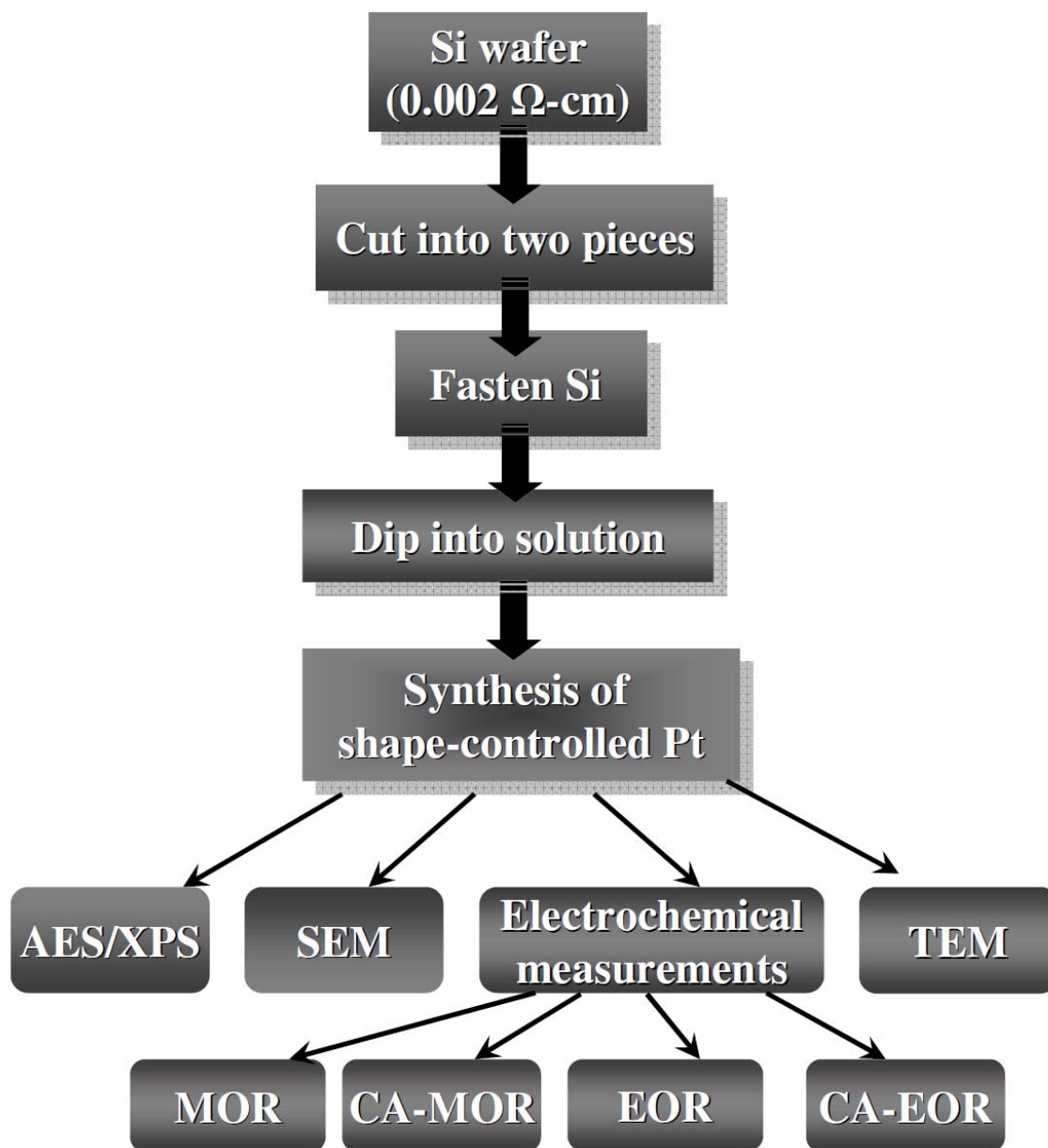


Figure 3-3 Experimental flowchart of synthesis and analyses of shape-controlled Pt nanoparticles.

3.3 Anodic aluminum oxide

The anode was the aluminum film specimen and a Pt foil was used as the cathode. The O-ring was clipped between the specimen and the tank fixed by a jig. Anodic oxidation of the Al film was carried out in 0.3 M oxalic acid ($\text{H}_2\text{C}_2\text{O}_4$) at 25°C under a constant polarization

voltage of 40 V. The anodic current was measured by a source -measure unit (Keithley Model 2400). Lab-view for GPIB interface with Keithley 2400 was employed to force voltage and measure current simultaneously. The program could also set up the anodic oxidation of Al film end current point. The schematic diagram of experimental setup for Al anodization is shown in Fig. 3-4.

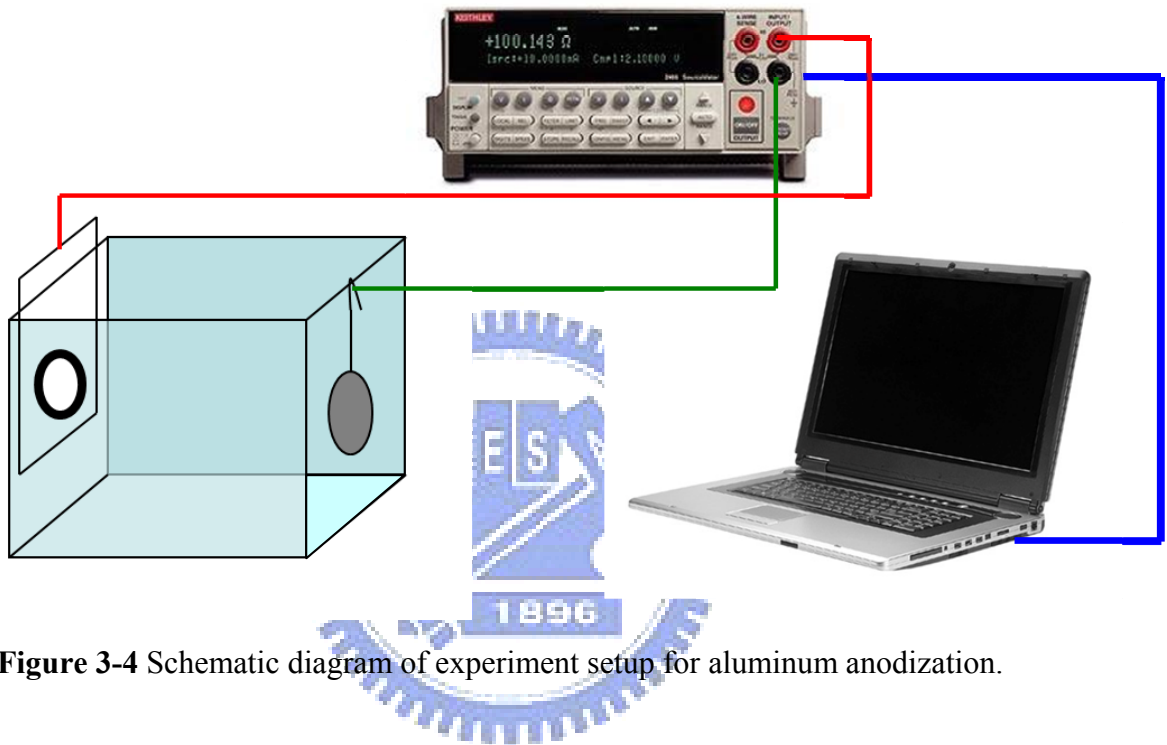


Figure 3-4 Schematic diagram of experiment setup for aluminum anodization.

3.4 Reactive-ion-etch system

The schematic diagram of the inductively coupled plasma (ICP) chamber is shown in **Fig. 3-5**. TiO_x nanodots were then used as nanomasks to etch the TiN layer and the underlying Si substrate in an ICP reactive-ion-etch (RIE) system (Duratek). An inductively coupled plasma source is also called a transformer-coupled plasma source because of its similar mechanism to a transformer. The inductive coils serve just like the initial coils of a transformer. When an RF current flows in the coils, it generates a changing magnetic field, which in turn generates a changing electric field through inductive coupling. The inductively coupled electric field accelerates electrons and initiates ionization collisions. Since the electric field is in the

angular direction, electrons are accelerated in the angular direction and travel a long distance without collision with the chamber wall or electrode. This is why an ICP system can generate high-density plasma at low pressure (a few 10 mTorr). The ICP design that includes high-density plasma (HDP) dielectric CVD system, silicon, metal, and dielectric HDP etching system, native oxide sputtering clean system and ionized metal plasma PVD system is very popular in the semiconductor industry.

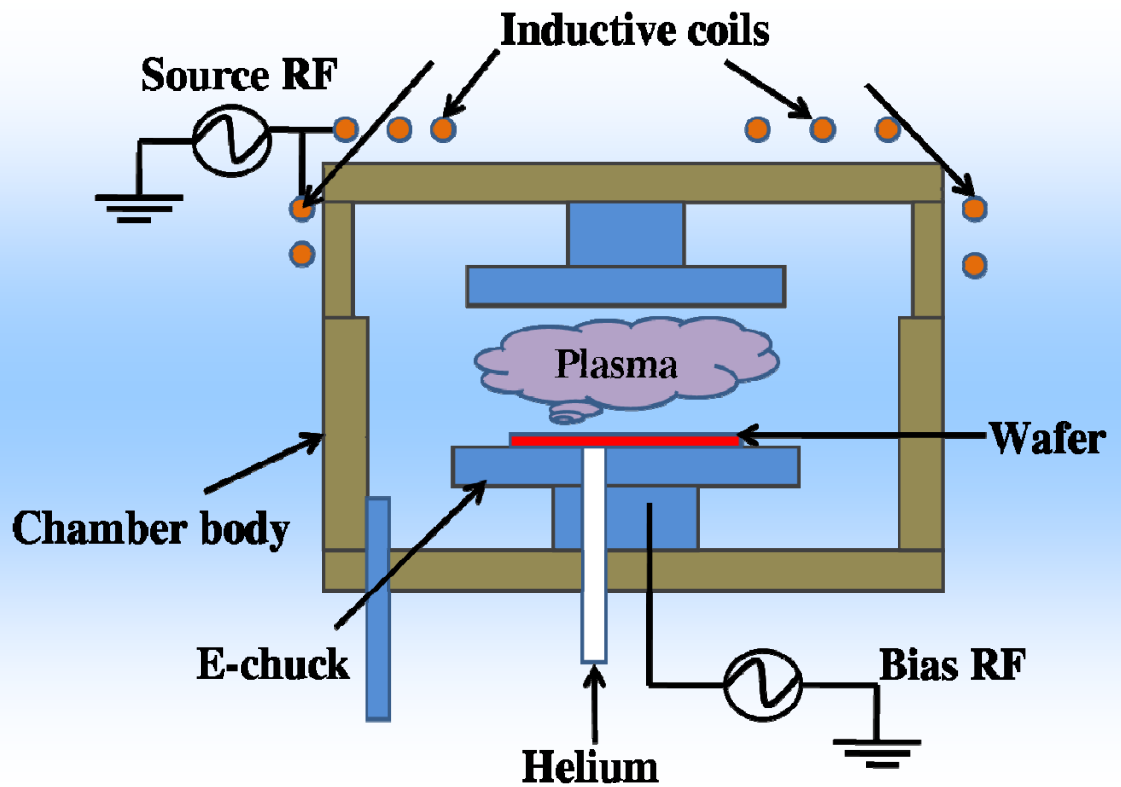


Figure 3-5 schematic diagram of ICP chamber

A bias RF system is added to the ICP chamber to generate self-bias and to control ion bombardment energy. Since ion bombardment from high-density plasma generates a lot of heat, a helium back-side cooling system with E-chuck is required for better wafer temperature control. In the ICP system, ion flux, mainly determined by the plasma density, is controlled by the source RF power and ion bombardment energy is controlled by the bias RF power.

3.5 MPCVD system

Fabrication of α -C coated Si nanotips was then carried out in a microwave plasma CVD (MPCVD) system. The overall MPCVD system layout is shown schematically in Fig.3-6. A quartz tube is vertically attached to a rectangular waveguide used as deposition chamber. The microwave from a magnetron source (model IMG 2502-S, IDX Tokyo, Japan) is supplied to the quartz tube through an isolator and a power meter. The

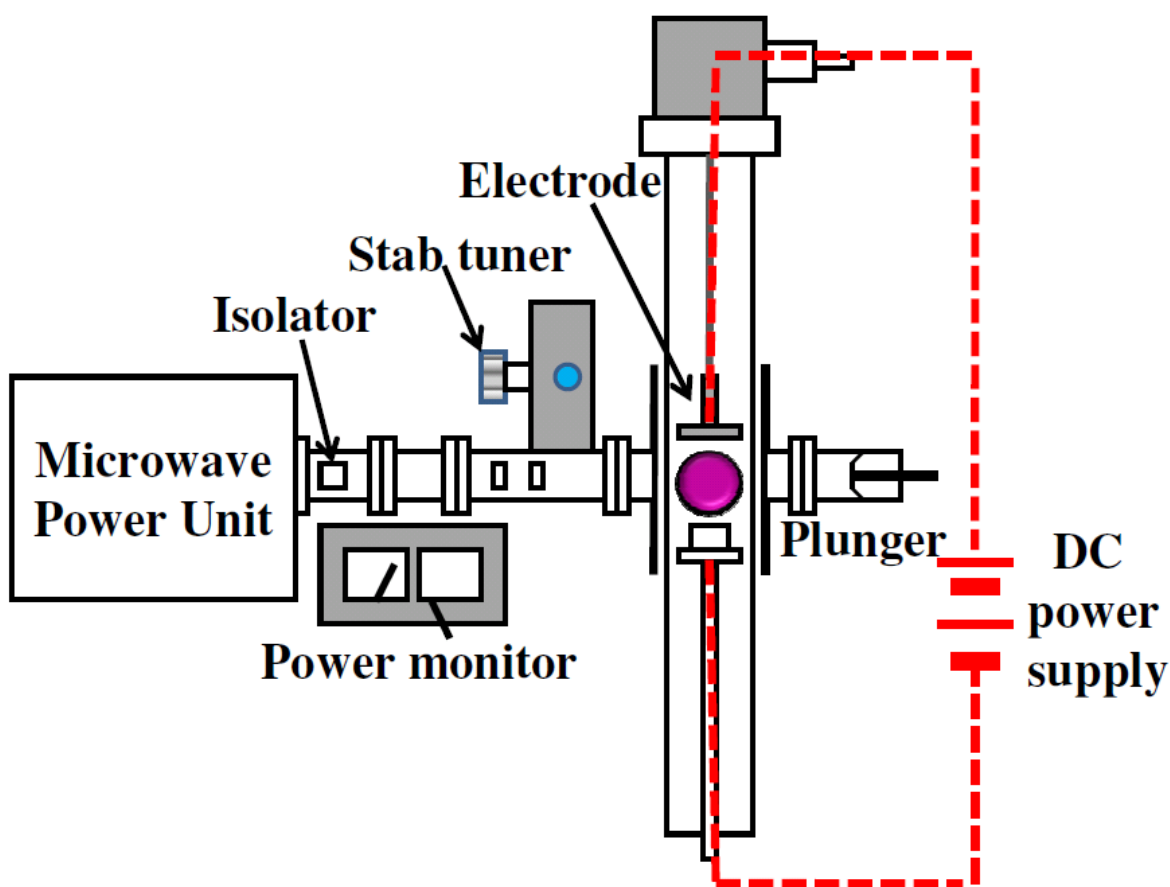


Figure 3-6 Schematic diagram of the bias assisted microwave plasma chemical vapor deposition system.

Then the microwave power is coupled to the quartz tube through an aluminum waveguide with a hole drilled through from top to bottom face. Aluminum tubes extend out from both holes. Tube extensions are water-cooled as well. A sliding short circuit is then attached at the end of the waveguide. The lower position of the quartz tube is connected with a stainless steel multi-port

chamber equipped with a rotary pump. Substrates are positioned in the middle of the quartz tube waveguide intersection and held vertically by a substrate holder of $\sim 1 \text{ cm}^2$ in diameter and made of molybdenum.

3.6 Electrodeposition of Pt nanostructures

Electrodeposition of Pt nanostructure films were carried out by using bipolar pulse electrodeposition (BPPE) in a three electrode cell system (Jiehan 5000 Electrochemical Workstation). Figure 3-7 shows the setup of an electrochemical deposition facility. As shown in **Fig. 3-7**, a thin Pt wire, saturated calomel electrode (SCE) and Si substrate (Si nanocones, amorphous carbon coated Si nanocones, and flat silicon), as counter, reference and working electrodes, respectively, were used.

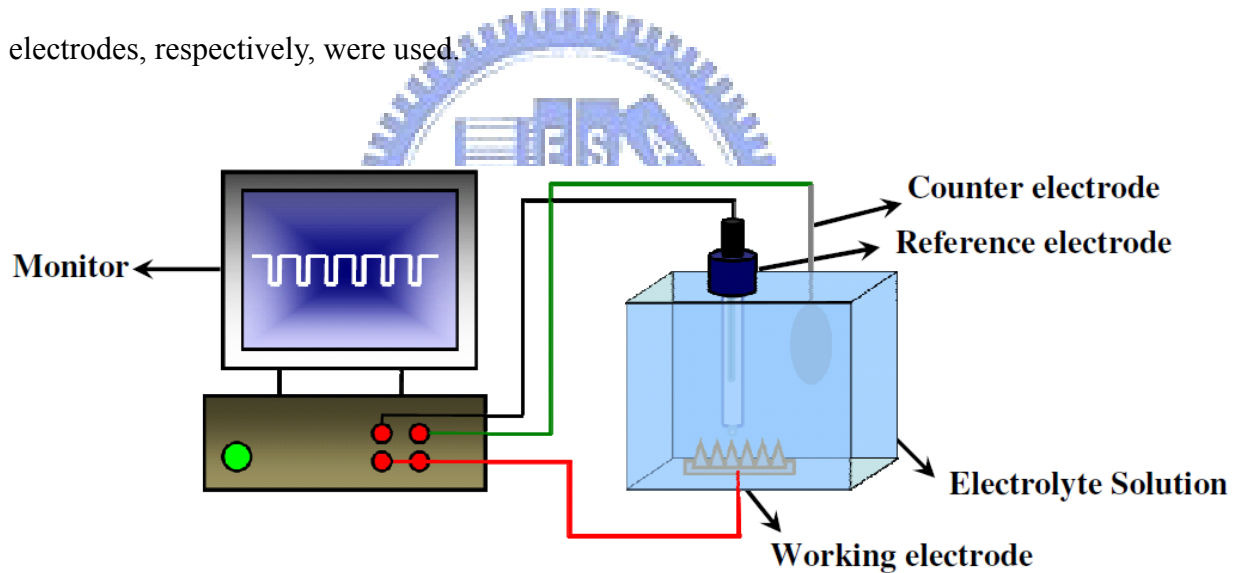


Figure 3-7 Schematic diagram of the electrochemical deposition setup.

In the BPPE, there are four operation parameters influencing the depositing of nanoparticles on the substrate: The high potential (V_H), the lower potential (V_L), the potential on time (T_{on}), and the potential off time (T_{off}). By applying specific potential pulses with time interval for the total experimental time (t_{exp}), Pt nanostructure films were deposited on the working electrode (Figure 3-7). All specimens used in this test had an area of 1.2 cm^2 .

3.7 Material analysis methods

3.7.1 Raman spectroscopy

While photons illuminate molecules or crystals, reaction between photons and atoms is always accompanied with momentum change or energy exchange. By collecting the scatter photons, sequence of spectrum, including Raman scattering (inelastic scattering) and Rayleigh scattering (elastic scattering) can be obtained. Photons of Raman scattering can be classified into two kinds, the Stoke side where photons loss energy or molecules gain energy and the anti-Stoke side where photons gain energy or molecules loss energy. Stoke side is generally used to characterize the material. As Raman spectrum provides the information of crystallinity and bonding, it has become the most direct and convenient way to identify carbon related materials. The Raman spectrum peak of sp^3 and sp^2 bonds in crystalline graphite are 1380 (D peak) and 1580 cm^{-1} (G-peak), respectively. The instrument in operation is a Renishaw's Raman microscope, Model 2000. The source available is He-Ne laser with the wavelength of 632.82nm and the power of 200mW. The spectral-slit width is 0.4cm^{-1} .

3.7.2 SEM

Scanning electron microscopy (SEM) is used to examine the surface morphology of the samples at a high magnification. The high magnification range of the SEM is achieved due to its resolving power of approximately 3-6 nm. The SEM is useful and popular for many reasons. One of the great advantages of SEM is its large depth of field (the amount of sample that is in sharp focus at one time). This makes it possible to examine surfaces with a relatively high level of surface variability (and at much higher magnifications). This is because the depth of field of the SEM can be up to four hundred times greater than that of a light microscope. Moreover, it has the advantage of easy sample preparation, and high image resolution. A common SEM is equipped with an electron gun to generate electron beams to be

accelerated under 0.4-40 kV voltage. By deflecting the incident beams with focusing coils, a two dimensional image can be obtained by detecting the reflected secondary electrons and the backscatter electrons.

The model mainly engaged is field emission type SEM JEOL-6500. Accelerating voltage is 15 kV with current of 10 μ A. Working distance is 10mm under 9.63x10⁻⁵Pa. The Fig. 3.7 shows a simple schematic drawing of the basic principle of the SEM.

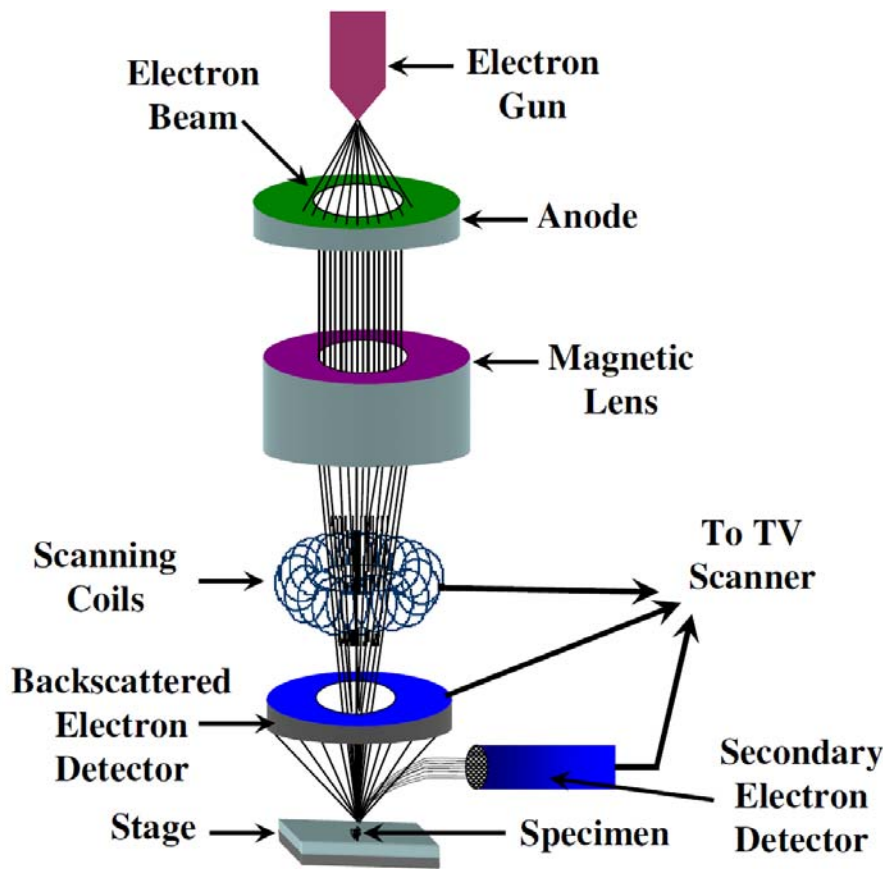


Figure 3-8 Schematic drawing of the basic principle of the SEM.

3.7.3 TEM

Transmission electron microscopy (TEM) (JEOL JEM-2010F) is operating at 200 kV accelerating voltage. This is the most important instrument to study defects in detail. Transmitted and diffracted electrons are recombined by objective lens to form a diffraction pattern in the back focal plane of that lens and a magnified image of the sample in its image plane. A number of

intermediate lenses are used to project either the image or the diffraction pattern onto a fluorescent screen for observation. The screen is usually lifted and the image is formed on photographic film for recording.

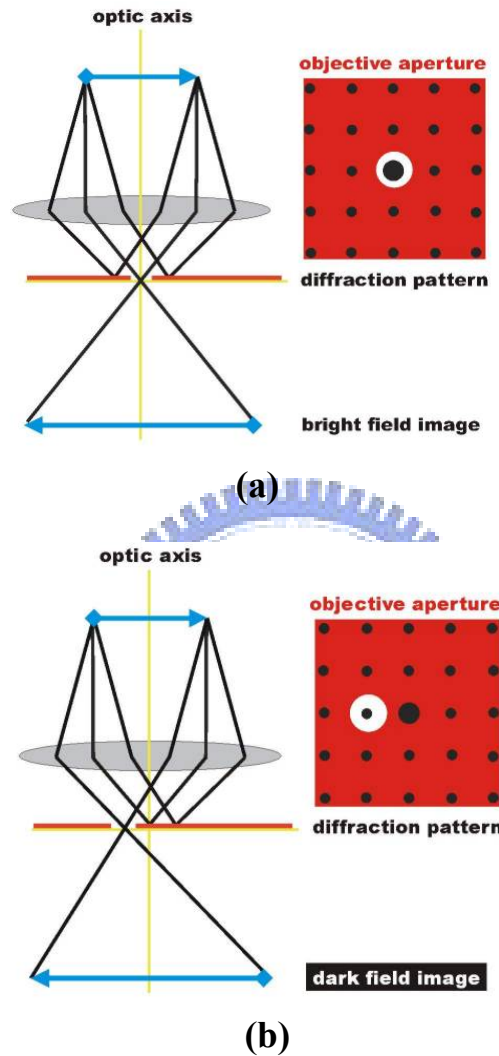


Figure 3-9 Schematic diagram of the TEM image modes (a) Bright field image (b) Dark field image. [http://www.microscopy.ethz.ch/TEM_imaging.htm].

The image modes in TEM are shown in Fig. 3-9. The TEM specimens were prepared by either mechanically scratching or ultrasonic agitation using dissecting forceps in the presence of a small drop of ethanol. The scratched specimens or ultrasonic agitation solution was put onto a holey-copper grid and dried in air at room temperature. Energy-dispersive X-ray

analysis (EDX) was employed to study the chemical composition of the specimens. Moreover, electron energy loss spectroscopy (EELS-Gatan GIF 2000) analyses were also performed in the TEM system to map the elemental distribution.

3.7.4 AES and XPS

Auger electron spectroscopy (AES) analysis technique employs an electron beam (2-30 keV) to irradiate the specimen surface and excite Auger electrons which possess specific energy. Through assaying the kinetics energy of Auger electrons by an electron energy analyzer, the element composition and the specimen chemical state are ready to be acquired. Because incident electrons with low-energies (1-3 keV) have very short inelastic mean free paths (5-20 Å) inside the solid phase materials, AES technique is usually used to obtain the information within 50 Å from the surface. In this study, AES was employed to investigate the chemical composition of specimens. The AES analyses were performed by using a VG Micro-lab 310F Auger system with a Schottky field emission electron source.

Surface analysis by X-ray photoelectron spectroscopy (XPS) involves irradiating a solid in vacuum with monoenergetic soft X-rays and analyzing the emitted electrons by energy. The spectrum is obtained as a plot of the number of detected electrons per energy interval versus their binding energy (or kinetic energy). Since the mean free path of the electrons is very small, the electrons which are detected originate from only the top few atomic layers. Quantitative data can be obtained from peak heights or peak areas, and the identification of chemical states often can be made from exact measurements of peak positions and separations. In this study, XPS was used to analyze the chemical states of Pt and Pt-Ru alloy catalysts. XPS analyses were performed on a VG Microlab 310F system with Al- $K\alpha$ (1486.6 eV) excitation. X-ray emission energy was 400 W with 15 kV accelerating voltage. Argon ion with ion energy of 5 keV was used for sputter profiling.

3.8 Electrochemical measurements

The electrochemical tests were performed with a model Jiehan 5000 Electrochemical Workstation System at 25°C. Figure 3-10 shows the setup of an electrochemical measurements facility. In these tests, a standard three-electrode electrochemical cell was used. In the experiments of all cyclic voltammetry (CVs), chronoamperometry (CA), and electrochemical impedance spectroscopy (EIS), the counter electrode was used as a thin Pt wire (99.99%), saturated calomel electrode (SCE) was used as the reference electrode, and a specimen were used as the working electrode. The thin Pt wire was connected to a high-quality screened cable. A high conductivity connection was made to the specimen for the working electrode. The electrodes of the probe were connected to a Jiehan 5000 Electrochemical Workstation system that controlled all experiments. Before each test, the Pt wire electrode was immersed in HCl (3:1, v/v) solution for about 1 min and then washed by distilled water. All specimens used in this test had an area of 1.2 cm².

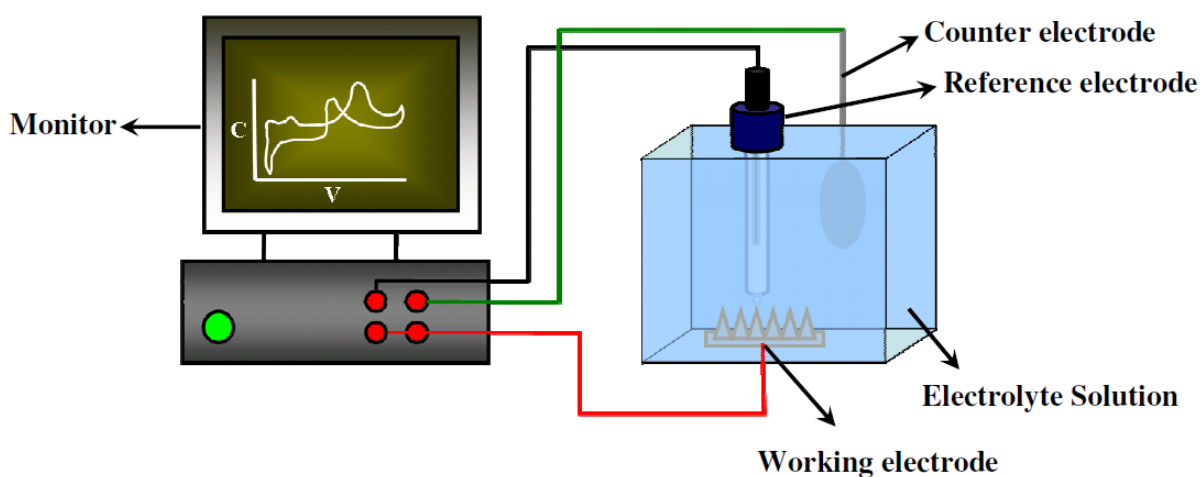


Figure 3-10 Schematic diagram of the electrochemical measurements setup.

Chapter 4

Pt Nanoparticles Supported on Ordered Si Nanocones as Catalyst for Methanol Oxidation

4.1 Introduction

Extensive studies have been devoted to the development of various nanostructured catalysts for energy-related technologies such as direct methanol fuel cells (DMFCs) for small portable electronic applications, such as the supplementary rechargeable battery for laptops and cellophanes etc. DMFCs fuel cell attracts such a wide attention is due to simple system design, low operation temperature, convenient fuel storage, high energy density and long life, as compared to conventional rechargeable power sources, such as Li ion batteries. In the fuel cells, nanostructured Pt are normally used as the catalyst in DMFCs because of the high electrocatalytic activity for methanol oxidation. A major issue in such applications is to increase the catalytic activity by increasing the surface area of the catalyst deposited on its support. In addition, In order to increase the electrocatalytic mass activity and reduce usage of the precious Pt catalyst, most methods of fabricating Pt catalyst-supporting electrodes tried to disperse Pt nanoparticles on the electrode support so that creating a high catalytic surface area and reducing Pt consumption could be achieved together. Much effort was done to improve catalyst mass activity by different approaches, such as nanoporous graphite with Pt nanoparticles [79], Pt particles supported on polymeric nanocones [80], carbon nanotubes (CNTs) with Pt-Ru [81, 82], MnO₂/CNT supported Pt-Ru [83], carbon nanocoils with Pt-Ru catalyst alloys [84] and carbon-coated anatase TiO₂ composite [85]. However, many complications of using Pt catalyst nanoparticles for DMFCs still exist and need to be solved for better utilization of the Pt catalyst. In particular, CO poisoning effect and catalyst loss during electrocatalytic reactions in DMFCs are among the major difficulties frequently

addressed and widely studied.

In this chapter, Pt nanoparticles were electrodeposited on a highly ordered Si nanocone (SNC) array, which was fabricated by means of anodic aluminum oxide (AAO) templation. The SNCs provided a high surface area for Pt catalyst loading, and the well ordered arrangement of the nanocones allowed a relatively uniform electric potential distribution over the nanocones during the Pt electrodeposition, thereby Pt nanoparticles could be well dispersed on the Si support and uniform in size. In addition, the SNCs were fabricated from a Si substrate of low resistivity, and thus the SNC support was very suitable for the use as the Pt electrocatalytic electrodes in respect of electrical conductivity. Moreover, the surface oxide formed on the SNC surface could enhance the CO tolerance of the Pt catalyst via bifunctional mechanism.

4.2 Fabrication procedure of the SNC array

The fabrication procedures of Si nanocones had been described elsewhere [86, 87] and illustrated in Figure 4-1. A p-type 4-inch Si wafer of low resistivity ($0.002 \Omega\text{-cm}$) was used as the substrate. A TiN thin film 30 nm thick was first sputter-deposited on the Si surface, followed by thermal evaporation of an aluminum thin film 1 μm thick. The TiN layer was used as an adhesion layer between the Si substrate and the Al thin film, and would be later used for preparation of the nanodot mask for fabrication the SNCs. The as-deposited Al/TiN film stack was then oxidized by electrochemical anodization, which was performed in 0.3 M oxalic acid ($\text{H}_2\text{C}_2\text{O}_4$) at 25°C under a constant polarization voltage of 40 V for 20 min. Anodic oxidation of the Al thin film under the anodization conditions would produce hexagonally arranged AAO nanopore channels. As the anodization reaction approached the interface between the Al and TiN thin films, local anodization of the underlying TiN layer occurred. Because the TiN oxidation reaction was confined in the nanosized AAO pore channels, dome-

shaped TiO_x nanodots were produced on the TiN layer. The AAO was then removed by the aqueous solution of 6 wt % H_3PO_4 and 1.5 wt % CrO_3 at 60°C for 40 min., thereby the TiO_2 nanomask was formed. To fabricate Si nanocones, the TiN capped Si substrate with the TiO_2 nanomask was etched in an inductively-coupled-plasma reactive-ion-etch (ICP-RIE) system for 50 sec., using a gas mixture of BCl_3 and Cl_2 as the plasma source. The RIE process was performed under the following working conditions: plasma power 400 W, substrate bias power 120 W, working pressure 10 mtorr with a flow rate of 35 sccm for the plasma gas source.

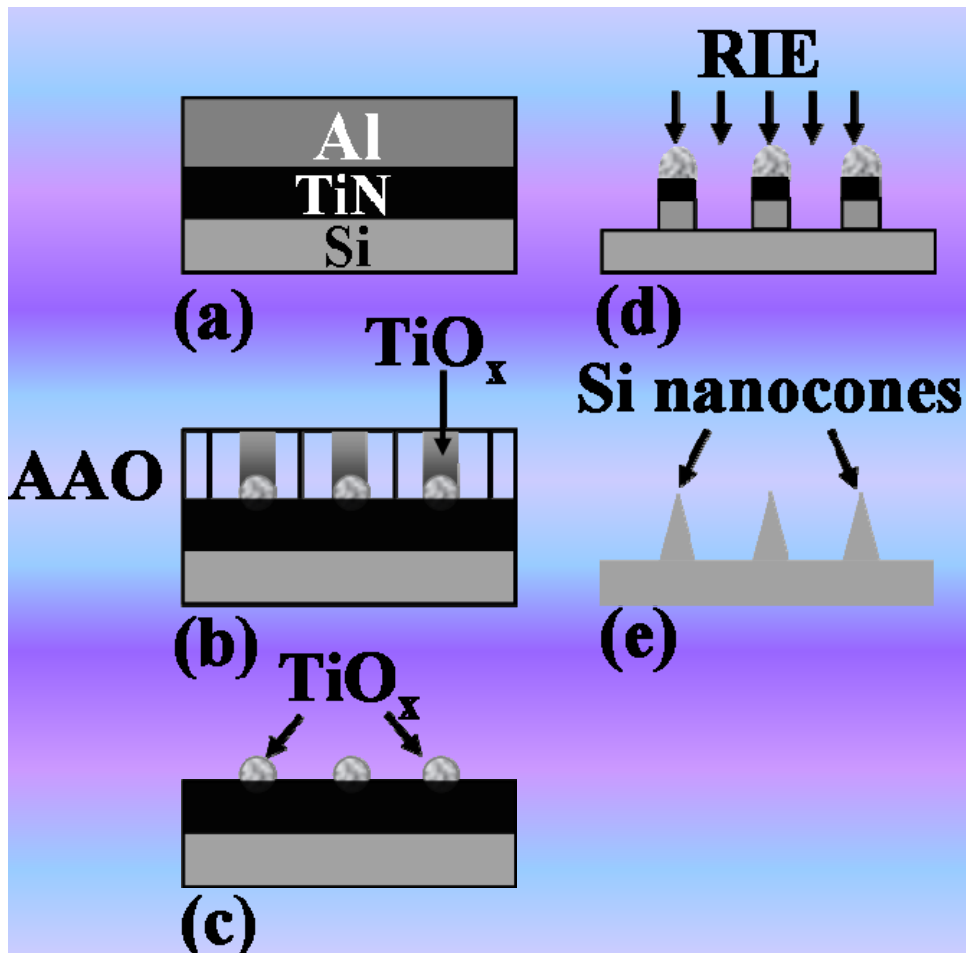


Figure 4-1 shows the fabrication scheme of SNC arrays: (a) deposition of TiN and Al thin film on the Si wafer by sputter deposition and thermal evaporation, respectively, (b) anodic oxidation of the Al film and formation of TiO_x nanodots, (c) removal of the AAO by wet etch, (d) reactive ion etch (RIE) of the remaining TiN and the Si substrate, and (e) formation of the SNC arrays.

4.3 Electrodeposition of Pt nanoparticles on SNC array

The Pt nanoparticles were electrodeposited on SNCs in an aqueous solution of 1M K_2PtCl_6 -1M HCl at 25°C by potentiostatic pulse plating in a three electrode cell system with SNCs as the working electrode, thin Pt wire as the counter electrode and saturated calomel electrode (SCE) as the reference electrode. Prior to electrodeposition of Pt catalyst on SNCs, the ordered SNC array was immersed in a deoxygenated aqueous solution of 1 M H_2PtCl_6 at 35°C for 3 hours. All solutions were prepared in deionized water (>18 M Ω). Bipolar pulses were used and the pulse height and duration were . 0.09mV and 7ms for negative pulse, and +0.02mV and 1ms for the positive pulse, respectively. The size of Pt nanoparticles and mass loading of platinum on SNCs were controlled by the applied potential and pulse duration. Chloride anions in the electrolyte solution tend to adsorb on Pt particles, making Pt nanoparticles better separated from each other due to electrostatic repulsion between negatively charged surface layers [88]. The size of Pt nanoparticles and mass loading of platinum on SNCs were controlled by the applied potential and pulse duration. The Pt/SNC electrode was rinsed thoroughly with deionized water to remove residual chlorine ions after Pt electrodeposition, and allowed to dry before use in the measurement cell. The Pt/SNC electrode was rinsed thoroughly with deionized water to remove residual chlorine ions after Pt electrodeposition, and allowed to dry before use in the measurement cell.

4.4 Structural characterization of SNC array

Figures 4-2 shows the side-view SEM images of the fabrication process of SNC arrays. The side-view SEM image in Fig.4-2 (a) reveals that the TiO_x nanomask arrangement was compliant with the pore arrangement of the AAO template and had a nanomask density of $\sim 1 \times 10^{10} \text{ cm}^{-2}$. To etch the TiN layer, a gas mixture of BCl_3 and Cl_2 was used as the plasma source in the ICP-RIE system. TiO_x and Si could also be etched by the Cl_2 -based plasma

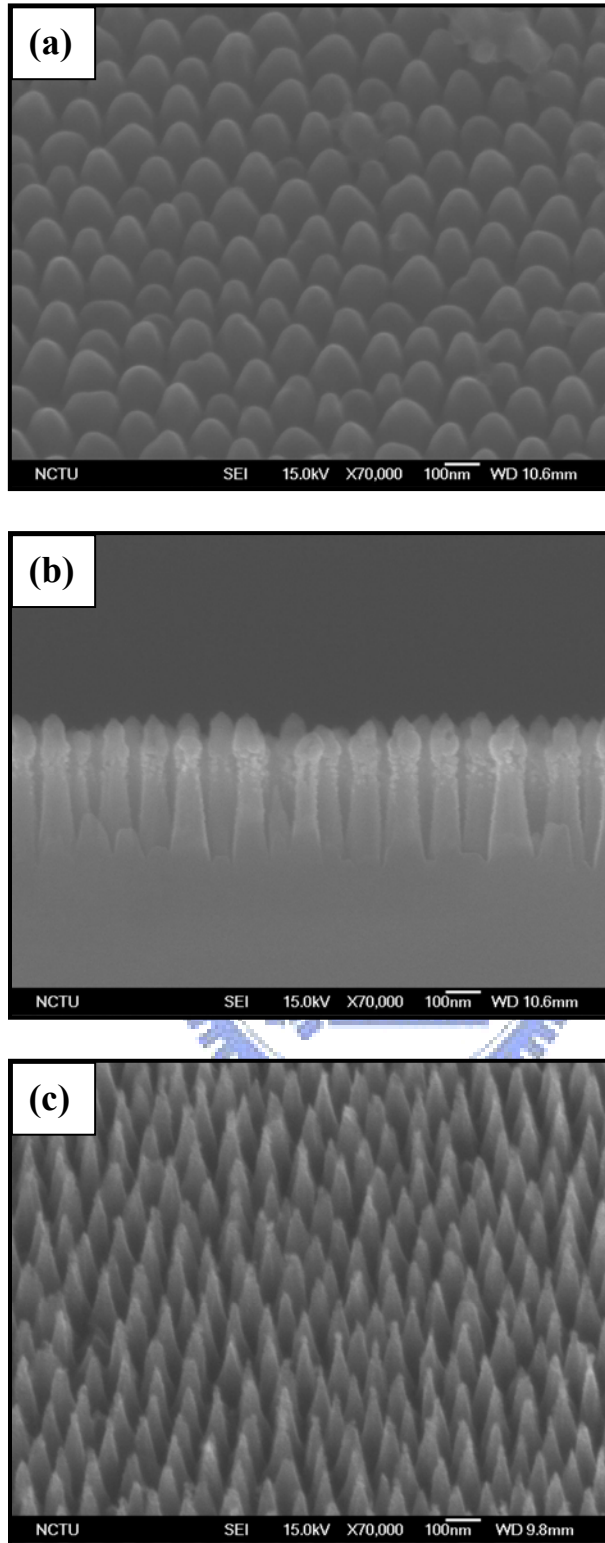


Figure 4-2 shows the side-view SEM images of the fabrication of SNC arrays: (a) TiO_x nanomasks after the removal of the AAO layer by wet etch, (b) the $\text{TiO}_x/\text{TiN}/\text{SNC}$ arrays after the RIE etch by SF_6 , Cl_2 and O_2 for 40 sec. and (c) removal of the oxide layer by wet chemical etch and the formation of highly ordered SNC arrays.

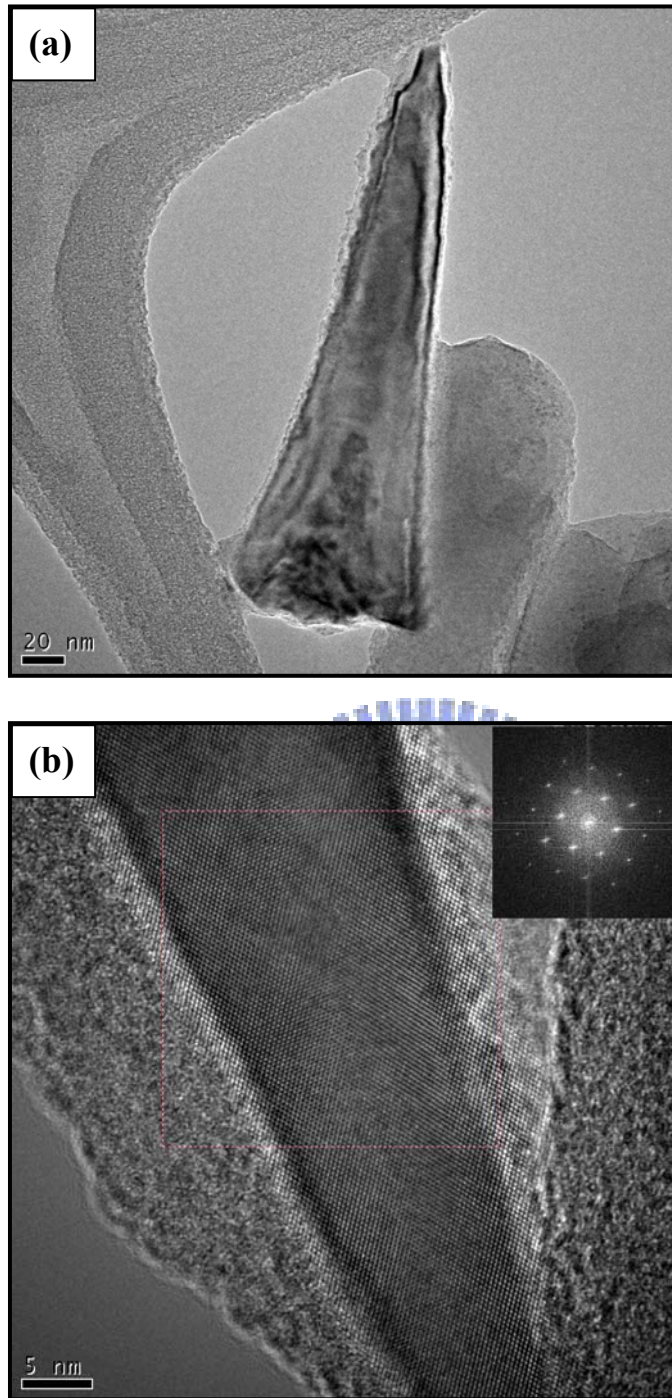
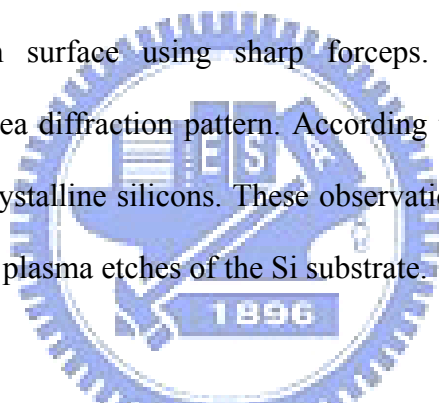


Figure 4-3 shows (a) TEM image of the SNC array and (b) high-resolution TEM image of the SNC array in which the inset reveals the selected area diffraction pattern.

source, but the relatively large height of the TiO_x nanomask provided sufficient masking thickness to the underlying TiN and Si substrate so that the arrangement pattern of nanopillars could be successfully transferred to the Si substrate. Then, gas mixture of Cl_2 , SF_6 and O_2

were used as the plasma source to etch Si substrates and form SNCs of high aspect ratio, as shown in Fig. 4-2 (b). The SNC array had an ordered hexagonal arrangement as AAO as well. The surface silicon oxide of the Si nanocones was removed by wet etching. Si nanocones were uniform in size and shape as shown in Fig. 4-2 (c). Most SNCs had a height of ~200 nm and a base width of 100 nm. The geometric shape and size of nanocones could be tailored by varying the RIE time.

Transmission electron microscope (TEM) was used to further characterize the morphology of an individual SNC. A bright-field TEM image of typical SNC is shown in Fig. 4-3 (a). The bright-field high resolution TEM image of SNC is shown in Fig. 4-3 (b) in which the nanocones are clearly evident as the final stage. Sample for TEM was made by simply scratching the specimen surface using sharp forceps. The inset to Fig. 4-3 shows corresponding selected area diffraction pattern. According to electron diffraction study (Fig. 4-3 inset), the SNCs is crystalline silicons. These observations indicated that formation of Si nanocones was a result of plasma etches of the Si substrate.



4.5 Structural characterization of Pt/SNC array

Pulse potentiostatic method was used for the depositing Pt nanoparticles on ACNC electrode. Pulse potentiostatic electrodeposition has advantages over the conventional direct current potentiostatic electrodeposition because of the possible beneficial effects on the morphology and compositional uniformity of the deposit [89]. Those effects are a consequence of the free choices of several variables independently, e.g., type of periodic waveform, potential, and duration of cathodic and anodic pulses for a particular deposition solution rather than simply the potential. The particles size control by applying the alternate positive and the negative potential pulses on the working electrode. The positive potential pulse was applied to avoid particle coalescence so that nanosized Pt nanoparticles could be

deposited on the Si nanocones.

Figure 4-4 shows the scanning electron microscopy (SEM) image of the SNC array with electrodeposited Pt nanoparticles. The well ordered SNCs, with a hexagonal arrangement, was ~ 300 nm high and had a base diameter of ~ 100 nm. X-ray photoelectron spectroscopy (XPS) indicated the presence of Pt on the SNCs after the electrodeposition (shown in Fig. 4-5). According to the cross-sectional SEM image, Pt particles seemed to slightly accumulate on the tip of SNCs, but nanoparticles agglomeration on the sidewall of the nanocones was insignificant. Due to the very small size, Pt nanoparticles are hardly observed to adhere on the sidewall of the SNCs from the SEM images.

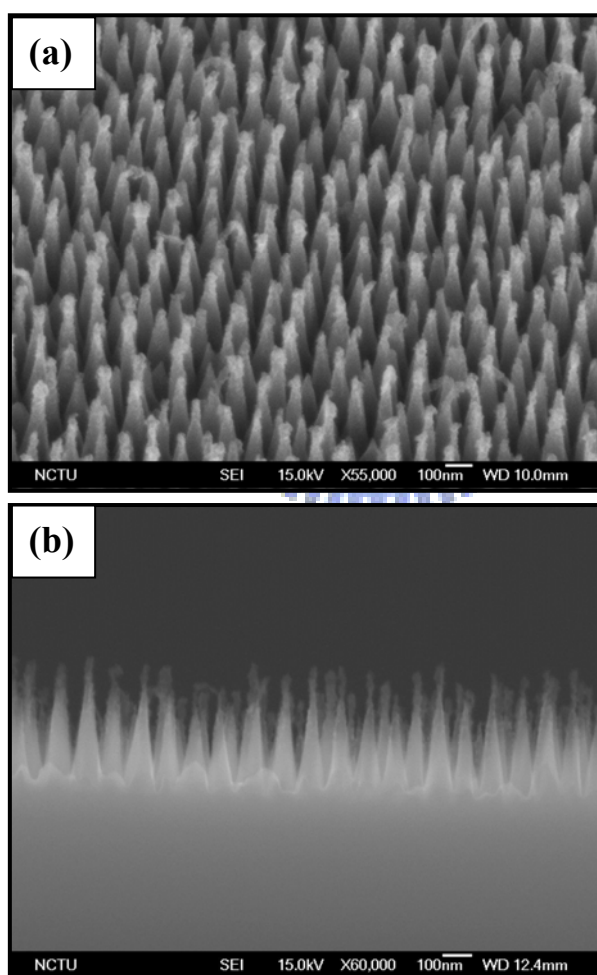


Figure 4-4 shows SEM images of the SNC array with electrodeposited Pt nanoparticles; (a) a side view, and (b) cross-sectional view.

The Pt nanoparticles had a size smaller than ~ 5 nm according to transmission electron

microscopy (TEM) study. Figure 4-6 shows the high-resolution TEM image of a silicon nanocone with well dispersed Pt nanoparticles on it. The selected area electron diffraction (SAED) pattern is shown in the inset of Fig. 4-6. Four diffraction rings can be indexed as (111), (110), (200) and (311) orientations for the Pt face center cubic (FCC) lattice structure. Electron energy loss spectroscopy (EELS) was also used to map the elemental distribution of Pt on the SNC, and the mapping clearly shows that Pt nanoparticles distributed on the tip and sidewall of the SNC (shown in Fig. 4-7).

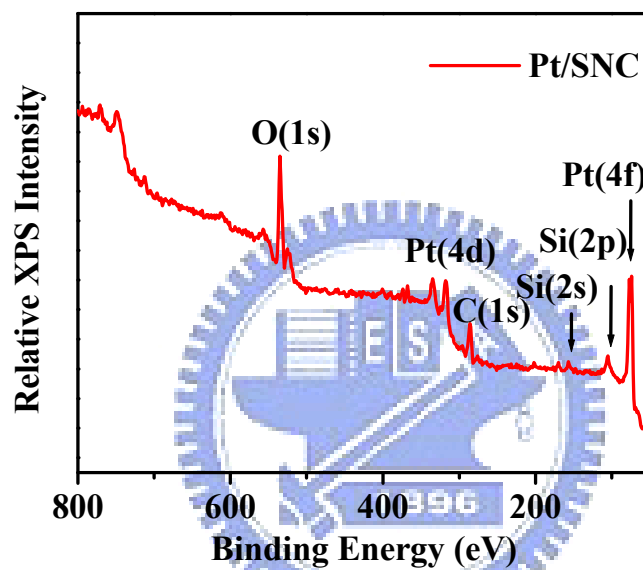


Figure 4-5 shows the XPS spectrum of the Pt/SNC arrays.

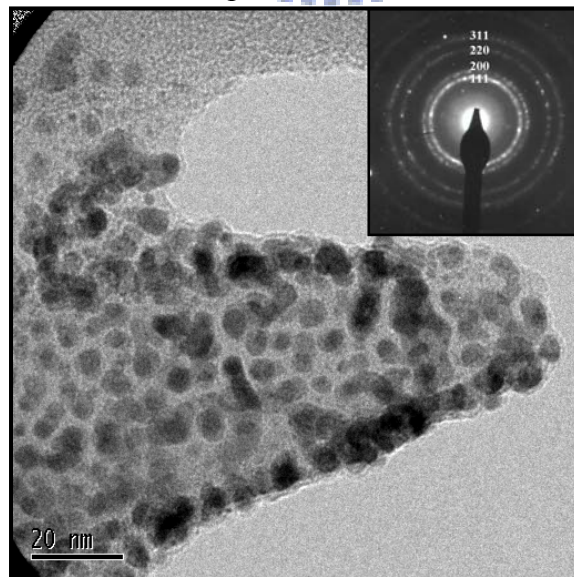


Figure 4-6 shows HRTEM image of the Pt/SNC array in which the inset reveals the selected area diffraction pattern of the nanocone.

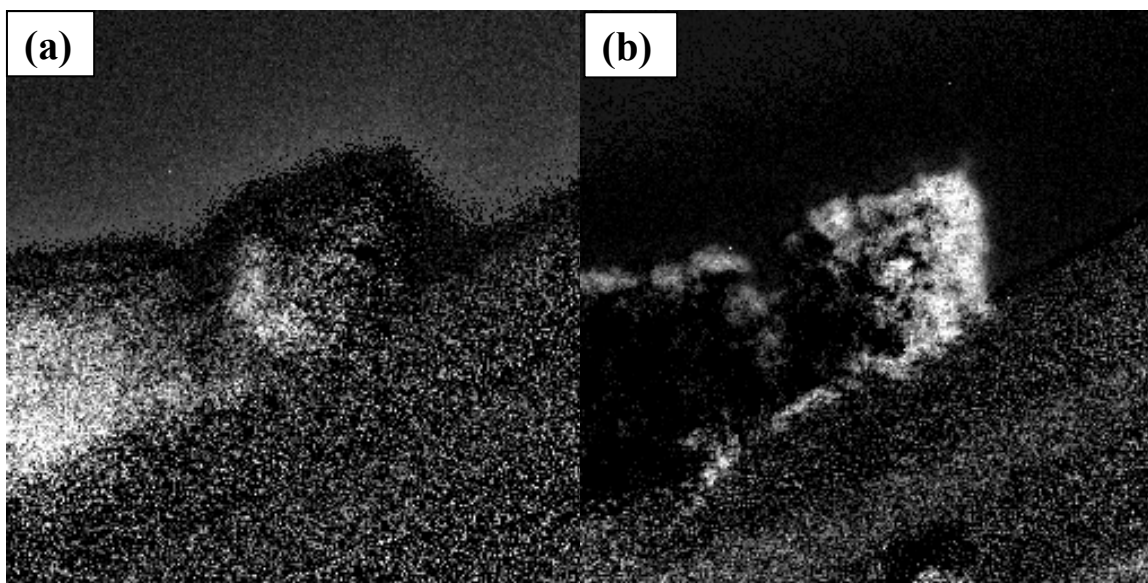


Figure 4-7 EELS mapping images of (a) Silicon, and (b) Pt for the Pt nanoparticles loaded SNCs.

4.5 Electrochemical characterization

The electroactive surface area (ESA) of the Pt loaded SNC electrode can be determined by CO stripping cyclic voltammetry. The CO stripping voltammogram for the Pt/SNC electrode in a CO saturated 1M H₂SO₄ aqueous solution is shown in Fig. 4-8 (a). A high ESA of ~317 m² g⁻¹ was obtained for the Pt/SNC electrode by integrating the CO electro-oxidation peak area, assuming an oxidation charge of 420 μC cm⁻² for one monolayer of CO on a smooth Pt surface [90]. For comparison, the ESA of the Pt film electrodeposited on a flat Si substrate (hereafter abbreviated as Pt/Si) was calculated to be 38.9 m² g⁻¹ from Fig. 4-8 (b).

The electrocatalytic stability of the Pt/SNC electrode was evaluated by repeating the cyclic voltammetric (CV) scan from -0.45 to 1.2V in the 1M H₂SO₄ solution for more than 1000 cycles. From Fig. 4-9, the CV curve of the 1000th cycle shows that the hydrogen adsorption/desorption peak had a peak current reduction by ~20% as compared with that of the second cycle, indicating possible Pt nanoparticle loss from the SNCs after 1000 cycles of hydrogen oxidation and reduction. Fig. 4-10 is the plots of the ESA as a function of the number of CV cycles for the Pt/SNC and the Pt/Si electrodes. The plots are normalized

against the ESA of the first cycle. The ESA of the Pt/SNC electrode had a moderate drop for the first 100 CV cycles, and then progressively decreased to 75% of the initial ESA after 1000 CV cycles. On the other hand, the Pt/Si electrode shows a dramatic drop in the ESA in the first 200 cycles, followed by continuous and significant ESA decrease. The much smaller ESA loss of the Pt/SNC electrode suggests that the electrodeposited Pt nanoparticles were well adhered to the Si nanocones.

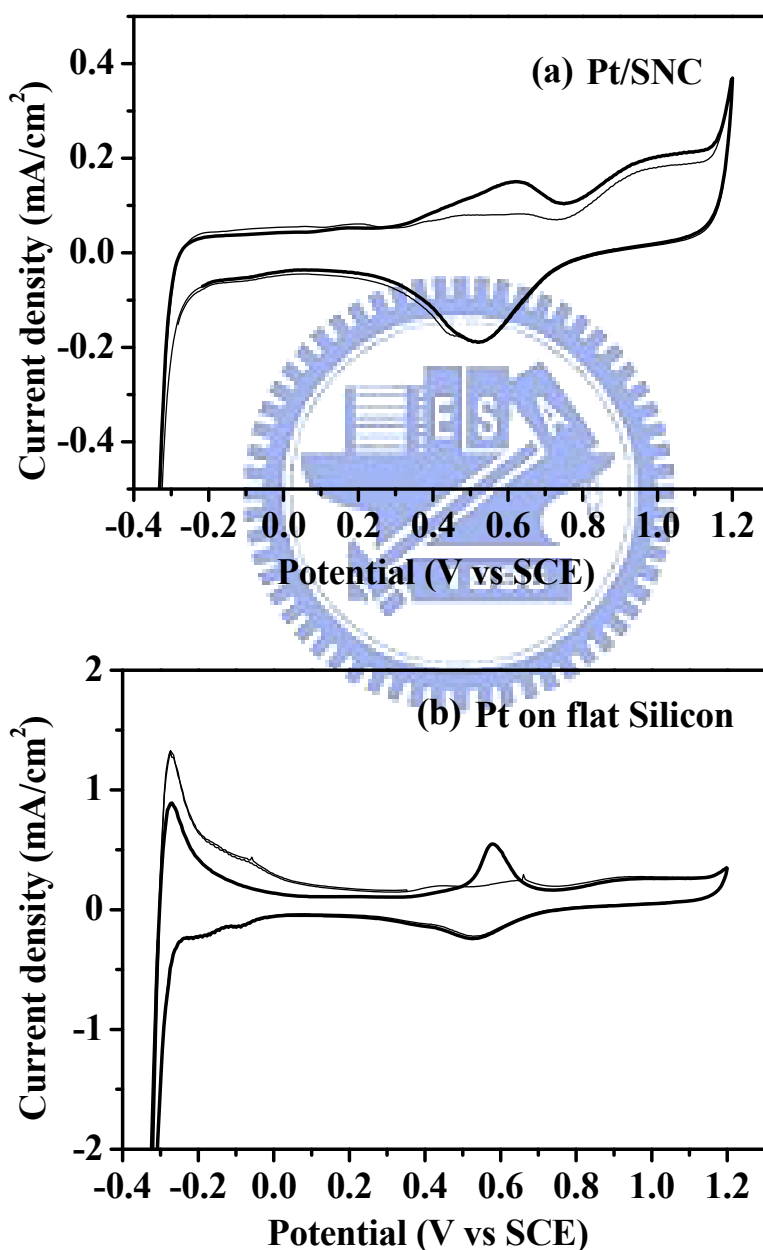


Figure 4-8 CO stripping cyclic voltammograms of (a) Pt nanoparticles electrodeposited on the ordered SNCs and (b) the Pt film electrodeposited on the flat silicon substrate in a CO saturated 1M H₂SO₄ solution. The scan rate is 20 mVs⁻¹.

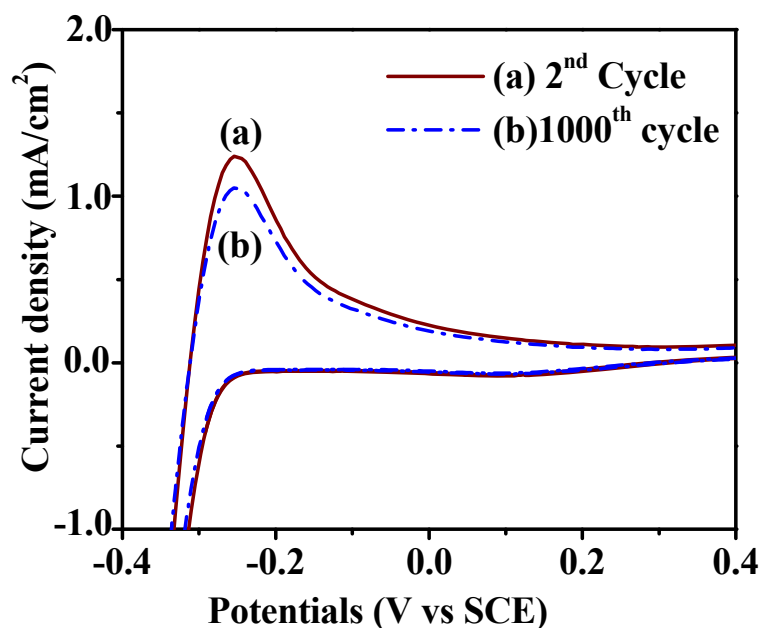


Figure 4-9 Cyclic voltammograms for Pt/SNC electrode in 1M H₂SO₄ aqueous solution at room temperature and with a scan rate of 25 mVs⁻¹: (a) the 2nd cycle and (b) the 1000th cycle.

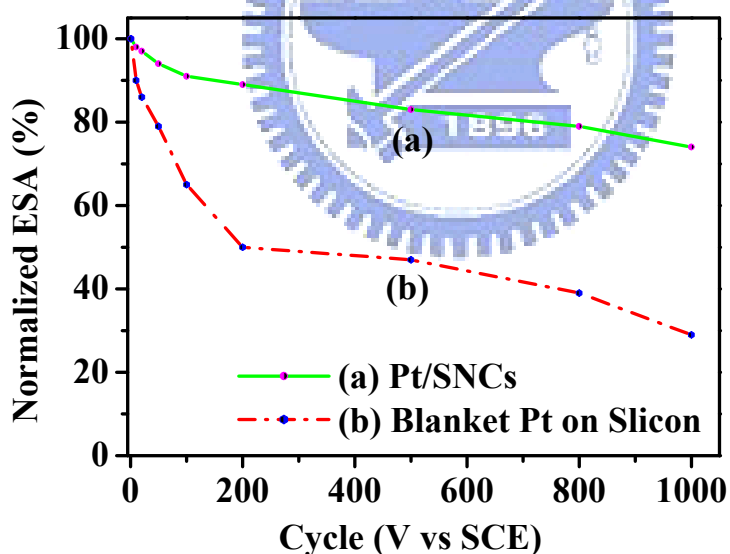


Figure 4-10 shows the plot of electroactive surface area (ESA) as a function of the number of the cyclic voltammetric scan for (a) the Pt film electrodeposited on the flat Si substrate and, (b) the ordered Pt/SNC electrode.

The Pt nanoparticles had a very high catalyst specific activity (current per ESA) for electro-oxidation of methanol. Figure 4 - 11 shows the cyclic voltammogram of the Pt/SNC

electrode in 1 M methanol/1 M H₂SO₄ aqueous solution. The unit of the y-axis of the CV plot is labeled by the current per ESA. The CV curve shows that the methanol oxidation peak had the maximum around 0.83 V vs. SCE and a very low onset potential of ~0.08 V.

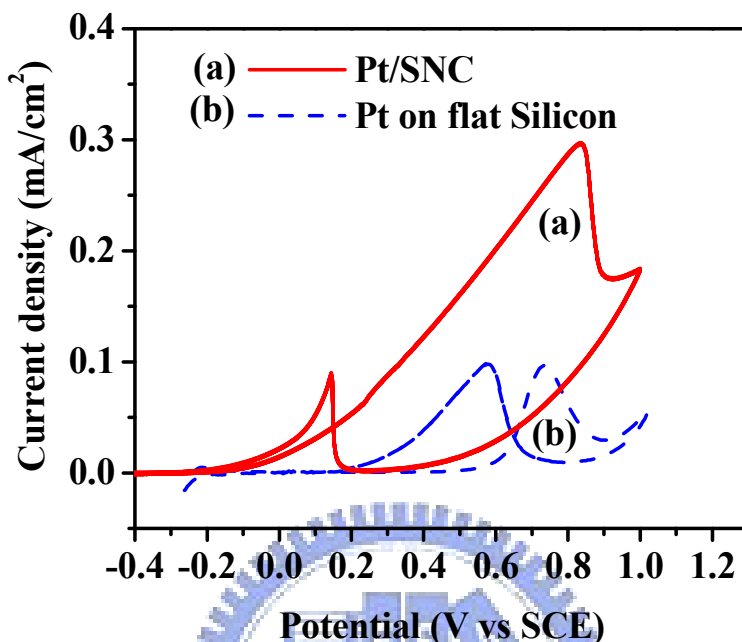


Figure 4-11 shows the cyclic voltammograms of (a) the Pt catalyst nanoparticles on the ordered SNC array and (b) the Pt film electrodeposited on the flat silicon substrate in an argon saturated 1 M CH₃OH/1 M H₂SO₄ aqueous solution. The scan rate is 25 mVs⁻¹.

Also shown in Fig. 4-11 is the CV curve of the Pt/Si electrode, which shows a much smaller specific activity with a high onset potential. The negative onset potential shifting indicated that the Pt nanoparticles on the ordered SNC array can effectively reduce overpotentials in the methanol electrooxidation reaction [91 – 94]. Because of the very large ESA, the Pt/SNC electrode had a better electrocatalytic mass activity compared with many previously reported electrodes made from nanostructured materials. The mass activity of the Pt/SNC electrode at 0.4V was ~0.53 A mg⁻¹ at room temperature, that was about six folds higher than that of the Pt loaded carbon nanocoils [84], and two folds higher than the carbon-coated anatase TiO₂ nanocomposite [85].

Figure 4-12 shows the chronoamperogram of electroactivity of the Pt/SNC electrode at the oxidation potential $\sim 0.3\text{V}$ in the 1 M methanol/1 M H_2SO_4 aqueous solution at 25°C . The chronoamperogram showed that electrocatalytic oxidation of methanol maintained a high activity and was very stable during the measurement for more than 2 h. The observation implied that most CO adspecies could be oxidized and removed from the Pt catalyst nanoparticles so that the catalytic oxidation of methanol could be kept proceeding efficiently on the Pt/SNC electrode. The argument was supported by the CO stripping cyclic voltammetry study. In Fig. 4-8, the CO stripping voltammogram of the Pt-SNC electrode was compared with that of the Pt/Si electrode. For the Pt/SNC electrode, the onset of electro-oxidation of CO took place below $\sim 0.3\text{V}$ vs. SCE and the peak potential was $\sim 0.6\text{V}$. On the other hand, the Pt/Si electrode had an onset potential for CO electrooxidation $\sim 0.5\text{V}$ vs. SCE. The observation that the Pt/SNC electrode had a much lower onset potential in the CO stripping voltammogram indicated that electrooxidation reaction of CO adspecies on Pt sites could be efficiently performed on the Pt/SNC electrode.

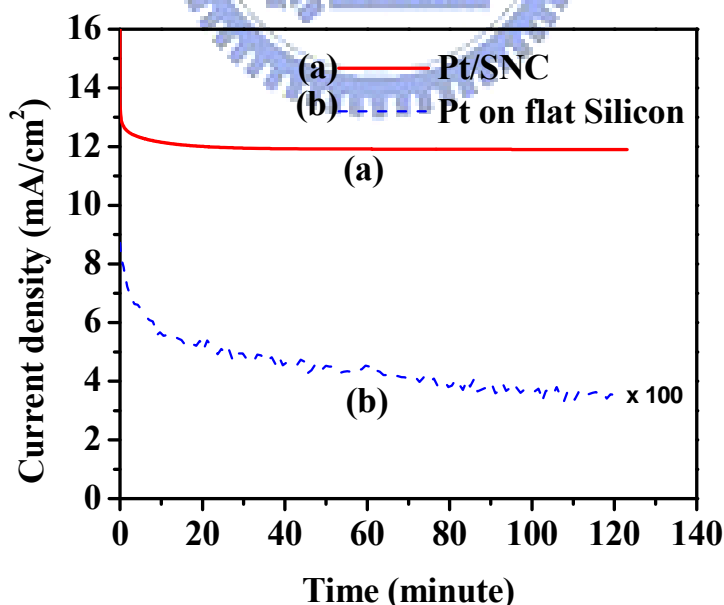


Figure 4-12 shows the chronoamperometric response of (a) Pt nanoparticles electrodeposited on the ordered SNCs, and (b) the Pt film electrodeposited on the flat Si substrate in a saturated 1 M $\text{CH}_3\text{OH}/1\text{ M H}_2\text{SO}_4$ aqueous solution at 0.3V (SCE) for 2 h. The scale of curve b is multiplies by 100.

The excellent electrocatalytic performance of the Pt-SNC electrode can be explained as follows. First, the SNCs provided a large surface area for Pt nanoparticles loading, resulting in a very high catalytic mass activity. With the present nanocone geometry, the SNCs provided a surface area applicable for Pt loading six times (the ratio of the cone surface area to the cone base area) larger than a flat Si surface, and thus increased the mass activity accordingly. Second, nanosized and highly dispersed Pt catalyst nanoparticles were deposited on the SNCs. Unlike many reported porous electrodes, which had a very large surface area as well, the ordered SNCs may provide better electrodeposition conditions for well dispersed Pt nanoparticles. Because the arrangement of the SNCs was highly ordered, the potential distribution over the SNC array should be even and, therefore, the deposited Pt particles were uniform in size. Besides, compared with many porous supports, the SNC array had a larger open volume, allowing ionic species to diffuse more freely between Si nanocones, and thus Pt particles could be readily electrodeposited on the SNCs without significant agglomeration. By carefully tuning the pulse voltage and pulse duration, we can limit the Pt particle size to the nanometer range and mitigate particle coalescence, thereby increasing the electroactive area. Third, silicon oxide grown on the Si nanocones can play an important role in enhancing CO tolerance of the electrode via the bifunctional mechanism [12]. A nature SiO₂ layer is usually terminated with silanol groups. The bifunctional model describes that hydroxyl surface groups are able to oxidize and remove adjacent CO adspecies from the Pt catalyst surface, thus avoiding CO poisoning. Because the Pt nanoparticles were well dispersed on the SNCs, CO adspecies bound on the periphery of Pt nanoparticles can be readily oxidized by surrounding silanol groups. Moreover, due to the nanoscaled size of Pt catalyst, OH adspecies can migrate over the Pt nanoparticle without much difficulty and react with adsorbed CO via a Langmuir – Hinshelwood type reaction mechanism, in which adsorbed reactants diffuse, collide and form products on the surface, thereby facilitating a better efficiency of CO oxidation.

4.6 Summary

We have electrodeposited Pt catalyst nanoparticles on highly ordered SNCs fabricated by AAO templation, and electrocatalytic oxidation of methanol on the Pt/SNC electrode was studied. Because of the large surface area of the Si nanocones and the highly dispersed nanosized Pt catalyst particles, the Pt/SNC electrode demonstrated a very high mass activity and a very low onset potential. CV measurements, CO stripping cyclic voltammogram and chronoamperometric study indicated that the Pt nanoparticles were well adhered to the Si nanocones and the Pt/SNC electrode had a very good CO tolerance. We ascribed the good CO tolerance to the efficient CO oxidation by the abundant silanol groups surrounding the Pt nanoparticles via bifunctional mechanism.



Chapter 5

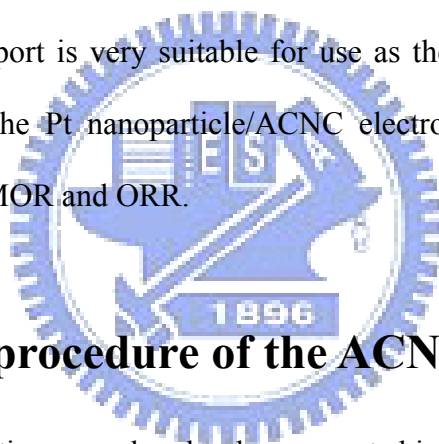
Fabrication and Electrocatalytic Properties of Pt Nanoparticles Electrodeposited on Amorphous Carbon Coated Silicon Nanocones

5.1 Introduction

Since direct methanol fuel cells (DMFCs) can operate at relatively low temperatures, and are lightweight and power efficient, they are very attractive for mobile power source applications, such as automotive systems and portable electronics. Significant progress has been made over the past decade to enhance the electrochemical performance of DMFCs. However, low methanol oxidation reaction (MOR) activity, poor kinetics of the oxygen-reduction reaction (ORR), and high cost of Pt-based electrocatalysts still pose a great challenge for commercialization. Different approaches have attempted to improve electrocatalytic activity to reduce precious Pt catalyst usage and increase electrocatalytic activity for MOR and ORR. To achieve this goal, well dispersed Pt catalyst nanoparticles are usually deposited on the catalyst support with a large surface area. Because carbon materials can usually be prepared to have a large surface area for Pt loading, they have been widely used as the support for the Pt catalyst, such as mesoporous graphite with Pt nanoparticles [96], graphene nanosheets decorated Pt nanoparticles [97], carbon nanocoils with Pt–Ru catalyst alloys [84] and carbon-coated anatase TiO₂ composites [85]. Carbon materials generally have a high content of oxygen surface groups, which act as anchoring centers for the Pt precursor and thus improve wettability of the Pt precursor on the carbon support, resulting in better Pt dispersion [98]. The large support surface and highly dispersed nanosized Pt catalyst create a large effective electrocatalytic surface area and, therefore, greatly enhance ORR and MOR activities. Moreover, π -bonding site on the carbon support improves Pt-C adhesion strength,

alleviating agglomeration and loss of Pt catalyst particles during electrochemical reactions [99-101]. Many studies have shown that carbon support significantly enhances MOR and ORR activities and Pt catalyst stability [102-104].

This study prepares amorphous carbon (α -C) coated nanostructured supports for Pt loading, and studies electrocatalytic performance of the nanostructured electrode in MOR and ORR for DMFC applications. The electrocatalyst support is a highly ordered silicon nanocone (SNC) array coated by an ultrathin α -C surface layer, which provides a large surface area for Pt loading. Nanometer scale Pt catalyst particles were deposited on the nanocones by potentiostatic bipolar pulse electrodeposition. Because the α -C coated Si nanocone (ACNC) array is fabricated directly on a low resistivity Si substrate ($0.002 \Omega\text{-cm}$), acting as the current collector, the ACNC support is very suitable for use as the Pt electrocatalytic electrode for electrical conductivity. The Pt nanoparticle/ACNC electrode exhibits high electrocatalytic activity and stability for MOR and ORR.



5.2 Fabrication procedure of the ACNC array

The SNC array fabrication procedure has been reported in detail previously [87, 105]. Figure 5-1 shows schematically the fabrication procedure. A p-type 4-inch Si wafer of low resistivity ($0.002 \Omega\text{-cm}$) was used as the substrate. A TiN thin film 30 nm thick was first sputter-deposited on the Si surface, followed by thermal evaporation of an aluminum thin film 1 μm thick. The TiN layer was used as the adhesion layer between the Si substrate and the Al thin film, and later used for preparing the nanodot mask for fabricating the SNC array. The as-deposited Al/TiN film stack was then oxidized by electrochemical anodization, performed in a 0.3 M oxalic acid ($\text{H}_2\text{C}_2\text{O}_4$) aqueous solution at 25°C under a constant polarization voltage of 40 V for 20 min. Anodic oxidation of the Al thin film under the anodization conditions produced hexagonally arranged anodic aluminum oxide (AAO) nanopore channels. As the anodization reaction approached the

interface between the Al and TiN thin films, local anodization of the underlying TiN layer occurred, forming the TiO₂ nanodot mask on the TiN layer. The AAO was then removed by the aqueous solution of 6 wt % H₃PO₄ and 1.5 wt % CrO₃ at 70°C for 40 min. Figure 5-2 shows the side-view SEM image of TiO_x nanopillars after the removal of AAO template, had well ordered hexagonal arrangement as shown in the inset of Fig. 5-2. Since TiO_x nanopillars were only formed

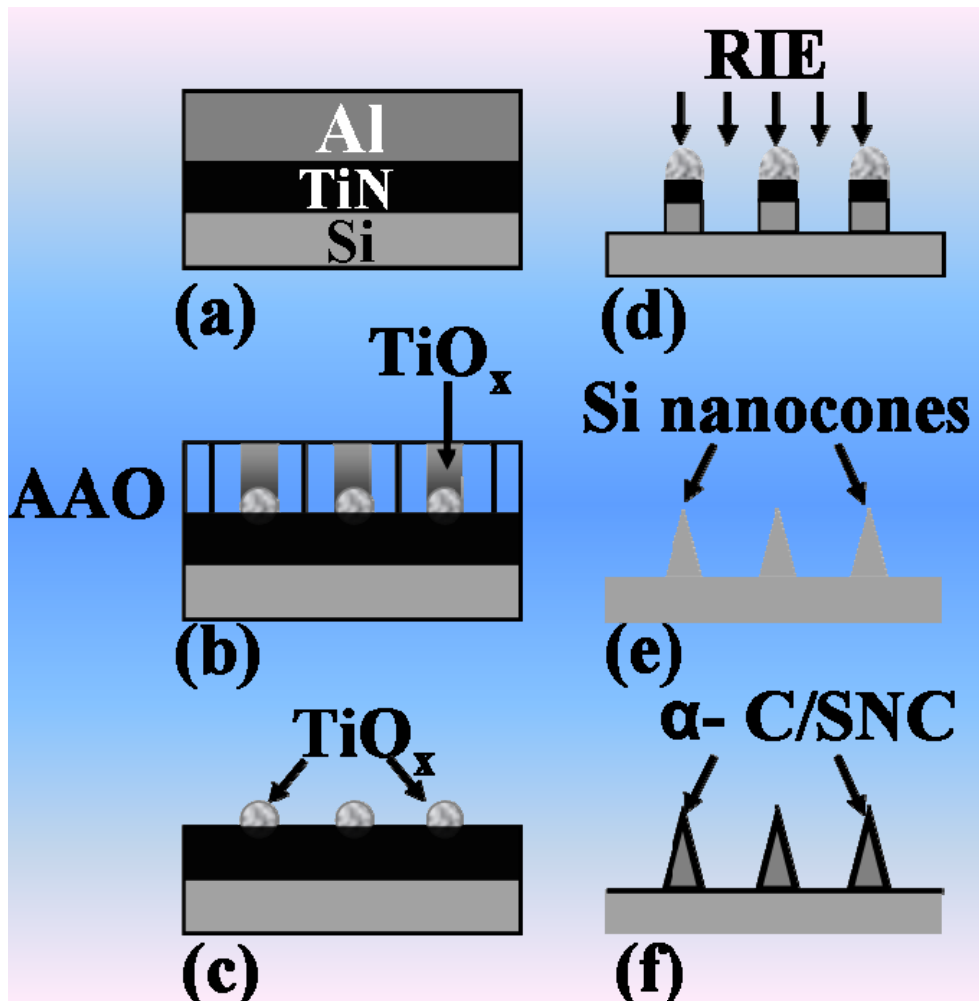


Figure 5-1 shows the fabrication processes of the ordered α -C coated SNC array: (a) deposition of TiN and Al thin films on the Si wafer by sputter deposition and thermal evaporation, respectively, (b) formation of the porous AAO template (c) formation of TiO_x nanodots in the AAO pore channels, (d) removal of AAO by wet etch, (e) RIE of the remaining TiN and silicon substrate, forming Si nanocones, and (f) deposition of the α -C layer on SNCs by MPCVD.

under the AAO pore bottom, it was necessary to remove the remaining TiNs before TiO_x pillars were used as nanomasks to fabricate Si nanocones. In order to etch the TiN layer, a gas mixture of BCl_3 and Cl_2 was used for 40 sec as plasma source in the inductively-coupled-plasma reactive-ion-etch (ICP-RIE) system. The RIE process was performed under the following working conditions: plasma power 400 W, substrate bias power 120 W, working pressure 10 mtorr with a flow rate of 35 sccm for the plasma gas source. Deposition of the $\alpha\text{-C}$ on the SNC array was carried out by microwave plasma chemical vapor deposition (MPCVD) with the following deposition conditions: the $\text{CH}_4\text{:H}_2$ gas flow rate ratio 20:80 sccm, plasma power 300 W, bias power 200 W, working pressure 1 torr, and deposition time 25 min.

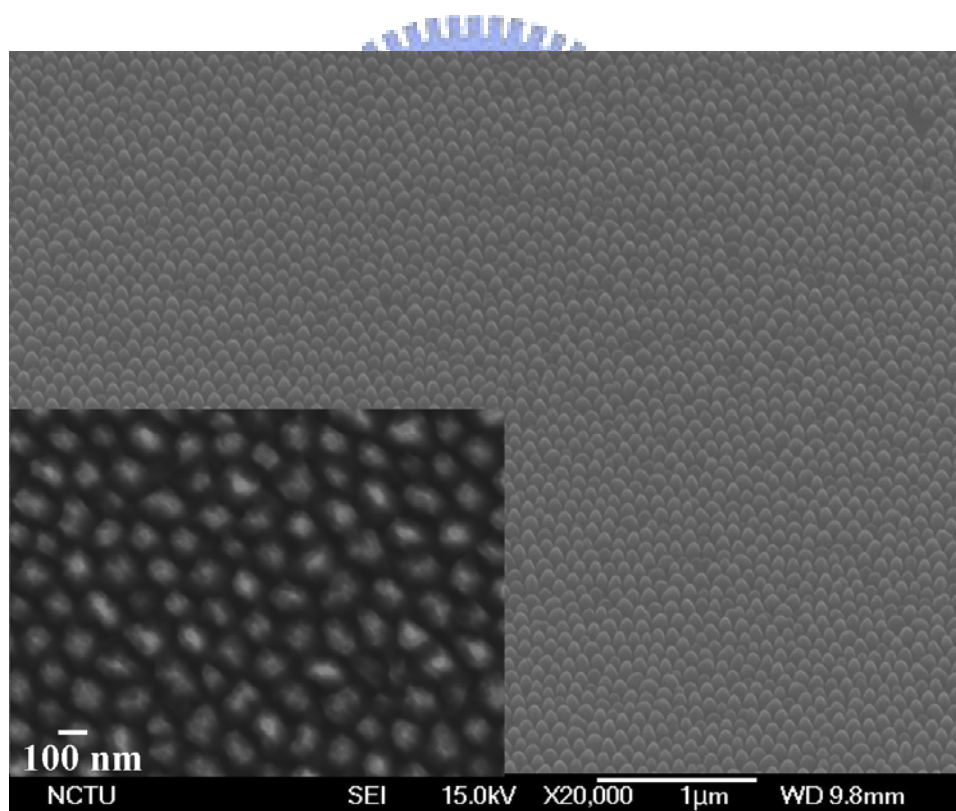


Figure 5-2 shows the side-view SEM image of TiO_x nanopillars after the removal of the AAO layer by wet etch. The inset shows the plane-view SEM image of TiO_x nanopillar arrays.

5.3 Electrodeposition of Pt nanoparticles

The potentiostatic pulse electrodeposition (PPE) has more advantages over the direct potential electrodeposition and the conventional physical vapor deposition. Because of the easy experimental setup, deposition at room temperature in a large surface area, control the distribution of electrodeposits, control of particles size, surface morphology, and time consuming. The desired size of nanoparticles was adjusted by properly tuning the anode and cathode potential parameter. In the PPE, there are four operation parameters influencing the depositing of nanoparticles on the substrate: The high potential (V_H), the lower potential (V_L), the potential on time (T_{on}), and the potential off time (T_{off}). However, in our experiments, Pt nanoparticles were electrodeposited on the ACNC array in the aqueous solution of 1 M K_2PtCl_6 – 0.5 M HCl at room temperature by potentiostatic pulse plating in a three electrode cell system with a saturated calomel reference electrode (SCE). The highly ordered ACNC array was the working electrode and the counter electrode was a thin Pt wire. The particle size and dispersion of Pt nanoparticles was controlled by tuning the pulse height of the applied potential and the pulse duration. The time durations for the high potential pulse (-0.08 mV) and the low potential pulse (+0.01 mV) were 7 and 1 ms, respectively. The particles size control by applying the alternate positive and the negative potential on the working electrode. The Pt nanoparticles uniformly deposited on α -C coated Si nanocones array because of following reasons: The rate of nuclei formation increases during the negative potential pulse because overpotential is lower and this causes that new nuclei are formed and crystallized before the deposited metal ion diffuses to the stable places. During the second positive potential pulse, the overpotential is higher and the growth of existing crystals is superior to the formation of nuclei. The amorphous carbon used to produce the homogeneous deposition of Pt particles. The small curvature on amorphous carbon nanocones is produced the proper electric fields, which help to uniform deposition of nanoparticles.

5.4 Material properties of the Pt-ACNC electrode

The α -C coated SNCs fabricated by the AAO templation method had a highly ordered hexagonal arrangement. Figure 5-3 (A) and (B) show SEM images of the ordered ACNC array before and after the electrodeposition of Pt nanoparticles. The well ordered nanocones were ~ 250 nm in height and had a base diameter of ~ 100 nm. The ACNCs provided a surface area applicable for Pt loading about five times (the ratio of the cone surface area to the cone base area) that of a flat Si substrate. Pt loading on the nanocone electrode by potentiostatic bipolar pulse electrodeposition is an effective approach to deposit crystalline nanoparticles of well-controlled quality on the cathode. The highly ordered ACNC arrangement allowed a relatively uniform potential distribution over the nanocone array in the electrolyte, crucial for electrodeposition of well dispersed Pt nanoparticles on the ACNC cathode. Because the Pt nanoparticles on the ACNC support were very small and without obvious agglomeration, the SEM image of Fig. 5-3 (B) hardly observed the Pt nanoparticles. Figure 5-4 (A) shows the bright-field TEM image of the ACNC with the electrodeposited Pt catalyst. The figure clearly shows that Pt nanoparticles were well dispersed on the nanocones. According to the high-resolution TEM image (Fig. 5-4 (B)), most of the deposited Pt nanoparticles had a size smaller than 5 nm. Figure 5-4 (C) shows the selected area electron diffraction (SAD) pattern. The distinct diffraction spots in the SAD image were due to the crystalline Si nanocone substrate. Two diffraction rings of discernible intensity were indexed as the (111) and (200) lattice planes of the Pt face center cubic (FCC) structure. The diffraction rings corresponding to the (220) and (311) lattice planes could also be perceived but with a very weak intensity. The TEM analysis indicated that crystalline Pt nanoparticles were uniformly electrodeposited on the ACNCs.

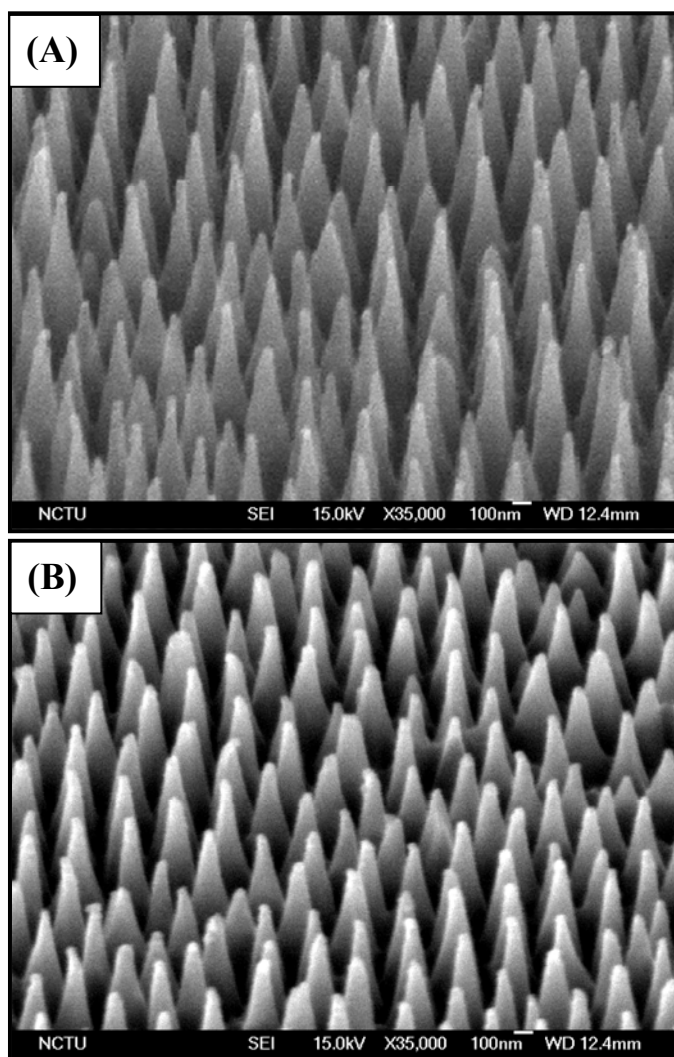


Figure 5-3 shows the side-view SEM images of the α -C coated SNC array (A) before and (B) after the electrodeposition of Pt nanoparticles.

Figure 5-5 (A) shows the XPS spectrum of the Pt loaded ACNC array. In addition to XPS signals due to Pt nanoparticles and the α -C overlayer, the XPS analysis also detected O(1s), Si(2p) and Si(2s) photoelectrons. The relatively strong O(1s) XPS signal suggested oxygen surface groups on the α -C layer. Curve fitting for the broad and asymmetric C(1s) XPS signal was performed, assuming a Gaussian-Lorentzian curve with a half-width-at-full-maximum of 1.9 eV for all the synthesized peaks. The curve fitting result (Fig. 5-5 (B)) revealed four chemical states with binding energies higher than that typically assigned to the C-C bonding

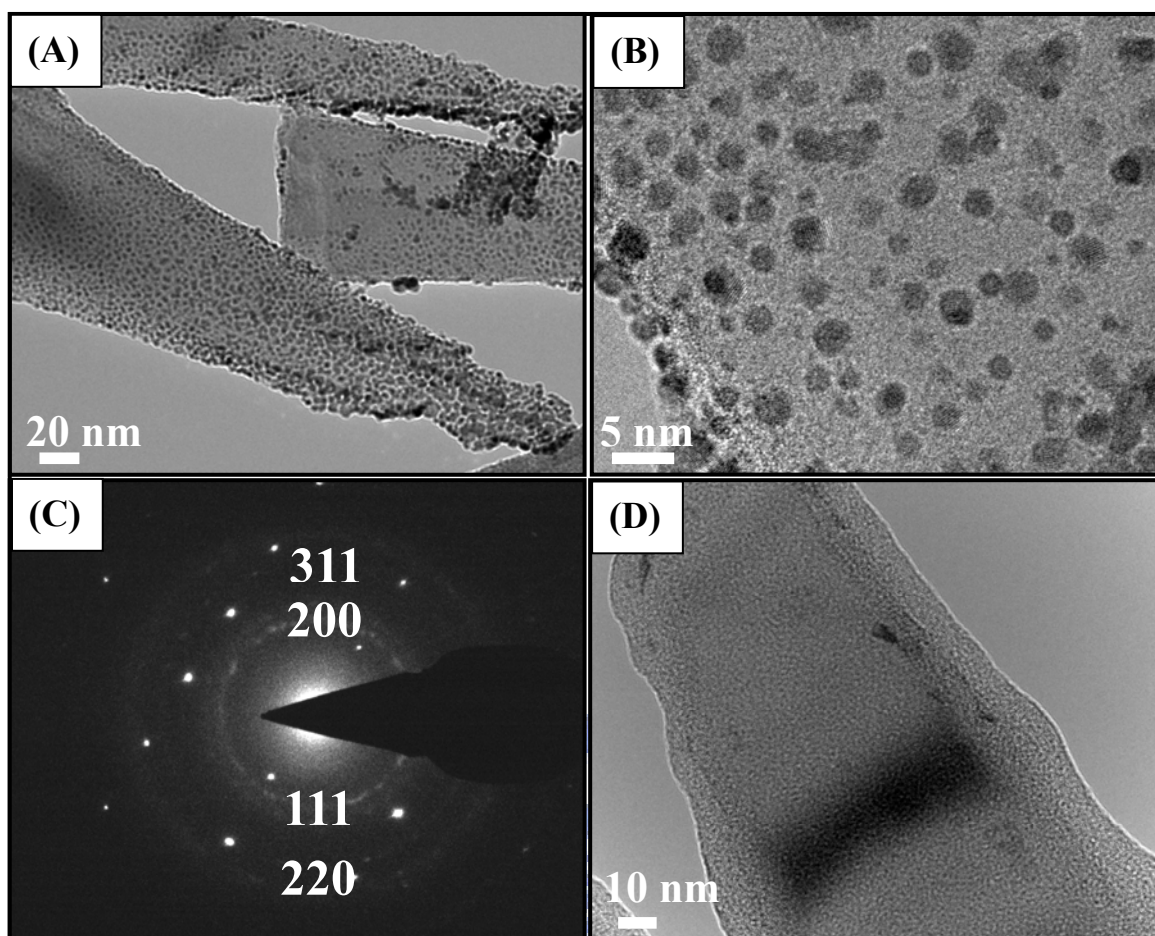


Figure 5-4 shows TEM images (A) Bright-field TEM image of the α -C coated SNC with electrodeposited Pt nanoparticles, (B) high resolution TEM image of the α -C coated SNC with Pt nanoparticles; (C) the SAD pattern, and (D) bright-field image of the α -C coated SNC without the Pt nanoparticle.

and/or graphitic structure (~ 284.6 eV) [106]. The curve-fitted peaks at 285.6, 286.8, 287.6 and 289.4 eV can be ascribed to C-O-C, C-OH, C=O and -COOH (RCOO-) functional groups, respectively [107, 108]. The Pt(4f) XPS spectrum shown in Fig. 5-5 (C) exhibited a broad doublet peak with the Pt(4f_{7/2}) peak maximum at 70.5 eV, which negatively shifted from that for bulk Pt by ~ 0.8 eV. As discussed later, we ascribe the negative binding energy shift of the Pt(4f) doublet peak to a combination effect of the Pt particle size and charge transfer between Pt nanoparticles and the ACNC support. Detection of the Si(2s) and Si(2p) XPS signals due to the Si nanocone

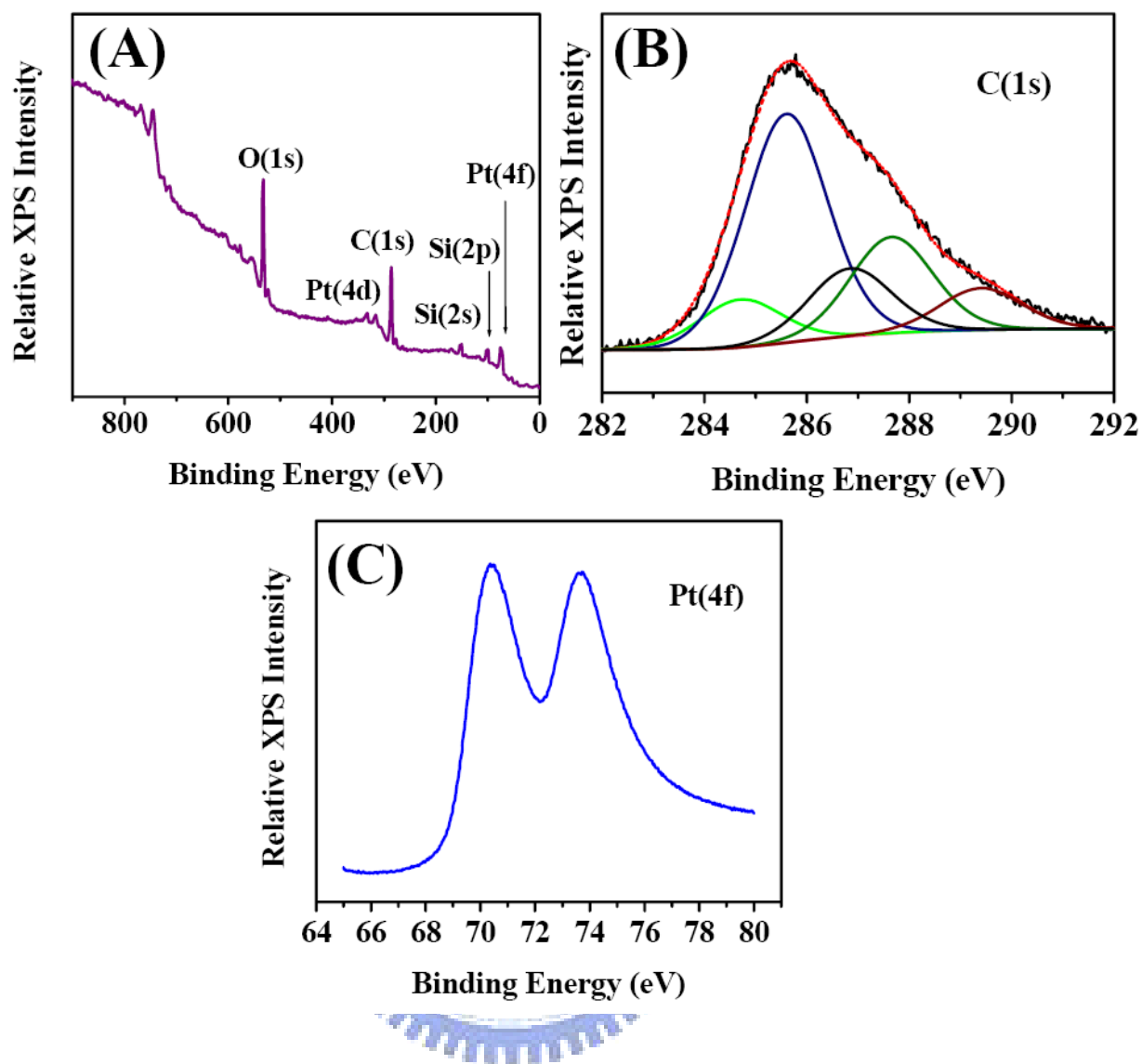


Figure 5-5 shows the wide scan XPS of the Pt nanoparticles deposited on the ACNC array, (B) the C(1s) XPS spectrum with curve fitted peaks, and (C) the Pt(4f) XPS spectrum.

substrate indicated that the thickness of the α -C layer was smaller than the probe depth of the Si(2s) and Si(2p) photoelectrons excited by the Mg $K\alpha$ source, which was roughly less than 10 nm. The TEM analysis did show an α -C layer ~5-10 nm thick deposited on the SNC (Fig. 5-4 (D)). Although thin, the α -C layer could greatly affect Pt electrodeposition and electrocatalytic characteristics of the Pt nanoparticles.

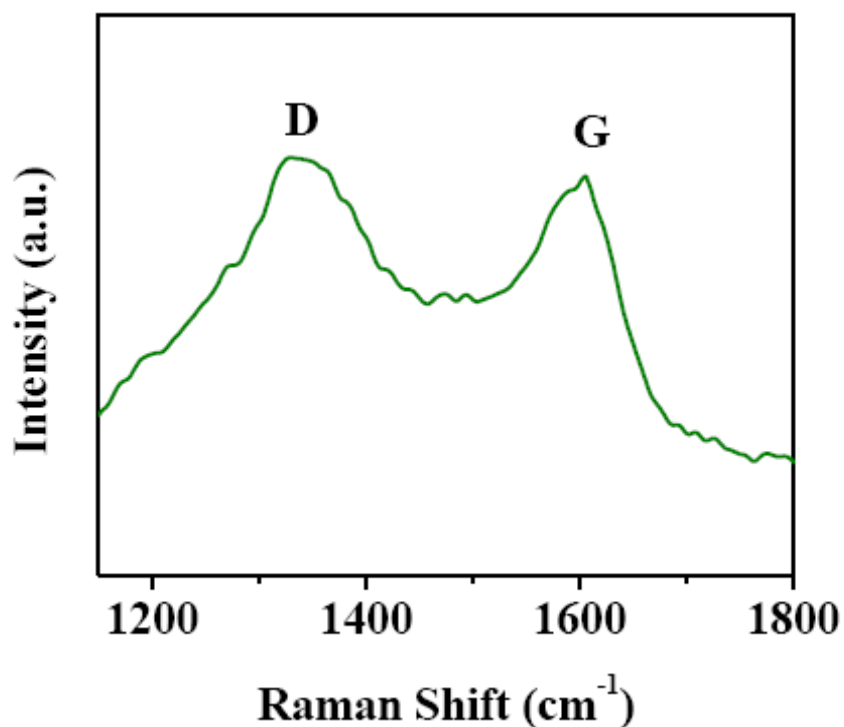


Figure 5-6 shows the Raman spectrum of the α -C coated SNCs without Pt nanoparticles.

Figure 5-6 shows the Raman spectrum in the range of 1150–1800 cm^{-1} of the ACNC array without the Pt catalyst. The two characteristic Raman peaks for disordered graphitic carbon materials in this range, the G and D peaks, were situated at ~ 1605 and ~ 1336 cm^{-1} , respectively. Peak features of both the Raman modes, such as peak position and intensity, greatly depend on the sp^2 bonding structure of CVD deposited carbon materials. The G peak is due to sp^2 bond stretching and the D peak is considered to be a ring breathing mode in a disordered graphitic structure [109]. The G peak is particularly useful to reveal nanocrystallinity of the graphitic structure [110]. When the size of the nanocrystalline graphite cluster is smaller than 2 nm, the G peak shifts to a position higher than 1600 cm^{-1} [109]. The peak position of the G mode at ~ 1605 cm^{-1} and the relative large D peak signal implied that a significant amount of nanosized graphitic structures were likely present in the α -C layer. Because of the disordered nanosized graphitic carbon structure, oxygen containing species,

such as those revealed by the XPS analysis, effectively adsorbed on defect sites of nanocrystalline graphite clusters in the α -C layer. The oxygen containing adspecies acted as anchoring centers on the nanocone surface for the Pt precursor during Pt electrodeposition, thereby resulting in a better Pt dispersion [98]. As discussed latter, π -bondings on nanosized graphitic clusters of the α -C layer improved adhesion between Pt nanoparticles and the ACNC support, greatly alleviating agglomeration and loss of Pt nanoparticles during electrocatalytic reactions [99-101].

5.5 Electrocatalytic activity

The electrochemical surface area (ESA) of the Pt film/Si and the Pt/ACNC electrodes was evaluated by the cyclic voltammetry (CV), which was performed in argon saturated 1M H_2SO_4 aqueous solution using a Pt wire as the counter electrode and a saturated calomel electrode (SCE) as reference electrode.

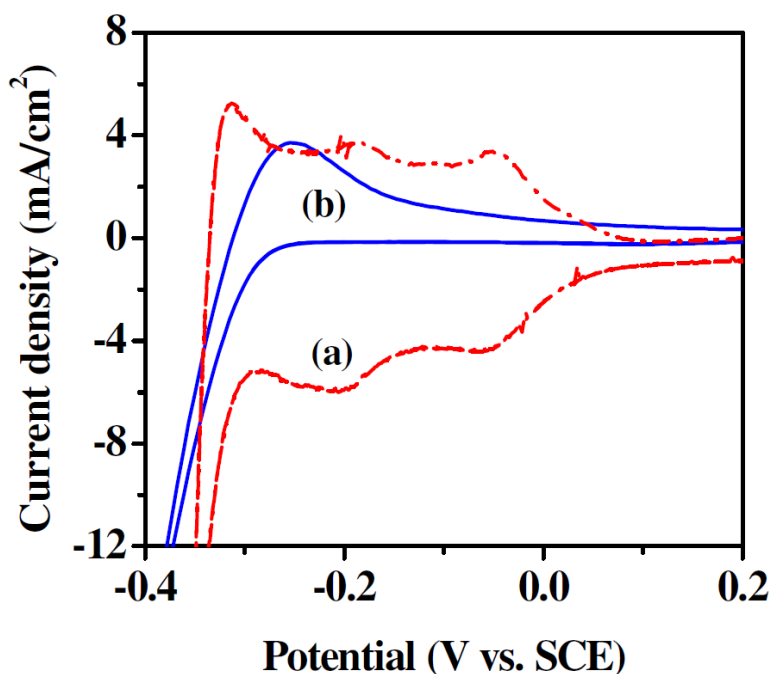


Figure 5-7 shows the room temperature cyclic voltammograms of (a) Pt/ACNC and (b) Pt film/Si electrodes measured at 25 mV s^{-1} in 1 M H_2SO_4 .

Typical CV curves of the both electrodes are shown in Fig. 5-7. The ESA values obtained from hydrogen adsorption/desorption peaks are 412 and 39 $\text{m}^2 \text{g}^{-1}$ for Pt/ACNC and Pt film/Si, respectively. The ESA for the Pt/ACNC higher than that of Pt film/Si, most likely due to the smaller size and much better dispersion of the Pt nanoparticles on ACNC arrays.

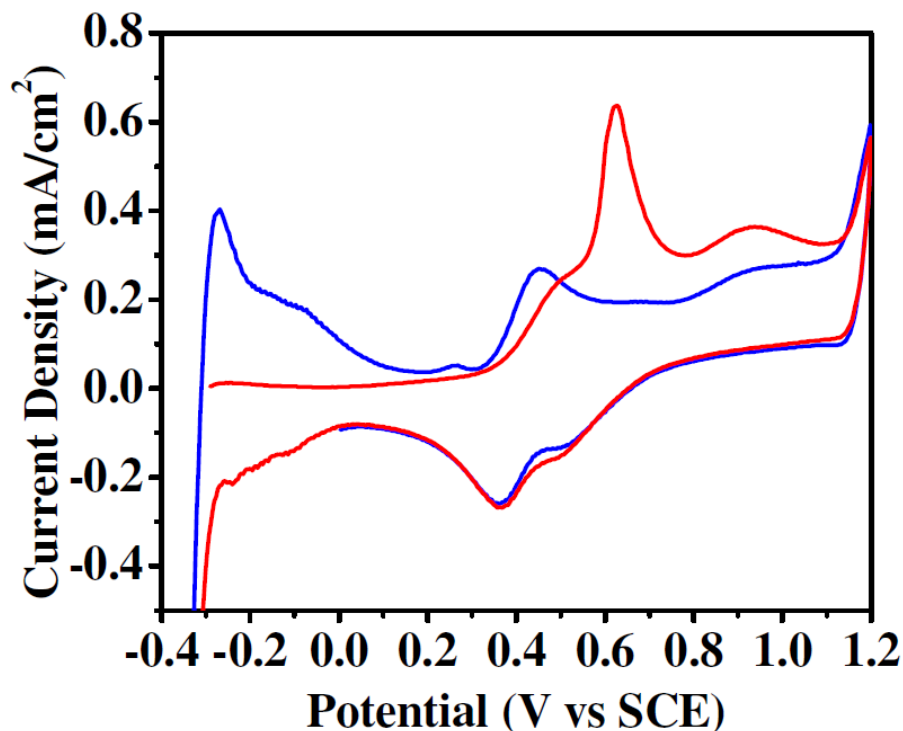


Figure 5-8 shows the CO stripping cyclic voltammograms of the Pt/ACNCs electrode in a CO saturated 1 M H_2SO_4 solution. The scan rate was 25 mV s^{-1} .

The electroactive surface areas (ESAs) of the Pt /ACNC were further reinvestigated by CO-stripping CV, performed in a CO saturated 1 M H_2SO_4 aqueous solution using a Pt wire as the counter electrode and SCE as the reference electrode. For comparison, the ESA of a Pt film/Si electrode, prepared by electrodepositing a continuous Pt film on the flat Si substrate, was also measured. Figure 5-8 shows a representative CO-stripping cyclic voltammogram for the Pt-ACNC electrode. A very high ESA of $327 \text{ m}^2/\text{g}$ was calculated for the Pt/ACNC electrode by integrating the electro-oxidation peak of adsorbed CO molecules, assuming an

electro-oxidation charge of $420 \mu\text{C}\cdot\text{cm}^{-2}$ for a monolayer of CO adspecies on a smooth Pt surface [90]. The ESA of the Pt/ACNC electrode was about eight times higher than that of the Pt film/Si electrode and much higher than that of many previously reported electrodes of carbon materials [85, 111, 112]. The high ESA ascribes to the large surface area of the nanocone array and the highly dispersed Pt nanoparticles. The discrepancy between surface area by hydrogen adsorption/desorption and from CO-stripping might be due to experimental error.

Efficient removal of the CO adspecies from the Pt catalyst surface is crucial for minimizing the poisoning effect in DMFCs. The CO stripping voltammograms of Fig. 5-8 also provide information about electro-oxidation of CO adspecies on the electrocatalyst. The onset potential of CO electrooxidation on the Pt/ACNC and the Pt film /Si electrodes was about ~ 0.36 and ~ 0.51 V, respectively. Improved electro-oxidation activity of CO adspecies on the Pt/ACNC electrode may be ascribed to the bi-functional mechanism, which describes that effective electrooxidation of CO adspecies can be achieved by reaction with neighboring oxygen containing functional groups. The XPS analysis discussed above showed plenty of oxygen containing adspecies on the α -C layer. The nanometer size of Pt catalyst particles made it easier for surrounding oxygen-containing groups on the ACNC support to access and interact with CO adspecies on the Pt nanoparticles, and allowed fast migration of adspecies over the particle surface. Therefore electro-oxidation of CO adspecies, in particular-C-OH adspecies, could readily proceed via the Langmuir-Hinshelwood mechanism. The lower onset potential of CO electro-oxidation and the higher ESA clearly demonstrate that the Pt/ACNC electrode effectively improves electro-activity of the Pt catalyst toward MOR.

MOR activity of these two electrodes in the 1 M CH_3OH + 1 M H_2SO_4 aqueous solution at room temperature was studied by CV. Figure 5-9 (A) shows the current density and mass activity of the Pt film/Si, and Pt/ACNC electrode. As Fig. 5-9 (A) shows, the Pt/ACNC had a higher mass activity and current density than the Pt film /Si electrode. The current ensity and

mass activity of the Pt/ACNC electrode were ~ 4 and ~ 10 times that of the Pt film/Si electrode, respectively. Even compared with many reported electrodes composed of carbon materials, such as carbon-coated anatase TiO₂ composites [85] and nanoporous materials synthesized by electrochemical lithiation [48],

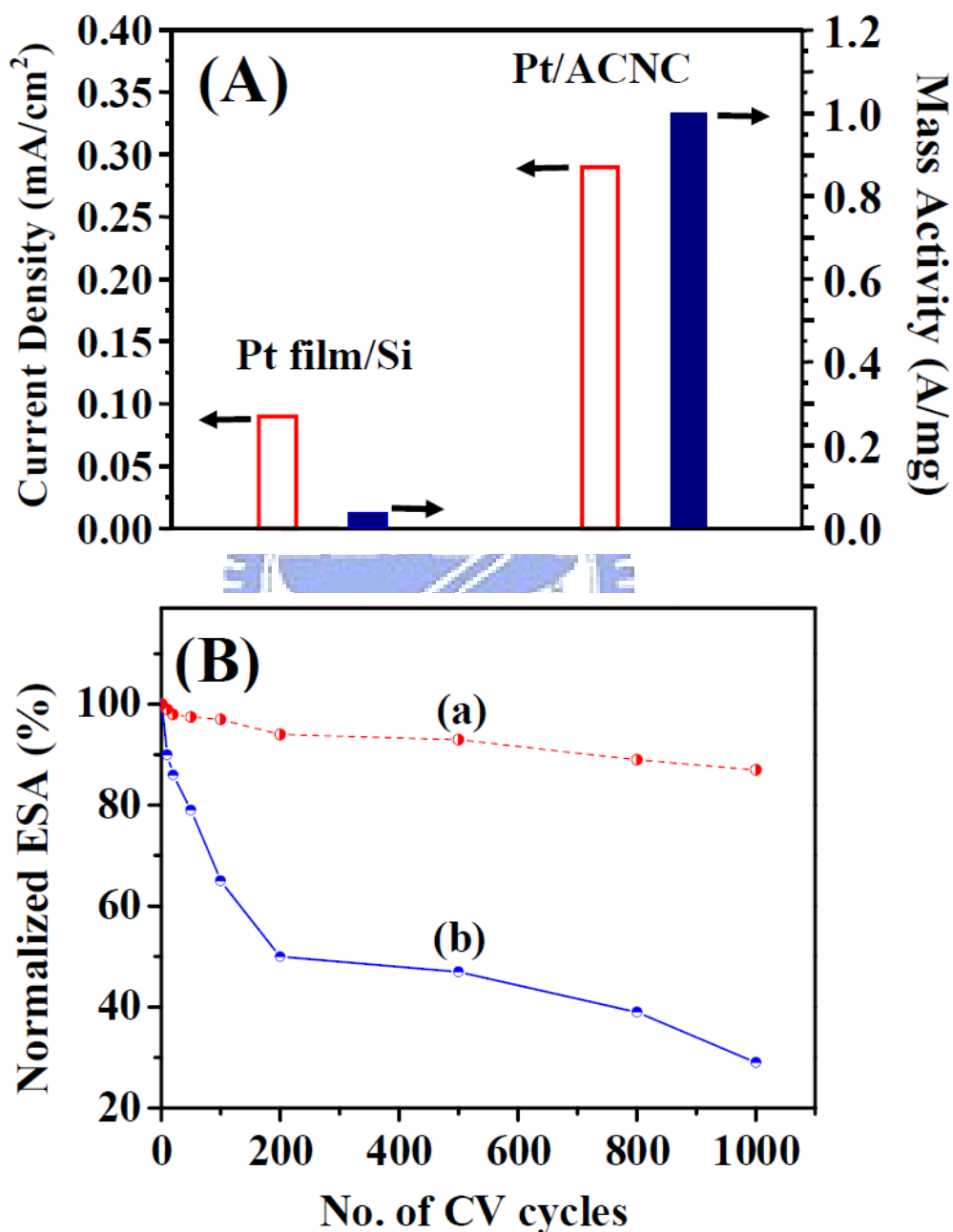


Figure 5-9 (A) Current density and mass activity of the Pt/ACNC electrode (solid rectangle) and the Pt film/Si electrode (open rectangle). (B) Loss of the Pt electrochemical surface area of (a) the Pt/ACNC electrode and (b) the Pt film/Si electrode as a function of the number of CV cycles in argon saturated 1 M H₂SO₄ aqueous solution at room temperature (scan rate: 25 mV s⁻¹).

the Pt/ACNC electrode also exhibited better MOR performance in terms of catalyst mass activity and current density. The excellent MOR activity of the Pt/ACNC electrode can ascribe to the large electrode surface area and the nanometer size of Pt nanoparticles. The geometric shape of ACNC support provided a surface area for Pt loading five times larger than that for the flat Si surface. The highly dispersed Pt nanoparticles also further increased the active surface area on the Pt/ACNC electrode, thus increasing mass activity. Furthermore, the nanometer-sized Pt catalyst particles enhanced electro-oxidation of CO adspecies via the bifunctional mechanism as discussed above, creating more active sites for MOR and thus improving MOR efficiency.

Electrocatalytic stability of the Pt film/Si and the Pt/ACNC electrodes for MOR was evaluated by CV within the potential range -0.4 – 1.2 V (vs. SCE) at a scan rate of 25 mVs^{-1} in an argon saturated $1 \text{ M H}_2\text{SO}_4$ aqueous solution for more than 1000 cycles. Figure 5-9(B) shows the ESA loss as a function of the number of CV cycles for the two electrodes. The Pt/ACNC electrode showed a much more moderate reduction in the ESA during the repeating CV scans. The ESA of the Pt/ACNC electrode decreased by $\sim 12\%$ after 1000 CV cycles in the acid solution, while the Pt films/Si electrode showed a decrease of more than 50%. Loss of the ESA of the Pt catalyst might result from two pathways, Pt particles detachment from the support and Pt catalyst dissolution during electrochemical measurements. We did not observe a noticeable decrease in Pt nanoparticle density after electrocatalytic stability measurement according to TEM analysis (not shown), indicating that Pt nanoparticle detachment from the ACNC support did not take place or was insignificant. Thus, the gradual decrease in the ESA of the Pt/ACNC during the stability test was likely due to Pt nanoparticle dissolution into the electrolyte solution at the high potential range during the CV sweep, which had a maximum of 1.2 V vs. SCE [113, 114]. The much smaller ESA loss for the Pt/ACNC electrode implied that Pt nanoparticles were relatively stable in the acidic electrolyte during the voltage scan. The nanocrystalline graphitic structure in the α -C layer as revealed by Raman scattering

spectroscopy might play a crucial role in making the Pt /ACNC electrode much more stable toward MOR than the Pt film/Si electrode. In the broad Pt(4f) doublet XPS spectrum shown in Fig. 5-5(C), the Pt(4f_{7/2}) peak reached a maximum at 70.5 eV, which was ~0.8 eV smaller than that of bulk Pt. A red shift of 0.5 eV for the Pt(4f) doublet peaks have been reported for nanometer-sized Pt colloids supported on highly oriented pyrolytic graphite [115]. The negative shift of the Pt(4f) doublet peak for Pt nanoparticles is generally ascribed to the reduced coordinated number of surface atoms in a nanometer sized cluster [116, 117]. Charge transfer between Pt nanoparticles and the support can also positively or negatively shift the Pt(4f) binding energies, depending on the chemical property of the support [118]. The large red shift observed in the study might be a combination effect of the particle size effect and the π -electron donation from the support to Pt nanoparticles. It has been widely reported that increasing the graphitization degree of carbon supports strengthens the metal-support interaction and enhances resistance to support oxidation and catalyst agglomeration [99-101, 119]. Charge transfer between π -sites of the α -C layer and Pt nanoparticles significantly alters the electronic structure of nanosized Pt catalyst particles, thereby enhancing electrochemical stability of the Pt catalyst and thus mitigating Pt dissolution due to electrooxidation. In addition to chemically stabilizing Pt nanoparticles, the charge transfer interaction also enhances the adhesion of electrodeposited Pt nanoparticles to the ACNC support, thus preventing Pt nanoparticles from separating from the ACNC electrode.

The slow ORR rate on the cathode is always a concern for DMFC applicability. We have also studied electrocatalytic activity of the Pt/ACNC electrode toward ORR by the CV measurement. Figure 5-10(A) shows typical ORR polarization curves of the Pt film/Si and the Pt/ACNC electrode, obtained in an O₂ saturated 1 M H₂SO₄ aqueous solution at room temperature. The ORR half-wave potentials for the Pt film/Si and Pt/ACNC electrodes were ~0.52 and ~0.60 V, respectively. The peak ORR current densities of the Pt film/Si and Pt/ACNC electrodes were -1.2 and -7.4 mA cm⁻², respectively. The current density of the

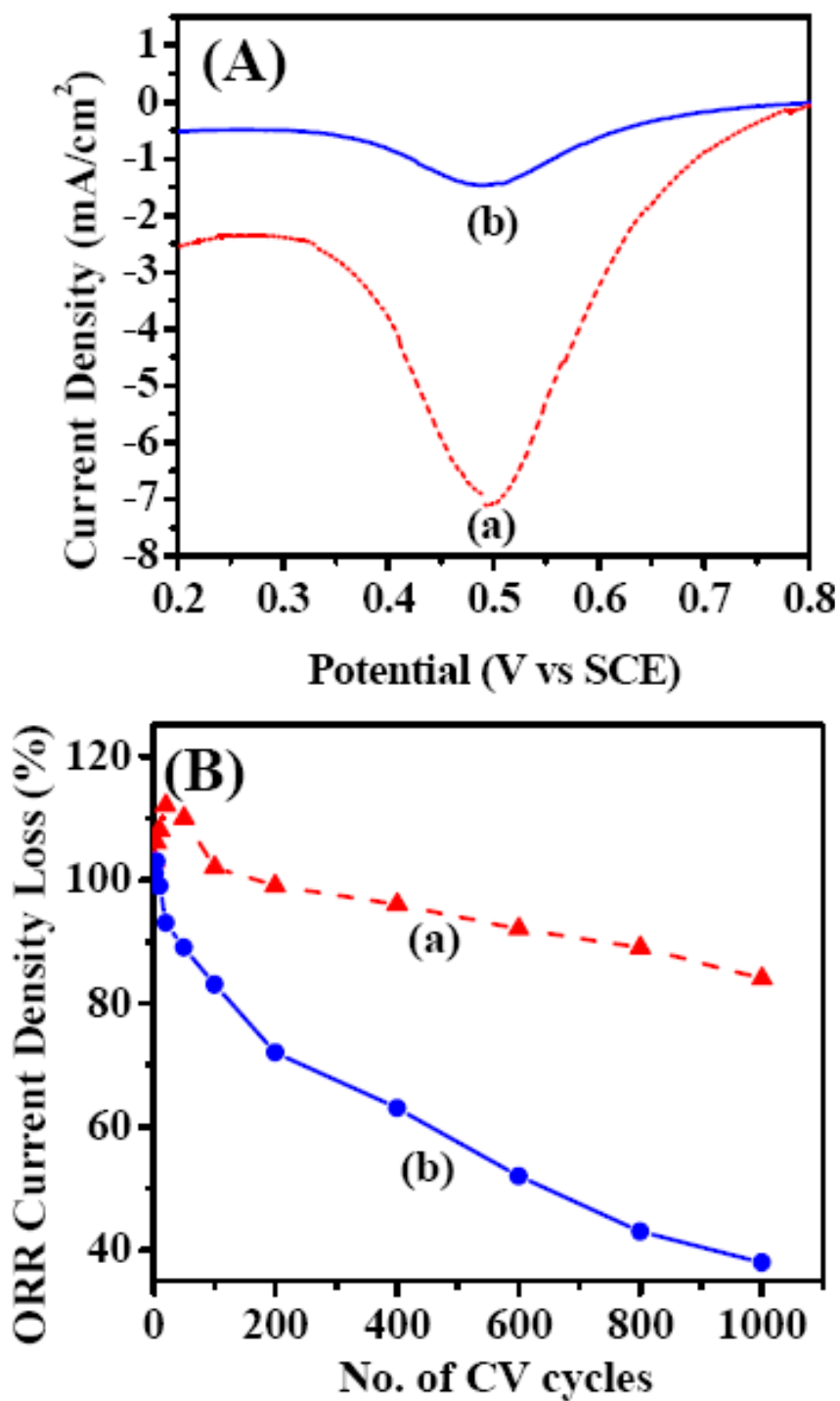


Figure 5-10 (A) Cyclic voltammograms of ORR in O₂ saturated 1 M H₂SO₄ aqueous solution at 25°C for (a) the Pt/ACNC electrode and (b) the Pt film/Si electrode; and (B) ORR current density loss as a function of the number of CV cycles in oxygen saturated 1 M H₂SO₄ at room temperature for (a) the Pt/ACNC electrode and (b) the Pt film/Si electrode (scan rate: 25 mV s⁻¹).

Pt/ACNC electrode was six times higher than that of the Pt film/Si electrode, indicating that the Pt/ACNC electrode significantly enhanced the ORR rate. Compared with many previous reported electrodes, such as Pt catalysts with gold clusters [120], Pt₃Ni(111) catalysts [121], supportless Pt and Pt-Pd nanotubes [122] and dealloyed Pt-Cu-Co nanoparticles [123], the Pt/ACNC electrode showed a higher peak current density as well. The great improvements on ORR electroactivity of the Pt catalyst on the ACNC support can be attributed to similar factors enhancing MOR electroactivity. The well dispersed Pt nanoparticles on the ACNC support provided a large ESA leading to a faster reaction rate of ORR. The size of Pt nanoparticles affects the potential distribution within the double layer around the catalyst and also enhances the mass transport of electroactive species on the Pt catalyst [124].

The Pt/ACNC electrode also demonstrated excellent electrocatalytic stability for ORR. The electrocatalytic stability test was performed in an O₂ saturated 1 M H₂SO₄ aqueous solution at 25°C. The CV measurement of more than 1000 cycles was conducted in the potential range between 0.2-0.8 V vs. SCE at a scan rate of 25 mV s⁻¹. Figure 5-10 (B) shows the ORR current density loss for the Pt film/Si and the Pt/ACNC electrodes as a function of the number of CV cycles. The decrease in ORR activity of the Pt/ACNC and the Pt film/Si electrodes after 1000 cycles was about 17% and >60%, respectively. The better ORR activity stability of the Pt/ACNC electrode may also be due to the unique chemical properties of the ACNC support, composed of nanocrystalline graphitic structures and full of oxygen containing adspecies.

5.6 Summary

This study has shown the excellent electrochemical performance of Pt nanoparticles pulse-electrodeposited on the highly ordered ACNC array, fabricated by the AAO templation. Because Pt nanoparticles were well dispersed on the ACNC support with a large surface area,

the Pt/ACNC electrode had a large ESA. The Pt-ACNC electrode exhibited high electrocatalytic activity and stability toward both ORR and MOR. According to Raman scattering and XPS analyses, the ACNC array was composed of nanocrystalline graphitic structures, and full of oxygen containing adspecies. The uniform dispersion of Pt nanoparticles on the α -C layer and the high resistance of the Pt/ACNC electrode against CO poisoning resulted from the presence of oxygen-containing adspecies. The nanocrystalline graphitic structure in the α -C layer was able to electronically stabilize the Pt nanoparticles via charge transfer, thereby enhancing electroactivity stability of the Pt/ACNC electrode.



Chapter 6

Novel New Approach to the Synthesis of Nanoporous Graphitic Carbon as a Unique Electrocatalyst Support for Methanol Oxidation

6.1 Introduction

Recently, the synthesis of nanostructure carbon materials has great potential for applications in electronic, [125, 126] catalytic, [127, 128] hydrogen-storage, [129, 130] electrochemical double-layer capacitors, [131] and lithium ion batteries, [132]. In an effort to improve catalyst activity and stability, Pt-Ru based catalysts, which are the most practical catalysts for fuel cell applications, have been synthesized for the purpose of reducing catalyst particle size (nanolevel) and increasing the surface area of the catalyst deposited on support. The one best way to accomplish this is to create 3D nanoporous graphitic carbon (g-C) structure. Several methods have been reported for the synthesis of carbon nanostructure with high surface area by using templates, stabilizers, or surfactants [96, 133, 134]. Therefore, preparation of ordered porous carbon with graphitic pore walls is of importance. To prepare ordered graphitic porous carbons, some unconventional carbon precursors such as mesophase pitch [131], acenaphthene [134], polyvinyl chloride [135], naphthalene, anthracene, pyrene [136], and polypyrrole [137] have been employed to infiltrate the pores of porous templates. However, infiltration and polymerization using these liquid carbon precursors are either difficult or time consuming because repeated infiltration and polymerization are required in order to obtain an ordered carbon replica. On the other hand, polymerization and pyrolysis of the carbon precursors during high-temperature carbonization often lead to the emission of a large amount of small molecules such as H₂O, which can deteriorate the pore structure of the templates [138], thus the structural ordering of the resultant carbon [139, 140]. However, the

synthesis of graphitic carbon with high surface area has been a great challenge and method for economically large scale production is still the vital task.

Herein, we describe new, simple and efficient method for the synthesis of a 3D nanoporous g-C structure by adamantane flame, which was utilized as a support for Pt and Pt₅₀-Ru₅₀ alloy catalysts at low temperature. Moreover, the electrochemical performance of the Pt₅₀-Ru₅₀/3D nanoporous g-C shows the potential application in liquid feed fuel cells.

6.2 Synthesis of 3D nanoporous g-C, Pt/3D nanoporous g-C and Pt₅₀-Ru₅₀/3D nanoporous g-C

The synthesis process of the 3D nanoporous g-C structure is illustrated in Fig. 6-1. The synthesis of 3D nanoporous g-C on the Si surface consists of three consecutive steps. First, the flat Si substrate was washed by acetone and deionized water (>18 MΩ), then it was treated with a 10 wt% HF at room temperature for 5 min to remove the thin native oxide layer and dry blown with nitrogen. Then, the polished side of Si substrate was immediately placed in front of adamantane (C₁₀H₁₆) flame for 7 min to deposit of thick layer of 3D nanoporous g-C. Further, for the better adhesion between Si and 3D nanoporous g-C, the sample was heated at 300°C for one hour. A precursor solution containing 10 ml acetone and H₂PtCl₆ was prepared. And then, the solution was poured drop by drop onto 3D nanoporous g-C at 100°C for 2 min for the deposition of Pt. To deposit Pt₅₀-Ru₅₀ alloy catalyst on the 3D nanoporous g-C, 10 ml acetone, H₂PtCl₆ and RuCl₃ solution was used, following the similar procedure as of Pt. The Pt/3D nanoporous g-C, and Pt₅₀-Ru₅₀/3D nanoporous g-C electrodes was rinsed thoroughly with deionized water to remove residual chlorine ions after Pt and Pt₅₀-Ru₅₀ deposition, and allowed to dry before using for electrochemical measurements.

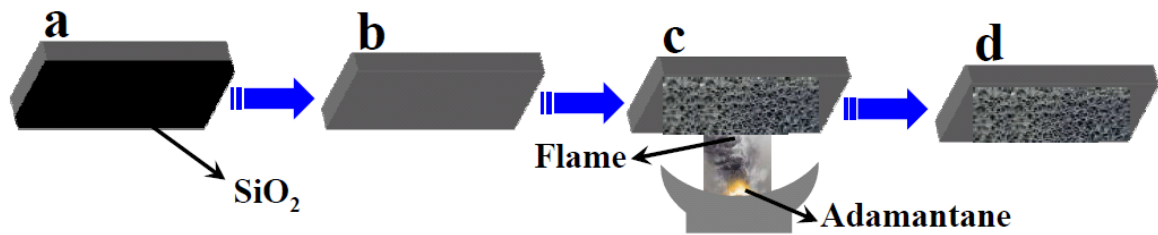


Figure 6-1 shows the synthesis scheme of 3D nanoporous g-C: (a) the Si wafer was cut into $2 \times 2 \text{ cm}^2$ dimension (b) SiO_2 layer was removed by treating with 10 % HF for 5 min and dried by N_2 gas (c) the cleaned sample was immediately placed in front of flame adamantane for 7 minute, and (d) finally, sample was heated at 300°C for one hour to obtain a good depositing of 3D nanoporous g-C over the silicon substrate.

6.3 Physico-chemical characterization

Scanning electron microscopy (SEM) was used to characterize the surface morphology of the synthesized 3D nanoporous g-C. Figure 6-2 shows a typical SEM image of 3D nanoporous g-C where the Pt and Ru content is zero. As is evident from the image, the Si substrate is well covered by 3D nanoporous carbon with pore sizes of 100–900 nm.

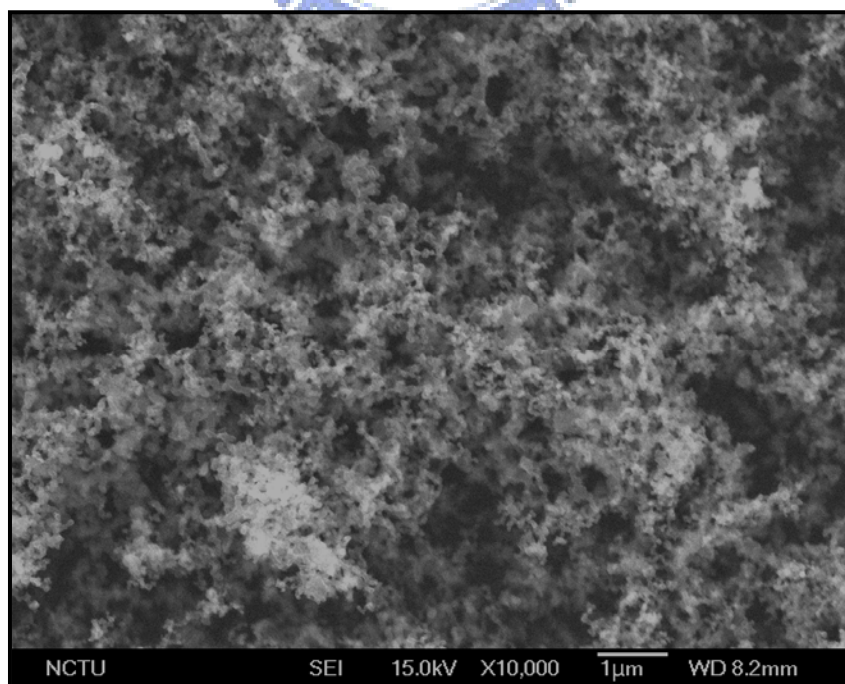


Figure 6-2 shows the SEM image of the resulting 3D nanoporous g-C.

The graphitization of the synthesized 3D nanoporous carbon was characterized by Raman spectroscopy. The Raman spectra of the 3D nanoporous carbon in the frequency range between 1200 and 1800 cm^{-1} are shown in Fig. 6-3. The two main peaks at 1594 and 1359 cm^{-1} illustrated in the spectra corresponds to G and D bands, respectively. The G band represents the E_{2g} vibration of g-C with a sp^2 electronic configuration and D band represents the A_{1g} mode of diamond-like carbon with a sp^3 electronic configuration. To determine the degree of graphitization, we estimated the intensities of D and G peaks from their peak heights and hence their ratio (I_D/I_G). As shown in Fig. 6-3, the I_D/I_G ratio less than 1, indicate the better graphitization of 3D nanoporous carbon [141]. Raman spectra suggest formation of g-C in 3D nanoporous carbon structure.

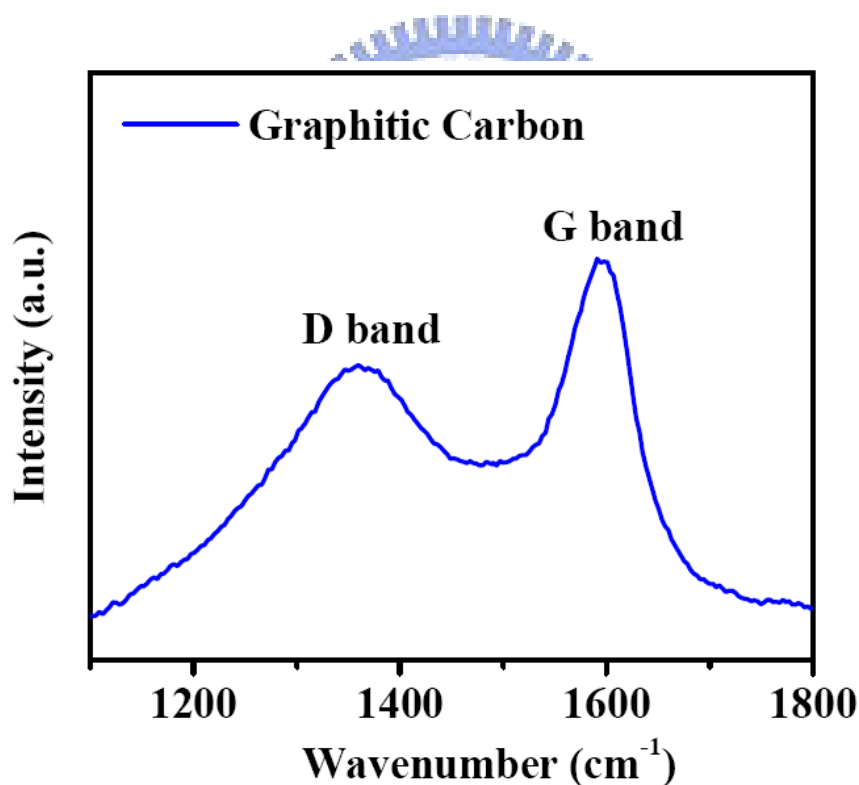


Figure 6-3 Raman spectrum of 3D nanoporous g-C deposited on Si substrate.

SEM was further used to characterize the surface morphologies of the synthesized Pt/3D nanoporous g-C, and Pt₅₀-Ru₅₀/3D nanoporous g-C. Fig. 6-4 (A) shows a typical SEM image

of Pt/nanoporous g-C where 3D nanoporous g-C surface is deposited by nanoparticles Pt. The pore size distribution of the synthesized 3D nanoporous g-C is 100-800 nm.

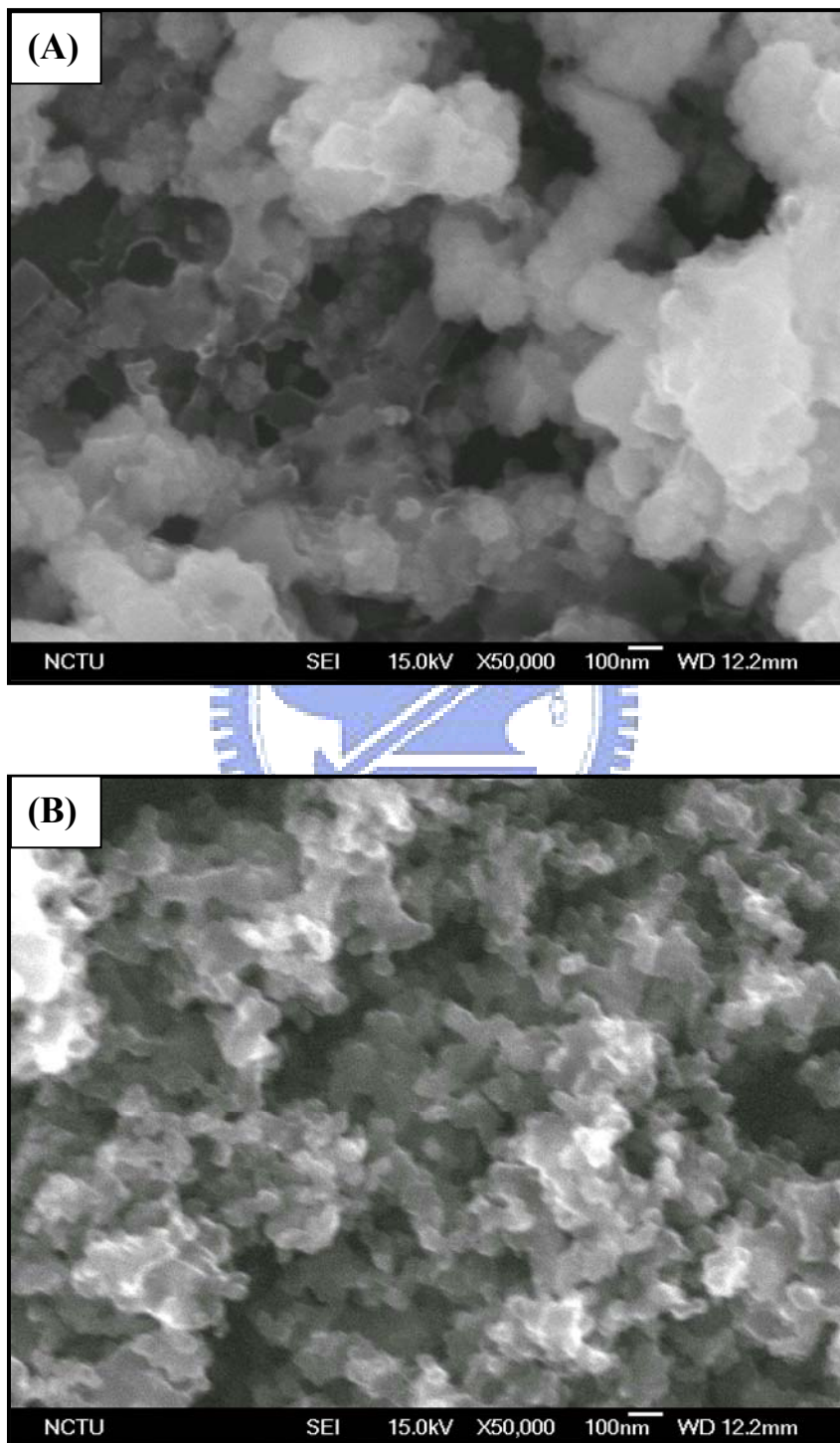


Figure 6-4 shows the plane-view SEM images (A) Pt/3D nanoporous g-C, and (B) typical Pt₅₀-Ru₅₀/3D nanoporous g-C.

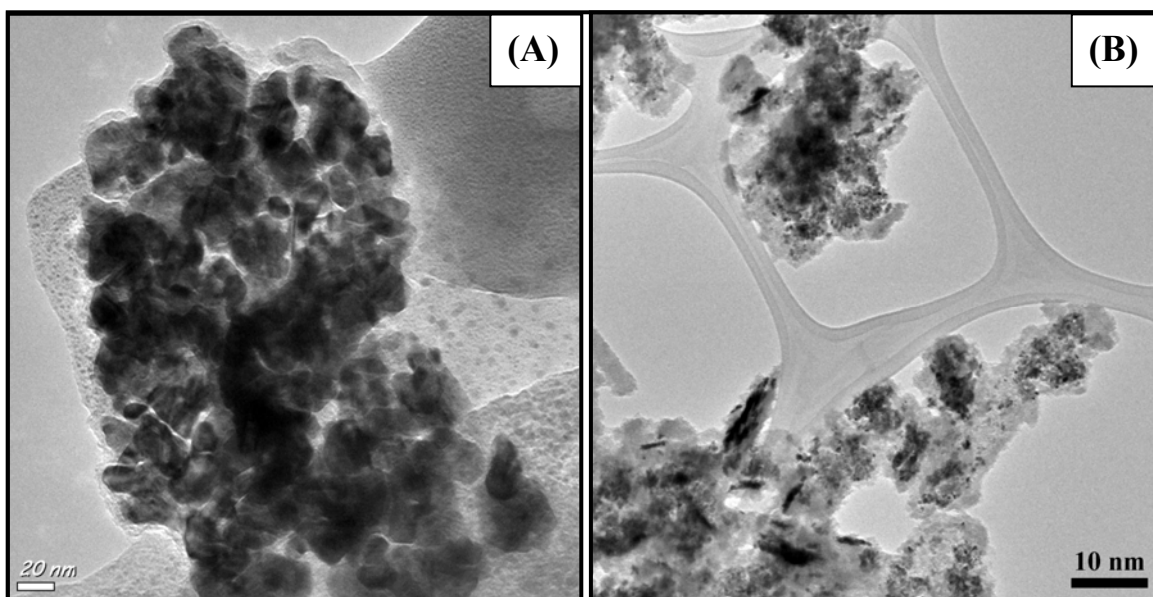


Figure 6-5 shows the TEM images (A) Pt/3D nanoporous g-C, and (B) typical Pt₅₀-Ru₅₀/3D nanoporous g-C.

It is evident that the some pores are filled due to the large size of the Pt nanoparticles. Figure 6-4 (B) shows a typical SEM image of Pt₅₀-Ru₅₀/nanoporous g-C, where 3D nanoporous g-C surface deposited by nanoparticles Pt and Ru. From the SEM image, we can see that the Pt₅₀-Ru₅₀/3D nanoporous g-C has more porous surface than the Pt/3D nanoporous g-C, showing has higher surface area than Pt/3D nanoporous g-C. Because the Pt and Pt₅₀-Ru₅₀ alloy catalysts on the g-C support were very small in size, Pt and Pt-Ru alloy catalyst was hardly observed from the SEM images of Fig. 6-4 (A and B).

The transmission electron microscopy (TEM) measurements were performed to reinvestigate the presence of Pt and Pt-Ru nanoparticles. A TEM image of the Pt/3D nanoporous g-C is shown in Fig. 6-5 (A). As seen from TEM images, Pt nanoparticles showing the agglomeration. And the Pt nanoparticles were ~ 20 nm in size. Figure 6-5 (B) shows the TEM image of the g-C with the deposited Pt-Ru alloy catalysts. It can be clearly seen that Pt-Ru alloy catalyst was dispersed on g-C. In addition, the composition of individual particles was probed using energy-dispersive X-ray analysis (EDX). An EDX spectrum of Pt

and Pt₅₀-Ru₅₀ alloy catalysts is shown in Fig. 6-6 and 6-7. The EDX indicated that Pt and Pt-Ru alloy catalysts was deposited on the g-C.

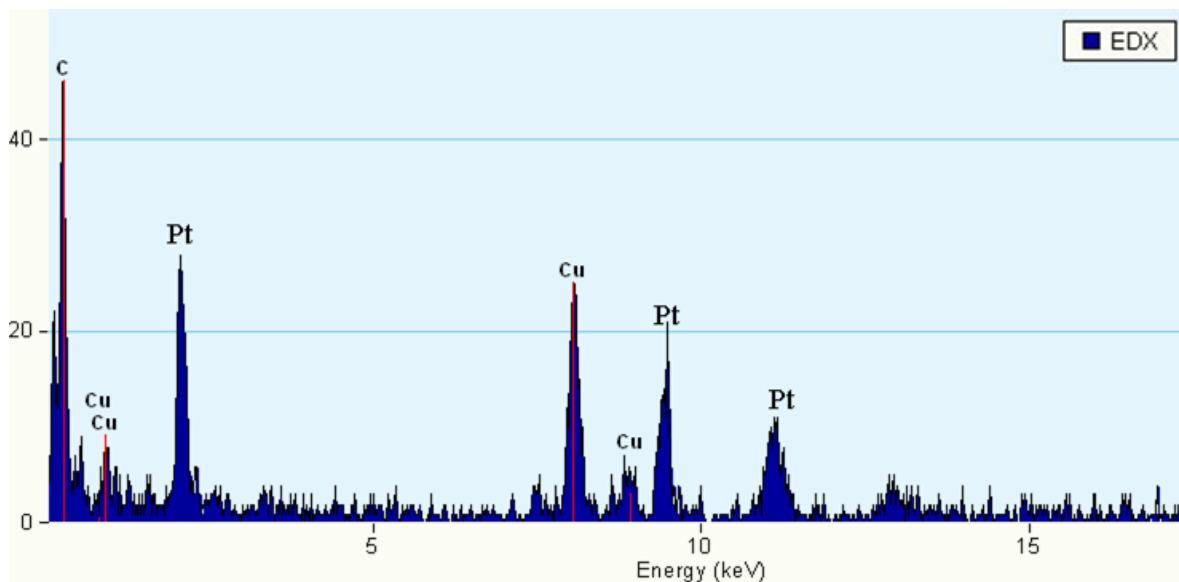


Figure 6-6 shows the EDX spectrum of the Pt catalyst on the g-C.

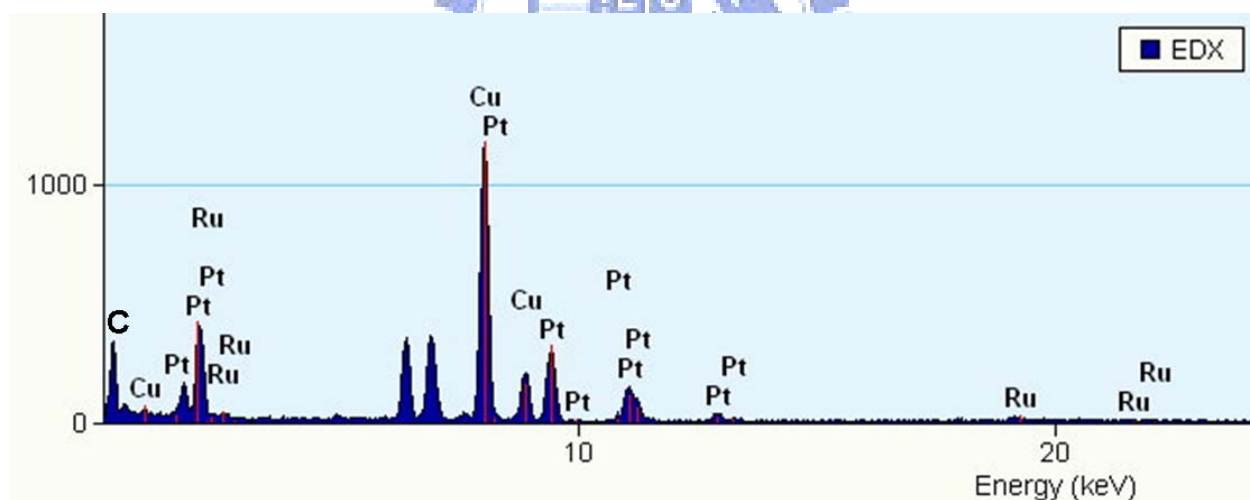


Figure 6-7 shows the EDX spectrum of the Pt₅₀-Ru₅₀ alloy catalyst on the g-C, showing the presence of Pt and Ru nanoparticles on the 3D nanoporous g-C.

X-ray photoelectron spectroscopic (XPS) system is a convenient tool to investigate the presence of Pt and Pt-Ru alloy catalysts on the g-C. The wide-scan XPS spectrum of the Pt/3D nanoporous g-C and Pt₅₀-Ru₅₀/3D nanoporous g-C are shown in Fig. 6-8. From the spectrum it is clear that the Pt and Pt-Ru alloy catalysts was deposited on the 3D nanoporous

g-C. The relatively strong O(1s) XPS signal suggests that the oxygen surface group was present on the 3D nanoporous g-C. This is greatly affects the nanoparticles deposition and electrocatalytic characteristics of the Pt and Pt-Ru nanoparticles. On the other hand, the weak signals of Si(2s) and Si(2p) were detected from XPS, indicates nanoporous g-C completely covered the Si surface. This is consistent with our SEM observation as shown in Fig. 6-4 (A and B).

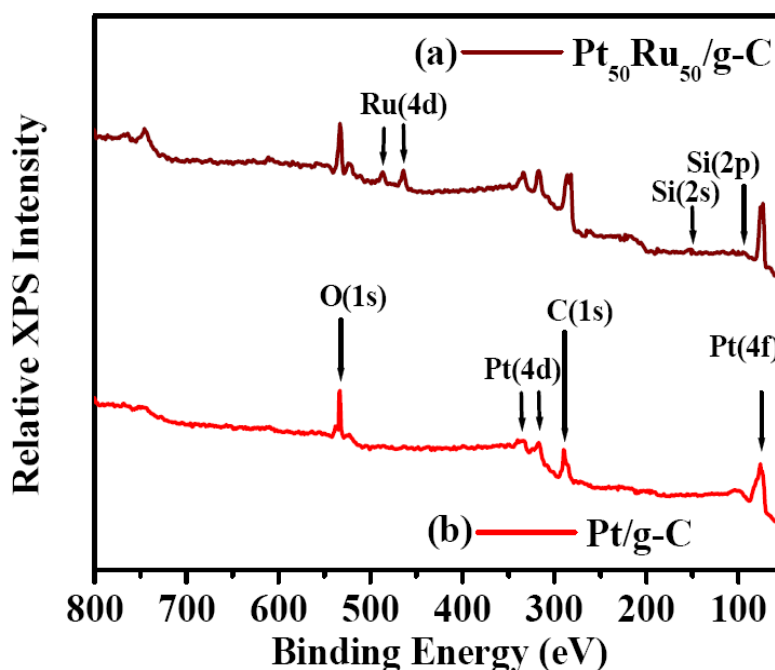


Figure 6-8 shows the XPS survey spectrum of the 3D nanoporous g-C supported Pt and Pt-Ru alloy catalysts.

6.4 Electrocatalytic activity

The hydrogen adsorption and desorption was used to investigate the electrochemical active surface area (ECSA) of these electrodes. Figure 6-9 shows the CV curves of the Pt/3D nanoporous g-C and Pt₅₀-Ru₅₀/3D nanoporous g-C electrodes in a 1 M H₂SO₄ aqueous solution. The potential was scanned between -0.4 and 1.2 V (vs. SCE) at the potential scan rate of 25 mV s⁻¹.

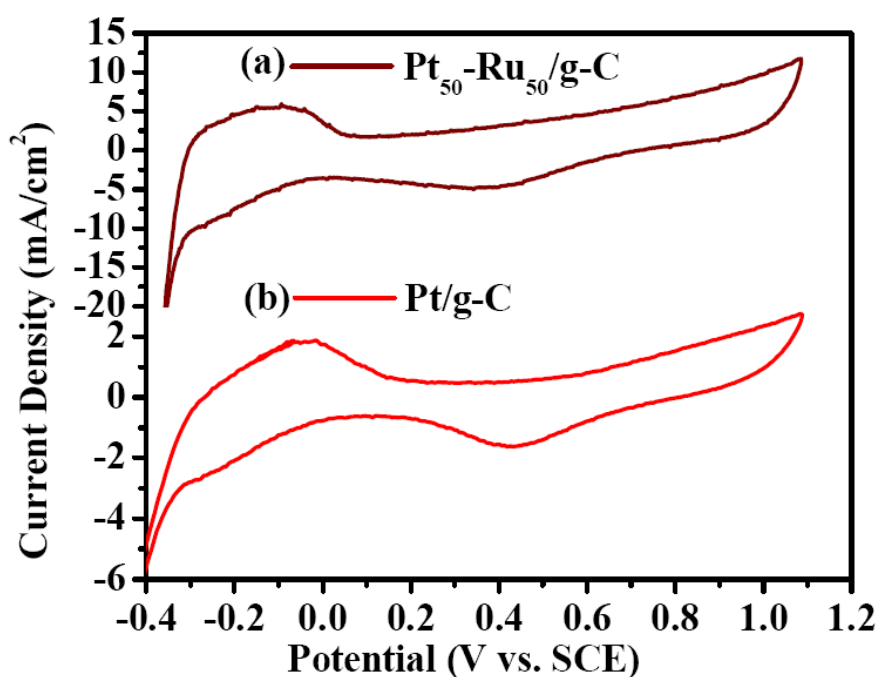


Figure 6-9 shows the cyclic voltammograms of the Pt₅₀-Ru₅₀/3D nanoporous g-C and Pt/3D nanoporous g-C electrodes in aqueous solution in N₂ saturated aqueous solution of 1 M H₂SO₄. The scan rate was 25 mV s⁻¹.

The peaks for the adsorption/desorption of hydrogen appearing between -0.35 and 0.15 V vs. SCE are clearly shown. The wide peak potentials shift slightly from Pt/3D nanoporous g-C (~ 0.14 V, -0.27 V) to that of Pt₅₀-Ru₅₀/3D nanoporous g-C (~ 0.05 V, -0.30 V). The double layer capacitance remarkably enhanced by addition of ruthenium into the platinum. The higher the ruthenium content, the larger the double layer capacitance [142]. The hydrogen adsorption charge (Q_H) has been calculated by taking the assumption that the double layer capacitance is constant across the entire investigated potential range. The Q_H of the Pt/3D nanoporous g-C and Pt₅₀-Ru₅₀/3D nanoporous g-C electrodes are 16.12 and 28.23 mC cm⁻², respectively. Q_H shows the number of sites of Pt available for hydrogen adsorption and desorption. These results show that, even their geometric surface area is the same, the active surface area of Pt₅₀-Ru₅₀/3D nanoporous g-C electrode is much larger than that of the Pt/3D nanoporous g-C electrode, and the high ECSA were favorable to electrochemical oxidation

toward methanol.

The electro-active surface area (ESA) of the Pt/3D nanoporous g-C, and the Pt₅₀-Ru₅₀/3D nanoporous g-C electrodes was measured by CO-stripping CV in 1 M H₂SO₄ solution at a scan rate of 25 mVs⁻¹. For CO-stripping CV measurements, CO adsorption on the Pt catalyst was conducted by flowing a 10% CO/N₂ gas mixture into 1 M H₂SO₄ electrolyte for 35 min at 0.1 V (vs. SCE), followed by purging with nitrogen gas for 30 min to eliminate any residual CO from the solution. The electrochemical active area of the electrodes was determined assuming the formation of a monolayer of linearly adsorbed CO molecules and the columbic charge required for oxidation of CO_{ads} to be 420 μC cm⁻² [90]. The CO-stripping CV curves for the Pt/3D nanoporous g-C and the Pt₅₀-Ru₅₀/3D nanoporous g-C electrodes are shown in Fig. 6-10 (A and B). The ESAs for Pt/3D nanoporous g-C and Pt₅₀-Ru₅₀/3D nanoporous g-C electrodes are 14.2 and 26.92 mC cm⁻², respectively. The above results indicate that the Pt₅₀-Ru₅₀/3D nanoporous g-C electrode possessed a much higher ESA compared to the Pt/3D nanoporous g-C electrode. This is consistent with the results presented in Fig. 6-9, further showing the large ESA of the synthesized 3D nanoporous Pt₅₀Ru₅₀ electrodes. However, one of the most important factors in direct methanol fuel cells is efficient removal of adsorbed CO-like species on the surface of the catalysts. The CO-stripping CV curves were also used to evaluate the CO tolerance over both Pt/3D nanoporous g-C, and Pt₅₀-Ru₅₀/3D nanoporous g-C electrodes. As shown in Fig. 6-10 (A and B) during the first cycle, when the potential was scanned from -0.3 to 0.0 V, the CV curve is flat indicating that hydrogen adsorption is completely suppressed due to that available active Pt sites were completely covered by the CO. The CO electrooxidation current peaks of the Pt₅₀Ru₅₀/3D nanoporous g-C and Pt/3D nanoporous g-C electrodes were centered at ~0.44 V and ~0.48 V, respectively. The earlier onset of the CO electrooxidation shown by the shoulder at 0.11 V for the Pt₅₀Ru₅₀/3D nanoporous g-C electrode vs. 0.36 V for the Pt/3D nanoporous g-C electrode and the higher current density in this region demonstrates that the Pt₅₀Ru₅₀/3D nanoporous g-C electrode can

oxidize the adsorbed CO-like adspecies more efficiently than Pt/3D nanoporous g-C at the lower electrode potentials.

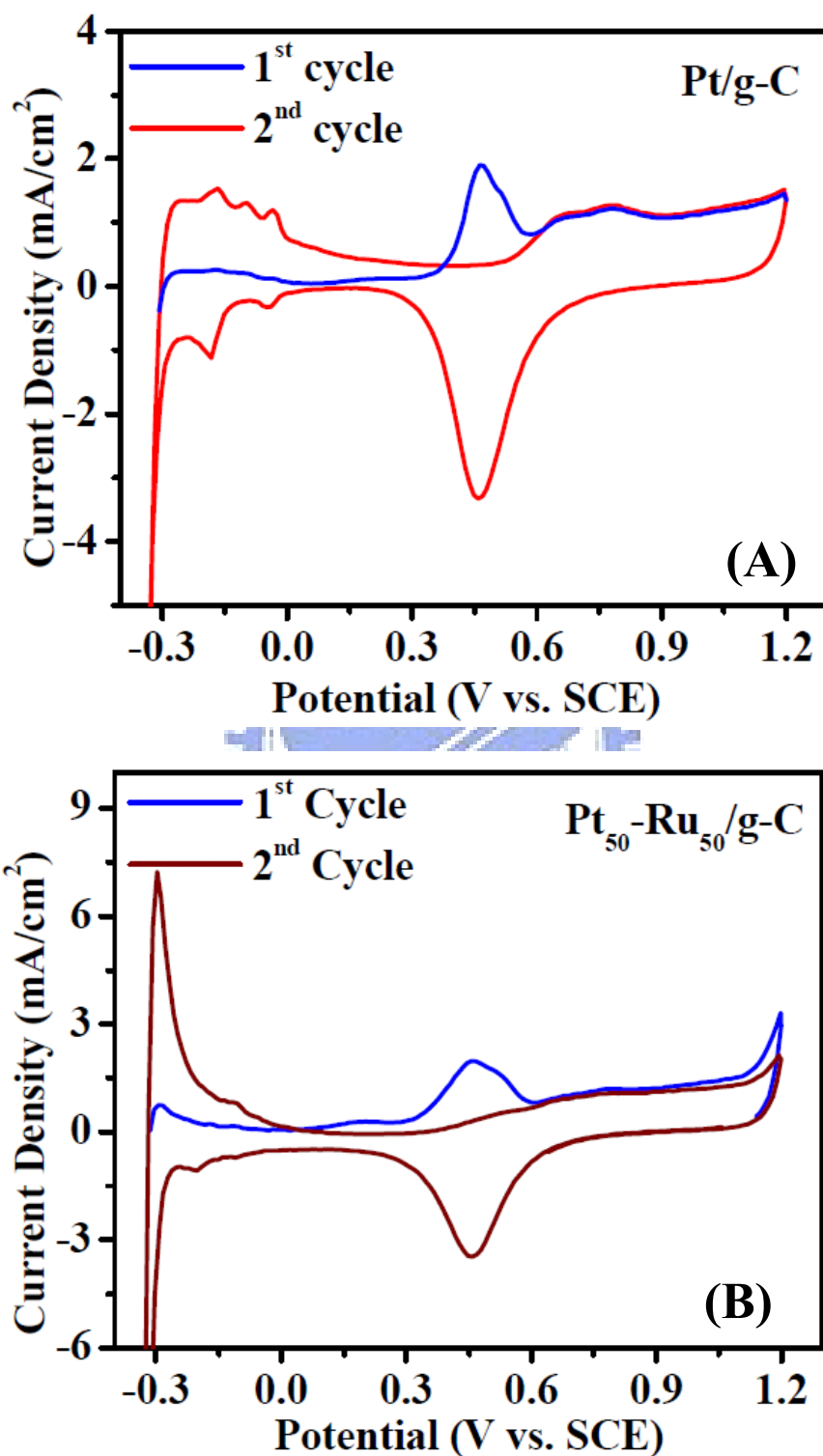


Figure 6-10 shows the CO-stripping CVs in a CO saturated 1 M H₂SO₄ solution (A) the 3D nanoporous g-C electrode; and (B) the Pt₅₀-Ru₅₀/3D nanoporous g-C electrode. The scan rate was 25 mV s⁻¹.

We further studied the electrocatalytic activity of the Pt/3D nanoporous g-C and Pt₅₀-Ru₅₀/3D nanoporous g-C electrodes in an aqueous solution of 1 M H₂SO₄ - 1 M methanol at a scan rate of 25 mV s⁻¹ are shown in Fig. 6-11 (A). As seen from Fig. 6-11 (A), the peak current density of methanol electrooxidation for the Pt₅₀-Ru₅₀/3D nanoporous g-C catalyst at the potential of 0.59 V (vs. SCE) was 8.93 mA cm⁻², which is twice of that on Pt/3D nanoporous g-C (4.1 mA cm⁻² at 0.74 V).

The Pt/3D nanoporous g-C and Pt₅₀-Ru₅₀/3D nanoporous g-C electrodes showed onset potentials of ~0.43 and ~0.25 V, respectively. An excellent catalyst for methanol electrooxidation is one that exhibits a low onset potential. Therefore, this implies that the Pt₅₀-Ru₅₀/3D nanoporous g-C for the methanol electrooxidation has superior electrocatalytic activity compared with the Pt/3D nanoporous g-C catalyst. In addition, the ratio of the forward current density (I_f) to the reverse anodic peak current density (I_b), (I_f/I_b) value could be used to describe the catalyst tolerance to carbonaceous species accumulation [143]. The I_f/I_b value for Pt₅₀-Ru₅₀/3D nanoporous g-C and Pt/3D nanoporous g-C electrodes were ~6.3 and ~1.84, respectively. A lower I_f/I_b value indicated poor oxidation of methanol to CO during the anodic scan and excessive accumulation of residual carbon species on the electrode surface, in other words, a greater extent of CO poisoning. It could be seen that the Pt₅₀-Ru₅₀/3D nanoporous g-C electrode had the highest I_f/I_b ratio than that of the Pt/3D nanoporous g-C electrode, indicating that the better CO tolerance of Pt₅₀-Ru₅₀/3D nanoporous g-C electrode. The electrocatalytic activity of both electrodes was further examined using chronoamperometry. Fig. 6-11 (B) represents the results obtained on the Pt₅₀-Ru₅₀/3D nanoporous g-C and Pt/3D nanoporous g-C electrodes in an N₂ saturated aqueous solution of 1 M CH₃OH - 1 M H₂SO₄ at 25°C at a constant potential of 0.4 V (vs. SCE). As shown in Fig. 6-11 (B), the potentiostatic current decreased gradually at the initial stage. The rapidly decreased in the potentiostatic current might be due to the formation of intermediate species, for instance CO and CHO adspecies etc., during the methanol oxidation reaction [144].

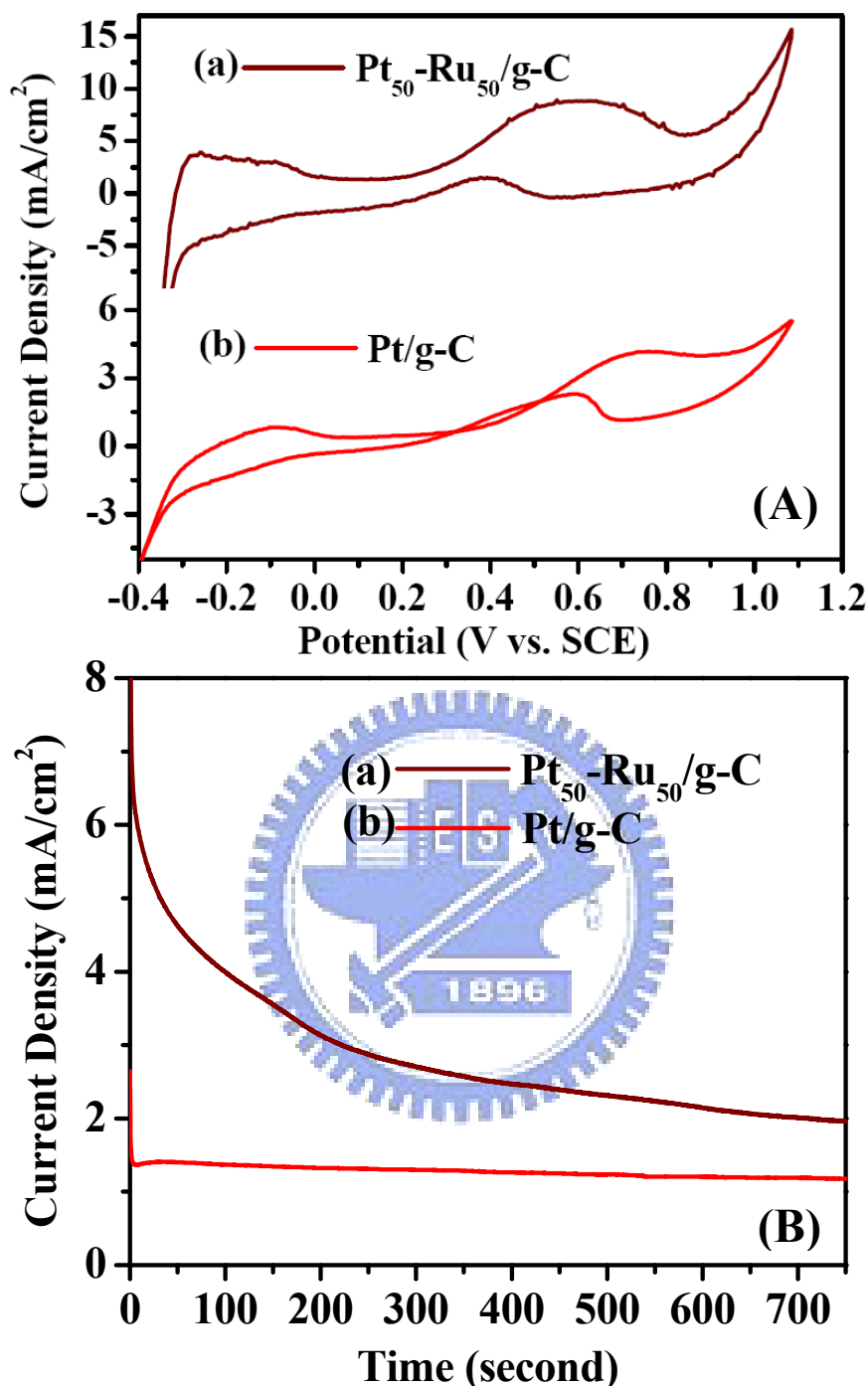


Figure 6-11 (A) CVs of the Pt₅₀-Ru₅₀/3D nanoporous g-C and Pt/3D nanoporous g-C electrodes in aqueous solution of 1 M H₂SO₄ - 1 M CH₃OH at a scan rate of 25 mV s⁻¹, and (B) Chronoamperometric curves for the Pt₅₀-Ru₅₀/3D nanoporous g-C and Pt/3D nanoporous g-C electrodes in aqueous solution of 1 M H₂SO₄ - 1 M CH₃OH at a constant potential of 0.4 V vs. SCE.

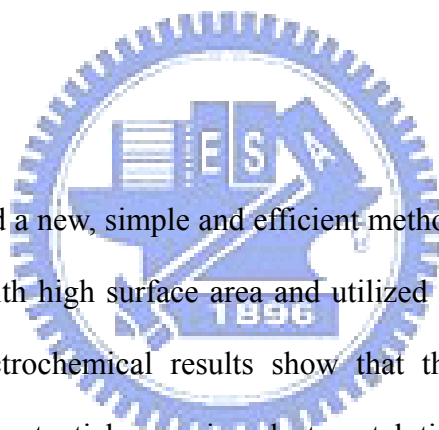
It can be clearly seen that the current density on the Pt₅₀-Ru₅₀/3D nanoporous g-C

electrode is evidently higher than that on the Pt/3D nanoporous g-C electrode. This result further confirms the superiority of the Pt₅₀-Ru₅₀/3D nanoporous g-C electrode over the Pt/3D nanoporous g-C electrode with respect to catalytic activity, CO tolerance, and stability.

The observed lower overpotential, superior electrocatalytic activity towards methanol oxidation and better CO tolerance at the Pt₅₀-Ru₅₀/3D nanoporous g-C electrode could be elucidated in terms of the bifunctional mechanism described elsewhere [145], in which Ru was proposed to be able to promote the oxidation of the strongly adsorbed CO on Pt by supplying an oxygen source (Ru-OH_{ad}). Moreover, the presence of 3D nanopores of g-C supports may also contribute to the observed higher current density because of the easy transport of methanol and the oxidation products in these nanopores [146].

6.5 Summary

We have demonstrated a new, simple and efficient method to synthesis the 3D nanoporous graphitic carbon (g-C) with high surface area and utilized as a support for Pt and Pt₅₀-Ru₅₀ alloy catalysts. The electrochemical results show that the Pt₅₀-Ru₅₀/3D nanoporous g-C electrode had lower overpotential, superior electrocatalytic performance towards methanol oxidation, and better CO tolerance, showing the direct synthesis 3D nanoporous g-C may have a better future as catalysts support in electrocatalysis and fuel cells.



Chapter 7

Synthesis of 2D Continuous Pt Island Networks for Methanol Electrooxidation

7.1 Introduction

Over the past few years, synthesis of nanostructured materials has received great interest in the technology due to its wide range of applications in biosensors [147], energy system [148], catalysis [149], and in self-assembly of supramolecular structures [150]. Nanostructured Pt metals materials are very attractive because of their superior electrocatalytic performance than the blanket Pt electrode. Recently several methods have been reported for the preparation on nanostructure but it is difficult and time-consuming to prepare the nanostructures [15-18, 151]. Besides, Pt is very expensive, resource limited and irreversibly inactivated by CO-like poisoning species. Therefore, it is essential that the utilization of platinum should be kept as low as possible without sacrificing the catalytic performance. The one best way to accomplish this is to create continuous Pt island networks. The interconnected structure could have additional advantages in enhancing catalytic activities for reactions that involve two or more reactants, because such networks supply enough absorption sites for reactant molecules over a close range [152].

Herein, we report a new and simple method for fabricating continuous Pt island networks by pulse-potentiostatic electrodeposition using Si substrates of low resistivity, which act as the current collector. And thus, the silicon support was very appropriate for use as the Pt electrocatalytic electrode in respect of electrical conductivity. As shown in Fig. 7-1, the presence of the surface oxide layer on the silicon substrate can greatly enhanced the oxidation of CO adsorbed on the active Pt sites according to the bifunctional mechanism. Moreover, the electrocatalytical study of the continuous Pt island network on the silicon substrate indicates

the potential application for electrodes in direct methanol fuel cells.

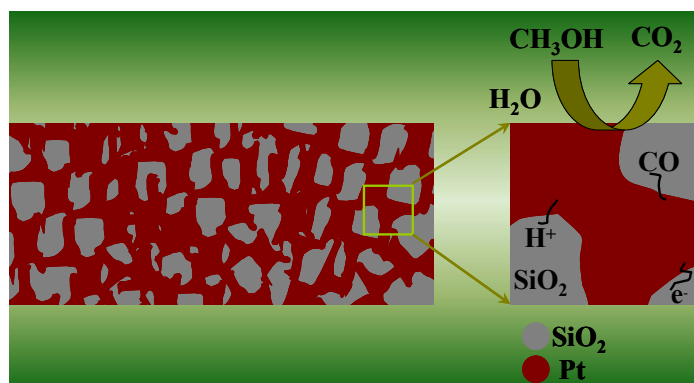


Figure 7-1 shows a schematic illustration of the continuous Pt island network on the flat silicon substrate. The right hand side exhibits the bifunctional mechanism of CO electrooxidation. The adsorbed oxygen containing species on the surface of SiO₂ can facilitate the oxidation of CO-like poisoning species adsorbed on the active Pt sites.

7.2 Fabrication steps for the continuous island Pt network electrode

The fabrication steps for the continuous island Pt network electrode are described in the following: a flat Si substrate was washed with acetone followed by DI water (>18 M Ω), then etched in 10 wt% HF at room temperature for 5 min to remove the thin native oxide layer on the silicon surface. Then, the Pt particles were electrodeposited on the etched Si in the aqueous solution of 1 M K₂PtCl₆/ 1 M H₂SO₄ (100 mL/100 mL) at room temperature by potentiostatic pulse plating in a three electrode cell system with a saturated calomel reference electrode (SCE) [105]. The time durations for the high potential pulse (+0.08 V) and the low potential pulse (-0.01 V) were 3 and 1 ms, respectively. The blanket Pt catalyst was prepared by potentiostatic pulse plating (1 M K₂PtCl₆/ 1 M H₂SO₄) on the silicon substrate. The time durations for the high potential pulse (+0.06 V) and the low potential pulse (-0.04 V) were 5

and 2 ms, respectively. The Ru decorated blanket Pt electrode were obtained by deposition of Ru on the blanket Pt by potentiostatic pulse plating at -0.07 and +0.02 V in a 1 M RuCl₃ (200 mL) solution for 5 and 1 ms respectively.

7.3 Structural characterization

Figure 7-2 (A) and (B) illustrates a representative scanning electron microscopy (SEM) image of the blanket Pt on silicon substrate and Ru decorated on blanket Pt, respectively.

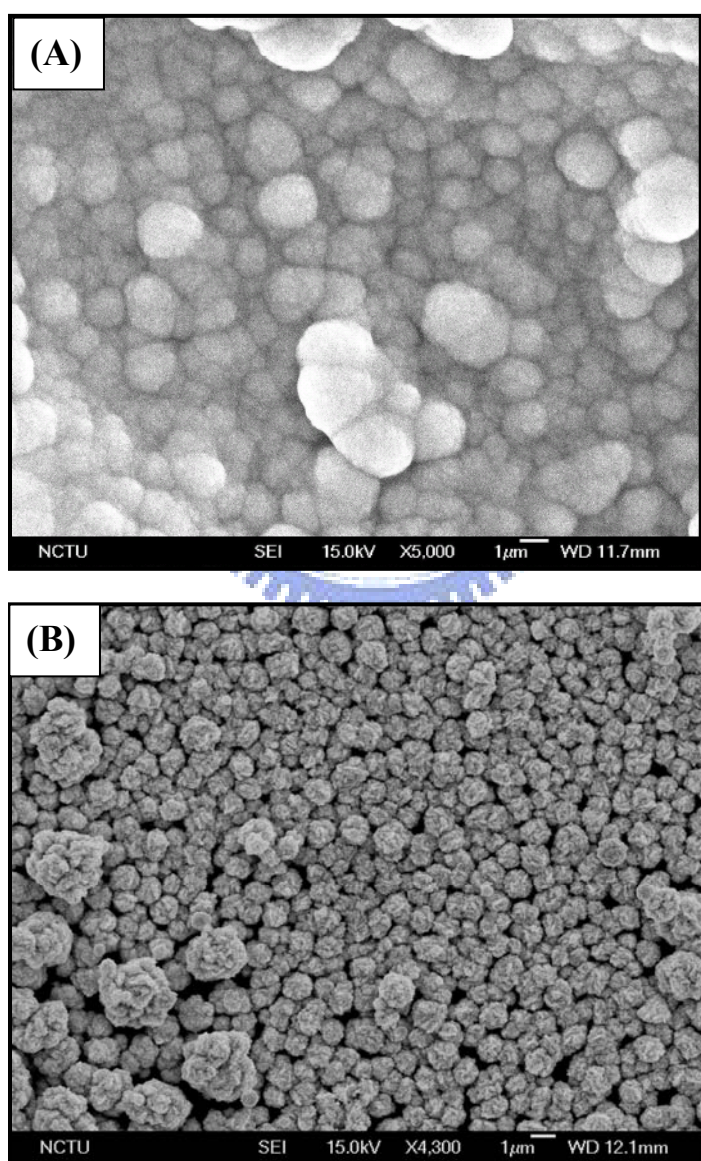


Figure 7-2 shows the SEM images: (A) blanket Pt on flat Si substrate; and (B) Ru on blanket Pt/Si.

From the SEM images, the blanket Pt and the Ru decorated on the blanket Pt were completely covered on the silicon substrate after the electrochemical deposition. Figure 7-3 show the surface morphology of the pulse electrodeposited Pt on the Si substrate. The Pt islands are mutually connected over the Si substrate. The Pt islands forming the continuous Pt island film have size distribution from ~200 nm to ~800 nm.

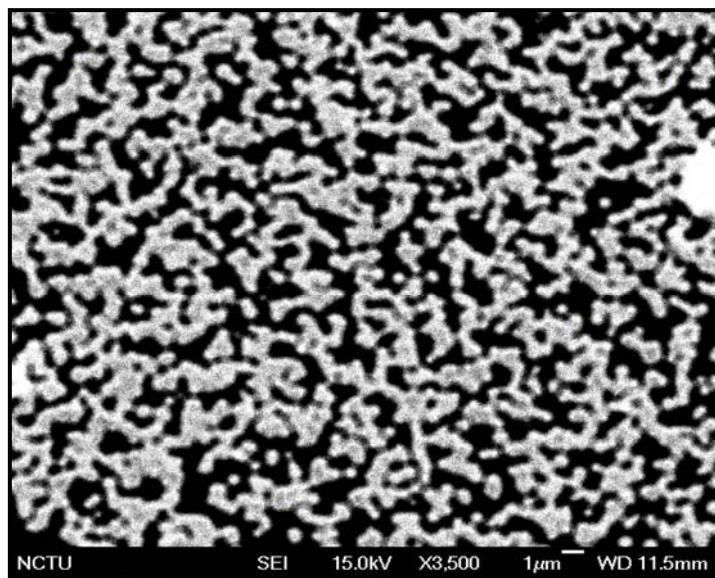


Figure 7-3 shows the SEM image of the continuous Pt island network on the flat silicon substrate.

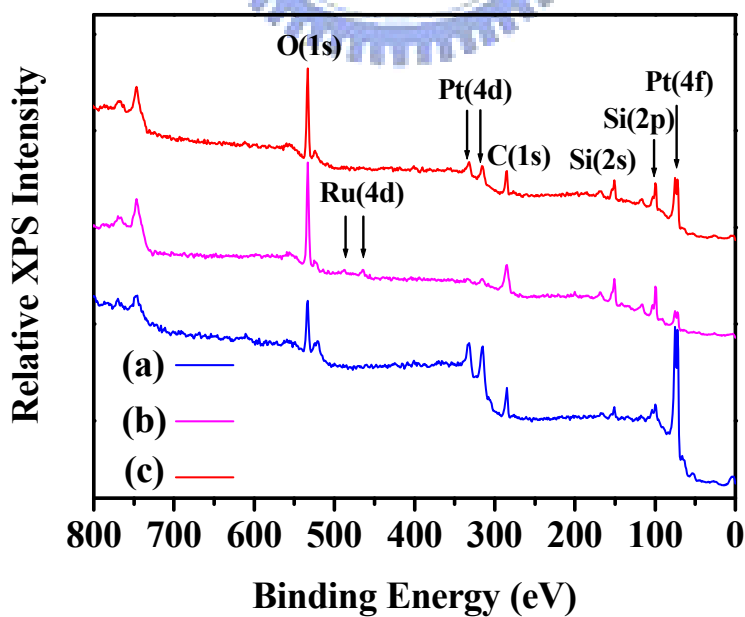


Figure 7-4 shows the x-ray photoelectron spectrum (XPS) of (a) blanket Pt/Si; (b) Ru decorated blanket Pt; and (c) continuous Pt island network.

X-ray photoelectron spectroscopy (XPS) shown in Fig. 7-4 indicated that Pt and Ru were successfully deposited on the silicon substrate by the pulse electrodeposition.

7.4 Electrochemical measurements

The electroactive surface area (ESA) of the electrodes was determined by the CO-stripping cyclic voltammetry, which was performed by flowing a 10% CO/N₂ gas mixture in the 1 M H₂SO₄ aqueous solution at +100 mV for 35 min, using a Pt wire as the counter electrode and a saturated calomel reference electrode (SCE). Before scanning, the solution was purged with N₂ gas for 30 min to remove CO remained in the solution. Representative CO-stripping voltammograms for the continuous Pt island network/Si, the Ru decorated Pt film and the blanket Pt/Si electrodes are illustrated in Fig. 7-5.

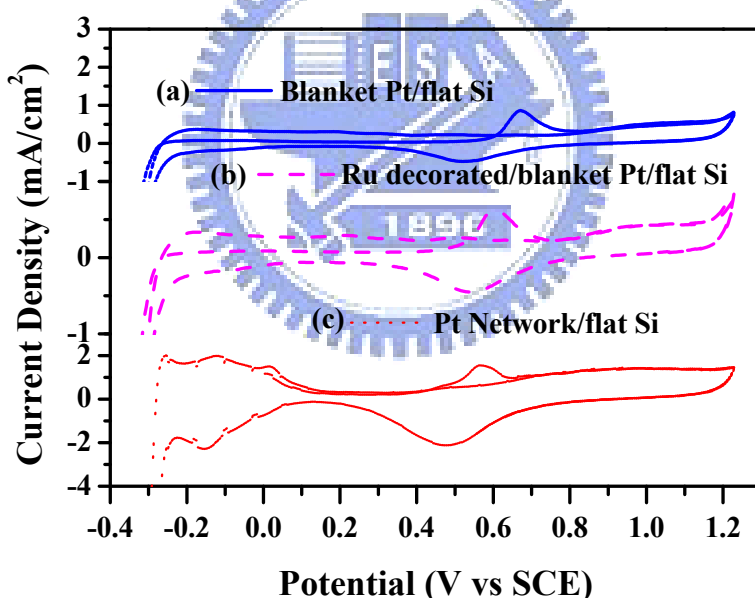


Figure 7-5 shows the CO stripping cyclic voltammetry curves recorded at room temperature in a CO saturated 1 M H₂SO₄ solution at a scan rate of 20 mV s⁻¹

A high ESA of 67 m² g⁻¹ was obtained for the continuous Pt island network/Si electrode by integrating the CO-electrooxidation peak of first CO stripping cycle, assuming an oxidation charge value of 420 μC cm⁻² for a monolayer of CO adsorbed on a smooth platinum surface

[90]. The ESA of the continuous Pt island network/Si electrode is much higher than that of the Ru decorated Pt film electrode ($21 \text{ m}^2 \text{ g}^{-1}$) and that of the blanket Pt electrode ($16 \text{ m}^2 \text{ g}^{-1}$). This shows that the continuous Pt island network/Si electrode has a relatively high ESA, most likely due to the interconnect structure of the Pt islands. Such well-defined continuous Pt island network structure provides abundant active sites for the electrooxidation reaction of methanol.

From the CO-stripping curve, we noticed a lower onset potential and smaller peak potential for CO oxidation on the continuous Pt island network electrode in comparison to the Ru decorated Pt film and the blanket Pt film/Si. Examination of the CO oxidation curves reveals that the onset potential of the continuous Pt island network/Si electrode ($\sim 0.43 \text{ V}$) is lower than that of the Ru decorated/Pt (~ 0.48) and the blanket Pt/Si ($\sim 0.60 \text{ V}$). The CO oxidation peak potential for the continuous Pt island network/Si ($\sim 0.57 \text{ V}$) is also lower than that for the Ru decorated Pt ($\sim 0.60 \text{ V}$) and the blanket Pt/Si ($\sim 0.64 \text{ V}$), probably due to an enhanced CO oxidation rate on the Pt islands surrounded by the chemical SiO_2 layer, which was formed on the Si substrate in the electrolyte. The presence of the oxide layer on the silicon substrate can promote the oxidation of CO adsorbed on the active Pt sites via the bifunctional mechanism [105]. The oxygen-containing species on SiO_2 (such as hydroxyl surface group) can transform CO-like poisoning species adsorbed on Pt to CO_2 , releasing the active sites on Pt for further electrochemical reaction, and hence the continuous Pt island network on the flat Si substrate possess higher activity towards CO oxidation compared to the blanket Pt on silicon and the Ru decorated Pt film.

Figure 7-6 shows the cyclic voltammograms of the three electrodes recorded in $1 \text{ M CH}_3\text{OH}/1 \text{ M H}_2\text{SO}_4$ aqueous solution at a potential scan rate of 20 mV s^{-1} . The CV curve of the continuous Pt island network/Si shows that the methanol oxidation peak had the maximum around 0.63 V vs. SCE and a very low onset potential of $\sim 0.38 \text{ V}$. Also shown in Fig. 7-6 is the CV curves of the blanket Pt film and the Ru decorated Pt film, which show a much

smaller current density with a higher onset potential. The negative onset potential shift indicated that the continuous Pt island network/Si can effectively reduce overpotentials in the methanol electrooxidation reaction [91-94].

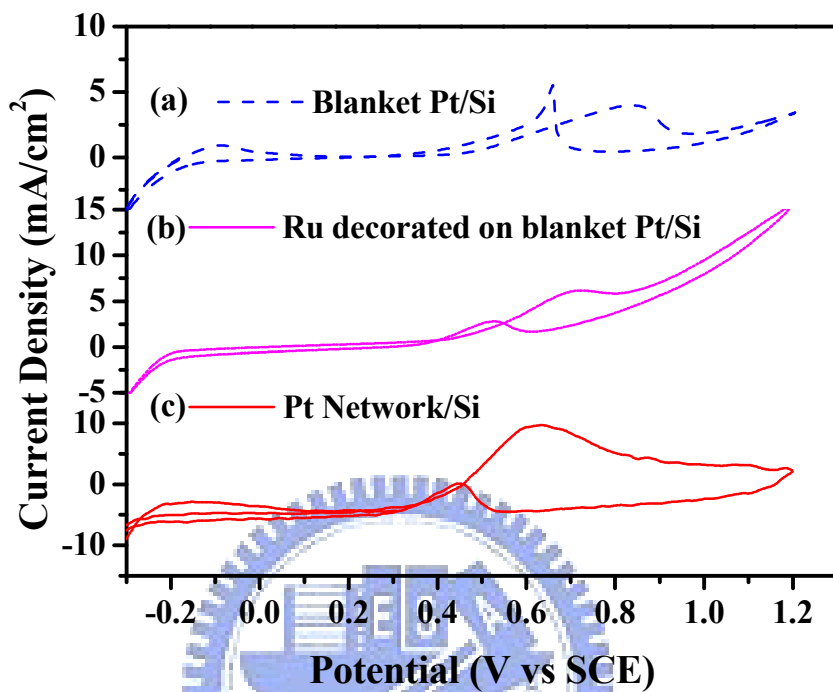


Figure 7-6 shows the cyclic voltammograms in 1 M CH₃OH+1 M H₂SO₄ at a scan rate of 25 mV s⁻¹.

Noted that the methanol oxidation peak in the forward scan for the continuous Pt island network/Si electrode was much larger than the peak in the region of 0.3 - 0.5 V in the reverse scan. In the cyclic voltammetric scan, the anodic peaks in the forward scan and in the reverse scan are associated with electrooxidation of methanol and removal of incompletely oxidized carbonaceous species (CO-like poisoning species) on the electrode, respectively. The catalyst tolerance against CO adsorption may be evaluated by the ratio of the current density of the forward anodic peak (I_f) to that of the reverse anodic peak (I_b), (I_f/I_b) [143]. For the continuous Pt island/Si electrode, the (I_f/I_b) ratio was calculated to be ~19. This ratio was more than 9 times and 20 times larger than that of the Ru decorated Pt film and the blanked Pt

film, respectively.

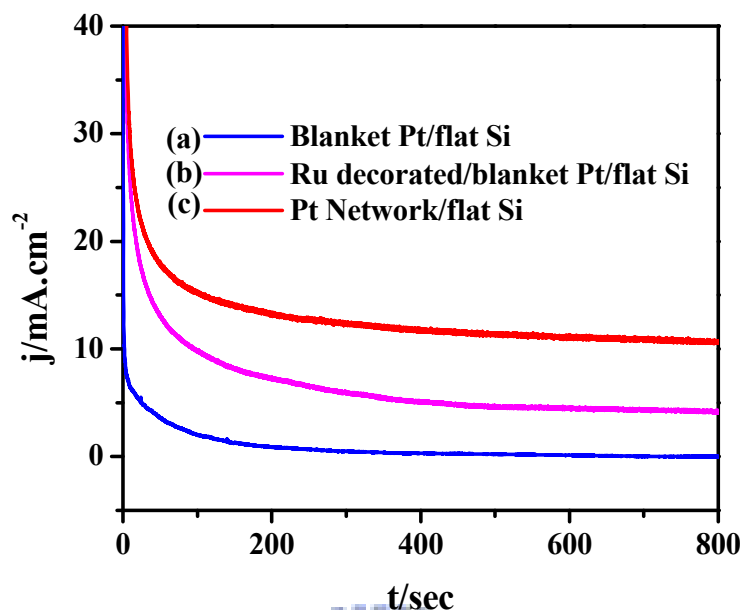


Figure 7-7 shows the chronoamperometry curves in 1 M CH₃OH+1 M H₂SO₄ at the potential of 0.4 V.

Chronoamperometry technique was employed to further test the activity of these three electrodes. Figure 7-7 shows the chronoamperogram of electroactivity of the three electrodes at the oxidation potential of ~ 0.4 V in the 1 M CH₃OH/1 M H₂SO₄ aqueous solutions at 25°C. Steady-state currents for methanol electrooxidation were measured for more than 800 s. At the oxidation potential of 0.4 V, the steady-state currents at 800 s for the continuous Pt island network/Si, Ru decorated Pt film and blanket Pt/Si are ~ 10 , ~ 4 , and ~ 0.05 mA cm⁻², respectively. The observation implied that most CO-like poisoning species could be oxidized and removed from the Pt catalyst so that the catalytic oxidation of methanol could be kept proceeding efficiently on the continuous Pt island network/Si electrode. Because oxygen containing species on the SiO₂ surface layer can promote the CO removal as described above, the improvement of the electrooxidation activity can be ascribed to the synergistic effect of the Pt island catalyst and the SiO₂ surface layer. These results are very consistent with the CV studies shown in Fig. 7-5 and 7-6.

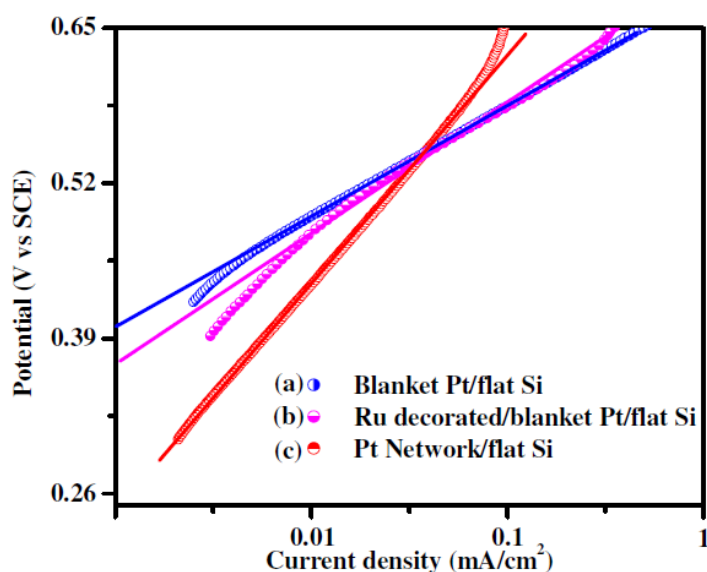


Figure 7-8 shows the Tafel plots for the electrochemical oxidation of 1 M CH₃OH/1 M H₂SO₄ aqueous solution at a scan rate of 1 mV/s.

Tafel plot for electrochemical oxidation of 1 M CH₃OH/1 M H₂SO₄ aqueous solution at a scan rate of 1 mV s⁻¹ is shown in Fig. 7-8. The blanket Pt/Si and Ru decorated Pt film have a Tafel slope of ~115 and ~137 mV dec⁻¹, respectively. On the other hand, the continuous Pt island network/Si exhibits a much larger Tafel slope (~245 mV dec⁻¹), suggesting a great difference in the electrooxidation mechanism for the continuous Pt island network/Si electrode from the other two electrodes. This might be ascribed to the Pt island network structure and the presence of active oxygenated on the SiO₂ surface layer [153, 154]. The mechanistic difference could result in the better catalytic activity and CO tolerance of the 2-D continuous Pt island network/Si electrode compared to the blanket Pt/Si and the Ru decorated/Pt film electrode.

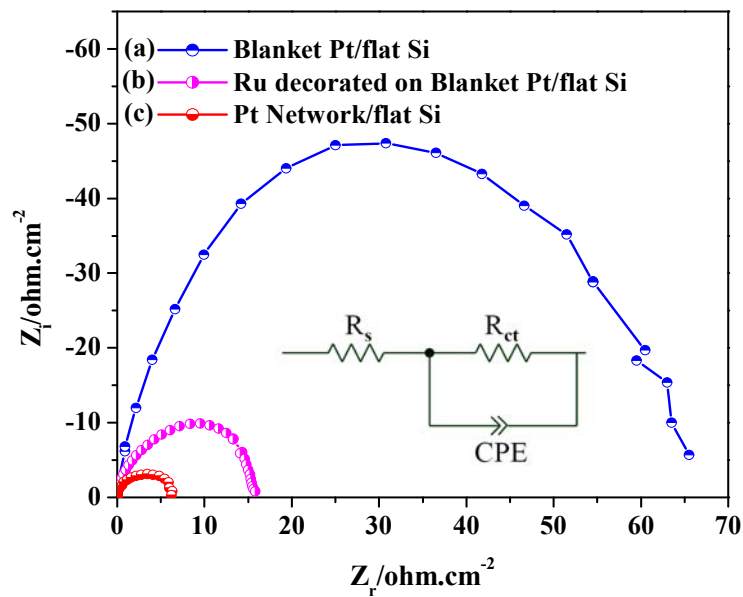


Figure 7-9 shows the electrochemical impedance spectra in 1 M CH₃OH + 1 M H₂SO₄ at the potential 0.3 V. The inset in figure shows the equivalent circuit model.

The electrochemical impedance spectroscopy (EIS) measurements were used to evaluate the charge-transfer resistance and the capacitance of these three electrodes during methanol electrooxidation. Figure 7-9 shows three Nyquist plots recorded in 1 M CH₃OH + 1 M H₂SO₄ at the oxidation potential of ~0.3 V, where Z_r and Z_i represent the real and imaginary components of the impedance, respectively. The equivalent circuit model shown in the inset of Fig. 7-9 was used to fit the experimental data. The R_s resistor represents the resistance of the electrolyte solution, R_{ct} the charge transfer resistance and CPE represents the constant phase element [151]. As shown in Fig. 7-9, the EIS well fits with the proposed model. The Ru decorated Pt film and the blanket Pt/Si electrodes have charge-transfer resistances about ~16 and ~68 $\Omega\text{-cm}^{-2}$, which is over 3 times and 11 times larger than that for the continuous Pt island network/Si (~6 $\Omega\text{-cm}^{-2}$).

7.5 Summary

A two-dimensional continuous island Pt network electrode have been successfully

fabricated by potentiostatic pulse plating on the flat silicon substrate, and electrochemical measurements confirm that this catalyst structure on the silicon substrate has a better electroactivity toward methanol oxidation than the blanket Pt/Si and the Ru decorated Pt film/Si electrodes. The good electrooxidation performance can be ascribed to the synergistic effect of the Pt island catalyst and the surrounding SiO₂ surface layer, which significantly enhanced the CO tolerance and thus improved the electrooxidation activity of the Pt catalyst.



Chapter 8

Synthesis of 3D Platinum Nanoflowers and Their Electrochemical Characteristics

8.1 Introduction

Recently, synthesis of nanostructured materials with a high specific surface area has attracted great interest in the development of fuel cell catalysts [105, 155, 156], applications for photocatalytic activity [157], biosensors [158], chemical sensors [159, 160], and in the reduction of pollutant emission from automobiles [161]. Among all precious catalyst metals, platinum has unique chemical and physical characteristics and has a wide range of industrial and environmental applications. But it is extremely susceptible to poisons such as CO-like species, which result in a dramatic decrease in efficiency. However, a critical problem with Pt catalyst is the high cost due to limited supply. Thus, one of the major challenges in fuel cell development is to reduce the usage of platinum catalyst. One effective approach to accomplish this goal is to synthesize Pt nanostructures well dispersed on the electrode so that a high surface/volume ratio can be obtained. The use of both larger surface area supports, such as porous substrates [153, 162-163] and porous platinum [16, 155, 164-170] has been explored. Herein, we report a new and facile method of synthesizing 3D platinum nanoflowers on the silicon substrate by potentiostatic pulse plating. The 3D nanostructured platinum catalyst shows excellent electrocatalytic activity toward oxidation of methanol and CO adspecies.

8.2 Synthesis of the 3D Pt nanoflowers

A p-type 4-inch Si wafer of low resistivity (0.002 Ω -cm) was used as the substrate for the synthesis of the 3D Pt nanoflowers. 1 M H_2PtCl_6 was first mixed with 1 M H_2SO_4 in an

aqueous solution at room temperature, and the mixture was stirred at 25°C for 5 h to make the mixture solution homogeneous. The Pt catalyst was then electrodeposited on the flat silicon substrate in the mixture solution by potentiostatic pulse plating in a three electrode cell system with a saturated calomel reference electrode (SCE). The time periods for the positive potential pulse (+0.05 V) and the negative potential pulse (-0.02 V) were 5 ms and 1 ms, respectively. Under the bipolar pulse electrodeposition conditions, 3D Pt nanoflowers could be synthesized on the Si substrate. After Pt electrodeposition, the sample was washed by DI water to removed contamination from the sample surface and dried in the ambient. For comparison, a blanket Pt thin film was also prepared on the Si substrate by electrodeposition, which will be referred to Pt thin film catalyst thereafter.

8.3 Characterization of the 3D Pt nanoflowers

Surface morphology of the 3D Pt nanoflowers was investigated by scanning electron microscopy (SEM). Figure 8-1 shows the SEM micrograph of the bipolar-pulse electrodeposited Pt catalyst thin film, which was composed of rose-like particles with a size between ~400 and ~800nm.

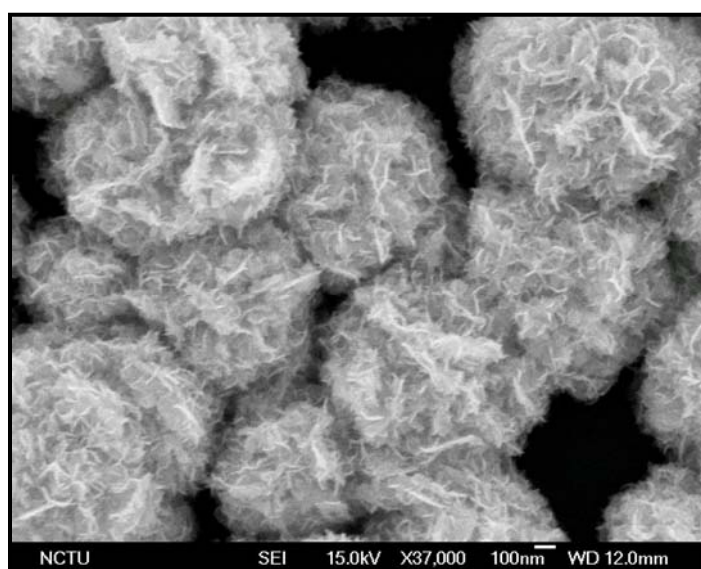


Figure 8-1 shows the scanning electron micrographs of the 3D Pt nanoflower on the Si substrate.

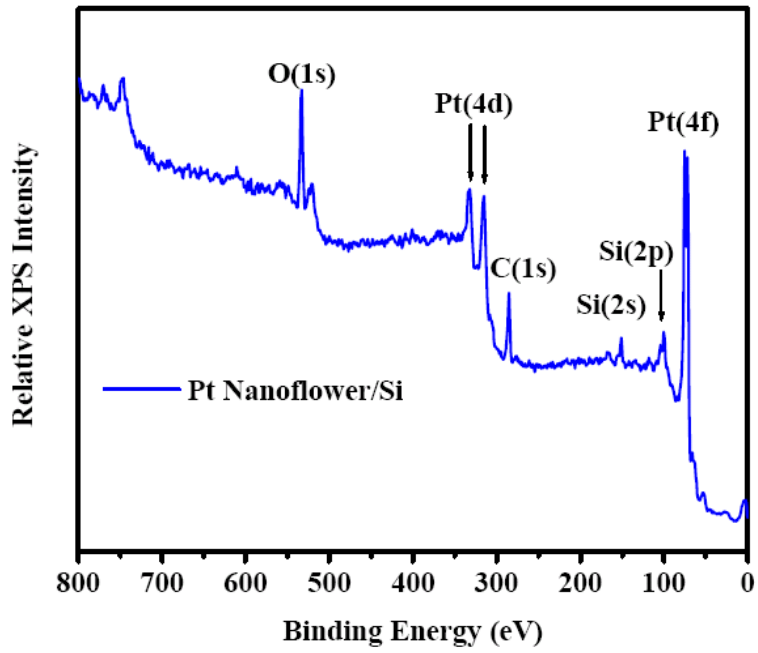


Figure 8-2 shows the XPS survey spectrum of the 3D Pt nanoflower on the silicon substrate.

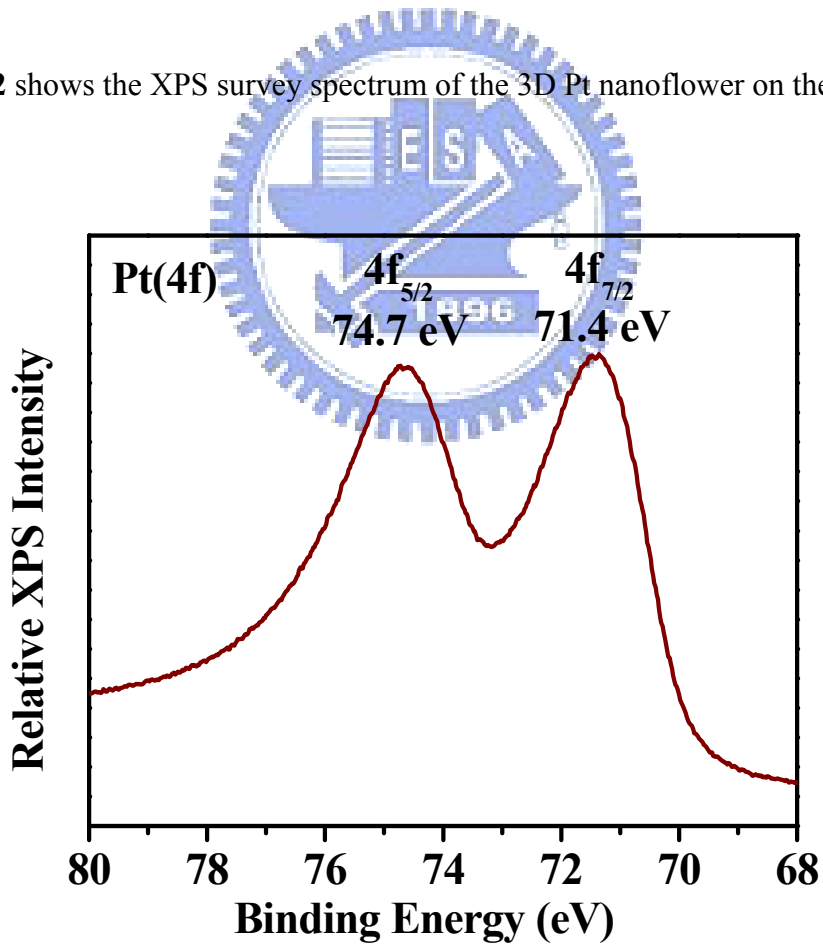


Figure 8-3 shows the energy window of Pt (4f) electrons.

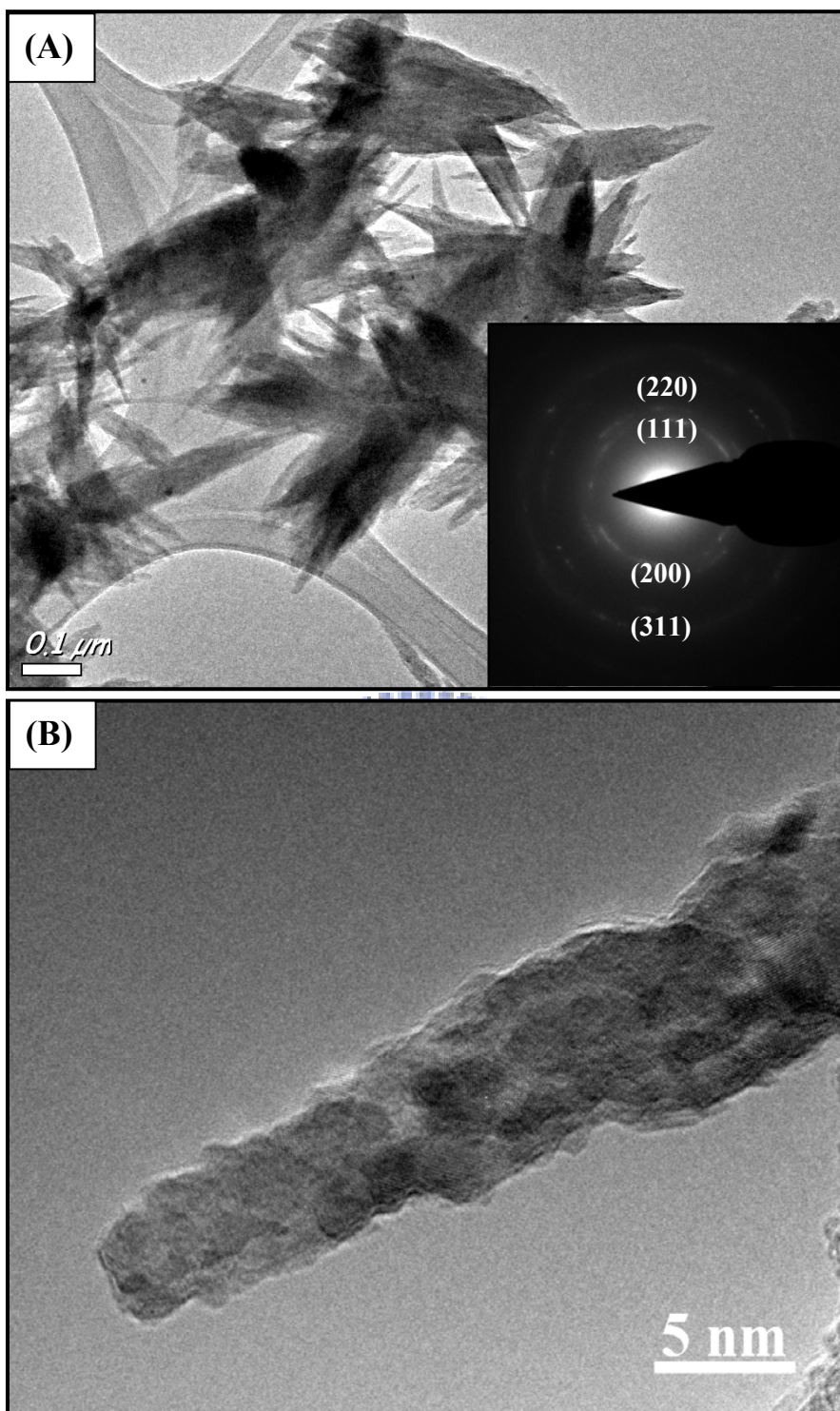
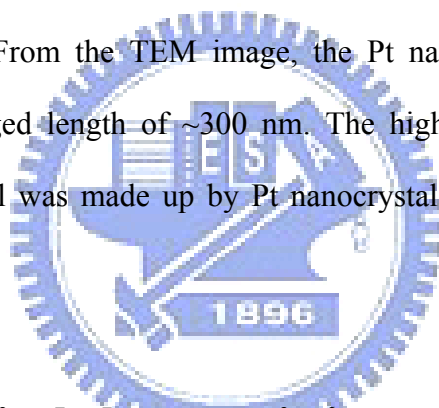


Figure 8-4 shows the TEM of nanopetals mechanical scratched off the 3D Pt nanoflower/Si sample. The inset shows the SAED pattern, and (B) a high resolution TEM image of a nanopetal.

The x-ray photoelectron spectrum (XPS) of the 3D Pt nanoflowers is shown in Fig. 8-2. Because the nanoflowers did not fully cover the Si substrate, O(1s) and Si(2p) XPS signals

from the native silicon oxide could still be detected. The XPS peak of the Pt(4f) shown in the Fig. 8-3. The binding energies of Pt ($4f_{7/2}$) and ($4f_{5/2}$) electrons were 71.4 and 74.7 eV, respectively, which are in good agreement with pure bulk platinum [171]. No XPS signal associated with oxidized Pt species (such as Pt^{2+} and Pt^{4+}) and chlorine from the Pt precursor were observed, suggesting that metallic platinum was likely the only constituent of the nanoflowers synthesized by pulse electrodeposition.

Figure 8-4 (A) shows the transmission electron microscopy (TEM) image of nanopetals, which were mechanically scratched off the Pt nanoflower thin film. A selected-area electron diffraction (SAED) pattern is shown in the inset of the figure. The bright diffraction rings can be indexed as the (111), (200), (220), and (311) lattice planes of the Pt face-centered-cube (FCC) lattice structure. From the TEM image, the Pt nanopetals had a bamboo-leaf like structure, with an averaged length of ~ 300 nm. The high resolution lattice image further reveals that the nanopetal was made up by Pt nanocrystals of a few nanometers in size as shown in Fig. 8-4 (B).



8.4 Electrochemical characteristics

The electroactive surface area of the catalyst was evaluated from charges associated with hydrogen adsorption/desorption on the electrode surface from cyclic voltammograms (CVs) in 1 M H_2SO_4 aqueous solution at a scan rate of 20 mV s^{-1} [172]. Figure 8-5 shows CVs of the 3D Pt nanoflower/Si and the Pt thin film/Si electrodes. In the potential range characteristic of hydrogen electrosorption in the sulfuric acid solution ($-0.4 - 0.0 \text{ V vs. SCE}$), the Pt thin film/Si electrode shows a very weak and featureless broad peak, while two peaks (at ca. -0.22 and -0.02 V vs. SCE) can be clearly observed on the CV curve of the Pt nanoflower/Si electrode. The peak feature in a cyclic voltammogram of Pt in sulfuric acid solutions strongly depends on the crystallographic orientation of the Pt surface. For the Pt(111) surface, the

cyclic voltammogram is characterized by a broad and flat hydrogen electroadsorption peak in the potential range ~ -0.4 V - 0.0 V (vs. SCE) [173]. On the other hand, in the same potential range, the Pt(100) surface gives two distinct hydrogen electroadsorption peaks, and a single peak can be found for the Pt(110) surface in the same potential range. Thus, from the CV curves of Fig. 8-5, we suggest that the (100) and (110) lattice planes prevailed over the (111) plane on the 3D Pt nanoflower surface.

The hydrogen adsorption charge (Q_H) evaluated from Fig. 7-5 is ~ 0.27 mC cm⁻² and ~ 31.17 mC cm⁻² for the Pt thin film/Si and the 3D Pt nanoflower/Si electrodes, respectively. Q_H is usually used to quantify active sites for hydrogen adsorption/desorption on the Pt catalyst. The measured Q_H values show that the active surface area of the 3D Pt nanoflowers/Si electrode is much higher than that of the Pt thin film/Si electrode by a factor of >110 .

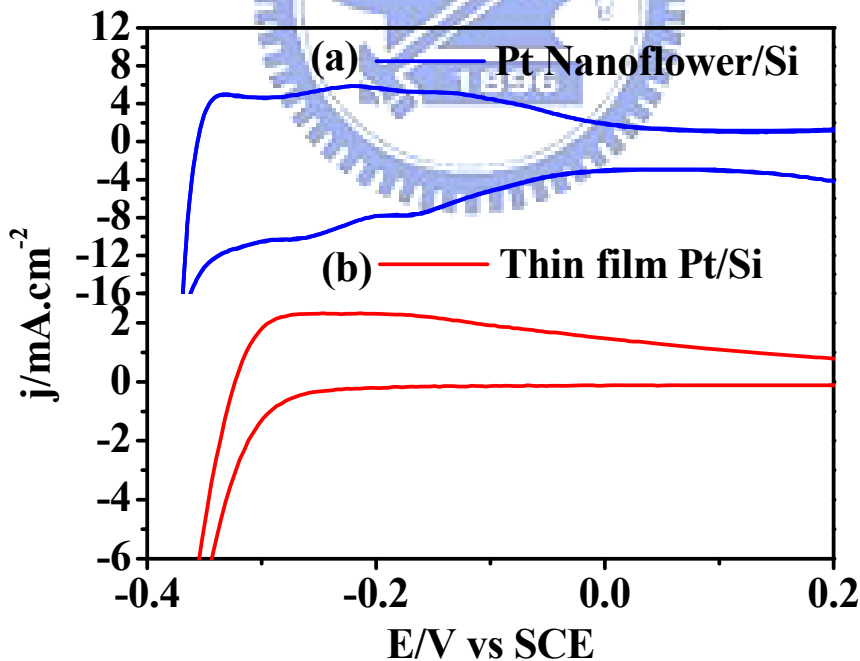


Figure 8-5 shows the CVs of the 3D Pt nanoflower/Si and the Pt thin film /Si electrodes in the 1 M H₂SO₄ solution. The scan rate was 20 mV s⁻¹.

Electrocatalytic activity of the 3D Pt nanoflower/Si and the Pt thin film/Si electrodes toward methanol oxidation reaction (MOR) was studied by cyclic voltammetry in a nitrogen-saturated 1 M CH₃OH/1 M H₂SO₄ solution at a scan rate of 25 mV s⁻¹, and the CV curves are shown in Fig. 8-6. The onset potential for methanol oxidation of the 3D Pt nanoflower catalyst was ~0.38 V, which was ~0.13 V lower than that of the Pt thin film catalyst, indicating faster electrode kinetics [174]. In addition, the oxidation current peak density of the 3D Pt nanoflower catalyst in the forward scan was higher than that of the blanket Pt thin film catalyst. This implies that the 3D Pt nanoflower catalyst has a better electrocatalytic activity toward the MOR compared with the blanket Pt thin film catalyst. In the CV scan, the anodic peak in the reverse scan might be attributed to the removal of CO-like poisoning species formed on the Pt catalyst in the forward scan. The catalyst tolerance against CO adsorption may be estimated by the ratio of the forward current density (I_f) to the reverse anodic peak current density (I_b), (I_f/I_b) [143]. A high I_f/I_b ratio suggests efficient electrooxidation of methanol during the forward scan and less accumulation of residues on the electrodes, whereas a low ratio indicates incomplete electrooxidation of methanol and excessive accumulation of carbonaceous residues on the electrode surface. The (I_f/I_b) ratio of the 3D Pt nanoflower/Si electrode and the Pt thin film/Si electrode are ~2.5 and ~0.93 respectively. This ratio for the 3D Pt nanoflower/Si electrode is ~2.68 times larger than that for the Pt thin film/Si electrode, indicating that the 3D Pt nanoflowers electrode had a higher electrocatalytic activity toward MOR and thus a better CO tolerance.

To study CO tolerance of the 3D Pt nanoflower/Si electrode, CO-stripping CV measurement was carried out. Figure 8-7 shows the CO stripping CV curves of the 3D Pt nanoflower/Si and the Pt thin film/Si electrodes in 1 M H₂SO₄ aqueous solution. For the CO stripping analysis, CO adsorption on the Pt catalyst was conducted by flowing a 10% CO/N₂ gas mixture into the (1 M H₂SO₄) electrolyte for 35 min at 0.1 V (vs. SCE), followed by purging with nitrogen gas for 30 min to remove any residual CO from the solution.

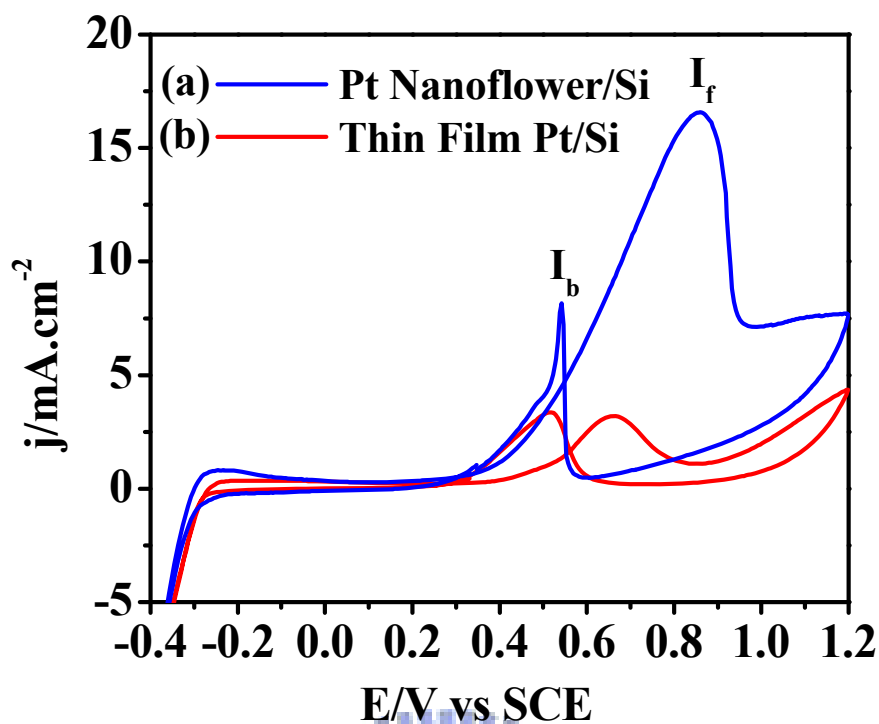


Figure 8-6 shows the CVs of the 3D Pt nanoflower/Si and the Pt thin film /Si electrodes in the 1 M CH₃OH/1 M H₂SO₄ solution. The scan rate was 25 mV s⁻¹.

As shown in Fig. 8-7, during the first cycle, the CV curve was flat in the potential range between -0.3 to 0.3 V indicating that the hydrogen adsorption was suppressed due to the complete coverage of available active Pt sites by CO adspecies. In the first scan, a broad anodic peak appeared between 0.4-0.8 V, which was absent in the subsequent scan, indicating that CO adspecies were effectively oxidized during the first scan. The CO oxidation current peaks of the 3D Pt nanoflower/Si and the thin film Pt/Si electrodes were centered at ~0.58 V and ~0.64 V, respectively. The peak current density of CO electrooxidation on the 3D Pt nanoflower/Si electrode was much larger than that on the Pt thin film electrode, further indicating that the 3D Pt nanoflower/Si electrode had a much larger electroactive surface area.

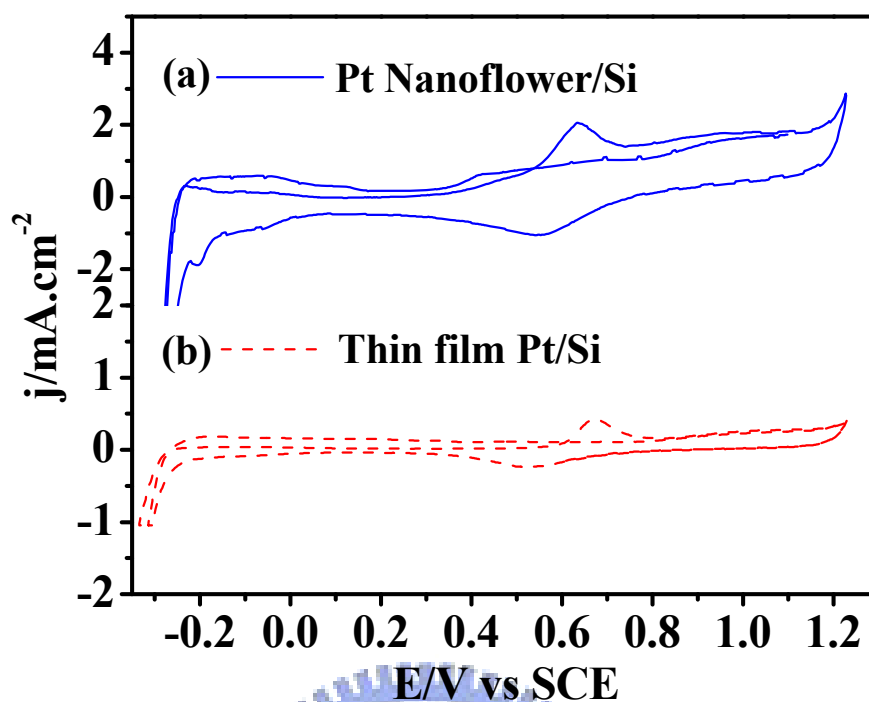


Figure 8-7 shows the CO stripping CVs of the 3D Pt nanoflower/Si and the Pt thin film /Si electrodes in the CO saturated 1 M H_2SO_4 solution. The scan rate was 25 mV s^{-1} .

The above electrochemical analysis results indicate that the 3D Pt nanoflower/Si electrode possessed a much higher electrocatalytic activity towards CO oxidation and MOR compared to the Pt thin film/Si electrode. This may be ascribed to that Pt catalysts on the two electrodes had different preferential surface lattice orientations. It is known that methanol oxidation reaction catalyzed by Pt in acidic aqueous solutions is sensitive to the surface structure of the Pt catalyst [175]. According to previous reports, the electrocatalytic activity of Pt toward MOR in H_2SO_4 aqueous solution increases in the order $\text{Pt}(100) > \text{Pt}(110) > \text{Pt}(111)$ [176]. As discussed above about the hydrogen eletrosorption peaks (Fig. 8-5), the Pt nanoflower/Si electrode had more surface areas with the Pt(100) and Pt(110) lattice orientations than the blanket Pt thin film electrode, of which the catalyst surface was Pt(111) preferentially oriented. Therefore, as shown in Fig. 8-6, a lower onset potential and a much higher current density

were obtained during the forward scan in the methanol oxidation CV measurement for the Pt nanoflower/Si electrode. In addition, the oxidation rate of CO adspecies on Pt also varies with the Pt surface orientation, with the electrocatalytic activity increasing in the order Pt(111) < Pt(110) < Pt(100) [177]. As a result, CO like adspecies on the Pt(100) and (110) surfaces can be oxidized more effectively than on the (111) surface, leaving more active sites for methanol adsorption. The better CO tolerance observed for the Pt nanoflower/Si electrode is likely due to the preferential (100) and (111) surface orientation on the Pt catalyst as well.

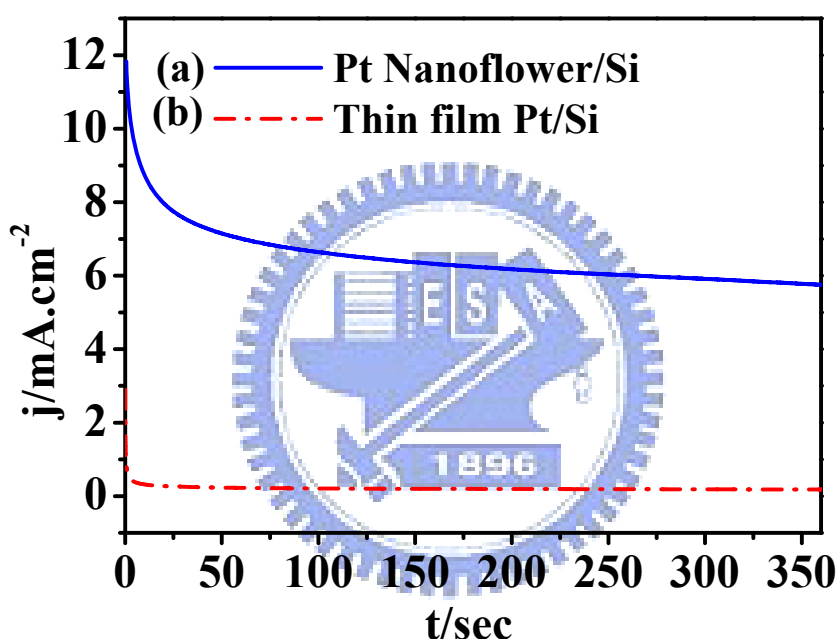


Figure 8-8 shows the chronoamperograms of the 3D Pt nanoflower/Si and the Pt thin film /Si electrodes in the 1 M CH₃OH/1 M H₂SO₄ solution at the polarization potential of 0.4 V.

Chronoamperometry was used to compare the stability of the electrocatalytic activity toward MOR of the 3D Pt nanoflower/Si electrode with that of the Pt thin film/Si electrode. Figure 8-8 shows the chronoamperograms of the two electrodes, which were obtained by measuring the steady-state reaction current density at the electrode potential of 0.4 V. After the polarization of 350 s, the current density of methanol electrooxidation for the Pt thin

film/Si and the 3D Pt nanoflower/Si electrode were $\sim 0.02 \text{ mA/cm}^2$, and $\sim 6.2 \text{ mA/cm}^2$, respectively. Compared with the blanket Pt thin film, the 3D Pt nanoflower/Si had a much higher activity with a steady-state currents density about 310 times that of the thin film Pt/Si electrode. These results are very consistent with the CV measurements shown in Figs. 8-5, 8-6, and 8-7.

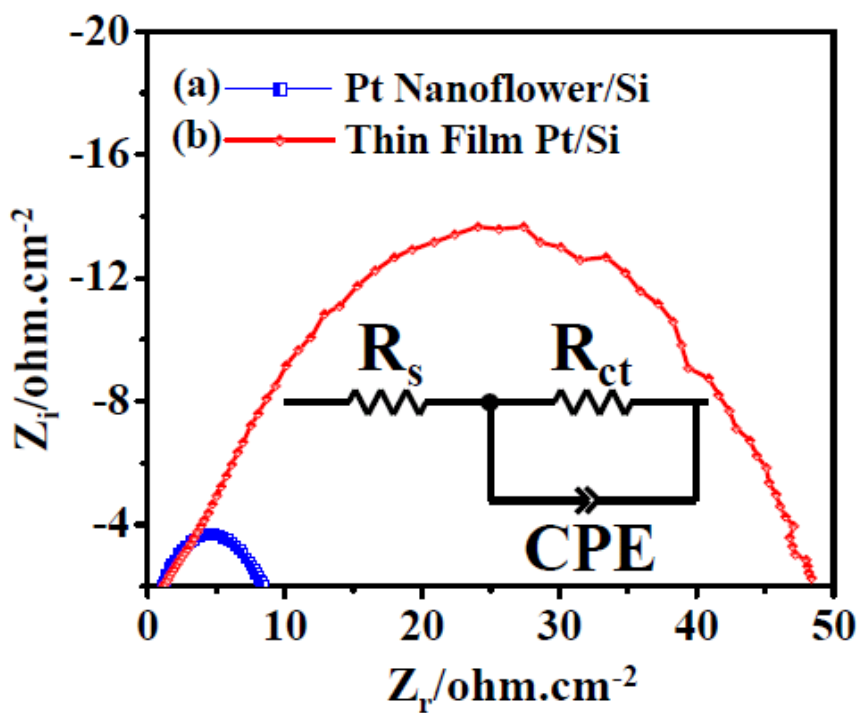


Figure 8-9 shows the Nyquist plot of electrochemical impedance spectra (EIS) of the 3D Pt nanoflowers and the Pt thin film catalysts in the 1 M CH_3OH + 1 M H_2SO_4 solution at the potential of 0.3 V. Insert is the equivalent circuit model used to fit the impedance spectra.

Electrochemical impedance spectroscopy (EIS) is a powerful analysis technique, which can provide a wealth of information on the charge transfer resistance and capacitance. The Nyquist plots of the 3D Pt nanoflower/Si and the Pt thin film/Si electrodes at the potential of 0.3 V in 1 M $\text{CH}_3\text{OH}/1 \text{ M H}_2\text{SO}_4$ aqueous solution are shown in Fig. 8-9, where Z_r and Z_i are the real and imaginary parts of the impedance. The thin lines are fitting results according to

the equivalent circuit shown as the inset in Fig. 8-9. R_s denote the solution resistance, R_{ct} represents the charge-transfer resistance and CPE is defined as the constant phase element, which takes into account methanol adsorption and oxidation [142]. As shown in Fig. 8-9, the proposed model fits well to the obtained EIS data points. The charge-transfer resistance at the 3D Pt nanoflower/Si and the Pt thin film/Si electrodes is ~ 9 and $\sim 50 \Omega\text{-cm}^{-2}$, respectively. The very low R_{ct} obtained with the Pt nanoflower/Si electrode suggests that this type of electrode could be suitable for direct methanol fuel cell applications.

8.4 Summary

We have demonstrated a facile and reproducible method to synthesize 3D Pt nanostructures on the silicon substrate at room temperature by potentiostatic pulse plating. The Pt nanostructure is made up of bamboo-leaf like nanopetals, and has a geometric shape of roses. Electrochemical analysis show that the 3D Pt nanoflower had a much larger active surface area than the Pt thin film by a factor of >110 , and were likely preferentially oriented in the (100) and (110) surface planes. Due to the preferential surface orientations and high surface area, the 3D Pt nanoflower catalyst had an excellent electrocatalytic activity toward methanol oxidation and a high CO tolerance as compared with the Pt thin film catalyst.

Chapter 9

Controlled Synthesis and Growth of Perfect Platinum Nanocubes by Fasten Silicon at NTP

9.1 Introduction

Currently, the synthesis and growth mechanism of the shape-controlled Pt nanostructures is fundamentally interesting, and potentially very useful because of their wide range of applications in photocatalytic activity [178], hydrogen production [179], liquid feed fuel cells catalyst [43, 105, 156], surface enhanced Raman scattering [180], fine chemical synthesis [181], reduction of pollutant gases emitted from automobiles and the synthesis of nitric acid, oil cracking [44]. The synthesis of well-controlled sizes, facets and shapes of metal nanoparticles can also effectively influence their optical, electrical, thermal, magnetic, chemical and catalytic properties [44, 47, 182]. Thus, different Pt nanoparticle shapes were synthesized in high yields, such as Pt nanocubes, [42, 183, 184] nanorods, [185] nanotubes, [185] and dendritic nanoparticles [186-188]. Among these shapes, well-controlled Pt nanocubes are particularly interesting due to their high catalytic activity in different catalytic reactions. For instance, Pt nanocubes with the high energy {100} facets are highly active and selective than that of conventional NO catalysts [189]. The oxidation of ammonia, almost exclusively takes place on the Pt {100} plane [190]. Many previous studies have also shown that Pt {100} plane enhanced the catalytic activity for hydrogen oxidation reactions and the oxygen reduction reaction [191, 192]. In the last few years several chemical methods have been developed for the synthesis of Pt nanocubes but most of the chemical methods are either tedious or difficult to controlled, making exceedingly challenging for the researchers to the synthesis of Pt nanocubes.

In this chapter, we describe a new, simple and efficient method for the synthesis and growth of well-dispersed perfect Pt nanocubes, employing a pair of low-resistivity silicon samples at normal temperature and pressure (NTP) in the absence of surfactant, additives and capping materials. Moreover, the perfect Pt nanocubes catalyst shows excellent electrocatalytic activity and better stability toward methanol and ethanol oxidation.

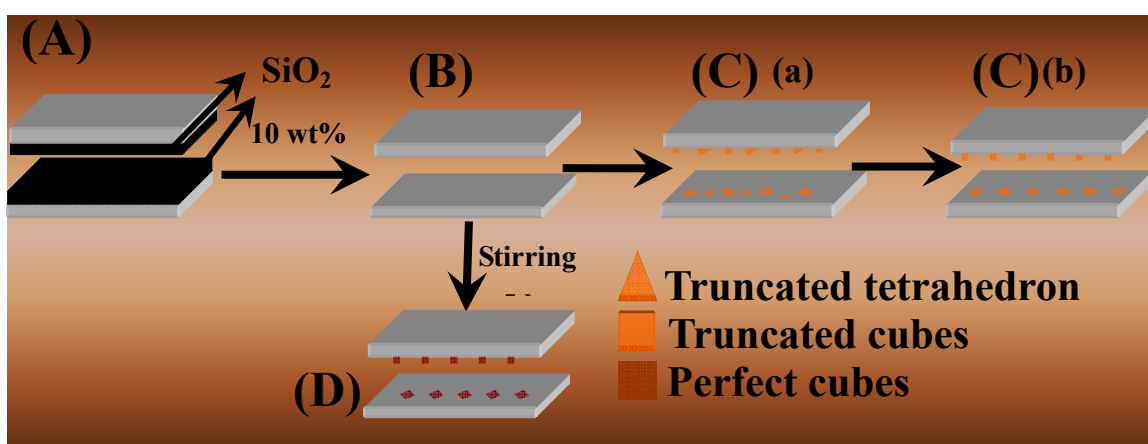


Figure 9-1 shows the synthesis procedure of Pt nanostructures: (A) the Si-wafer is cut into $1.5 \times 2 \text{ cm}^2$ samples, (B) dipped into HF aqueous solution for 5 minutes in order to remove any native oxide layer on the Si samples, (C) then the polished side of cut two identical piece of the Si-wafer was fasten together and dipped into stirred $1 \text{ M H}_2\text{PtCl}_6 + 1 \text{ M H}_2\text{SO}_4$ aqueous solutions, {after stirring for (a) 3 hr and (b) 5 hr to form the truncated (cubes + tetrahedron) and truncated cubes respectively}, (D) furthermore, the perfect Pt nanocubes produced by mixing 1 M HCl into $1 \text{ M H}_2\text{PtCl}_6 + 1 \text{ M H}_2\text{SO}_4$ aqueous solutions (vigorous stirring for 5 hr).

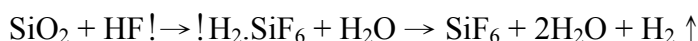
9.2 Synthesis process of Pt nanostructures

The synthesis process of Pt nanocubes is illustrated in Fig. 9-1. The *p*-type 4-inch Si wafer of low resistivity ($0.002 \text{ } \Omega\text{-cm}$) was used as the substrate. A pair of Si wafer was dipped in 10 wt. % HF aqueous solution for 5 min. in order to remove any native SiO₂ layer from the silicon sample. Two kinds of aqueous solution were prepared for the synthesis of Pt

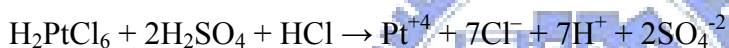
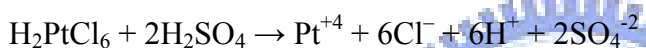
nanostructures, (a) 2 M H₂PtCl₆ + 1 M H₂SO₄, and (b) 2 M H₂PtCl₆ + 1 M H₂SO₄ + 1 M HCl. Aqueous solution (a) was prepared by constant stirring for 3 h and 5 h at normal temperature and pressure (NTP). Solution (b) was prepared by constant stirring for 5 h at NTP. Subsequently, for the typical synthesis of truncated tetrahedron, truncated nanocubes, truncated nanorods and perfect nanocubes, a pair of silicon sample was fasten together and dipped in a solution of (a) and solution (b).

The possible chemical reaction in the solution may be summarized as follows:

First half cell reactions



Second half cell reactions



The two half-cell electrochemical reactions may be involved in the Pt deposition process. After Pt nanostructures deposition, the sample was washed by DI water to removed contamination from the sample surface and dried in the ambient. All solutions were prepared from Milli-Q water (~18 MΩ) and analytical grade chemicals.

9.3 Structural characterization of Pt nanostructures

The synthesis and growth of Pt nanocubes were affected by physical and chemical conditions. For example, stirring time of the solution and dipping time of FS sample affects physically while the concentration of H₂PtCl₆, H₂SO₄ and HCl affect chemically. In our perfect Pt nanocubes synthesis, we optimized the concentration of HCl, H₂PtCl₆, H₂SO₄ and stirring time of aqueous solution.

Scanning electron microscopy (SEM) study was carried out to investigate the surface morphology of the synthesized Pt nanostructures onto the surface of fasten silicon (FS)

sample. Figure 9-2 (A to C), show the plane-view SEM images of the truncated Pt (cubes + tetrahedron), obtained by varying the dipping times 10 min, 13 min and 15 min respectively, in the aqueous solution of 2 M H_2PtCl_6 + 1 M H_2SO_4 at NTP. As shown in Fig. 9-2 (A to C), the Pt nanostructure sized is increased as the dipping time of FS sample increased. The Fig. 9-2 (C) clearly indicates that the products were mainly composed of the truncated Pt nanocubes with the truncated Pt tetrahedron, after 15 min dipping in an aqueous solution. The morphology of the truncated Pt tetrahedron nanostructures was further investigated by transmission electron microscopy (TEM) and high-resolution transmission electron microscopy (HRTEM). Figure 9-2 (D) shows a bright field TEM image of individual truncated Pt tetrahedron nanostructure. It can be clearly seen that the truncated Pt tetrahedron had a size smaller than $\sim 80\text{nm}$. Figure 9-2 (E) shows a HRTEM image taken from the corner of truncated Pt tetrahedron. The measured atomic spacing from the HRTEM image (Fig. 9-2 (E)) is $\sim 0.23\text{ nm}$, which corresponds to the set of $\{111\}$ lattice plane. The above results confirm the truncated Pt tetrahedron grew along the $\{111\}$ direction. The inset of Fig. 9-2 (E) shows the fast Fourier transform (FFT) image and confirmed that the truncated Pt tetrahedron is single crystalline.

In addition, to investigate the influence of stirred time on the shape of the Pt nanostructure, 5 h stirred solution (2 M H_2PtCl_6 + 1 M H_2SO_4) was used for the experiment. Figure 9-3 (A to C), display the plane-view SEM images of the truncated Pt nanocubes deposited on the FS sample in 13, 15, and 20 min, respectively. The obtained Pt nanostructured were 98% truncated nanocubes (Fig. 9-3, A and B). In the case of 20 min dipping, the nanostructure obtained was well dispersed truncated Pt nanocubes with nanorods (Fig. 9-3 (C)). The morphological evolution of the nanocubes indicates that the larger nanocubes or nanorods originated because of the surface energy minimization and Ostwald ripening (Fig. 9-5).

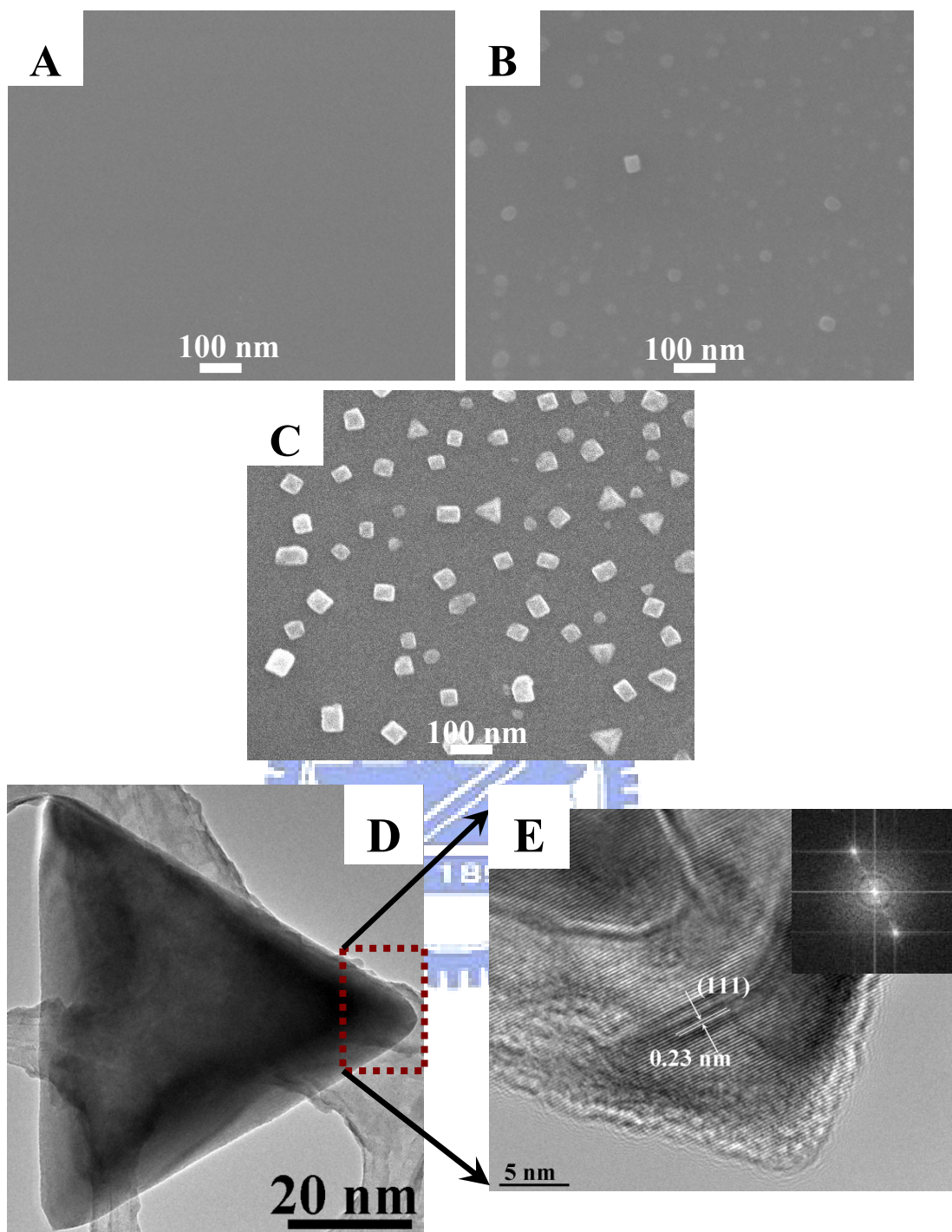


Figure 9-2 shows the SEM images of truncated Pt (cubes + tetrahedron) deposited on the FS sample at NTP for (A) 10, (B) 13, and (C) 15 min; (solution stirring for 3 hr). (D) Low-magnification TEM image of individual truncated Pt tetrahedron synthesized with the FS sample. (E) High-resolution TEM lattice image of the square region in single truncated Pt tetrahedron. The d -spacing between the fringes was ~ 0.23 nm, which was identified $\{111\}$ plane of Pt; the inset shows the FFT of the lattice image gives the optical diffractogram, which clearly shows the presence of $\{111\}$ plane.

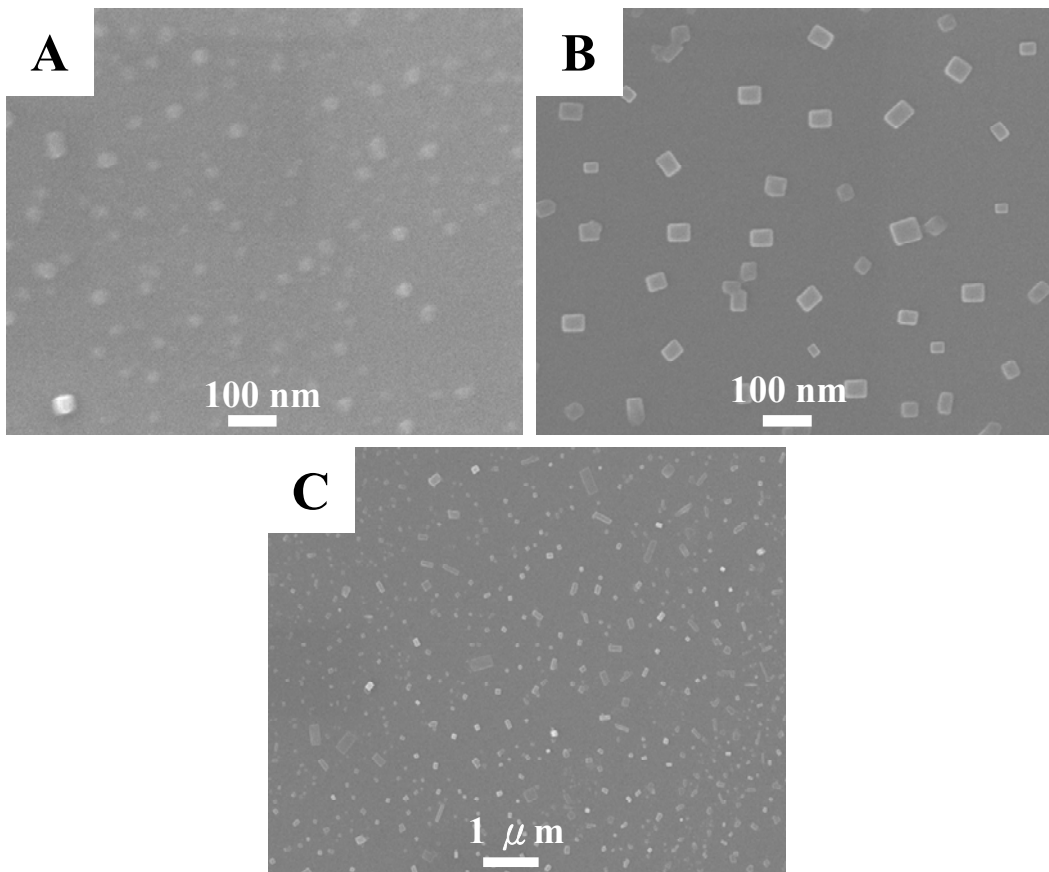


Figure 9-3 shows the SEM images of truncated Pt nanocubes deposited on the FS sample at NTP for (A) 13, (B) 15, and (C) 20 min; (solution stirring for 5 hr).

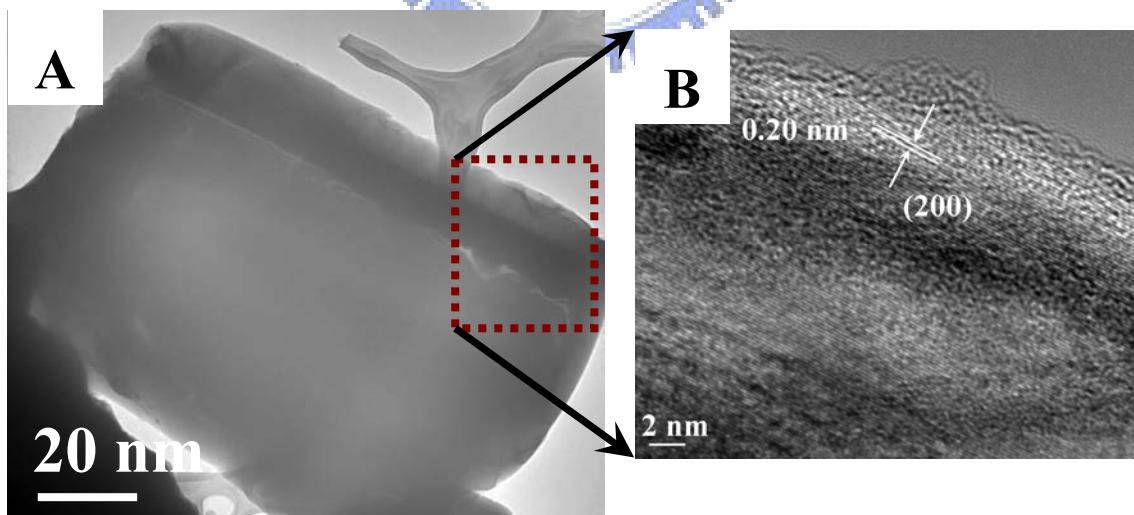


Figure 9-4 (A) Low-magnification TEM image of individual truncated Pt nanocubes and (B) High-resolution TEM lattice image of the square region in single truncated Pt nanocubes. The d -spacing between the fringes was ~ 0.20 nm, which was identified $\{200\}$ plane of Pt.

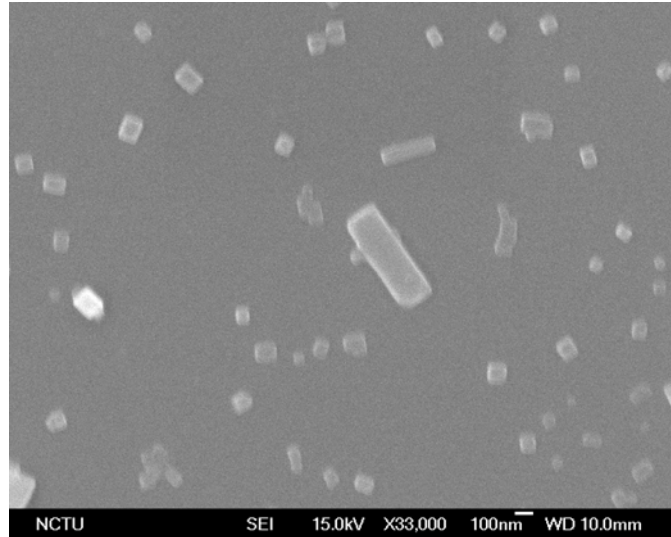


Figure 9-5 Shows the SEM images of Pt nanostructures formed by immersing FS samples into aqueous solutions of H_2SO_4 - H_2PtCl_6 for 20 min at NTP (stirring time = 5 h). The images clearly show the presence of Pt nanocrystals with cube and rod shapes. The mechanism of rod growth is Ostwald ripening, define as the dissolution of the fine particles and their redeposition on large particles [198]. According to the well-known Gibbs–Thomson law, there is energy difference between large particles and small particles result in vanishing of smaller particles and formation of longer nanorods with the reaction in progress [199].

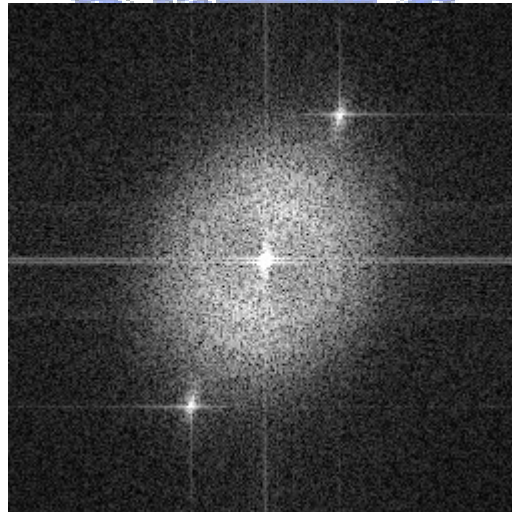


Figure 9-6 FFT image obtained from fig. 3E. The FFT pattern exhibits only a diffraction spots, revealing a good single-crystal property.

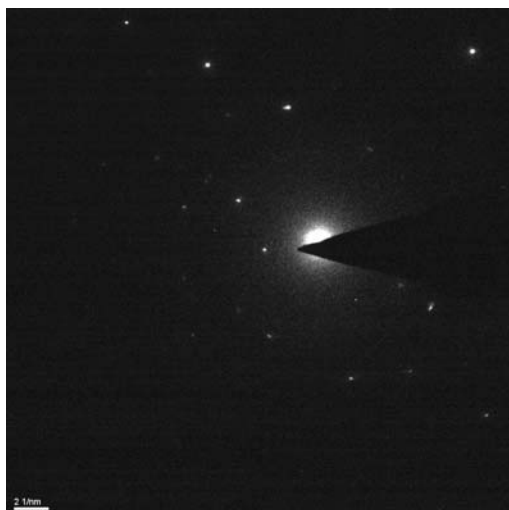


Figure 9-7 SAED image obtained from fig. 9-5 (A). SAED pattern also confirms the single crystal structure of the truncated Pt nanocubes.

As shown in Fig. 9-2 (C), when the stirring time was 3 h, a large number of the truncated Pt tetrahedron with truncated Pt nanocubes was formed. While on the other hand, when the stirring time was 5 h, only the Pt nanocubes were observed (Fig. 9-3(B)). This might be partly due to the homogeneity of aqueous solution controlled by stirred time. Figure 9-4 (A and B), shows the representative TEM and HRTEM-images of an individual truncated Pt nanocube. The size of truncated Pt nanocubes from TEM image was estimated ~80nm. The HRTEM image in Fig. 9-4 (B) recorded from a Fig. 9-3 (A) shows continuous lattice fringes with lattice spacing of ~0.20 nm, which corresponds to the {100} planes of Pt. The FFT image (Fig. 9-6) indicates that each truncated Pt nanocubes was a single crystalline. Furthermore, the selected area electron diffraction (SAED) pattern obtained by directing the electron beam perpendicular to individual truncated Pt nanocube (Fig. 9-7). The SAED pattern also confirmed that the truncated Pt nanocube was a single crystalline.

However, for the synthesis and growth of perfect Pt nanocubes, we used the same aqueous solution (2 M H_2PtCl_6 + 1 M H_2SO_4) mixed with 1 M HCl. To explore the synthesis and growth mechanism of the Pt nanocubes, again time-dependent experiments were carried out at NTP.

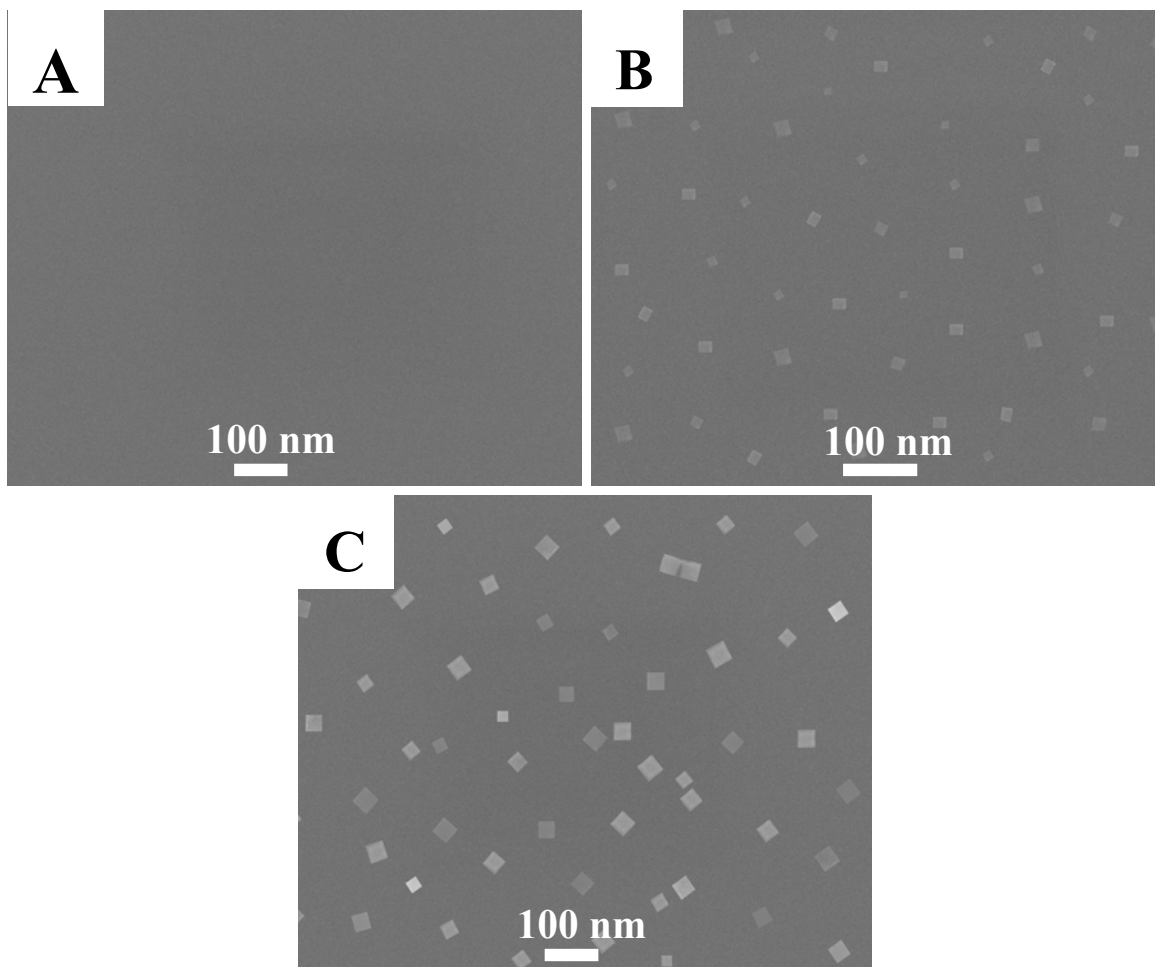


Figure 9-8 shows the SEM images of perfect Pt nanocubes deposited on the FS sample at NTP for (A) 10, (B) 13, and (C) 15 min; (solution stirring for 5 hr).

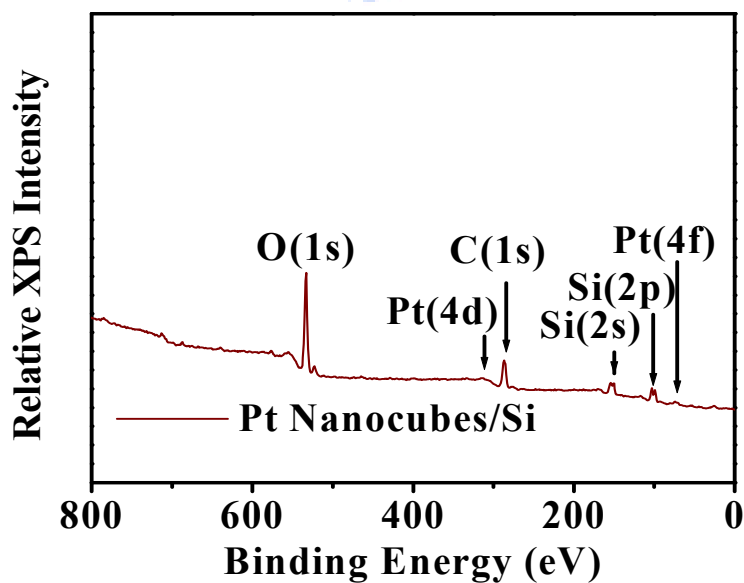


Figure 9-9 shows the typical XPS survey spectrum of perfect Pt nanocubes deposited on the surface of FS sample. XPS clearly show the presence of Pt nanocube catalyst.

A series of SEM images taken at different dipping times (t) are presented in (Fig. 9-8, A to C). As shown in Fig. 9-8 (A), at $t = 10$ min, the Pt nanocubes were very hard to observed by SEM image. When $t = 13$ min, the Pt nanocubes were start to develop on the both side of the FS sample (Fig. 9-8 (B)). At $t = 15$ min, the Pt nanocubes were start to grow in all directions, which is considered as evidence for a growth of Pt nanocubes (Fig. 9-8 (C)).

The x-ray photoelectron spectroscopy (XPS) data were collected to further confirm the deposition of perfect Pt nanocubes onto the silicon. Figure 9-9 shows an XPS survey analysis of a Pt nanocube deposited onto a FS sample. Two distinct Pt ($4f_{7/2}$) and Pt ($4f_{5/2}$) peaks at 71.0 and 74.2 eV, respectively, were clearly observed (Fig. 9-10). These are typical values for zero valent Pt, [193] indicating that the perfect Pt nanocubes were zero valence. Furthermore, no obvious shoulders at higher binding energies, representing Pt^{2+} and Pt^{4+} , were found, and no peak of chlorine from the Pt precursor was

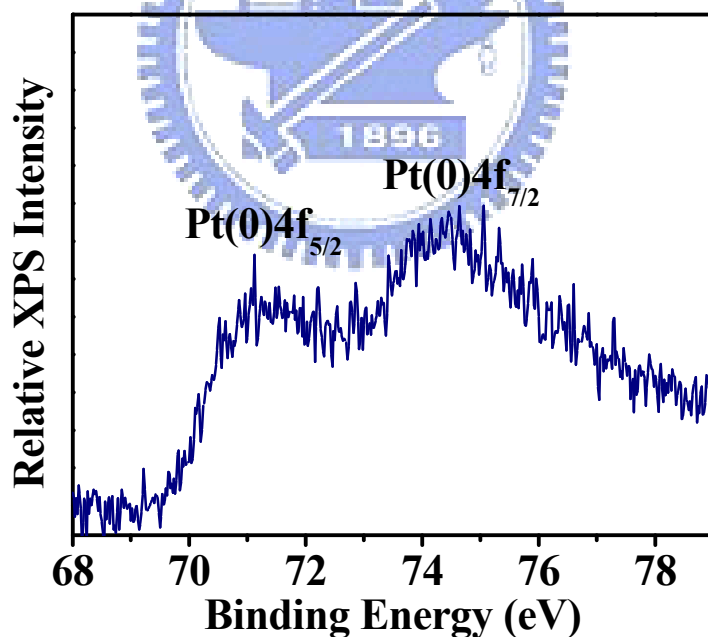


Figure 9-10 XPS deconvoluted Pt(4f) doublet of perfect Pt nanocubes deposited on the surface of FS sample. The peaks can be attributed to Pt($4f_{7/2}$) and Pt($4f_{5/2}$) of metallic Pt, respectively.

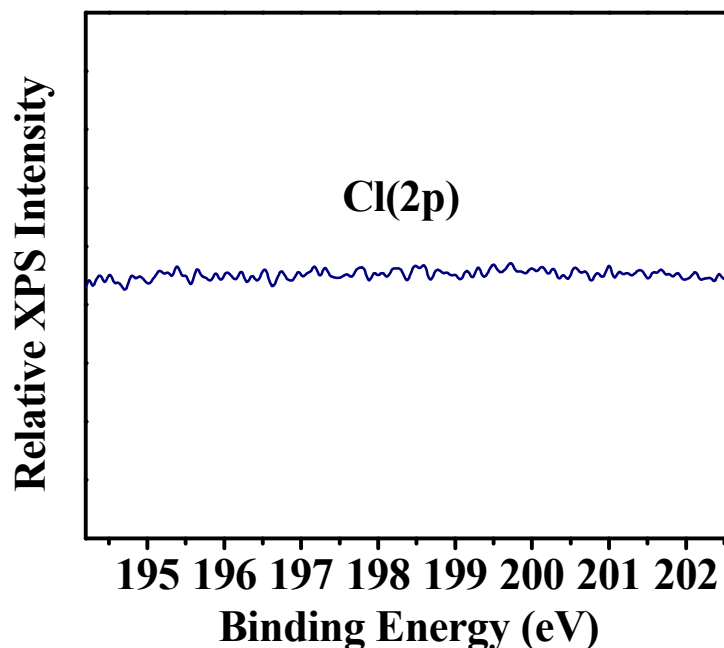


Figure 9-11 Cl(2p) XPS narrow scan spectra of the perfect Pt nanocubes deposited on the surface of FS sample. This figure clearly shows the complete absence of chloride ion at the perfect Pt nanocubes.

detected by XPS (Fig. 9-11). From XPS analyses, we conclude that the Pt nanocubes were composed of metallic platinum. The morphology of the perfect Pt nanocubes was further investigated by HRTEM. Figure 9-12 (A) shows the HRTEM images of individual Pt nanocube. From the TEM image, it is clear that the Pt nanocubes have perfect shape, with a sized of ~10 nm. Figure 9-12 (B) displays a representative electron diffraction pattern recorded by directing the electron beam perpendicular to the {100} facets of an individual nanocube and confirms that the platinum particles are single crystals. The FFT of the atomic lattice fringing apparent in the inset of Fig. 9-12 (A), corresponding to the perfect individual platinum nanocube, further demonstrating the single crystallinity of the nanocubes. All of these results also confirm the perfect platinum nanocubes grew along the {100} direction. We also found that the nanocubes are formed as a result of fast growth along {111} directions, and the surfaces of the final nanocubes correspond to {100} planes [194].

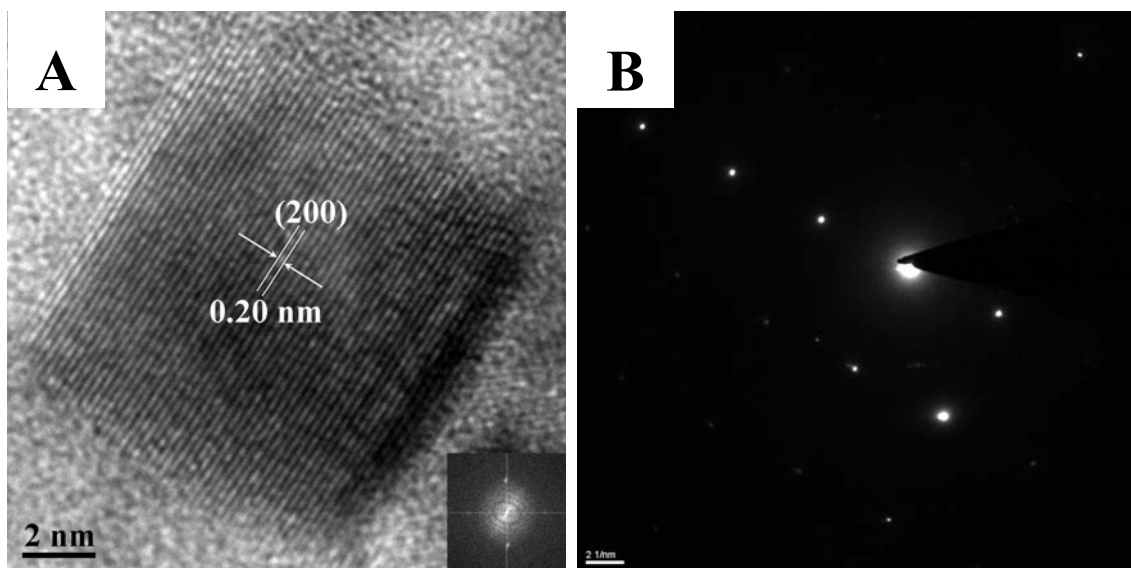


Figure 9-12 (A) High-resolution TEM image of individual perfect Pt nanocube. The d -spacing between the fringes was ~ 0.20 nm, which was identified $\{200\}$ plane of Pt; the inset shows the FFT of the lattice image gives the optical diffractogram, which clearly shows the presence of $\{200\}$ plane and (B) Corresponding SAED pattern, showing the single crystal structure of the perfect Pt nanocubes.

To compare the geometrical structure of Pt, kinetic effect and the effect of fasten pair silicon, Pt nanoparticles were also deposited on the single Si substrate by electroless deposition. The etched native SiO_2 layer from the Si sample dipped in a solution of 1 M HCl + 1 M H_2PtCl_6 + 1 M H_2SO_4 , prepared by vigorously stirred for 5 h at NTP. Figure 9-13 (A and B) shows the growth of Pt nanoparticles on the single silicon substrate with an immersion time of 6 h. The deposition times were too longer so the kinetic factor has negligible effect on the synthesis and growth of Pt nanoparticles. The Fig. 9-13 (A and B) also conformed that the Pt nanoparticles were nanospherical. This is might be due to low charge density on the single silicon wafer compare to that of a pair of FS sample when they were in very close proximity in aqueous solution. The charges were developed on the silicon surface by etching with HF.

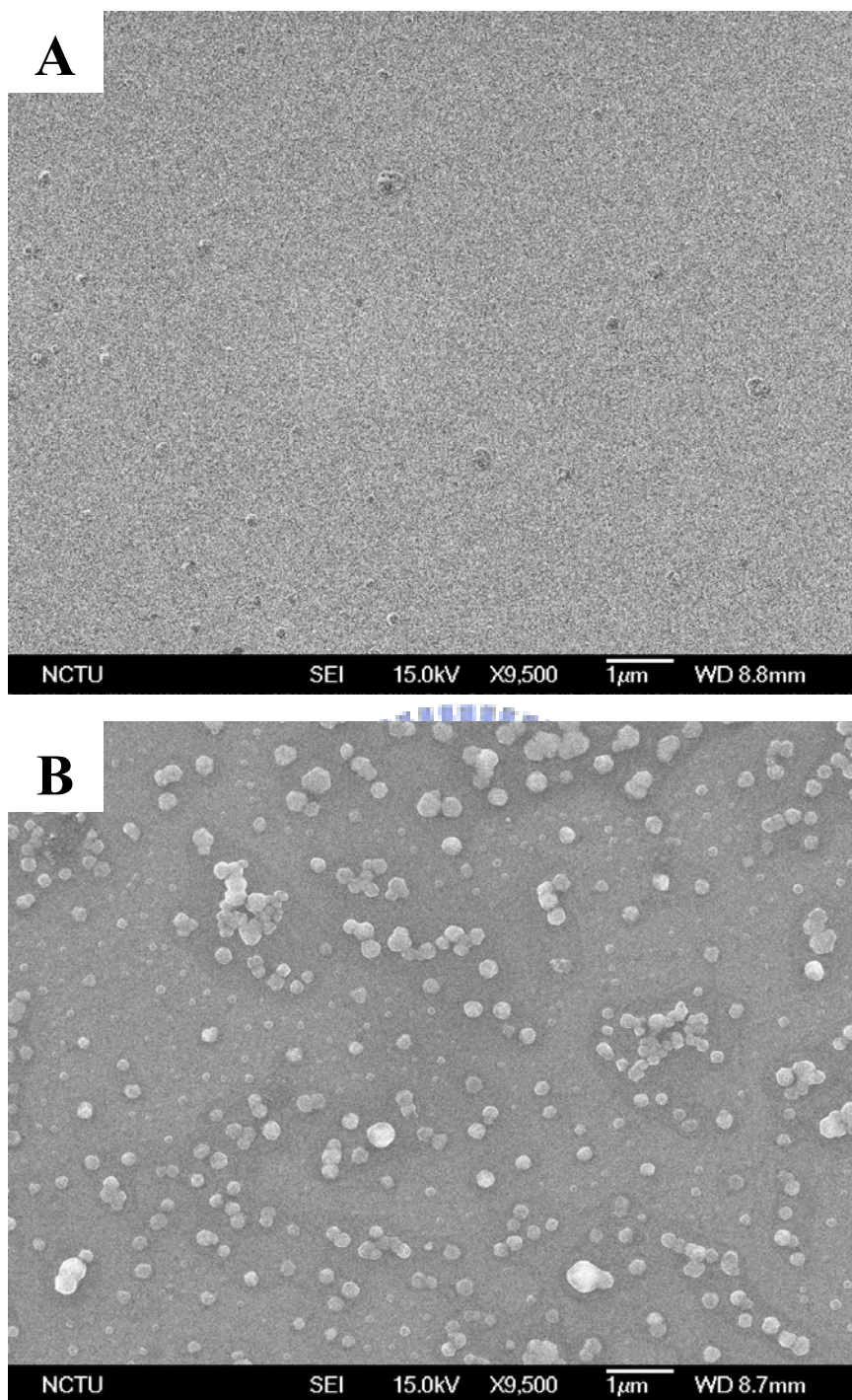


Figure 9-13 Plane views SEM images of the silicon after electroless deposition of Pt for 6 h. Compositions of solutions were (A) 2 M H_2PtCl_6 + 1 M H_2SO_4 + 1 HCl and (B) 2 M H_2PtCl_6 + 1 M H_2SO_4 . Both the aqueous solution was stirred continuously for 5 h.

The idea originated from Faraday's first law of electrolysis, the mass of a substance altered at an electrode during electrolysis is directly proportional to the quantity of charge transferred at that electrode. The negative potential and the electrostatic force of interaction developed in between two silicon wafers is comparatively higher than that of the single silicon wafer resulting in fast deposition of Pt nanoparticles on the FS sample.

From the results above, we can conclude that the separate role played by 1 M HCl and 1 M H₂SO₄ aqueous solution. In the absence of HCl in aqueous solution of 2 M H₂PtCl₆ + 1 M H₂SO₄, SO₄⁻ ions from H₂SO₄ have a negligible effect on the synthesis of Pt nanocubes because the concentration of H₂SO₄ was lower compared to the concentration of H₂PtCl₆. Figure 9-3 (C) shows a typical SEM image of the truncated Pt nanocubes at t = 20 min, that consisted a mixture of small Pt cubes and rods. This observation implies that sulfuric acid alone is able to induce the etching and dissolution of seeds and thus channel the product into truncated single crystal nanocubes. The potential reasons for occurrence a truncated shape may be due to enough H⁺ and Cl⁻ ions needed for etching and dissolutions. On the other hand, when HCl was added to the aqueous solution of 2 M H₂PtCl₆ + 1 M H₂SO₄, Cl⁻ ions from HCl should have a strong effects on the synthesis of perfect Pt nanocubes because chloride ions can reduce the surface energies of the {100} facets of the seeds by binding strongly to them, thus leading to the formation of perfect nanocubes [195, 196]. The presence of Cl⁻ ions in the aqueous solution stabilize the single crystal and therefore Cl⁻ ions also can prevent the nanocubes from aggregating and sedimentation by providing electrostatic repulsion forces between the Pt nanocubes [197]. Moreover, we found that the morphology and dimensions of Pt nanocubes were greatly influenced by concentration and homogeneity of solution, dipping time and substrate surface energy. For example, the number of Pt nanocubes formed is proportional to the concentration of solution. With increase in the homogeneity of solution > 98% cubes formed were sharp edge. Prolong dipping times of FS sample results in formation of cubes with rods. Surface energy accelerates the deposition of Pt cubes as evident in FS

surface.

9.4 Electrocatalytic activity

The synthesis of sizes, shapes and structure control of platinum nanoparticles allows us to study surface dependent properties such as catalytic activity. Figure 9-15 (A and B) shows cyclic voltammograms for methanol and ethanol oxidation on the perfect Pt nanocubes (Fig. 9-8 (B)), the truncated Pt nanocubes (Fig. 9-3 (B)), the truncated Pt (cubes + tetrahedron) (Fig. 9-2 (C)), and the spherical Pt nanoparticles (Fig. 9-14) at NTP. As shown in Fig. 9-15 (A and B), the onset potential for methanol and ethanol electrooxidation of the perfect Pt nanocubes was lower than that of truncated Pt nanocubes, truncated Pt (cubes + tetrahedron), and spherical Pt nanoparticles, indicating the faster electrodes kinetics [174]. In addition, the perfect Pt nanocubes show a peak current density is higher than that of truncated Pt nanocubes, truncated Pt (cubes + tetrahedron), and spherical Pt nanoparticles.

Furthermore, the chronoamperometry study was carried out to determine the stability of electrocatalytic activity toward methanol oxidation reduction and ethanol oxidation reduction. Figure 9-15 (C and D) shows the chronoamperograms of the four electrodes, which were obtained by measuring the steady-state reaction current density at the electrode potential of 0.4 V. After the polarization of 200 s, the current density of methanol electrooxidation for the perfect Pt nanocubes, the truncated Pt nanocubes, the truncated Pt (cubes + tetrahedron), and the spherical Pt nanoparticles are ~ 1.45 , ~ 0.29 , ~ 0.18 , and ~ 0.16 mA/cm² respectively. The perfect Pt nanocubes indicate much higher activity than the truncated Pt nanocubes, truncated Pt (cubes + tetrahedron), and spherical Pt nanoparticles, whose steady-state currents are over five times, eight times and nine times higher than that of truncated Pt nanocubes, truncated Pt (cubes + tetrahedron), and spherical Pt nanoparticles, respectively.

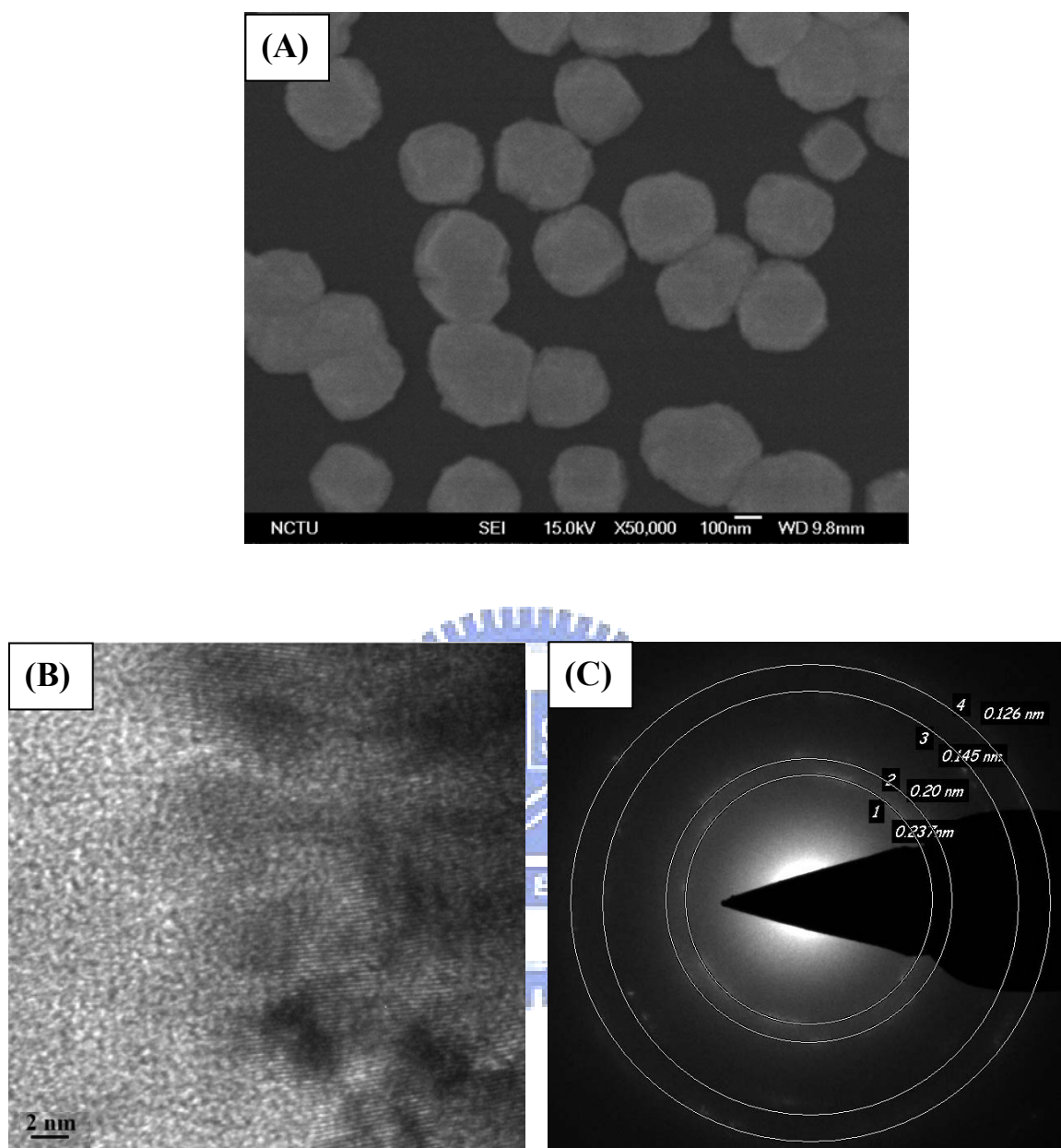


Figure 9-14 (A) FE-SEM image of the electrodeposited polycrystalline Pt nanosphere on silicon substrate. (B) HRTEM image recorded from a region at the edge of a sphere, showing that the surfaces are covered by Pt nanoparticles of a few nanometers in size, and the Pt nanocrystallites dominated by $\{111\}$ -type exposed surface. (C) SAED pattern showing that the formed nanoparticles are polycrystalline. The as-labelled diffraction rings 1–4 correspond to $\{111\}$, $\{200\}$, $\{220\}$, and $\{311\}$ reflections, respectively, all of which reveal the fcc crystal structure.

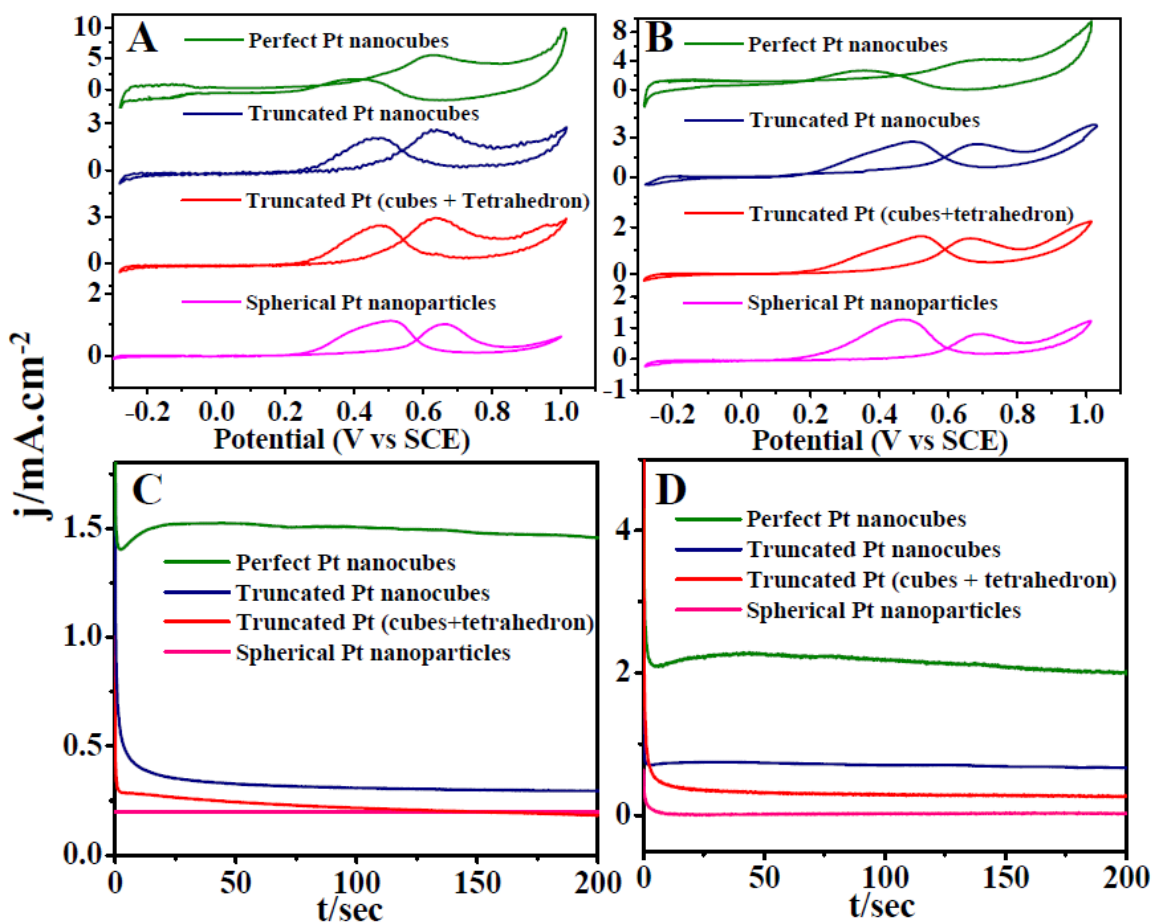


Figure 9-15 Comparison of catalytic activity and stability of the Pt nanoshapes. (A) and (B) Cyclic voltammograms for (a) perfect Pt nanocubes, (b) truncated Pt nanocubes, (c) truncated Pt (cubes + tetrahedron), and (d) spherical Pt nanoparticles were obtained at a scan rate 25 mVs^{-1} in $1 \text{ M H}_2\text{SO}_4 + 1 \text{ M methanol}$ and $1 \text{ M H}_2\text{SO}_4 + 1 \text{ M ethanol}$ respectively. (C) and (D) Chronoamperometric curves for (a) perfect Pt nanocubes, (b) truncated Pt nanocubes, (c) truncated Pt (cubes + tetrahedron), and (d) spherical Pt nanoparticles were recorded at 0.40 V in oxygen free $1 \text{ M H}_2\text{SO}_4 + 1 \text{ M methanol}$ and $1 \text{ M H}_2\text{SO}_4 + 1 \text{ M ethanol}$, respectively. The results demonstrate that the perfect Pt nanocube electrode showed excellent catalytic activity and stability for oxidation of methanol and ethanol.

On the other hand, the current density of ethanol electrooxidation for the perfect Pt nanocubes, the truncated Pt nanocubes, the truncated Pt (cubes + tetrahedron), and the spherical Pt nanoparticles are ~ 2.01 , ~ 0.66 , ~ 0.27 , and $\sim 0.016 \text{ mA cm}^{-2}$ respectively. Again, the perfect Pt nanocubes indicate much higher activity than that of truncated Pt nanocubes,

truncated Pt (cubes + tetrahedron), and spherical Pt nanoparticles, whose steady-state currents are over three times, seven times, and 125 times higher than that of truncated Pt nanocubes, truncated Pt (cubes + tetrahedron), and spherical Pt nanoparticles, respectively. The above result implies that the perfect Pt nanocubes have a better electrocatalytic toward both methanol and ethanol electrooxidation, which are promising alternative fuels for liquid feed fuel cells.

9.5 Summary

We have demonstrated, for the first time simple and efficient method for the synthesis and growth of well-dispersed perfect platinum nanocubes, employing a pair of low-resistivity fasten silicon (FS) sample at normal temperature and pressure (NTP) in the absence of surfactant, additives and capping materials and so on. The perfect Pt nanocubes deposited on the FS sample exhibited an excellent catalytic activity and stability for methanol and ethanol oxidation, as compared to the truncated Pt nanocubes, the truncated Pt (cubes + tetrahedron) and the spherical Pt nanoparticles. We believed that these new and simple concepts will open the door for the synthesis of the well-controlled shape, sizes and facets of not only Pt nanocubes but also other metal as well (for instance silver, gold and copper), for optical, electrical, thermal, magnetic and catalytic applications. Study of the mechanism behind the origin of perfect Pt nanocubes from fasten silicon wafer is still underway in our laboratory.

Chapter 10

Conclusions and Future Works

10.1 Conclusions

In this study, ordered arrays of nanostructures including Pt/Si nanocone, and Pt/ α -C/Si nanocone are successfully fabricated by using the nanoporous anodic aluminum oxide (AAO) membrane as a template. Well-ordered nanomask arrays of TiO_x are constructed by anodizing the Al/TiN bilayered films. The TiO_x nanodots were then used as the nanomask for etching the TiN layer and the underlying layer in an inductively coupled plasma reactive-ion-etch (ICP-RIE) system. On the other hand, the Pt nanostructured materials were synthesized by direct electrochemical deposition and fasten silicon. In addition, we have synthesized the nanoporous graphitic carbon (g-C), which was utilized as a support for Pt-Ru alloy catalysts. The electro-catalytic characteristics of the nanostructures have been investigated. The primary results of this thesis are summarized as follows:

- (1) We have fabricated well-ordered Si nanocones (SNCs) using AAO templation, and electrodeposited Pt nanoparticles on the SNC arrays by potentiostatic pulse electrodeposition. The pulse electrodeposition led to the formation of well-dispersed Pt nanoparticles on the SNCs. The Pt nanoparticles were predominantly spherical in shape and had a size of < 5 nm. Because of uniform dispersion of Pt nanoparticles and the high surface area, the Pt-SNC electrode exhibited superior electrocatalytic properties toward the methanol electro-oxidation, with the onset potential of 0.08 V (vs. SCE). The catalyst mass activity was several times higher than that of the blanket Pt film/flat Si. Moreover, chronoamperometric analyses and CO stripping cyclic voltammetric (CV) study indicated that the Pt-SNC electrode had a stable electrooxidation activity with a very good CO tolerance. The Si surface oxide surrounding the Pt nanoparticles on the SNCs was

suggested to play a key role in improving the CO tolerance via the bifunctional mechanism.

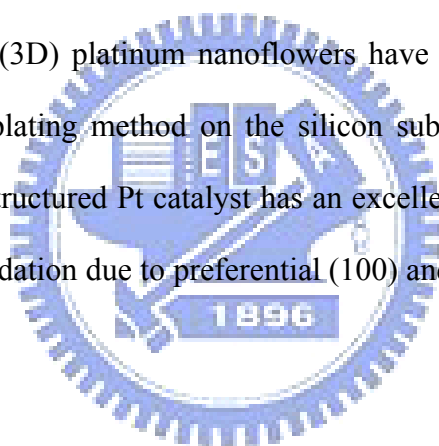
(2) This study pulse-electrodeposited Pt nanoparticles on amorphous carbon coated silicon nanocones (ACNCs) and explored them as the electrocatalyst for methanol oxidation reaction (MOR) and oxygen reduction reaction (ORR) for direct methanol fuel cell applications. The work prepared silicon nanocones on the Si wafer using porous anodic aluminum oxide as the template and then deposited the amorphous carbon layer on the nanocones by microwave plasma chemical vapor deposition. According to Raman scattering and x-ray photoelectron spectroscopies, the surface of the ACNC support is composed of a nanocrystalline graphitic structure, and rich in oxygen containing adspecies. The Pt nanoparticles pulse-electrodeposited on the highly ordered ACNC support dispersed well with a large electrocatalytic surface area. The Pt-ACNC electrode exhibited excellent electrocatalytic activity and stability toward both MOR and ORR. This study suggests the abundant oxygen containing surface species and the nanocrystalline graphitic structure as the two major factors enhancing electrocatalytic performance of Pt catalyst nanoparticles.

(3) A three-dimensional (3D) nanoporous graphitic carbon (g-C) was synthesized by flame of adamantane ($C_{10}H_{16}$), which was utilized as the support for Pt₅₀-Ru₅₀ alloy catalyst. The electrochemical investigations show the Pt₅₀-Ru₅₀ supported on 3D nanoporous g-C have excellent activity towards methanol oxidation, and better CO tolerance due to the presence of Ru nanoparticles, in which Ru was proposed to be able to promote the oxidation of the strongly adsorbed CO on Pt by supplying an oxygen source (Ru-OH_{ad}). Moreover, the presence of 3D nanopores in g-C supports may also contribute to the observed higher current density because of the easy transport of methanol and the

oxidation products in these nanopores.

(4) Two-dimensional (2D) continuous Pt island network was successfully synthesized by pulse-potentiostatic electrodeposition on the flat silicon substrate, and electrochemical investigations confirm that this catalyst structure on the silicon substrate has a better electroactivity toward methanol oxidation than the blanket Pt/Si and the Ru decorated Pt film/Si electrodes. The electrooxidation performance is better than that of the other two electrodes, due to the synergistic effect of the Pt island catalyst and surrounding SiO₂ surface layer.

(5) A three-dimensional (3D) platinum nanoflowers have been successfully synthesized by potentiostatic pulse plating method on the silicon substrate, and electrochemical study shows that the nanostructured Pt catalyst has an excellent electrocatalytic activity toward methanol and CO oxidation due to preferential (100) and (110) surface orientations on the Pt nanoflowers.



(6) A well-controlled perfect Pt nanocube in high yields has been synthesized by reduction of hexachloroplatinic acid in the presence of hydrochloric acid and sulfuric acid, employing a pair of fastens silicon (FS) wafer at normal temperature and pressure. The additive charges in between the interface of the FS surface results in high charge density, facilitates fast deposition of Pt. The surface energy, H₂SO₄, HCl, stirring time determines the geometrical shapes of the Pt nanoparticles. The perfect Pt nanocubes were single crystals with the high energy {100} facets. And the perfect Pt nanocubes show enhanced catalytic activity for equivalent Pt surface areas for electrooxidation of liquid feed fuels such as methanol and ethanol. Moreover, these perfect Pt nanocubes are technologically important due to the strong correlation with the optical, electrical, thermal, magnetic and

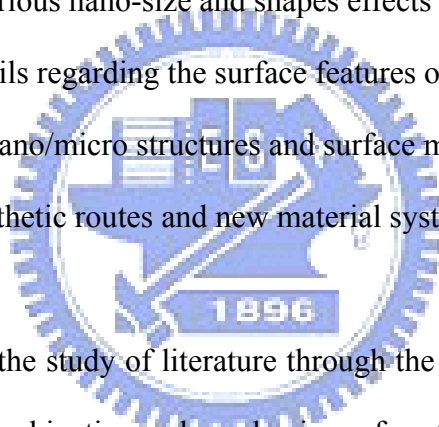
catalytic properties.



10.2 Future Works

We have shown that the nanostructured materials will play a more and more important role in improving the performance of electrochemical energy conversion such as direct methanol fuel cells (DMFCs) because of their high surface area, novel size effects and so on. On one hand, nanomaterials show favorable properties such as enhanced kinetics and activity, which may lead to low-cost and/or high performance energy devices. On the other hand, 'nano' also has disadvantages such as low thermodynamic stability, high side reactions as well as handle problems. The remaining challenges include are highlighted below:

- (1) well understanding various nano-size and shapes effects and developing new theories;
- (2) investigating fine details regarding the surface features of 'nano';
- (3) designing optimized nano/micro structures and surface modifications;
- (4) searching for new synthetic routes and new material systems;



In addition, based on the study of literature through the year 2009, there are several open questions pertaining to the kinetics and mechanism of methanol oxidation in acid medium, which are listed below:

- (1) What is the nature and distribution of the products – on bulk platinum, promoted platinum and technical catalyst – 50/50 Pt/Ru?
- (2) Is it necessary to form a single phase alloy for the best catalytic activity or will a multiphase system or even a mixture work equally well?
- (3) What species are *intermediates* and what is the *poison*?
- (4) Is the oxidation of the poisoning residue brought about by H_2O^* or OH_{ads} ?
- (5) What is the rate determining step – on platinum, on promoted platinum?
- (6) Does the rate determining step change from *poison oxidation* to C-H activation at higher

potentials?

(7) What is the influence of temperature on the mechanism?

Future work aims to solve these challenges from a range of disciplines, and their success will promote the development of next generation green and sustainable energy devices.



References

- [1] X. Ren, P. Zelenay, S. Thomas, J. Davey and S. Gottesfeld, *J. Power Sources*, 86 (2000) 111, “Recent advances in direct methanol fuel cells at Los Alamos National Laboratory”.
- [2] A. S. Arico, P. Bruce, B. Scrosati, J. M. Tarascon and W. Van Schalkwijk, *Nat. Mater.*, 4 (2005) 366, “Nanostructured materials for advanced energy conversion and storage devices”.
- [3] H.P. Liang, H.M. Zhang, J.S. Hu, Y.G. Guo, L.J. Wan and C.L. Bai, *Angew. Chem. Int. Ed.*, 43 (2004) 1540, “Pt hollow nanospheres: facile synthesis and enhanced electrocatalysts”.
- [4] Y.Y. Mu, H.P. Liang, J.S. Hu, L. Jiang and L.J. Wan, *J. Phys. Chem. B*, 109 (2005), 22212. “Controllable Pt nanoparticle deposition on carbon nanotubes as an anode catalyst for direct methanol fuel cells”.
- [5] L.J. Wan, T. Moriyama, M. Ito, H. Uchida and M. Watanabe, *Chem. Commun.*, 1 (2002) 58, “In situ STM imaging of surface dissolution and rearrangement of a Pt–Fe alloy electrocatalyst in electrolyte solution”.
- [6] J. Wang, P. Holt-Hindle, D. MacDonald, D. F. Thomas and A. Chen, *Electrochim. Acta*, 53 (2008) 6944, “Synthesis and electrochemical study of Pt-based nanoporous materials”.
- [7] Y.-G. Guo, J.-S. Hu and L.-J. Wan, *Adv. Mater.*, 20 (2008) 2878, “Nanostructured

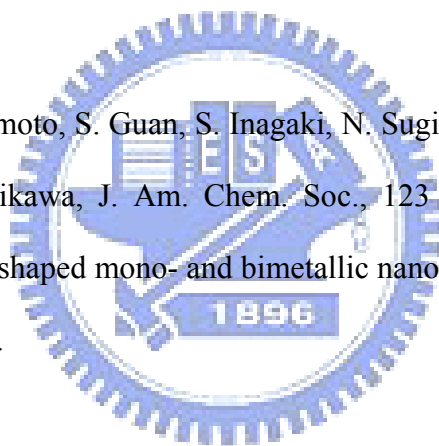
materials for electrochemical energy conversion and storage devices”.

[8] M. T. Bore, T. L. Ward, A. Fukuoka and A. K. Datye, *Catal. Lett.*, 98 (2004) 167, “Synthesis of Pt nanowires inside aerosol derived spherical mesoporous silica particles”.

[9] G. L. Egan, J. Yu, C. H. Kim, S. J. Lee, R. E. Schaak and T. E. Mallouk, *Adv. Mater.*, 12 (2000) 1040, “Nanoscale metal replicas of colloidal crystals”.

[10] H. J. Shin, C. H. Ko and R. Ryoo, *J. Mater. Chem.*, 11 (2001) 260 “Synthesis of platinum networks with nanoscopic periodicity using mesoporous silica as template”.

[11] A. Fukuoka, Y. Sakamoto, S. Guan, S. Inagaki, N. Sugimoto, Y. Fukushima, K. Hirahara, S. Iijima and M. Ichikawa, *J. Am. Chem. Soc.*, 123 (2001) 3373, “Novel templating synthesis of necklace-shaped mono- and bimetallic nanowires in hybrid organic–inorganic mesoporous material”.



[12] W. C. Choi and S. I. Woo, *J. Power Sources*, 124 (2003) 420, “Bimetallic Pt–Ru nanowire network for anode material in a direct-methanol fuel cell”.

[13] K. S. Napolskii, P.J. Barczuk, S. Yu. Vassiliev, A. G. Veresov, G. A. Tsirlina and P.J. Kulesza, *Electrochim. Acta*, 52 (2007) 7910, “Templating of electrodeposited platinum group metals as a tool to control catalytic activity”.

[14] Y. Zhong, C. L. Xu, L.-B. Kong and H.-L. Li, *Appl. Surf. Sci.*, 255 (2008) 3388, “Synthesis and high catalytic properties of mesoporous Pt nanowire array by novel conjunct template method”.

- [15] S. Park, T. D. Chung and H. C. Park, *Anal. Chem.*, 75 (2003) 3046, “Nonenzymatic glucose detection using mesoporous platinum”.
- [16] H. Boo, S. Park, B. Ku, Y. Kim, J. H. Park, H. C. Kim and T. D. Chung, *J. Am. Chem. Soc.*, 126 (2004) 4524, “Ionic strength-controlled virtual area of mesoporous platinum electrode.
- [17] S. A. G. Evans, J. M. Elliott, L. M. Andrews, P. N. Bartlett, P. J. Doyle and G. Denuault, *Anal. Chem.*, 74 (2002) 1322, “Detection of hydrogen peroxide at mesoporous platinum microelectrodes”.
- [18] J. M. Elliott, G. S. Attard, P. N. Bartlett, N. R. B. Coleman, D. A. S. Merckel and J. R. Owen, *Chem. Mater.*, 11 (1999) 3602, “Nanostructured platinum (H₁-ePt) films: effects of electrodeposition conditions on film properties”
- [19] Z. Liu, J. Y. Lee, M. Han, W. Chen and L. M. Gan, *J. Mater. Chem.*, 12 (2002) 2453, “Synthesis and characterization of PtRu/C catalysts from microemulsions and emulsions”.
- [20] G. S. Attard, P. N. Bartlett, N. R. B. Coleman, J. M. Elliott, J. R. Owen and J. H. Wang, *Science*, 278 (1997) 838, “Crystalline phases mesoporous platinum films from lyotropic liquid”.
- [21] W. Yu, W. Tu and H. Liu, *Langmuir*, 15 (1999) 6, “Synthesis of nanoscale platinum colloids by microwave dielectric heating”.
- [22] K. Okitsu, H. Bandow, Y. Maeda and Y. Nagata, *Chem. Mater.*, 8 (1996) 315,

“Sonochemical preparation of ultrafine palladium particles”.

[23] K. Okitsu, A. Yue, S. Tanabe and H. Matsumoto, *Chem. Mater.*, 12 (2000) 3006, “Sonochemical preparation and catalytic behavior of highly dispersed palladium nanoparticles on alumina”.

[24] Trevor L. Knutson, Matthew L. Bollinger and William H. Smyrl, *J. Electrochem. Soc.*, 155 (2008) F17, “Mesoporous microspheres of Pt and Pt/Ru formed by electrodeposition: characterization of high surface area”.

[25] J. Y. Kim, Z. G. Yang, C. Chang, T. I. Valdez, S. R. Narayanan and P. N. Kumta, *J. Electrochem. Soc.*, 150 (2003) A1421, “A sol-gel-based approach to synthesize high-surface-area Pt-Ru catalysts as anodes for DMFCs”

[26] J. Jiang and A. Kucernak, *Chem. Mater.*, 16 (2004) 1362, “Mesoporous microspheres composed of PtRu alloy”.

[27] L. Carrette, K. A. Friedrich and U. Stimming, *Chem. Phys. Chem.*, 1 (2000) 162, *Fuel cells: principles, types, fuels, and applications*.

[28] L. J. M. J. Blomen and M. N. Mugerwa, Plenum Press, (1993) 19-485, “Fuel cell systems”.

[29] X. Li, *International J. Global Energy Issues*, 17 (2002) 68, “Fuel cells - the environmentally friendly energy converter and power generator”.

[30] G.G. Scherer, Solid State Ionics, 94 (1997) 249, “Interfacial aspects in the development of polymer electrolyte fuel cells”.

[31] S. Gilman, J. Phys. Chem., 68 (1964) 70, “Anodic oxidation of methanol”.

[32] P. Shiller and A. B. Anderson, J. Electroanal. Chem., 339 (1992) 201, “Molecular orbital study of methanol oxidation on Pt(III) surfaces”.

[33] A. Wieckowski, J. Electroanal. Chem., 78 (1977) 229, “Complex formation during oxidation of methanol”.

[34] J. O'M. Bockris and H. Wroblowa, J. Electroanal. Chem., 7 (1964) 428, “Electrooxidation of methanol”.

[35] A. S. Arico, S. Srinivasan and V. Antonucci, Fuel Cells, 1 (2001) 133, “DMFC: from fundamental aspects to technological developments”.

[36] J. T. Wang, S. Wasmus and R.F. Savinell, J. Electrochem. Soc., 143 (1996) 1233, “Real time mass spectroscopic study of the methanol crossover in a DMFC”.

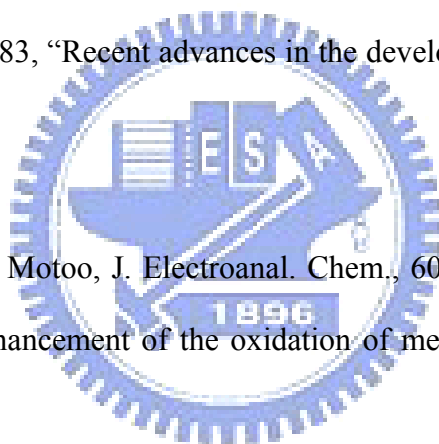
[37] R. Parsons and T. Vandernoot, J. Electroanal. Chem., 257 (1988) 9, “The oxidation of small organic molecules. A survey of recent fuel cell related research”.

[38] A. Hamnett, Catal. Today, 38 (1997) 445, “Mechanism and electrocatalysis in the direct methanol fuel cell”.

- [39] Z. Liu, L. M. Gan, L. Hong, W. Chen and J. Y. Lee, *J. Power Sources*, 139 (2005) 73, “Carbon-supported Pt nanoparticles as catalysts for proton exchange membrane fuel cells”.
- [40] E. P. Lee, Z. Peng, D. M. Cate, H. Yang, C. T. Campbell and Y. Xia, *J. Am. Chem. Soc.*, 129 (2007) 10634, “Growing Pt nanowires as a densely packed array on metal gauze”.
- [41] E. P. Lee, Z. Peng, W. Chen, S. Chen, H. Yang, and Y. Xia, *ACS Nano*, 2 (2008) 2167, “Electrocatalytic properties of Pt nanowires supported on Pt and W gauzes”.
- [42] C. Wang, H. Daimon, Y. Lee, J. Kim and S. Sun, *J. Am. Chem. Soc.*, 129 (2007) 6974, “Synthesis of monodisperse Pt nanocubes and their enhanced catalysis for oxygen reduction”.
- [43] J. N. Tiwari, F. M. Pan and K. L. Lin, *New J. Chem.*, 33 (2009) 1482, “Facile approach to the synthesis of 3D platinum nanoflowers and their electrochemical characteristics”.
- [44] J. Chen, T. Herricks and Y. Xia, *Angew. Chem. Int. Ed.*, 44 (2005) 2589 “Polyol synthesis of platinum nanostructures: control of morphology through the manipulation of reduction kinetics”.
- [45] K. Yamada, K. Miyazaki, S. Koji, Y. Okumura and M. Shibata, *J. Power Sources*, 180 (2008) 181, “Catalytic performance of Pt film with dendritic structure for PEFC”.
- [46] Y. Bi and G. Lu, *Electrochem. Commun.*, 11 (2009) 45, “Control growth of uniform platinum nanotubes and their catalytic properties for methanol electrooxidation”.

- [47] N. Tian, Z. Y. Zhou, S. G. Sun, Y. Ding and Z. L. Wang, *Science*, 316 (2007) 732, “Synthesis of tetrahedral platinum nanocrystals with high-index facets and high electro-oxidation activity”.
- [48] Y. S. Hu, Y. G. Guo, W. Sigle, S. Hore, P. Balaya and J. Maier, *Nat. Mater.* 5 (2006) 713, “Electrochemical lithiation synthesis of nanoporous materials with superior catalytic and capacitive activity”.
- [49] S. Wasmus and A. Kuver, *J. Electroanalytical Chem.*, 461 (1999) 14, “Methanol oxidation and direct methanol fuel cells: a selective review”.
- [50] E. Antolini, J. R. C. Salgado and E. R. Gonzalez, *Appl. Catal. B*, 63 (2006) 137, “The methanol oxidation reaction on platinum alloys with the first row transition metals, The case of Pt–Co and –Ni alloy electrocatalysts for DMFCs: a short review”.
- [51] K. Sundmacher, T. Schultz, S. Zhou, K. Schott, M. Ginkel and E. D. Gilles, *Chem. Eng. Sci.*, 56 (2001) 333, “Dynamics of the direct methanol fuel cell (DMFC): experiments and model-based analysis”.
- [52] E. Antolini, J. R. C. Salgado and E. R. Gonzalez, *J. Electroanal. Chem.*, 580 (2005) 145, “Carbon supported Pt₇₅M₂₅ (M = Co, Ni) alloys as anode and cathode electrocatalysts for direct methanol fuel cells”.
- [53] H. Liu, C. Song, L. Zhang, J. Zhang, H. Wang and D. P. Wilkinson, *J. Power Sources*, 155 (2006) 95, “A review of anode catalysis in the direct methanol fuel cell”.

- [54] N.M. Marković and P.N. Ross Jr., *Surf. Sci. Rep.*, 45 (2002) 117, “Surface science studied of model fuel cell electrocatalysts”.
- [55] U. B. Demirci, *J. Power Sources*, 173 (2007) 11, “Theoretical means for searching bimetallic alloys as anode electrocatalysts for direct liquid-feed fuel cells”.
- [56] B. Hammer and J. K. Nørskov, *Adv. Catal.*, 45 (2000) 71, “Theoretical surface science and catalysis—calculations and concepts”.
- [57] C. Lamy, A. Lima, V. LeRhun, F. Delime, C. Coutanceau and J.M. Léger, *J. Power Sources*, 105 (2002) 283, “Recent advances in the development of direct alcohol fuel cells (DAFCs).”
- [58] M. Watanabe and S. Motoo, *J. Electroanal. Chem.*, 60 (1975) 267, “Electrocatalysis by ad-atoms: Part II. Enhancement of the oxidation of methanol on platinum by ruthenium ad-atoms”.
- [59] M. Watanabe and S. Motoo, *J. Electroanal. Chem.*, 60 (1975) 275, “Electrocatalysis by ad-atoms: Part III. Enhancement of the oxidation of carbon monoxide on platinum by ruthenium ad-atoms”.
- [60] J. C. Bertolini, *Appl. Catal. A*, 191 (2000) 15, “Surface stress and chemical reactivity of Pt and Pd overlayers”.
- [61] J. H. Choi, K. W. Park, I. S. Park, W. H. Nam and Y. E. Sung, *Electrochim. Acta*, 50 (2004) 787, “Methanol electro-oxidation and direct methanol fuel cell using Pt/Rh and



Pt/Ru/Rh alloy catalysts”.

[62] J. H. Choi, K. J. Jeong, Y. Dong, J. Han, T. H. Lim, J. S. Lee and Y. E. Sung, *J. Power Sources*, 163 (2006) 71, “Electro-oxidation of methanol and formic acid on PtRu and PtAu for direct liquid fuel cells”.

[63] A. Ruban, B. Hammer, P. Stoltze, H. L. Skriver and J. K. Nørskov, *J. Mol. Catal. A*, 115 (1997) 421, “Surface electronic structure and reactivity of transition and noble metals”.

[64] B. Hammer and J.K. Nørskov, *Adv. Catal.*, 45 (2000) 71, “Theoretical surface science and catalysis-calculations and concepts”.

[65] J. Greeley, J. K. Nørskov and M. Maurikakis, *Annu. Rev. Phys. Chem.*, 53 (2002) 319, “Electronic structure and catalysis on metal surfaces”.

[66] B. Gurau, R. Viswanathan, R. Liu, T.J. Lafrenz, K.L. Ley, E.S. Smotkin, E. Reddington, A. Sapienza, B.C. Chan, T.E. Mallouk and S. Sarangapani, *J. Phys. Chem. B*, 102 (1998) 9997, “Structural and electrochemical characterization of binary, ternary, and quaternary platinum alloy catalysts for methanol electro-oxidation”.

[67] P. Sivakumar and V. Tricoli, *Electrochem. Solid-State Lett.*, 9 (2006) A167, “Pt-Ru-Ir nanoparticles prepared by vapor deposition as a very efficient anode catalyst for methanol fuel cells”.

[68] P. Piela, C. Eickes, E. Brosha, F. Garzon and P. Zelenay, *J. Electrochem. Soc.*, 151 (2004) A2053, “Ruthenium crossover in direct methanol fuel cell with Pt-Ru black anode”.

- [69] S. F. Zheng, J. S. Hu, L. S. Zhong, L. J. Wan and W. G. Song, *J. Phys. Chem. C.*, 111 (2007) 11174, “In situ one-step method for preparing carbon nanotubes and Pt composite catalysts and their performance for methanol oxidation”.
- [70] M.S. Chandrasekar and M. Pushpavanam, *Electrochim. Acta*, 53 (2008) 3313, “Pulse and pulse reverse plating—conceptual, advantages and applications”.
- [71] J. C. Puipe, N. Ibl, H. Angerer and H. J. Schenk, *Oberfläche Surf.*, 20 (1979) 77, “Electrodeposition by current impulses”.
- [72] M. Ghaemi and L. Binder, *J. Power Sources*, 111 (2002) 248, “Effects of direct and pulse current on electrodeposition of manganese dioxide”.
- [73] A. Marlot, P. Kern and D. Landolt, *Electrochim. Acta*, 48 (2002) 29, “Pulse plating of Ni-Mo alloys from Ni-rich electrolytes”.
- [74] K.M. Yin, S.L. Jan and C.C. Lee, *Surf. Coat. Technol.*, 88 (1997) 219, “Current pulse with reverse plating of nickel-iron alloys in a sulphate bath”.
- [75] T. Houga, A. Yamada and Y. Ueda, *J. Jpn. Inst. Met.*, 64 (2000) 739, “Resistivity and magnetism of Co/Cu films produced by computer controlled pulse electrodeposition”.
- [76] Y. Ueda, N. Hataya and H. Zaman, *J. Magn. Magn. Mater.*, 156 (1996) 350, “Magnetoresistance effect of Co/Cu multilayer film produced by electrodeposition method”.

- [77] H.Y. Cheh, *J. Electrochem. Soc.*, 118 (1971) 1132, “The limiting rate of deposition by P-R plating”.
- [78] S. Toshev and I. Markov. *Electrochim. Acta*, 12 (1967) 281, “Electrolytic nucleation of cadmium”.
- [79] S. H. Joo, S. J. Choi, I. Oh, J. Kwak, Z. Liu, O. Terasaki and R. Ryoo, *Nature*, 412 (2001) 169, “Ordered nanoporous arrays of carbon supporting high dispersions of platinum nanoparticles”.
- [80] B. Rajesh, K. R. Thampi, J.-M. Bonard, A. J. McEvoy, N. Xanthopoulos, H. J. Mathieu and B. Viswanathan, *J. Power Sources*, 133 (2004) 155, “Pt particles supported on conducting polymeric nanocones as electro-catalysts for methanol oxidation”.
- [81] Y. Lin and X. Cui, *Langmuir*, 21 (2005) 11474, “PtRu/Carbon nanotube nanocomposite synthesized in supercritical fluid: a novel electrocatalyst for direct methanol fuel cells”.
- [82] W. Li, X. Wang, Z. Chen, M. Waje and Y. Yan, *J. Phys. Chem. B*, 110 (2006) 15353, “Pt–Ru supported on double-walled carbon nanotubes as high-performance anode catalysts for direct methanol fuel cells”.
- [83] C. Zhou, H. Wang, F. Peng, J. Liang, H. Yu and J. Yang, *Langmuir*, (2009) DOI: 10.1021/la900250w, “MnO₂/CNT supported Pt and PtRu nanocatalysts for direct methanol fuel cells”.

[84] T. Hyeon, S. Han, Y-E. Sung, K. W. Park and Y. W. Kim, *Angew. Chem. Int. Ed.*, 42 (2003) 4352, “High-performance direct methanol fuel cell electrodes using solid-phase-synthesized carbon nanocoils”.

[85] S. Shanmugam and A. Gedanken, *Small*, 3 (2007) 1189, “Carbon-coated anatase TiO₂ nanocomposite as a high-performance electrocatalyst support”.

[86] P. L. Chen, C. T. Kuo, T. G. Tsai, B. W. Wu, C. C. Hsu and F. M. Pan, *Appl. Phys. Lett.*, 82 (2003) 2796, “Self-organized titanium oxide nanodot arrays by electrochemical anodization”.

[87] T. M. Chen, F. M. Pan, J. Y. Hung, L. Chang, S. C. Wu and C. F. Chen, *J. Electrochem. Soc.*, 154 (2007) D215, “Amorphous carbon coated silicon nanotips fabricated by MPCVD using anodic aluminum oxide as the template”.

[88] I. Lee, K.-Y. Chan and D.L. Phillips, *Appl. Surf. Sci.*, 136 (1998) 321, “Growth of electrodeposited platinum nanocrystals studied by atomic force microscopy”.

[89] G. C. Morris and R. Vanderveen, *J. Appl. Surf. Sci.*, 92 (1996) 630, “Solar cells from thin films prepared by periodic pulse electrodeposition”.

[90] J. W. Guo, T. S. Zhao, J. Prabhuram, R. Chen and C. W. Wong, *Electrochim. Acta*, 51 (2005) 754, “Preparation and characterization of a PtRu/C nanocatalyst for direct methanol fuel cells”.

[91] C. T. Hable and M. S. Wrighton, *Langmuir*, 7 (1991) 1305, “Electrocatalytic oxidation of

methanol by assemblies of platinum/tin catalyst particles in a conducting polyaniline matrix”.

[92] M. J. Gonzalez, C. T. Hable and M. S. Wrighton, *J. Phys. Chem. B*, 102 (1998) 9881, “Electrocatalytic oxidation of small carbohydrate fuels at Pt–Sn modified electrodes”.

[93] M. J. Gonzalez, C. H. Peters and M. S. Wrighton, *J. Phys. Chem. B*, 105 (2001) 5470, “Pt–Sn microfabricated surfaces as catalysts for organic electro-oxidation”.

[94] C. T. Hable and M. S. Wrighton, *Langmuir*, 9 (1993) 3284, “Electrocatalytic oxidation of methanol and ethanol: a comparison of platinum-tin and platinum-ruthenium catalyst particles in a conducting polyaniline matrix”.

[95] B. Liu, J. H. Chen, X. X. Zhong, K. Z. Cui, H. H. Zhou and Y. F. Kuang, *J. Colloid Interface Sci.*, 307 (2007) 139, “Preparation and electrocatalytic properties of Pt–SiO₂ nanocatalysts for ethanol electrooxidation”.

[96] F. Su, J. Zeng, X. Bao, Y. Yu, J. Y. Lee and X. S. Zhao, *Chem. Mater.*, 17 (2005) 3960, “Preparation and characterization of highly ordered graphitic mesoporous carbon as a Pt catalyst support for direct methanol fuel cells”.

[97] Y. Li, L. Tang and J. Li, *Electrochem. Comm.*, 11 (2009) 846, “Preparation and electrochemical performance for methanol oxidation of Pt/graphene nanocomposites”.

[98] F. Rodriguez-Reinoso, *Carbon*, 36 (1998) 159, “The role of carbon materials in heterogeneous catalysis”.

- [99] F. Coloma, A. Sepulveda-Escribano and J. L.G. Fierro, *Langmuir*, 10 (1994) 750
“Preparation of platinum supported on pregraphitized carbon blacks”.
- [100] Y. Y. Shao, G. P. Yin and Y. Z. Gao, *J. Power Sources*, 171 (2007) 558, “Understanding and approaches for the durability issues of Pt-based catalysts for PEM fuel cell”.
- [101] X. W. Yu and S. Y. Ye, *J. Power Sources*, 172 (2007) 145, “Recent advances in activity and durability enhancement of Pt/C catalytic cathode in PEMFC: Part II: Degradation mechanism and durability enhancement of carbon supported platinum catalyst”.
- [102] J. Zeng, F. Su, J. Y. Lee, W. Zhou and X. S. Zhao, *Carbon*, 44 (2006) 1713, “Methanol oxidation activities of Pt nanoparticles supported on microporous carbon with and without a graphitic shell”.
- [103] W. Xu, X. Zhou, C. Liu, W. Xing and T. Lu, *Electrochem. Comm.*, 9 (2007) 1002, “The real role of carbon in Pt/C catalysts for oxygen reduction reaction”.
- [104] W. Chen, Q. Xin, G. Sun, Q. Wang, Q. Mao and H. Su, *J. Power Sources*, 180 (2008) 199, “The effect of carbon support treatment on the stability of Pt/C electrocatalysts”.
- [105] J. N. Tiwari, T.-M. Chen, F. M. Pan and K.-L. Lin, *J. Power Sources*, 182 (2008) 510, “Ordered silicon nanocones as a highly efficient platinum catalyst support for direct methanol fuel cells”.
- [106] T. L. Barr and M. Yin, *J. Vac. Sci. Technol. A*, 10 (1992) 2788, “Concerted x-ray

photoelectron spectroscopy study of the character of select carbonaceous materials”.

[107] S. Biniak, G. Szymanski, J. Siedlewski and A. Swiatkowski, *Carbon*, 35 (1997) 1799, “The characterization of activated carbons with oxygen and nitrogen surface groups”.

[108] E. A. Hoffmann, T. Kortvelyesia, E. Wiluszb, L. S. Korugic-Karaszc, F. E. Karaszcz and Z. A. Feketea, *J. Mol. Struct. Theochem.*, 725 (2005) 5, “Relation between C1s XPS binding energy and calculated partial charge of carbon atoms in polymers”.

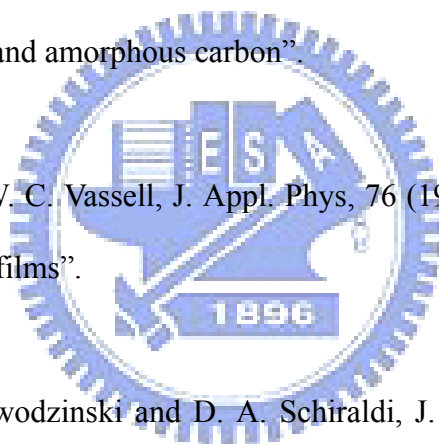
[109] A. C. Ferrari and J. Robertson, *Phys. Rev. B*, 61 (2000) 14095, “Interpretation of Raman spectra of disordered and amorphous carbon”.

[110] M. A. Tamor and W. C. Vassell, *J. Appl. Phys*, 76 (1994) 3823, “Raman fingerprinting of amorphous carbon films”.

[111] A. Guha, T. A. Zawodzinski and D. A. Schiraldi, *J. Power Sources*, 172 (2007) 530, “Evaluation of electrochemical performance for surface-modified carbons as catalyst support in polymer electrolyte membrane (PEM) fuel cells”.

[112] A. Pozio, M. De Francesco, A. Cemmi, F. Cardellini and L. Giorgi, *J. Power Sources*, 105 (2002) 13, “Comparison of high surface Pt/C catalysts by cyclic voltammetry”.

[113] P. J. Ferreira, G. J. la O', Y. Shao-Horn, D. Morgan, R. Makharia, S. Kocha and H. A. Gasteiger, *J. Electrochem. Soc.*, 152 (2005) A2256, “Instability of Pt/C electrocatalysts in proton exchange membrane fuel cells”.



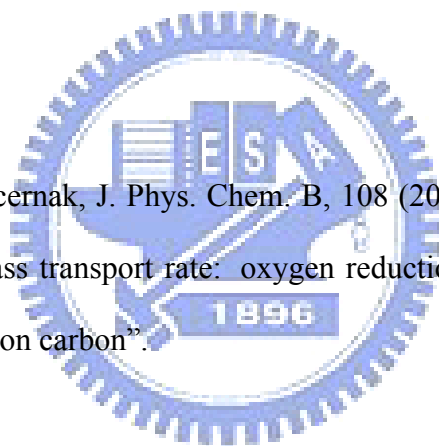
- [114] R. M. Darling and J. P. Meyers, *J. Electrochem. Soc.*, 150 (2003) A1523, “Kinetic model of platinum dissolution in PEMFCs”.
- [115] Sh.K. Shaikhutdinov, M. Schildenberger, M. Noeske and G. Mestl, *React. Kinet. Catal. Lett.*, 67 (1999) 129, “Platinum colloid supported on graphite: x-ray photoelectron spectroscopy study”.
- [116] X. Wang, J. C. Yu, H. Y. Yip, L. Wu, P. K. Wong and S. Y. Lai, *Chem. Eur. J.*, 11 (2005) 2997, “A mesoporous Pt/TiO₂ nanoarchitecture with catalytic and photocatalytic functions”.
- [117] J. Radnik, C. Mohr and P. Claus, *Phys. Chem. Chem. Phys.*, 5 (2003) 172, “On the origin of binding energy shifts of core levels of supported gold nanoparticles and dependence of pretreatment and material synthesis”.
- [118] J. R. Croy, S. Mostafa, J. Liu, Y. Sohn, H. Heinrich and B. R. Cuenya, *Catal Lett*, 119 (2007) 209, “Support dependence of MeOH decomposition over size-selected Pt nanoparticles”.
- [119] Y. Li, F. P. Hu, X. Wang and P. K. Shen, *Electrochem. Comm.*, 10 (2008) 1101, “Anchoring metal nanoparticles on hydrofluoric acid treated multiwalled carbon nanotubes as stable electrocatalysts”.
- [120] J. Zhang, K. Sasaki, E. Sutter and R. R. Adzic, *Science*, 315 (2007) 220, “Stabilization of platinum oxygen-reduction electrocatalysts using gold clusters”.

[121] V. R. Stamenkovic, B. Fowler, B. S. Mun, G. Wang, P. N. Ross, C. A. Lucas and N. M. Marković, *Science* 315 (2007) 493, “Improved oxygen reduction activity on Pt₃Ni(111) via increased surface site availability”.

[122] Z. Chen, M. Waje, W. Li and Y. Yan, *Angew. Chem. Int. Ed.*, 46 (2007) 4060, “Supportless Pt and PtPd nanotubes as electrocatalysts for oxygen-reduction reactions”.

[123] R. Srivastava, P. Mani, N. Hahn and P. Strasser, *Angew. Chem. Int. Ed.*, 46 (2007) 8988, “Efficient oxygen reduction fuel cell electrocatalysis on voltammetrically dealloyed Pt-Cu-Co nanoparticles”.

[124] S. Chen and A. Kucernak, *J. Phys. Chem. B*, 108 (2004) 3262, “Electrocatalysis under conditions of high mass transport rate: oxygen reduction on single submicrometer-sized Pt particles supported on carbon”.



[125] S. Fan, M. G. Chapline, N. R. Franklin, T. W. Tomblor, A. M. Cassell and H. Dai, *Science*, 283 (1999) 512, “Self-oriented regular arrays of carbon nanotubes and their field emission properties”.

[126] T. Rueckes, K. Kim, E. Joselevich, G. Y. Tseng, C. L. Cheung and C. M. Lieber, *Science*, 289 (2000) 94, “Carbon nanotube-based nonvolatile random access memory for molecular computing”.

[127] J. M. Planeix, N. Coustel, B. Coq, V. Bretons, P. S. Kumbhar, R. Dutartre, P. Geneste, P. Bernier and P. M. Ajayan, *J. Am. Chem. Soc.*, 116 (1994) 7935, “Application of carbon

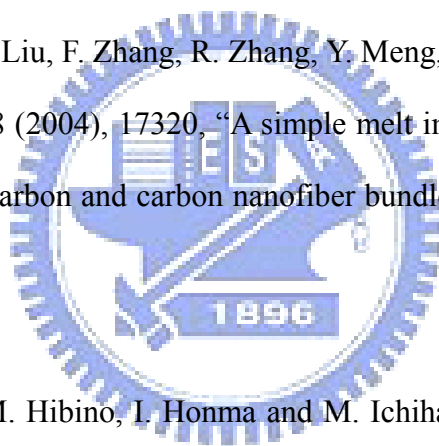
nanotubes as supports in heterogeneous catalysis”.

[128] N. M. Rodriguez, A. Chambers and R. T. K. Baker, *Langmuir*, 11 (1995) 3862, “Catalytic engineering of carbon nanostructures”.

[129] A. C. Dillon, K. M. Jones, T. A. Bekkedahl, C. H. Kiang, D. S. Bethune and M. J. Heben, *Nature*, 386 (1997) 377, “Storage of hydrogen in single-walled carbon nanotubes”.

[130] J. Lin, *Science*, 287 (2000) 1929, “Hydrogen storage in nanotubes”.

[131] H. Yang, Y. Yan, Y. Liu, F. Zhang, R. Zhang, Y. Meng, M. Li, S. Xie, B. Tu and D. Zhao, *J. Phys. Chem. B*, 108 (2004), 17320, “A simple melt impregnation method to synthesize ordered mesoporous carbon and carbon nanofiber bundles with graphitized structure from pitches”.



[132] H. Zhou, S. Zhu, M. Hibino, I. Honma and M. Ichihara, *Adv. Mater.*, 15 (2003) 2107, “Lithium storage in ordered mesoporous carbon (CMK-3) with high reversible specific energy capacity and good cycling performance”.

[133] J.-S. Yu, S. Kang, S. B. Yoon and G. Chai, *J. Am. Chem. Soc.*, 124 (2002) 9382, “Fabrication of ordered uniform porous carbon networks and their application to a catalyst supporter”.

[134] T. W. Kim, I. S. Park and R. Ryoo., *Angew. Chem. Int. Ed.*, 42 (2003) 4375, “A synthetic route to ordered mesoporous carbon materials with graphitic pore walls”.

- [135] A. B. Fuertes and S. Alvarez., Carbon, 42 (2004) 3049, “Graphitic mesoporous carbons synthesised through mesostructured silica templates”.
- [136] C. H. Kim, D. K. Lee and T. J. Pinnavaia, Langmuir, 20 (2004) 5157, “Graphitic mesostructured carbon prepared from aromatic precursors”.
- [137] C. M. Yang, C. Weidenthaler, B. Spliethoff, M. Mayanna and F. Schuth., Chem. Mater., 17 (2005) 355, “Facile template synthesis of ordered mesoporous carbon with polypyrrole as carbon precursor”.
- [138] F. Zhang, Y. Yan, H. Yang, Y. Meng, C. Yu, B. Tu and D.J. Zhao, J. Phys. Chem. B, 109 (2005) 8723, “Understanding effect of wall structure on the hydrothermal stability of mesostructured silica SBA-15”.
- [139] F. Ehrburger-Dolle, I. Morfin, E. Geissler, F. Bley, F. Livet, C. Vix-Guterl, S. Saadallah, P. Julien, M. Reda, J. Patarin, M. Ilescu and J. Werckmann, Langmuir, 19 (2003) 4303, “Small-angle x-ray scattering and electron microscopy investigation of silica and carbon replicas with ordered porosity”.
- [140] J. Parmentier, C. Vix-Guterl, P. Gibot, M. Reda, M. Ilescu, J. Werckmann and J. Patarin, Microporous. Mesoporous. Mater., 62 (2003) 87, “Study of the structural evolutions of mesoporous MCM-48 silica infiltrated with carbon by different techniques”.
- [141] Y. Gogotsi, A. Nikitin, H. Ye, W. Zhou, J. E. Fischer, B. Yi, H. C. Foley and M. W. Barsoum, Nat. Mater., 2 (2003) 591, “Nanoporous carbide-derived carbon with tunable pore size”.

- [142] K. Koczkur, Q. Yi and A. Chen, *Adv. Mater.*, 19 (2007) 2648, “Nanoporous Pt-Ru networks and their electrocatalytical properties”.
- [143] Z. L. Liu, X. Y. Ling, X. D. Su and J. Y. Lee, *J. Phys. Chem. B*, 108 (2004) 8234, “Carbon-supported Pt and PtRu nanoparticles as catalysts for a direct methanol fuel cell”.
- [144] A. Kabbabi, R. Faure, R. Durand, B. Beden, F. Hahn, J.-M. Leger and C. Lamy, *J. Electroanal. Chem.*, 444 (1998) 41, “In situ FTIRS study of the electrocatalytic oxidation of carbon monoxide and methanol at platinum–ruthenium bulk alloy electrodes”.
- [145] M. Watanabe, Y. M. Zhu, H. Igarashi and H. Uchida, *Electrochem.*, 68 (2000) 244, “Mechanism of CO tolerance at Pt-Alloy anode catalysts for polymer electrolyte fuel cells”.
- [146] G. S. Chai, I. S. Shin and J. S. Yu, *Adv. Mater.*, 16 (2004) 2057, “Synthesis of ordered, uniform, macroporous carbons with mesoporous walls templated by aggregates of polystyrene spheres and silica particles for use as catalyst supports in direct methanol fuel cells”.
- [147] R. V. Parthasarathy and C. R. Martin, *Nature*, 369 (1994) 298, “Synthesis of polymeric microcapsule arrays and their use for enzyme immobilization”.
- [148] G. Che, B. B. Lakshmi, E. R. Fisher and C. R. Martin, *Nature*, 393 (1998) 346, “Carbon nanotubule membranes for electrochemical energy storage and production”.

- [149] B. B. Lakshmi, P. K. Dorhout and C. R. Martin, *Chem. Mater.*, 9 (1997) 857, “Sol–gel template synthesis of semiconductor nanostructures”.
- [150] S. A. Sapp, D. T. Mitchell and C. R. Martin, *Chem. Mater.*, 11 (1999) 1183, “Using template-synthesized micro- and nanowires as building blocks for self-assembly of supramolecular architectures”.
- [151] X. Peng, K. Koczkur, S. Nigro and A. Chen, *Chem. Commun.*, 24 (2004) 2872, “Fabrication and electrochemical properties of novel nanoporous platinum network electrodes”.
- [152] X. Teng, X. Liang, S. Maksimuk and H. Yang, *Small*, 2 (2006) 249, “Synthesis of porous platinum nanoparticles”.
- [153] F. Cloaguen, J.-M. Leger and C. Lamy, *J. Appl. Electrochem.*, 27 (1997) 1052, “Electrocatalytic oxidation of methanol on platinum nanoparticles electrodeposited onto porous carbon substrates”.
- [154] G. R. Salazar-Banda, K. I. B. Eguiluz and L. A. Avaca, *Electrochem. Commun.*, 9 (2007) 59, “Boron-doped diamond powder as catalyst support for fuel cell applications”.
- [155] X. Teng, X. Liang, S. Rahman and H. Yang, *Adv. Mater.*, 17 (2005) 2237, “Porous nanoparticle membranes: synthesis and application as fuel-cell catalysts”.
- [156] J. N. Tiwari, F. M. Pan, R. N. Tiwari and S. K. Nandi, *Chem. Commun.*, 48 (2008) 6516,

“Facile synthesis of continuous Pt island networks and their electrochemical properties for methanol electro oxidation”.

[157] X. Peng and A. Chen, *Adv. Funct. Mater.*, 16 (2006) 1355, “Large-scale synthesis and characterization of TiO₂-based nanostructures on titanium substrate”.

[158] S. Hrapovic, Y. L. Liu, K. B. Male and J. H. T. Luong, *Anal. Chem.*, 76 (2004) 1083, “Electrochemical biosensing platforms using platinum nanoparticles and carbon nanotubes”.

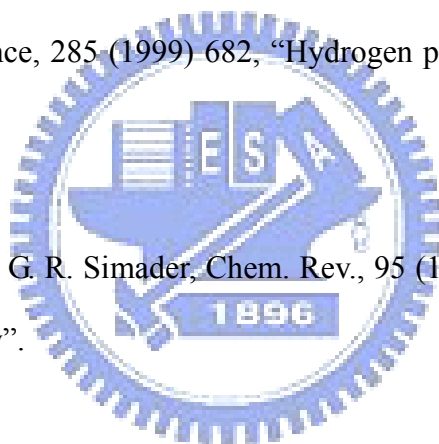
[159] R. F. Service, *Science*, 285 (1999) 682, “Hydrogen power: bringing fuel cells down to earth”.

[160] K. V. Kordesch and G. R. Simader, *Chem. Rev.*, 95 (1995) 191, “Environmental impact of fuel cell technology”.

[162] A. Rouxoux, J. Schulz and H. Patin, *Chem. Rev.* 102 (2002) 3757, “Reduced transition metal colloids: a novel family of reusable catalysts?”.

[162] S. H. Liu, R. F. Lu, S. J. Huang, A. Y. Lo, S. H. Chien and S. B. Liu, *Chem. Commun.*, 32 (2006) 3435, “Controlled synthesis of highly dispersed platinum nanoparticles in ordered mesoporous carbons”.

[163] R. M. Rioux, H. Song, J. D. Hoefelmeyer, P. Yang and G. A. Somorjai, *J. Phys. Chem. B*, 109 (2005) 2192, “High-surface-area catalyst design: synthesis, characterization, and reaction studies of platinum nanoparticles in mesoporous SBA-15 silica”.



[164] P. Jiang, J. F. Bertone and V. L. Colvin, *Science*, 291 (2001) 453, “A lost-wax approach to monodisperse colloids and their crystals”.

[165] K. S. Choi, E. W. Mcfarland and G. D. Stucky, *Adv. Mater.*, 15 (2003) 2018, “Electrocatalytic properties of thin mesoporous platinum films synthesized utilizing potential-controlled surfactant assembly”.

[166] G. S. Attard, P. N. Bartlett, N. R. B. Coleman, J. M. Elliott, J. R. Owen and J. H. Wang, *Science*, 278 (1997) 838, “Mesoporous platinum films from lyotropic liquid crystalline phases”.

[167] A. Fukuoka, H. Araki, Y. Sakamoto, N. Sugimoto, H. Tsukada, Y. Kumai, Y. Akimoto and M. Ichikawa, *Nano Lett.*, 2 (2002) 793, “Template synthesis of nanoparticle arrays of gold and platinum in mesoporous silica films”.

[168] D. V. Pugh, A. Dursun and S. G. Corcoran, *J. Mater. Res.*, 18 (2003) 216, “Formation of nanoporous platinum by selective dissolution of Cu from $\text{Pt}_{0.25}\text{Cu}_{0.75}$ ”.

[169] J. F. Huang and I. W. Sun, *Chem. Mater.*, 16 (2004) 1829, “Formation of nanoporous platinum by selective anodic dissolution of PtZn surface alloy in a Lewis acidic zinc chloride-1-Ethyl-3-methylimidazolium chloride ionic liquid”.

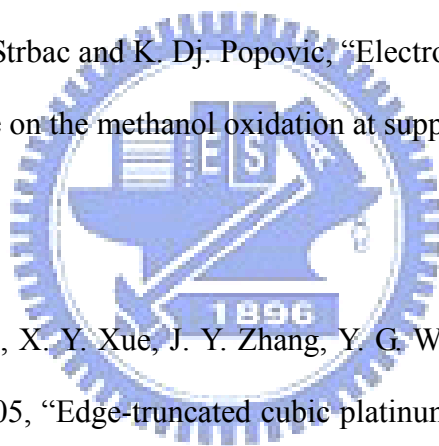
[170] H. T. Liu, P. He, Z. Y. Li and J. H. Li, *Nanotech.*, 17 (2006) 2167, “High surface area nanoporous platinum: facile fabrication and electrocatalytic activity”.

[171] P. Marcus and C. Hinnen, *Surf. Sci.*, 392 (1997) 134, “XPS study of the early stages of deposition of Ni, Cu and Pt on HOPG”.

[172] D. Kardash and C. Korzeniewski, *Langmuir*, 16 (2000) 8419, “Temperature effects on methanol dissociative chemisorption and water activation at polycrystalline platinum electrodes”.

[173] M. Bergelin, J. M. Feliu and M. Wasberg, *Electrochim. Acta*, 44 (1998) 1069, “Study of carbon monoxide adsorption and oxidation on Pt(111) by using an electrochemical impinging jet cell”.

[174] A. V. Tripkovic, S. Strbac and K. Dj. Popovic, *Electrochem. Commun.*, 5 (2003) 484, “Effect of temperature on the methanol oxidation at supported Pt and PtRu catalysts in alkaline solution



[175] Y. G. Liu, S. L. Shi, X. Y. Xue, J. Y. Zhang, Y. G. Wang and T. H. Wang, *Appl. Phys. Lett.*, 92 (2008) 203105, “Edge-truncated cubic platinum nanoparticles as anode catalysts for direct methanol fuel cells”.

[176] T. H. M. Housmans, A. H. Wonders and M. T. M. Koper, *J. Phys. Chem. B*, 110 (2006) 10021, “Structure sensitivity of methanol electrooxidation pathways on platinum: an on-line electrochemical mass spectrometry study”.

[177] N. M. Markovic and P. N. Ross Jr., *Surf. Sci. Rep.*, 45 (2002) 117, “Surface science studies of model fuel cell electrocatalysts”.

[178] E. Elmalem, A. E. Saunders, R. Costi, A. Salant and U. Banin, *Adv. Mater.*, 20 (2008)

4312, "Growth of photocatalytic CdSe–Pt nanorods and nanonets".

[179] L. Sun, D. V. Ca and J. A. Cox, *J. Solid State Electrochem.*, 9 (2005) 816, "Electrocatalysis of the hydrogen evolution reaction by nanocomposites of poly(amidoamine)-encapsulated platinum nanoparticles and phosphotungstic acid".

[180] N. Tian, Z. Y. Zhou, S. G. Sun, L. Cui, B. Ren and Z. Q. Tian, *Chem. Commun.*, 39 (2006) 4090, "Electrochemical preparation of platinum nanothorn assemblies with high surface enhanced Raman scattering activity".

[181] N. Toshima, Y. Shiraishi, T. Teranishi, M. Miyake, T. Dominica, H. Watanabe, W. Brijoux, H. Bonnemann and G. Schmid, *Appl. Organomet. Chem.*, 15 (2001) 178, "Various ligand-stabilized metal nanoclusters as homogeneous and heterogeneous catalysts in the liquid phase".

[182] Y. Sun and Y. Xia, *Science*, 298 (2002) 2176, "Shape-controlled synthesis of gold and silver nanoparticles".

[183] H. Lee, S. E. Habas, S. Kwekin, D. Butcher, G. A. Somorjai and P. D. Yang, *Angew. Chem. Int. Ed.*, 45 (2006) 7828, "Morphological control of catalytically active platinum nanocrystals".

[184] T. S. Ahmadi, Z. L. Wang, T. C. Green, A. Henglein and M. A. El-Sayed, *Science*, 271 (1996) 1924, "Shape-controlled synthesis of colloidal platinum nanoparticles".

[185] J. Y. Chen, T. Herricks, M. Geissler and Y. N. Xia, *J. Am. Chem. Soc.*, 126 (2004)

10854, "Single-crystal nanowires of platinum can be synthesized by controlling the reaction rate of a polyol process".

[186] T. Kijima, T. Yoshimura, M. Uota, T. Ikeda, D. Fujikawa, S. Mouri and S. Uoyama, *Angew. Chem. Int. Ed.*, 43 (2004) 228, "Noble-metal nanotubes (Pt, Pd, Ag) from lyotropic mixed-surfactant liquid-crystal templates".

[187] X. W. Teng and H. Yang, *Nano Lett.*, 5 (2005) 885, "Synthesis of platinum multipods: an induced anisotropic growth".

[188] M. H. Ullah, W. S. Chung, I. Kim and C. S. Ha, *Small*, 2 (2006) 870 "pH-Selective synthesis of monodisperse nanoparticles and 3D dendritic nanoclusters of CTAB-stabilized platinum for electrocatalytic O₂ reduction".

[189] I. Balint, A. Miyazaki and K. Aika, *Appl. Catal. B*, 37 (2002) 217, "NO reduction by CH₄ over well-structured Pt nanocrystals supported on γ -Al₂O₃".

[190] F. J. Vidal-Iglesias, J. Solla-Gullon, P. Rodriguez, E. Herrero, V. Montiel, J. M. Feliu and A. Aldaz, *Electrochem. Commun.*, 6 (2004) 1080, "Shape-dependent electrocatalysis: ammonia oxidation on platinum nanoparticles with preferential (100) surfaces".

[191] M. Inaba, M. Ando, A. Hatanaka, A. Nomoto, K. Matsuzawa, A. Tasaka, T. Kinumoto, Y. Iriyama and Z. Ogumi, *Electrochim. Acta*, 52 (2006) 1632, "Controlled growth and shape formation of platinum nanoparticles and their electrochemical properties".

[192] H. C. Ye and R. M. Crooks, *J. Am. Chem. Soc.*, 127 (2005) 4930, "Electrocatalytic O₂

reduction at glassy carbon electrodes modified with dendrimer-encapsulated Pt nanoparticles”.

[193] W. Yang, X. Wang, F. Yang, C. Yang and X. Yang, *Adv. Mater.*, 20 (2008) 2579, “Carbon nanotubes decorated with Pt nanocubes by a noncovalent functionalization method and their role in oxygen reduction”.

[194] D. Kim, N. Lee, M. Park, B. H. Kim, K. An and T. Hyeon, *J. Am. Chem. Soc.*, 131 (2009) 454, “Synthesis of uniform ferrimagnetic magnetite nanocubes”.

[195] B. Wiley, T. Herricks, Y. Sun and Y. Xia, *Nano Lett.*, 4 (2004) 1733, “Polyol synthesis of silver nanoparticles: use of chloride and oxygen to promote the formation of single-crystal, truncated cubes and tetrahedrons”.

[196] S. H. Im, Y. T. Lee, B. Wiley and Y. Xia, *Angew. Chem., Int. Ed.*, 44 (2005) 2154, “Large-scale synthesis of silver nanocubes: the role of HCl in promoting cube perfection and monodispersity”.

[197] M. H. Kim, B. Lim, E. P. Lee and Y. Xia, *J. Mater. Chem.*, 18 (2008) 4069, “Polyol synthesis of Cu₂O nanoparticles: use of chloride to promote the formation of a cubic morphology”.

[198] R. Zott, *Angew. Chem. Int. Ed.* 42, (2003), 3990, “Friedrich Wilhelm Ostwald (1853–1932), now 150 years young”.

[199] B. Liu, S. H. Yu, L. J. Li, F. Zhang, Q. Zhang, M. Yoshimura and P. Shen, *J. Phys.*

Chem. B, 108 (2004) 2788, Nanorod-direct oriented attachment growth and promoted crystallization processes evidenced in case of $ZnWO_4$.



Appendix

List of Publications

Journal papers:

- I. **Jitendra N. Tiwari** and Fu-Ming Pan “Synthesis and growth of platinum nanocubes at NTP” manuscript under preparation.
- II. **Jitendra N. Tiwari**, Rajanish N. Tiwari and Kun-Lin Lin “New approach to the synthesis of 3-D graphitic carbon for electrochemical application” manuscript under preparation.
- III. **Jitendra N. Tiwari**, Fu-Ming Pan, Te-Ming Chen, Rajanish N. Tiwari and Kun-Lin Lin “Electrocatalytic activity of Pt nanoparticles electrodeposited on amorphous carbon coated silicon nanocones” under review “*J. Power Sources*”.
- IV. **Jitendra N. Tiwari**, Fu-Ming Pan and Kun-Kun Lin “Facile approach to the synthesis of 3D platinum nanoflowers and their electrochemical characteristics” accepted “*New Journal of Chemistry*” 33 (2009) 1482-1485 .
- V. **Jitendra N. Tiwari**, Fu-Ming Pan, Rajanish N. Tiwari and S.K. Nandi “Facile synthesis of continuous Pt island networks and their electrochemical properties for methanol electrooxidation” *Chem. Commun.* 48 (2008) 6516-6518 .

- VI. **Jitendra N. Tiwari**, Te-Ming Chen, Fu-Ming Pan and Kun-Lin Lin “Ordered silicon nanocones as a highly efficient platinum catalyst support for direct methanol fuel cells” *J. Power Sources* 182 (2008) 510–514.
- VII. M. K. Bera, C. Mahata, A. K. Chakraborty, S. K. Nandi, **Jitendra N. Tiwari**, Jui-Yi Hung and C. K. Maiti “TiO₂/GeO_xN_y stacked gate dielectrics for Ge-MOSFETs” *Semicond. Sci. Technol.* 22 (2007) 1352–1361.

International conference

- I. S. K. Nandi and **Jitendra N. Tiwari** “High Temperature Electrical Properties of Ultra thin Ta₂O₅ Films on ZnO/n-Si Heterolayers” *IEEE, 10.1109/TWPSD* (2007) 417-419.
- II. **Jitendra N. Tiwari**, Te-Ming Chen, Rajanish N. Tiwari and Fu-Ming Pan “Oxygen Reduction Reaction Activity of Pt Nanoparticles Electrodeposited on Amorphous Carbon Coated Silicon Nanocones” Accepted for oral Presentation in “*214th ECS Meeting - Honolulu, HI*”, Abstract # 963 (15 Oct, 2008) .